



HAL
open science

Supercritical Antisolvent (SAS) Process Intensification through the use of High Pressure (HP) Microfluidic Mixing

Fan Zhang

► **To cite this version:**

Fan Zhang. Supercritical Antisolvent (SAS) Process Intensification through the use of High Pressure (HP) Microfluidic Mixing. Chemical and Process Engineering. Université de Bordeaux, 2019. English. NNT : 2019BORD0269 . tel-03456309

HAL Id: tel-03456309

<https://theses.hal.science/tel-03456309>

Submitted on 30 Nov 2021

HAL is a multi-disciplinary open access archive for the deposit and dissemination of scientific research documents, whether they are published or not. The documents may come from teaching and research institutions in France or abroad, or from public or private research centers.

L'archive ouverte pluridisciplinaire **HAL**, est destinée au dépôt et à la diffusion de documents scientifiques de niveau recherche, publiés ou non, émanant des établissements d'enseignement et de recherche français ou étrangers, des laboratoires publics ou privés.

THÈSE PRÉSENTÉE
POUR OBTENIR LE GRADE DE
DOCTEUR DE
L'UNIVERSITÉ DE BORDEAUX

ÉCOLE DOCTORALE DES SCIENCES CHIMIQUES
SPÉCIALITÉ Génie des procédés

Par Fan ZHANG

**Supercritical Antisolvent (SAS) Process Intensification
Through The Use Of High Pressure (HP) Microfluidic Mixing**

Sous la direction de : Samuel MARRE, Arnaud ERRIGUIBLE

Soutenue le 29 novembre 2019

Membres du jury :

Mme. AUBIN, Joelle	Chargée de Recherche CNRS - LGC, Toulouse	Examineur
Mme. BADENS, Elisabeth	Professeur, Univ. Aix-Marseille	Rapporteur
M. ERRIGUIBLE, Arnaud	Maître de Conférences, Bordeaux INP	Co-directeur
M. FALK, Laurent	Directeur de Recherche CNRS - LRGP, Nancy	Rapporteur
M. MAGLIONE, Mario	Directeur de Recherche CNRS - ICMCB, Univ. Bordeaux	Examineur
M. MARRE, Samuel	Chargé de Recherche CNRS - ICMCB, Bordeaux	Co-directeur

Contents

Acknowledgments	vii
Abstract	ix
Abstract in French	xi
Nomenclatures	xiii
Summary in French	1
Chapter I: General introduction	9
1.1 Precipitation by antisolvent process	9
1.2 Introduction to supercritical fluids	10
1.3 Development of supercritical antisolvent (SAS) processes	12
1.3.1 Role of the thermodynamics	15
1.3.1.1 Phase diagram of solvent-antisolvent mixture	16
1.3.1.2 Influence of the solute on the ternary mixture	18
1.3.1.3 Influence of the solvent	19
1.3.2 Role of hydrodynamics in SAS	24
1.3.2.1 Solution jet break-up observation	24
1.3.2.2 Jet break-up VS. dynamic surface tension	25
1.3.2.3 Direct experimental method for quantifying micromixing	28
1.3.2.4 Mixing hydrodynamics related to reactor configuration	29
1.3.3 Phenomena of nucleation and particle growth	32
1.4 Intensification towards the μ SAS and our contribution	33

Chapter II: Tools and methodologies	35
2.1 Experimental systems	35
2.1.1 Microfabrication	35
2.1.1.1 Materials	35
2.1.1.2 Facilities	37
2.1.1.3 Microfabrication steps	37
2.1.2 Micro Particle Image Velocimetry (μ PIV)	42
2.1.2.1 μ PIV principle	42
2.1.2.2 Chemicals and materials	43
2.1.2.3 Set-up	43
2.1.2.4 μ PIV experiment procedures	44
2.1.2.5 Software tools for processing velocity field	45
2.1.3 Turbulent mixing observation	46
2.2 Numerical modeling	47
2.2.1 Governing equations of the fluid mixing	48
2.2.1.1 Mass and momentum conservation equations	48
2.2.1.2 Mixture thermophysical properties	49
2.2.2 Precipitation modeling	51
2.2.2.1 Population balance equation	51
2.2.2.2 Supersaturation	52
2.2.2.3 Nucleation kinetic	52
2.2.2.4 Particle growth rate	54
2.2.3 Numerical procedure	55
2.2.3.1 Description of NOTUS CFD	55

2.2.3.2	Numerical methods	56
2.2.3.3	Geometry and boundary conditions	57
2.3	Summary	59
Chapter III: Hydrodynamics in microreactor: quantification of mixing		61
3.1	Fundamental mechanism of mixing	61
3.1.1	Fluid mixing categories for turbulent conditions	61
3.1.2	Experimental method for micromixing analysis	65
3.1.3	Micromixing modeling	68
3.1.3.1	Generalized mixing model (GMM)	68
3.1.3.2	Interaction by exchange with the mean (IEM)	69
3.1.3.3	Engulfment deformation diffusion (EDD) model	70
3.2	Methods for mixing quality estimation in this thesis	71
3.2.1	Model validation	72
3.2.2	Turbulent mixing observed by the high speed camera	75
3.2.3	Influence of non-ideal diffusion for turbulent mixing	76
3.2.4	Mixing quality determination and mixing time estimation	78
3.2.4.1	Intensity of segregation I_m	78
3.2.4.2	Time axis t	80
3.2.4.3	Characteristic mixing time t_m	82
3.2.5	Calculation of the energy dissipation rate ϵ	83
3.2.5.1	ϵ for laminar mixing	84
3.2.5.2	ϵ for turbulent mixing	86
3.3	Study of the laminar mixing in the microreactor	86

3.3.1	Fluid velocity and ethanol mass fraction field	88
3.3.2	Effects of the mixing conditions on the mixing quality	90
3.3.2.1	Influence of the total Reynolds number	90
3.3.2.2	Influence of the temperature	92
3.3.2.3	Influence of the CO ₂ fraction	93
3.4	DNS study of turbulent mixing	94
3.4.1	Grid sensitivity analysis	95
3.4.2	Simulation cases and turbulent mixing time	97
3.4.2.1	Influence of operating conditions	97
3.4.2.2	Influence of microchannel dimensions	101
3.4.3	General analysis of turbulent mixing conditions	103
3.5	Mixing time analysis	106
3.5.1	Mixing times for laminar conditions	106
3.5.2	Mixing times for turbulent conditions	106
3.5.3	Comparison with other micromixers	109
3.6	Summary	111
Chapter IV: Application on μSAS precipitation		113
4.1	μ SAS experiments in the microreactor	113
4.1.1	Solubility study of the TPE	114
4.1.2	μ SAS set-up	115
4.2	μ SAS simulation details	117
4.3	Determination of the interfacial tension σ	118
4.4	Interpretations of μ SAS simulation	121

4.4.1	General observations of the test No.1	121
4.4.2	Effects of operating parameters	128
4.4.3	Characteristic times of the precipitation	131
4.5	Summary	135
General conclusion and perspectives		137
References		141
Appendix I: Complementary details		149
Appendix II: Inertia-driven jetting regimes in microfluidic coflows		153

Acknowledgments

This PhD thesis has been mainly accomplished at the Institute of Condensed Matter Chemistry of Bordeaux, in French "Institut de Chimie de la Matière Condensée de Bordeaux" (ICMCB - CNRS UMR 5026 - France). The part of the numerical simulation in this work is based on the computational fluid dynamic code "NOTUS CFD", developed in the Institute of Mechanics and Engineering, in French "Institut de mécanique et d'ingénierie" (I2M - CNRS UMR 5295 - France). The massively parallel computing carried out in this thesis is guaranteed by the high performance computing resources of the MCIA (Mésocentre de Calcul Intensif Aquitaine). My researches have been financially supported by the French National Research Agency (ANR-17-CE07-0029 - SUPERFON) and the University of Bordeaux.

My sincere gratitude goes to the members of the jury who have taken the time to review, examine and report my manuscript, Ms. Elisabeth Badens, professor at the Aix-Marseille University, the rapporteur M. Laurent Falk, director of the LRGP (Laboratoire Réaction et Génie des Procédés), Ms. Joelle Aubin, research officer of the LGC (Laboratoire de Génie Chimique) and M. Mario Maglione, director of the ICMCB.

Moreover, I would like to thank all my colleagues and co-workers involved in this project, especially the group of the supercritical fluid of ICMCB and the department TREFLE of I2M. They have provided an excellent working atmosphere and guided me to achieve my research goals. Specifically, I would like thank M. Mario Maglione, director of the ICMCB, M. Cyril Aymonier, head of the supercritical fluid group for their warm welcome. I would express my greatest thanks to my thesis supervisors, M. Samuel Marre and M. Arnaud Erriguible for their valuable advices and guidance. The scientific helps offered by them encouraged me to overcome all encountered difficulties. I would acknowledge M. Stéphane Glockner, M. Antoine Jost, M. Antoine Lemoine and M. Mathieu Coquerelle for their assistance concerning the simulation code. I would also thank the members of the follow-up committee, Ms. Pascale Subra-Paternault and M. Christophe Pradere, for their supports at the mid-term of the thesis. Thanks to the experimental data of my colleague Thomas Jaouhari, I was able to determine numerically some parameters in the simulation part.

Finally, I would like to thank my parents and my family for their endless support dur-

ing my study. I appreciate the wonderful moments passed in France with all my friends: Alexandre, Angélique, Anthony, Aude, Baptiste, Béatrice, Corentin, Cyril, Damien, Farah, Guillaume, Jérémy, Junjie, Laura, Maria, Marie, Mathias, Nicolas, Olivier, Pauline, Pierre, Romain, Simon, Théo, Thomas, Valentina, Yongxian. Also I am thankful for the friendships with my Chinese friends in spite of the distance (En, Nan, Shuo, Yang, Yue, Yushen...).

Abstract

In the context of this thesis, we propose to study the thermo-hydrodynamic behavior of a mixture, a solvent and a supercritical antisolvent (CO₂) in a microfluidic chip, for conditions used in the Supercritical Antisolvent (SAS) process. This work is based on a complementary approach of both experiments and simulations through the use of advanced research techniques, such as the *in situ* characterization inside the microfluidic reactor (Micro-Particle Image Velocimetry) and the High Performance Computing. The objective of the thesis is to determine the favorable conditions for a "very good" mixture (total and fast) of species in terms of velocity, temperature, pressure and injector "design". The simulations are performed with the massively parallel code Notus. After the first chapter detailing the state of the art on the supercritical antisolvent processes, then the second concerning the applied methodologies (numerical model, microfluidic tools), we first compare the results of the numerical simulations to the experimental data obtained by micro-PIV in laminar flow conditions. The simulation results are in good agreement with the experiments. After the validation of the numerical code, we propose to use the numerical tool to determine the optimal operating conditions of mixing. For this, simulations of the mixture of two fluids (typically CO₂ and ethanol) are performed for different operating conditions (velocity, temperature, pressure) for laminar conditions but also for turbulent conditions, a regime rarely reached in microreactors. Indeed, we have shown experimentally that the turbulent mixing could be reached in the microchannel thanks to the "high pressure microfluidic" technology developed in the laboratory. The study of the mixing quality is based on two criteria commonly used in the literature. The first is the segregation intensity based on the variance of the ethanol concentration. This can be estimated for all simulation cases, from laminar to turbulent mixing. The second criterion is the micromixing time related to the turbulent kinetic energy dissipation rate directly estimated from the local velocity fluctuations in turbulent flow conditions. One of the major interests of the use of microfluidic reactors lies especially in its small scales of time and space. From a numerical point of view, such scales allow, within reasonable CPU time, to perform direct numerical simulations (DNS), i.e., in which the grid size is smaller or very close to the Kolmogorov scale. This is of primary interest because we are able to capture the smallest scales of the mixture including the micromixing. Thus, the simulation results allow us to propose a reliable analysis of the mixture from both qualitative and quantitative point of view, proving that the mixing conditions

in this type of device are particularly favorable for the material synthesis by supercritical antisolvent. After determining the optimal mixing conditions, we propose in a final part to simulate the synthesis of organic nanoparticles in such devices. The numerical approach is based on the coupling between the CFD code and a population balance equation to take into account the nucleation and growth of particles. The simulation results are also in a good agreement with the experimental measurements performed in the laboratory.

Abstract in French

Dans le cadre de cette thèse, nous nous proposons d'étudier le comportement thermo-hydrodynamique d'un mélange solvant/antisolvant supercritique dans une puce microfluidique, pour des conditions utilisées dans le procédé SAS (Supercritical Antisolvent System). Ce travail se base sur une approche complémentaire expérience/simulation via l'utilisation de techniques de recherches avancées telles que la caractérisation *in situ* sur puce microfluidique (micro-PIV - micro-Particle Image Velocimetry) et la simulation numérique intensive. L'objectif de la thèse est de définir les conditions favorables à un « très bon » mélange (total et rapide) des espèces en termes de vitesse, température, pression et « design » d'injecteur. Les simulations sont effectuées avec le code de calcul Notus, massivement parallèle. Après un premier chapitre détaillant l'état de l'art sur les procédés antisolvant supercritiques, puis un second concernant les méthodologies utilisées (modèle numérique, outils microfluidiques), nous comparons dans un premier temps les résultats des simulations numériques à ceux obtenus avec les expériences de micro-PIV en écoulement laminaire. La comparaison est très bonne pour l'ensemble des expériences réalisées. Le code de calcul ainsi validé, nous proposons d'utiliser l'outil numérique comme véritable outil de recherche des meilleures conditions opératoires pour favoriser le mélange. Pour cela, des simulations du mélange de deux fluides (typiquement CO₂ et éthanol) sont effectuées pour différentes conditions opératoires (vitesse, température, pression) pour des conditions laminaires mais également en conditions turbulentes, régime rarement atteint à ces échelles de réacteur. En effet, nous avons montré expérimentalement que le régime turbulent pouvait être atteint dans le microcanal grâce à la technologie « microfluidique haute pression » développé au laboratoire. L'étude de la qualité du mélange se base sur deux critères communément utilisées dans la littérature. Le premier est l'index de ségrégation basé sur la variance du champ de concentration ou fraction massique dans notre cas. Celui-ci peut être estimé pour tous les cas de simulation, du laminaire au turbulent. Le deuxième critère est le temps de micromélange basé sur l'estimation du taux de dissipation de l'énergie cinétique turbulente. Celui-ci est calculé uniquement dans les cas turbulents car basé sur les fluctuations des vitesses par rapport à la valeur moyenne. Un des intérêts majeurs de l'utilisation des puces microfluidiques réside notamment dans ses faibles échelles de temps et d'espace. D'un point de vue numérique, de telles échelles permettent, dans des temps de calcul raisonnables, de proposer des simulations numériques directes (DNS), i.e., dont les plus petites mailles sont inférieures ou très proches de l'échelle

de Kolmogorov. Ceci est de tout premier intérêt car nous sommes capables de capter les plus petites échelles du mélange et notamment le micromélange. Ainsi, les résultats de simulation nous ont permis de proposer une analyse fiable du mélange d'un point de vue qualitatif et quantitatif, faisant la preuve que les conditions de mélange dans ce type de dispositif sont particulièrement favorables pour l'élaboration de matériaux par antisolvant supercritique. Les conditions optimales de mélange ainsi déterminées, nous proposons dans une dernière partie de simuler la synthèse de nanoparticules organiques dans de tels dispositifs. L'approche numérique est basée sur un couplage des équations de la mécanique des fluides et d'une équation de bilan de population permettant de prendre en compte la nucléation et croissance des particules. Les résultats de simulation ont été comparés avec succès avec ceux expérimentaux obtenues au laboratoire.

Nomenclature

A	area	m^2
B	nucleation rate	$m^{-3}s^{-1}$
C	concentration (mass fraction in this study)	
D	diffusion coefficient	$m^2 \cdot s^{-1}$
D_{ID}	inner diameter of capillary	μm
D_{OD}	outer diameter of capillary	μm
D_h	hydraulic diameter	μm
Da	Damköhler number	
E	engulfment rate	s^{-1}
G	growth rate	$m \cdot s^{-1}$
I_m	intensity of segregation	
L	length	m
L_p	larger side length of trapezoidal channel cross-section	μm
L_s	smaller side length of trapezoidal channel cross-section	μm
M	molar mass	$kg \cdot mol^{-1}$
N	Total number	
N_a	Avogadro constant	
Pe	Péclet number for mass transfer	
Q	flowrate	$m^3 \cdot s^{-1}$
R	ideal gas constant	$J \cdot kg^{-1} \cdot K^{-1}$
R_{ID}	inner radius of capillary	μm

R_{OD}	outer radius of capillary	μm
Re	Reynolds number	
S	supersaturation degree	
Sc	Schmidt number	
Sh	Sherwood number	
$Solub$	solubility	
T	temperature	K
V	molar volume	$m^3 \cdot mol^{-1}$
\mathbf{g}	gravitational acceleration	$m \cdot s^{-2}$
\mathbf{u}	velocity vector	$m \cdot s^{-1}$
a	attraction parameter in Peng–Robinson equation of state	
b	covolume parameter in Peng–Robinson equation of state	
d	depth of microchannel	μm
$d^{non-ideal}$	driving force of the non-ideal diffusion	m^{-1}
d_p	particle size (diameter)	nm
j, k	coordinates in y and z directions	
k_a	surface factor of particle	
k_b	Boltzmann constant	
k_g	mass transfer coefficient	
k_{ij}, l_{ij}	interaction parameters in Peng–Robinson equation of state	
k_v	volume factor of particle	
l	mixing channel length	m
m_0	moment 0 (total particle number per unit volume)	$N \cdot m^{-3}$
m_1	moment 1 (total particle length per unit volume)	$m \cdot m^{-3}$

m_2	moment 2 (total particle surface per unit volume)	$m^2 \cdot m^{-3}$
m_3	moment 3 (total particle volume per unit volume)	$m^3 \cdot m^{-3}$
n	number density function	
p	pressure	<i>bar</i>
r^*	critical radius of nucleus	<i>nm</i>
t	time	<i>s</i>
t_d	time delay of the first order system	<i>s</i>
t_g	characteristic growth time	<i>s</i>
t_m	mixing time	<i>s</i>
t_n	nucleation time	<i>s</i>
t_p	precipitation time	<i>s</i>
t_v	hydrodynamic lifetime of vortex	<i>s</i>
u	absolute velocity in x direction	$m \cdot s^{-1}$
v	absolute velocity in y direction	$m \cdot s^{-1}$
w	absolute velocity in z direction	$m \cdot s^{-1}$
x	mass fraction	

Greek symbols

α	α function in Peng–Robinson equation of state	
ϵ	energy dissipation rate	$W \cdot kg^{-1}$ or $m^2 \cdot s^{-3}$
λ	microscale	μm
μ	dynamic viscosity	<i>Pa · s</i>
ν	kinematic viscosity	$m^2 \cdot s^{-1}$
ω	acentric factor	
ϕ	association factor in the Wilke-Chang correlation	

ρ	density	$kg \cdot m^{-3}$
ρ_p	density of solid particle	$kg \cdot m^{-3}$
σ	surface tension	$mN \cdot m^{-1}$
τ	characteristic time	s
φ	pressure increment	bar
$\hat{\varphi}$	fugacity coefficient	

Subscripts

0	initial conditions (initial temperature of pumps for fluid flowrates and temperature in channel for fluid velocities)
B	Batchelor
c	critical point
E	engulfment
$EtOH$	ethanol
exp	experiment
in	inner fluid
K	Kolmogorov
m	mixture
num	numerical simulation
out	outer fluid
sat	saturation

Summary in French

Cette thèse, dédiée à la compréhension du rôle prépondérant de l'hydrodynamique dans les procédés de précipitation par antisolvant supercritique (SAS), est divisée en 4 chapitres : une introduction générale sur ce procédé, les outils et les méthodologies proposés de cette étude, les analyses de l'hydrodynamique et notamment du mélange solvant-antisolvant dans notre microsystème et une application de l'approche pour précipiter des nanoparticules dans le microréacteur.

La première partie débute par la description des divers mécanismes impliqués lors de la précipitation par antisolvant. Le principe consiste à mélanger une solution (un soluté dissous dans un solvant) avec un autre fluide, appelé antisolvant, dans lequel le soluté a une très faible solubilité. Le mélange provoque alors la sursaturation du soluté. Les germes sont alors créés puis les particules commencent à croître jusqu'à l'équilibre thermodynamique dans le mélange des fluides. Après l'introduction du principe du procédé SAS, un état de l'art concernant l'étude des phénomènes physiques intervenant dans le procédé, la thermodynamique, l'hydrodynamique et la nucléation et la croissance des particules est présenté. La thermodynamique concerne l'équilibre des phases et la non-idéalité des fluides supercritiques. Les conditions opératoires du procédé, généralement permettant d'obtenir un mélange monophasique, sont ajustées par rapport au diagramme de phase du système solvant/antisolvant. Des conditions monophasiques de mélange solvant-anti-solvant sont recommandées pour un meilleur mélange afin de réduire la taille des particules produites. Si la pression et la température ne peuvent assurer une seule phase pour toutes les compositions de mélange, un équilibre gaz-liquide peut exister localement dans le réacteur, conduisant à une hydrodynamique complexe avec des écoulements diphasiques et une faible efficacité de mélange. Généralement, seuls les mélanges binaires solvant-antisolvant sont pris en compte dans la littérature car les effets thermodynamiques du soluté peuvent être négligés en raison de sa faible concentration. Cependant, des chercheurs ont montré que certains solutés pouvaient affecter l'équilibre du système quand sa concentration est élevée. Il est recommandé de vérifier l'influence du soluté sur l'équilibre thermodynamique du mélange, en particulier lors des concentrations élevées de soluté. L'influence de la concentration de soluté sur les tailles de particules précipitées reste incertaine pour divers solutés et différents équipements. Il semble qu'une conclusion générale soit compliquée à tirer concernant l'influence de la concentration car le changement de celle-ci peut entraîner une série

de variations de paramètres souvent corrélés entre eux. En conséquence, les changements de sursaturation, de nucléation et de vitesse de croissance dus à la concentration initiale du soluté doivent être étudiés en tenant compte du mélange des fluides. Un autre aspect thermodynamique est le choix du solvant. Le solvant doit offrir au soluté une solubilité considérable pour créer une sursaturation potentiellement élevée lorsqu'il est mélangé avec l'antisolvant. Ensuite, il doit être facilement miscible avec l'antisolvant supercritique, ce qui signifie que le point critique du mélange fluide doit être suffisamment bas dans le diagramme de phase pour éviter que trop d'énergie ne se dissipe entraînant alors une augmentation de la température et de la pression. Il convient de noter qu'une variation de température peut se produire dans le mélange due aux enthalpies d'excès de mélange des espèces. Le mélange de la solution et de l'antisolvant supercritique joue donc un rôle crucial dans le procédé SAS. En effet, le mélange affecte largement la sursaturation, la force motrice de la précipitation, et par conséquent la taille finale des particules et également la distribution de taille. Il est important d'accélérer le mélange des fluides afin d'intensifier le procédé. Dans la littérature, des études expérimentales ont été réalisées par analyse optique du mélange des fluides dans les réacteurs. La dynamique des jets de solvant pur et de solution a révélé qualitativement le comportement de mélange des fluides autour du point critique du mélange. D'après ces observations, lorsque le mélange de fluides est dans sa zone complètement miscible au-dessus du point critique de mélange, les deux fluides impliqués sont beaucoup mieux mélangés, fournissant un degré de sursaturation plus élevé de sorte que des particules produites soient plus petites. Étant donné que l'hydrodynamique du mélange aux échelles de diffusion moléculaire est essentielle pour comprendre et contrôler le procédé, des recherches récentes ont proposé une approche *in situ* de spectroscopie Raman unidimensionnelle pour capturer directement le micromélange de fluides. Des études supplémentaires sont nécessaires pour optimiser le micromélange. Le dernier aspect hydrodynamique de mélange est la configuration de réacteur. Afin d'avoir un mélange rapide, différents systèmes peuvent être trouvés dans la littérature avec différents types de configurations d'introduction de fluide. Le mécanisme de précipitation des particules a été bien étudié depuis des décennies et son modèle cinétique est connu et appliqué dans de nombreuses recherches. Cependant, pour le procédé SAS, il est difficile d'étudier expérimentalement la nucléation et la croissance des particules en raison d'une vitesse de nucléation extrêmement rapide. Une autre difficulté réside dans la méconnaissance de la tension superficielle entre particules solides et mélange fluide supercritique qui est difficilement mesurable par l'expérience. Afin de mieux compren-

dre le procédé et l'influence des paramètres, la modélisation numérique est appliquée pour simuler la mise en forme des particules et est alors comparée aux résultats expérimentaux. Plusieurs challenges concernant la modélisation numérique sont relevés dans la littérature et concerne notamment une meilleure prise en compte de la turbulence et du micro-mélange ainsi que l'estimation de la tension surface fluide/solide.

Dans le cadre de cette thèse, nous nous proposons d'étudier le comportement thermohydrodynamique d'un mélange solvant/antisolvant supercritique dans une puce microfluidique dans lequel les conditions opératoires sont mieux contrôlées que dans les réacteurs conventionnels, pour des conditions utilisées dans le procédé SAS (Supercritical Antisolvent System). Ce travail se base sur une approche complémentaire expérience/simulation via l'utilisation de techniques de recherches avancées telles que la caractérisation *in situ* sur puce microfluidique (micro-PIV) et la simulation numérique intensive. L'objectif de la thèse est de définir les conditions favorables à un « très bon » mélange (total et rapide) des espèces en termes de vitesse, température, pression et « design » d'injecteur.

Dans le deuxième chapitre, nous présentons les outils expérimentaux et numériques. Premièrement, la microfabrication, comprenant plusieurs étapes, est détaillée. Les canaux sont gravés par une réaction chimique et le collage anodique assure la résistance à haute pression, qui permet d'atteindre les conditions du procédé SAS. Une fois la micropuce fabriquée, elle est intégrée dans notre système expérimental de la micro vélocimétrie par images de particules (μ PIV). Dans cette méthode, des particules fluorescentes sont initialement ajoutées dans le solvant et suivent les lignes de courant du fluide. Leurs vitesses peuvent être simplement calculées grâce aux suivis du déplacement des particules pour une courte durée Δt . Avec ce montage, nous avons effectué des séries de mesures sur le profil des vitesses de fluide dans le microcanal d'intérêt. Ces mesures *in situ* nous ont permis de valider notre modèle numérique. Grâce à une caméra à haute vitesse, nous sommes également capables d'observer le mélange turbulent dans le microcanal sous pression. D'un point de vue de la modélisation physique, les 3 phénomènes doivent être considérés, la thermodynamique, l'hydrodynamique et la nucléation et la croissance de particules. Concernant la méthode numérique, nous avons choisi le code de calcul intensif (HPC), développé au sein du département TREFLE à l'I2M. Le code massivement parallèle nous permet de réaliser des simulations en 3 dimensions aux petites échelles, notamment à celles de Kolmogorov et de Batchelor. Les équations utilisées pour le mélange des fluides comprennent l'équation

Navier-Stokes pour la conservation de la quantité de mouvement, l'équation de transport d'espèce pour calculer les fractions des composants dans le mélange des fluides. Les propriétés de mélange, telle que la masse volumique, la viscosité et le coefficient de diffusion, sont calculées respectivement par l'équation d'état de Peng-Robinson, la moyenne molaire logarithmique et la corrélation Hayduk-Minhas pour la diffusion idéale. La turbulence de l'écoulement est prise en compte par simulation numérique directe (DNS) à l'échelle de Kolmogorov. La formation des particules solides est prise en compte par l'équation de bilan de population. Afin de résoudre numériquement cette équation, nous utilisons la méthode standard des moments (SMOM). Le degré de sursaturation est également quantifié ainsi que la vitesse de la croissance des particules. La nucléation et la croissance des particules se produisant à des échelles de diffusion moléculaire ou l'échelle de Batchelor, le mélange turbulent du solvant et de l'antisolvant estimé à cette échelle est un paramètre clé afin de calculer avec précision la sursaturation.

La troisième partie est dédiée à l'étude du mélange l'éthanol et CO₂ supercritique dans notre microsystème. Les résultats sont présentés séparément pour les écoulements laminaires et turbulents. Nous avons tout d'abord validé notre modèle numérique avec des résultats expérimentaux pour des conditions laminaires. Après avoir comparé les profils de vitesses dans le microcanal sous plusieurs conditions différentes, nous avons prouvé que le modèle est capable de simuler correctement le comportement hydrodynamique du mélange de solvant et d'antisolvant. De plus, avec la caméra rapide, nous avons observé le mélange turbulent sous pression dans le microréacteur. Après la validation du modèle, la qualité du mélange est examinée et quantifiée en considérant une constante de temps de mélange, calculée à partir de l'intensité de ségrégation. L'évolution de cette intensité correspond à la rapidité du système pour atteindre un mélange homogène ou complet. Afin de valider les constantes de temps déterminées par l'intensité de ségrégation, nous avons ensuite calculé le taux de dissipation d'énergie. Dans les conditions laminaires, celle-ci est calculée par une relation analytique. Pour les conditions turbulentes, elle est déterminée localement à partir des gradients de fluctuations de vitesse. Les résultats obtenus sont comparés avec les relations de la littérature et notamment celle proposée par Baldyga et son modèle EDD. Nous avons déterminé le temps de mélange aux conditions laminaires pour différentes conditions opératoires. Nous concluons que même s'il est compliqué d'extraire l'influence d'un seul paramètre sur l'efficacité de mélange, nous avons pu identifier quelques tendances générales basées sur les cas simulés. Un nombre de Reynolds global plus élevé mène à une meilleure

qualité de mélange. En effet, l'augmentation du nombre de Reynolds indique normalement un taux de dissipation d'énergie plus élevé, de sorte que le temps de mélange est réduit. Une augmentation du rapport CO₂/éthanol améliore le transfert de masse dans le mélange en augmentant le cisaillement généré par une différence importante entre les vitesses des fluides à la sortie de l'injecteur. Ce cisaillement dans certains cas génère des tourbillons à la sortie de l'injecteur, ce qui contribue largement à diminuer le temps de mélange. Selon les résultats de la simulation, une augmentation de la température améliore le mélange en raison à la fois d'une diffusion plus efficace et d'une contrainte de cisaillement lié au changement de la masse volumique. En général, un nombre de Reynolds plus élevé, une température élevée et un fort ratio CO₂/éthanol sont recommandés pour accélérer le mélange des fluides. Pour les mêmes fluides, le mélange turbulent a été analysé quantitativement par la simulation numérique directe dont la taille de maille est réduite en dessous de l'échelle Kolmogorov. La taille de maille a été déterminée selon une étude de convergence. Nous avons déterminé comme aux régimes laminaires les temps de mélange avec l'intensité de ségrégation. La dissipation d'énergie a été aussi calculée pour définir la zone de mélange pour les écoulements turbulents. Dans cette zone, nous avons sélectionné la dissipation moyenne pour calculer le temps de mélange selon le modèle EDD. Comme pour les conditions laminaires, nous avons analysé l'influence des conditions opératoires. Pour les deux régimes, les temps de mélange caractéristiques estimés dans notre étude sont en bon accord avec les relations théoriques. En comparant les performances du mélange de fluides dans notre microréacteur aux autres micromélangeurs de la littérature, nous avons pu montrer la capacité de notre micropuce à atteindre des temps de mélange deux ordres de grandeur plus petits que ceux rapportés dans les études précédentes, jusqu'à 0,01 ms. Ce résultat est réalisable grâce à l'utilisation de fluides supercritiques dans les systèmes microfluidiques. Après avoir démontré la haute performance du mélange de fluides dans le microréacteur, nous avons proposé d'examiner examiné numériquement la précipitation dans le procédé μ SAS dans le dernier chapitre. Ces résultats simulés ont été comparés aux résultats expérimentaux réalisés dans une autre thèse à l'ICMCB.

Dans le dernier chapitre, le code numérique est utilisé pour prédire la distribution de taille de particules dans le cas de la mise en forme de nanoparticules fluorescentes. La méthodologie consiste à coupler les équations hydrodynamiques avec une équation de bilan de population. Ici, la difficulté principale est d'estimer la tension surface entre le solide et le mélange des fluides supercritiques. Celle-ci a alors été ajustée par rapport aux données ex-

périmentales de la distribution en taille. Cette approche couplée numérique/expérimentale permet de déterminer ce paramètre important avec une grande confiance. Le travail expérimental de Thomas Jaouhari à l'ICMCB est brièvement présenté dans cette partie : la mesure de la solubilité du soluté 1,1,2,2-tétraphényléthylène (TPE) dans le mélange de solvant tétrahydrofurane (THF) et d'antisolvant CO₂ supercritique, la précipitation des nanoparticules par le procédé μ SAS, et la caractérisation de la distribution de taille. La distribution granulométrique est calculée en appliquant une distribution log-normale en fonction des valeurs moyennes temporelles des moments. La tension surface a été estimée et sa valeur représente le meilleur accord avec la taille et la distribution des particules obtenues à partir de l'expérience. Il est observé une très forte influence de la tension superficielle sur la distribution. En effet, une légère variation peut conduire à une distribution très différente (taille et largeur de la distribution). Même si peu d'information peut être trouvée dans la littérature pour la tension surface d'un solide dans un fluide supercritique, la valeur déterminée semble être cohérente avec certains travaux précédents. Plusieurs champs de variables importantes sont illustrés et analysés. Les variables examinées comprennent les fractions massiques de THF et TPE, le temps de mélange, le degré de la sursaturation, les cinétiques de la nucléation et la croissance des particules, les moments et les tailles des particules. L'influence des vitesses des fluides et de la concentration initiale du soluté TPE a été discutée. Une diminution de vitesses engendre un mélange inefficace avec un temps de mélange important. Dans ce cas, les tailles de particule sont plus grandes, prouvé par l'expérience et la simulation. Quant aux effets de la concentration de TPE, une concentration plus forte change peu les tailles de particules. Néanmoins, plus de tests devront être effectués afin de discuter plus en profondeur l'influence de la concentration du soluté sur la tension surface. Il est important de rappeler que le modèle numérique fournit des résultats très fiables par rapport aux données expérimentales avec seulement un paramètre ajustable. Afin de comparer le mélange aux phénomènes de la précipitation, les temps de nucléation et de précipitation ont été estimés. Le temps caractéristique des précipitations est défini dans cette étude comme le moment où la taille moyenne des particules atteint une valeur stable. Plusieurs méthodes ont été utilisées pour déterminer le temps de nucléation dans cette thèse. La définition la plus pertinente est l'inverse du taux de nucléation dans la cellule discrétisée. Le nombre adimensionnel de Damköhler (Da) est utilisé pour relier l'échelle de temps de nucléation et de précipitation à la vitesse des phénomènes de transport se produisant dans le microsystème. En général, un mélange extrêmement rapide peut être

atteint dans notre microréacteur pour le procédé μ SAS de l'ordre de 10^{-5} s (0,01 ms). Le même ordre de grandeur a été trouvé pour la nucléation, beaucoup plus petit que le temps de précipitation global. Par conséquent, ces conditions sont très favorables pour précipiter les nanoparticules de TPE avec une distribution de taille étroite.

En conclusion, l'objectif principal de cette thèse était d'examiner et de quantifier les comportements de mélange dans des conditions de procédé SAS dans un réacteur microfluidique. Nous avons pu montrer que le μ SAS offre des conditions très favorables au procédé. Une attention particulière a été portée sur la « capture » du micromélange pour des conditions turbulentes pour des échelles comprises entre l'échelle de Kolmogorov et l'échelle de Batchelor. Nous avons proposé dans cette thèse d'étudier les mécanismes fondamentaux d'un procédé μ SAS intensifié grâce à des approches expérimentales/numériques complémentaires. L'originalité de cette thèse a été d'offrir un aperçu du micromélange en conditions SAS par des expériences et des simulations numériques. Grâce à des résultats de simulation vérifiés sur la thermo-hydrodynamique du mélange, nous avons été capables de déterminer correctement les effets des paramètres et de prédire précisément les propriétés des nanoparticules dans notre microréacteur.

Chapter I: General introduction

Nanoparticle precipitation or crystallization is an important chemical process in many medical applications and in the electronic industry as well. In this thesis, we are interested in the supercritical antisolvent (SAS) process because of its fascinating potential to fabricate tiny nanoparticles with narrow size distribution. Indeed, the process benefits of the special properties of the supercritical fluids, a liquid-like density and a gas-like diffusivity. In this part, after the presentation of the SAS process and the involved physical phenomena, we focused on fundamental studies of the literature which allowed a better understanding of this complex process. The analysis of the literature will bring us to present the strategy that we aim to develop: the use of microfluidic system for a process intensification and for a deep understanding of the mechanism, facilitated by very well controlled operating conditions.

1.1 Precipitation by antisolvent process

The methods to fabricate small powders can be generally divided into two categories: top-down and bottom-up. The former one consists of mechanical ways to reduce particle size, as grinding. Contrariwise, the bottom-up approach aims to create the solid phase of particles and the classical method is the precipitation (or crystallization). Compared to the top-down method, it is more likely to produce nanoparticles in narrow size distribution by the bottom-up approach with no mechanic energy dissipated during the process. Among all the bottom-up methods, the antisolvent process is an interesting one. The principle consists of mixing a solution (a solute dissolved in a solvent) with another fluid, named antisolvent, in which the solute has a very low solubility. The mixing causes solute supersaturation. Solute nuclei are created then the particles begin to grow until the thermodynamic equilibrium of the fluid mixture.

Unlike the conventional precipitation process by changing the temperature to induce the supersaturation in the solution, the antisolvent process works in isothermal conditions so it is an energy saving method. As the supersaturation is related to the mixing of the solution and the antisolvent, some limitations exist for the antisolvent process. The selected solute must have a relatively high solubility in the solvent and the solvent should be miscible with the antisolvent. This requirement limits the choice of the target solute, often the organic materials because some good solvents commonly used are not miscible with water, which

plays normally the role of the antisolvent. Another disadvantage is related to the separation of the solvent and the antisolvent at the end of process and this step may involve a large quantity of energy for liquid recovery. Furthermore, it seems that the precipitated particle sizes can vary from 10 nanometer to 10 micrometer, depending largely on the fluid mixing in the reactor (Thorat and Dalvi, 2012). In order to decrease the particle size, high and homogeneous supersaturation is needed so the mixing of solvent and antisolvent is crucial. Some unusual methods are often applied into the reactor, as the ultrasound, to improve mixing, leaving complex fluid hydrodynamics.

The inconvenience of solvent/antisolvent miscibility in the antisolvent process can be improved when the antisolvent is replaced by a supercritical fluid, often the supercritical CO₂. It can be easily mixed with many organic solvents. Additionally, the separation issue can also be easily solved by using a supercritical fluid as antisolvent. Before to present the supercritical antisolvent process, we first introduce the supercritical fluids.

1.2 Introduction to supercritical fluids

By following the liquid-gas equilibrium curve in a temperature-pressure phase diagram, each fluid can reach to its critical point. When the temperature and the pressure are above the critical point, the fluid becomes supercritical in one single phase with no more interface between liquid and vapor. The properties of the supercritical fluids are comprised between the ones of the liquid and the ones of the gas and these properties give supercritical fluids many advantages to improve the conventional chemical processes. An example is shown in Figure 1 for CO₂. As can be seen, by following the liquid-gas equilibrium curve, the critical point can be reached (around $T = 31\text{ }^{\circ}\text{C}$, $P = 7.38\text{ MPa}$). The molecule distance of the supercritical CO₂ illustrated in Figure 1 indicates that the distance between two molecules can vary. It can be long as a gas and short as a liquid at microscopic scale but the supercritical fluid is homogeneous at macroscopic length. Consequently, supercritical conditions offer special fluid properties: a density closed to a liquid and a viscosity like a gas, allowing supercritical fluids to be an excellent medium for numerous applications in the chemical industry (Jung and Perrut, 2001; Beckman, 2004; Reverchon and De Marco, 2006; Cooper, 2000).

Despite many advantages of using supercritical fluids, it may be costly to reach supercritical conditions because of the harsh conditions of some critical points (temperature,

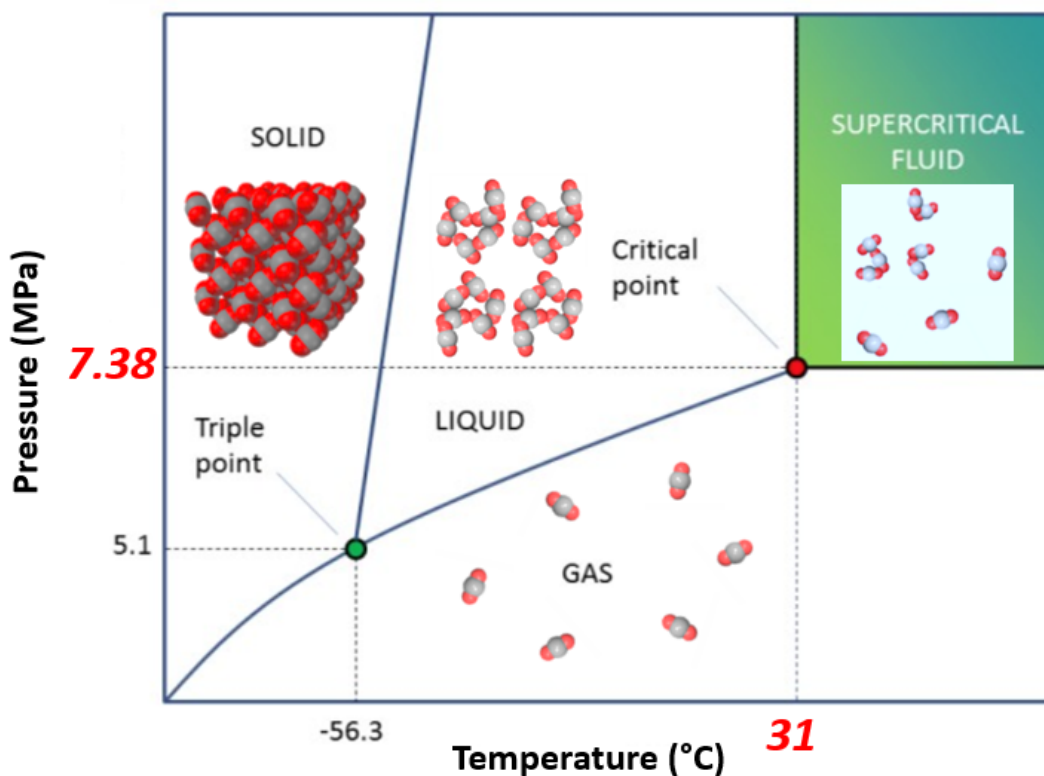


Figure 1: Phase diagram of CO₂ with supercritical zone.

pressure) for certain fluids (see Table 1). Besides the energy expense for the temperature and the pressure increase, process safety and facilities are also questioned when some highly reactive fluids are used under extreme conditions. After decades of technology development, this aspect has largely progressed and intriguing inventions, as high pressure resistant pumps, tubes and reactors, support researchers to study and use supercritical fluid in their processes.

The Table 1 reports the critical coordinates of the most usual and most used fluids. One of the most interesting one is carbon dioxide CO₂, due to its low critical point at 30.978 °C and 73.773 bar. Additionally, CO₂ is quite easily purchased at low price and quite inert chemically speaking. Thanks to its properties' sensitivity to temperature and pressure, the supercritical CO₂ is attractive for fundamental studies, allowing finely tuning the medium's properties (density, viscosity, etc...). The supercritical CO₂ can be well mixed with a lot of ordinary organic solvents as ethanol, acetone, tetrahydrofuran (THF) in their monophasic conditions. Therefore, as a solvent, supercritical CO₂ has been largely studied for extraction due to the high solubility of certain molecules of interest (Sahena *et al.*, 2009). On the other

Table 1: Critical points of some common fluids and their densities at critical points (data from NIST, "Dimethyl Sulfoxide (DMSO) – Technical" ^[a] and Majer and Svoboda (1985) ^[b]).

Fluid	T_c (°C)	P_c (bar)	ρ_c (kg/m ³)
Acetone	234.95	47.0	272.97
Ammonia	132.25	113.33	225.0
Butane	151.98	37.96	228.0
Carbon dioxide	30.978	73.773	467.6
Carbon monoxide	-140.29	34.94	303.91
Dimethyl sulfoxide ^[a]	447	56.3	
Ethanol	241.56	62.68	273.19
Hexane	234.67	30.34	233.18
Methanol	239.45	81.035	275.56
Pentane	196.55	33.7	232.0
Propane	96.74	42.512	220.48
Tetrahydrofuran ^[b]	267.05	51.9	
Toluene	318.6	41.263	297.99
Water	373.95	220.64	322.0

hand, due to the low solubility of many organic materials and polymers in supercritical CO₂, this one can also serve as antisolvent (Kalani and Yunus, 2011). According to the reasons mentioned above, despite the acceptable cost to attain it supercritical conditions, the use of supercritical CO₂ as antisolvent shows a great interest and has drawn researchers' attention for decades.

1.3 Development of supercritical antisolvent (SAS) processes

The principle of the SAS process is shown in Figure 2. Similar to the liquid antisolvent process, the supersaturation is induced by the mixing of solution (solute + solvent) and antisolvent under supercritical conditions. The system is initially pressurized. At a stable and higher pressure than the critical pressure of CO₂, the solution and the liquid CO₂ are injected and heated before entering into the reactor. The precipitation occurs in the reactor due to supersaturation, created by the mixing of the solvent and the CO₂ in their monophasic supercritical phase. The precipitated particles are filtered in the reactor and the supercritical fluid mixture is recovered in a downstream container. The separation of fluid mixture can be carried out simply by depressurizing the system.

The SAS process is considered as a very promising way to produce fine precipitated

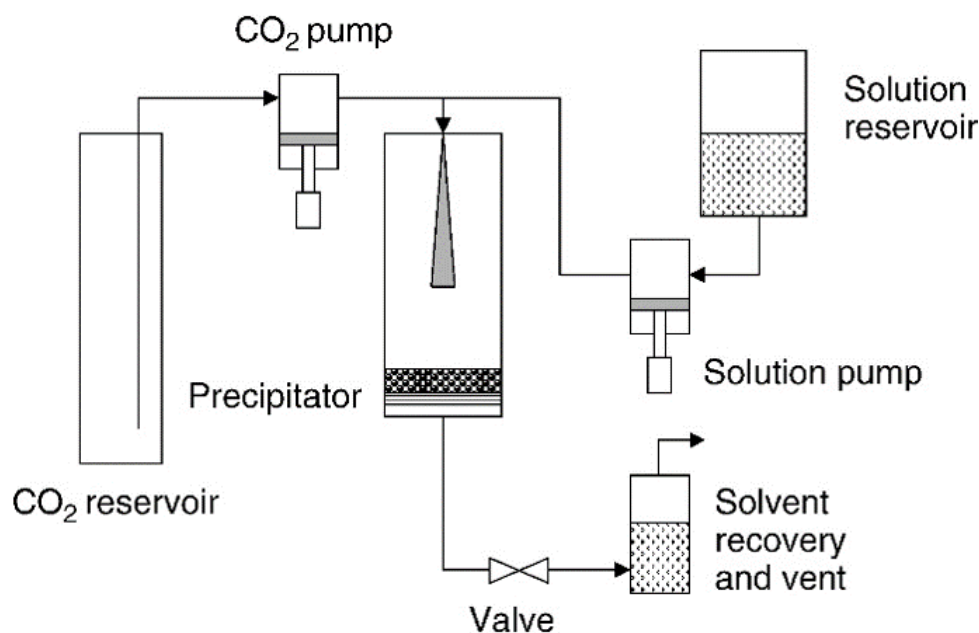


Figure 2: Scheme of the SAS process and principle explanation (image adapted from (Martin and Cocero, 2008)).

particles. Compared to the liquid antisolvent (room temperature and atmosphere pressure), the advantages of the SAS process with the supercritical CO₂ as antisolvent are summarized in three aspects.

- 1. The miscibility of the solvent and the antisolvent is largely enhanced. Supercritical CO₂ is miscible with numerous commonly used organic solvents to provide potentially efficient fluid mixing. As many ordinary solutes have a very low solubility in supercritical CO₂, more choices of organic solutes can be applied in the SAS process.
- 2. The viscosity of the fluid mixture is decreased, close to the viscosity of gas. It is possible to mix fluids at high velocity with low energy cost and low pressure drop, involving an efficient mixing.
- 3. The separation of the solvent and the antisolvent can be easily achieved only by depressurizing the fluid mixture at the end of the process. The solvent is recycled in the liquid phase and the CO₂ antisolvent in the gas. Because of the ease of fluid recycling as well as the non-toxic and harmless properties of CO₂, the SAS precipitation is a green process and it meets the requirements of the sustainable development.

During the SAS process, the driven force of the nucleation and the particle growth is the supersaturation, which can be simply expressed as the supersaturation degree S , the ratio of the actual solute concentration C to its solubility C_{sat} in the fluid mixture ($S = \frac{C}{C_{sat}}$). This value in a real reactor is mainly affected by the intrinsic thermodynamic properties of the ternary system (solute, solvent and antisolvent), the process conditions (temperature and pressure) as well as the fluid hydrodynamics during the mixing of the solution and the antisolvent. In the case of an inefficient mixing (slow and segregated), the supersaturation gradient is significant, which implies that solute nuclei grow at different rates, resulting in a large particle size distributions. On the contrary, a fast mixing promotes less solute concentration gradient and consequently, the precipitated particles are smaller with a narrow size distribution. Consequently, the mixing is an essential aspect of the SAS process because the chief objective is to produce particles as fine and homogeneous as possible.

In order to obtain the optimal process conditions through experiments, researchers aim at figuring out the influences of the operational parameters, mainly the temperature, the pressure, the initial solute concentration in the solution, the selection of solvents, the fluid flow rates and the fluid introduction configuration (*eg.* concentric coflow, impinging flow, other designs and geometries of fluid introduction).

However, some controversial results are found in the literature, concerning the influence of the parameters. Some authors demonstrated that an increase of the initial solute concentration leads to an increase of the mean particle size (De Marco and Reverchon, 2011; Rossmann *et al.*, 2014). Whereas, based on the results of Boutin (2012), opposite effects were found and a concentration increase in initial solution leads to a decrease of the mean particle size. Concerning the temperature, several teams made opposite claims on the temperature dependency of the particle size (Miguel *et al.*, 2008). For most of researches, temperature increase produces larger particles (De Marco and Reverchon, 2011; Campardelli *et al.*, 2017; Chang *et al.*, 2008). However, Miguel *et al.* (2008) fixed other conditions and increased the temperature from 308K to 318K without any evidence of particle average size change. Even smaller particles were precipitated at 250 bar with a temperature increase of 30 degrees in the study of Montes *et al.* (2015). These controversial conclusions imply the complexity of SAS precipitation and the necessity of a fundamental study coupled with numerical modeling to understand this process in depth.

Indeed, behind the apparent simplicity of process mechanism, the SAS precipitation is

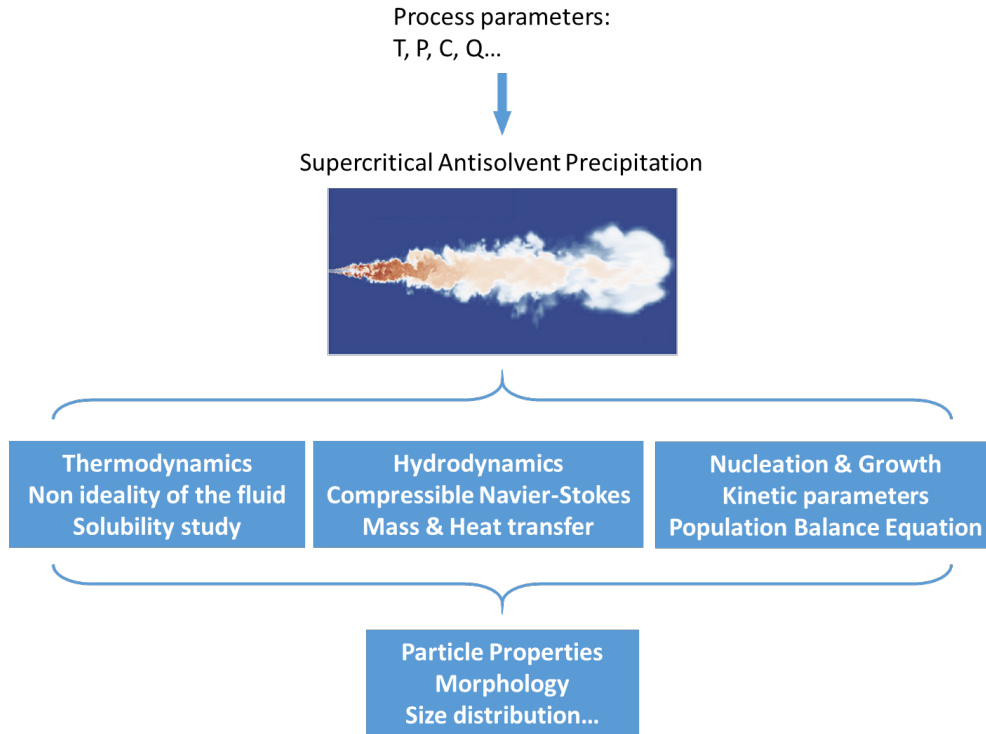


Figure 3: Schema of a brief understanding of SAS (picture imported from (Neurohr *et al.*, 2016)).

driven by various physical phenomena indicated in Figure 3, namely:

- the thermodynamics, concerning the phase equilibrium and the non ideality of supercritical fluids;
- the hydrodynamics, especially mass transfer during fluid mixing;
- the nucleation and the particle growth.

The properties of the final precipitated particles are influenced by all the phenomena working together. So, for a better understanding of the process, several fundamental studies are reviewed in the next parts, concerning the different phenomena occurring in the SAS process: the thermodynamics, the hydrodynamics, the nucleation and particle growth.

1.3.1 Role of the thermodynamics

This section presents the studies focused on the thermodynamics in SAS.

1.3.1.1 Phase diagram of solvent-antisolvent mixture

The phase diagram is an important and useful tool to study the thermodynamics of a pure fluid or a fluid mixture. In this thesis, we analyze the binary system of solvent and antisolvent (ethanol and CO₂ respectively) by the phase diagram of Pxy type, for instance Figure 4. In this kind of phase diagram, the x axis is the CO₂ fraction and the y axis is the pressure. The bubble points and the dew points are plotted for different temperatures. For a mixture of constant CO₂ fraction, while the pressure of the mixture in gas phase increases under isothermal conditions, the pressure corresponds to the dew point when the first liquid drop appears and the mixture steps into a liquid-vapor equilibrium zone. As the pressure continues to rise, when the last gas bubble disappears in the mixture, the corresponding pressure is the bubble point for this fixed binary mixture composition. The curves of the liquid-vapor equilibrium can be drawn based on the interpolation of measured bubble points and dew points for several different compositions. The intersection of the highest pressure is the mixture critical point and above this point, the mixture is technically monophasic at thermodynamic equilibrium for all compositions.

As an example, in a SAS precipitator at 100 bar and 363 K, a CO₂-ethanol mixture can be found in either a gas-liquid phase equilibrium for the region of CO₂ mole fraction between 0.42 and 0.92, or one phase in the region outside the two phase zone, as indicated in a phase diagram (Figure 4). As a matter of fact, temperature decreases drop the bubble point and the dew point curves in the phase diagram and the mixture is monophasic for any composition of the mixture at 100 bar and 313 K. Petit-Gas *et al.* (2009) reviewed phase transition pressures from gas-liquid equilibrium to monophasic region in a temperature interval between 308K and 313K for regular solvent-antisolvent binary mixtures used in SAS. They pointed out that a mixture at a pressure over its critical point could be still in a partial miscible region, due to a possible inhomogeneity of the pressure and the temperature in the reactor.

Process conditions should always be verified on phase diagram once solvent and antisolvent are selected. Monophasic conditions of solvent-antisolvent mixture are recommended for better mixing to reduce the produced particle size. If the pressure and the temperature can not ensure a single phase for all mixture compositions, gas-liquid equilibrium may exist locally in reactor, leading to complex hydrodynamics with diphasic flows and low mixing efficiency. Several studies gave evidence to support the above argument. Prosapio *et al.*

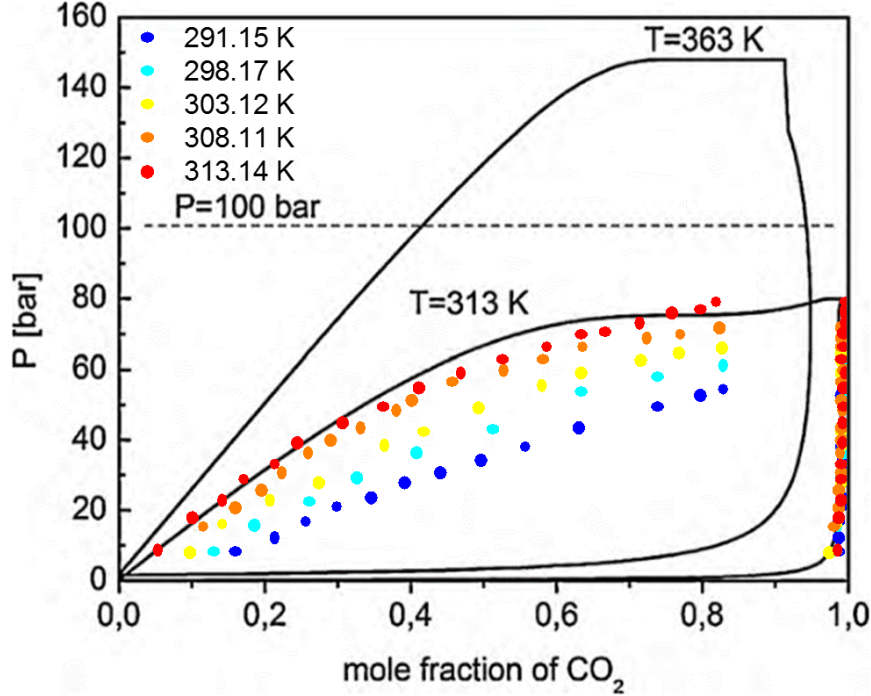


Figure 4: Phase diagram of mixture CO₂-ethanol with experimental data (point in color) extracted from (Day *et al.*, 1996) and calculated curve (Baldyga *et al.*, 2010) based on PengRobinson equation of state (Peng and Robinson, 1976).

(2015) mentioned that the majority of solute processed in SAS has been performed under conditions in which solution and antisolvent are completely miscible, corresponding to the region above the mixture critical point and no interfacial tension exists between two fluids. Nevertheless, either in the transition phase or gas-liquid equilibrium, larger particles are precipitated normally at a micrometre range. This conclusion reveals the importance of fluid mixture conditions on particle morphology. Therefore, thermodynamics, largely influenced by temperature and pressure, should be indispensably taken into account in the SAS parameter studies. It is meaningless to capture the effects of temperature and pressure by varying them separately with the mixture thermodynamics unverified. For example, a temperature increase from 313K to 318K moves up the vapor liquid equilibrium curve according to the phase diagram of DMSO-CO₂ binary mixture, which means that to attain the monophasic conditions, a higher pressure is required. As a consequence, a higher temperature may cause the solvent-antisolvent mixture switching from one single phase to a gas-liquid equilibrium at a fixed pressure, resulting in larger particles (De Marco *et al.*, 2011; Campardelli *et al.*, 2017; Chang *et al.*, 2008). The effect of temperature and pressure

on particle sizes can be discussed only without fluid phase change. For example, Montes *et al.* (2015) studied temperature effect on quercetin particle size at 250 bar, and under this high pressure, the fluid mixture CO₂-ethanol is monophasic for any possible composition and for all the considered temperatures. Similarly to the pressure effect, one should keep the fluid system without phase change, while the pressure is tuned. Higher pressures are suggested to produce smaller particles due to an improvement of the solvent power of CO₂, so that an enhanced mixing provides higher supersaturation and therefore a high level of nucleation.

1.3.1.2 Influence of the solute on the ternary mixture

The state of whole ternary system in a SAS process is rarely studied since most researchers considered that the solute thermodynamic effects can be neglected because of its low concentration. Generally, only solvent-antisolvent binary mixtures are taken into consideration. To verify this assumption, Giufrida *et al.* (2010) measured the vapor-liquid equilibrium for ternary systems of CO₂, organic solvents (ethyl acetate and ethanol) and curcumin as solute and pointed out that the presence of the solute can be neglected when its concentration is low (less than 0.01g/mL). However, Campardelli *et al.* (2017) reported that cefonicid sodium salts can affect the liquid-vapor equilibrium of dimethylsulfoxide and CO₂. At constant temperature, the solute addition increases the dew curve and the bubble curve in its phase diagram of Pxy type. The form of the equilibrium curves can be largely changed when cefonicid concentration is up to 0.09 g/mL. Moreover, while the temperature increases, lower concentration at 0.03g/mL may intrigue this equilibrium curve change. Braeuer *et al.* (2011) proved experimentally by *in situ* elastic light scattering techniques that a low solute concentration (10 mg mL⁻¹ of yttrium acetate in dimethylsulfoxide) did not affect the solvent/antisolvent interface. Whereas, the degradation of fluid interface was completely changed due to a higher initial solute concentration (50 mg mL⁻¹), resulting in large and porous particles. It is evident that for certain solutes, especially when working at high concentrations, it is recommended to verify the influence of the solute on the mixture thermodynamic equilibrium.

As mentioned above, the effects of the initial solute concentration have been examined in several experimental researches (De Marco and Reverchon, 2011; Rossmann *et al.*, 2014; Boutin, 2012) but its influence on the precipitated particle sizes remains unclear for various

solutes and different equipments. It seems that a general conclusion is complicated to be drawn for the influence of the solute initial concentration on particle size because the change of solute concentration may cause a series of parameter variations and these parameters are often correlated. Indeed, the increase of the solute concentration creates higher supersaturation. In the case that the solute concentration do not affect much the nucleation and the particle growth mechanisms, a fast mixing ensures a good homogeneity of the supersaturation. As more nuclei are formed at the beginning of the precipitation, smaller particles with narrow size distribution can be obtained. However, for some experimental researches in which a higher solute concentration results in larger particles, the explanation can be a reduced nucleation rate related to the increase of the solute concentration. As a consequence, more solute molecules participate in the growth part. For both cases, an inefficient mixing should be prevented while the solute concentration increases. The heterogeneous and higher supersaturation field leads to particle precipitation at different rates in the precipitator, resulting in bigger particles and large size distribution. As a consequence, the changes of supersaturation, nucleation and growth rate due to the solute initial concentration must be studied by taking account the fluid mixing.

1.3.1.3 Influence of the solvent

The solvent used in SAS should be, first, a good solvent for the selected solute. The solvent offers the solute a considerable solubility to create potentially high supersaturation while mixed with the antisolvent. Then, it should be easily miscible with the supercritical antisolvent, meaning that the critical point of the fluid mixture should be low enough in the phase diagram to prevent too much energy dissipated for temperature and pressure increase.

To meet these requirements, pure solvents, as well as some solvent mixtures have been tested experimentally. Concerning some common pure solvents, namely the dichloromethane (DCM), the ethanol and the ethyl acetate, the critical points of the solvents and the CO₂ have been determined. Figure 5 shows that to attain the complete miscibility, a pressure above 8.5 MPa is required for all the three solvents at 40 °C.

The phase diagrams of solvent-antisolvent have equally been tested for solvent mixtures instead of one single solvent (Prosapio *et al.*, 2015; De Marco *et al.*, 2015). In these studies, the mixture of acetone and CO₂ has a lower critical pressure than other tested mixtures (ethanol-CO₂, dimethylsulfoxide-CO₂ and N-methylpyrrolidone-CO₂) at 40 °C. When the

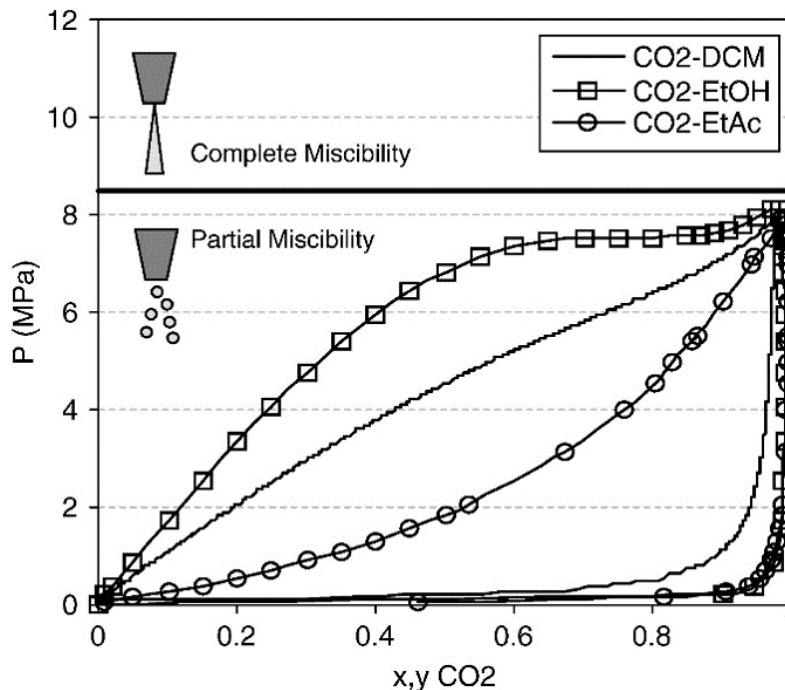


Figure 5: Phase diagram of mixture CO₂-solvent at 40 °C imported from (Martin and Cocero, 2008) and the solvents are dichloromethane (DCM), ethanol (EtOH) and ethyl acetate (EtAc).

acetone is added into the later mixtures, the critical pressure decreases for a constant temperature. Comparison also shows that the addition of acetone reduces the average size of precipitated particles through SAS process.

Another aspect of solvent-antisolvent mixing in SAS is the excess enthalpy. When two different fluids are mixed, a thermal effect occurs inside the mixture, either exothermal or endothermal, related to the excess enthalpy. Studies have been conducted to estimate this thermal effect by both experiments and numerical methods. Experimental measurements have been conducted in the vicinity of the critical points for several mixtures of solvents and CO₂ (CO₂-ethanol, CO₂-toluene, CO₂-alkanol, CO₂-cyclohexane) (Cordray *et al.*, 1988a; Cordray *et al.*, 1988b; Christensen *et al.*, 1988; Cordray *et al.*, 1988c). The excess molar enthalpies were obtained by a high-temperature high-pressure flow calorimeter for some fixed temperatures and pressures. The mixture compositions were ensured by fixed flow rates controlled by high pressure pumps. The results in Figure 6 show that the excess enthalpy of CO₂ and ethanol depends on temperature, pressure and mixture composition.

At 325.15 K and 10 MPa, a mixing of CO₂ and ethanol causes always exothermal effect for any possible CO₂ composition, with values as high as 2030 J/mol (Cordray *et al.*,

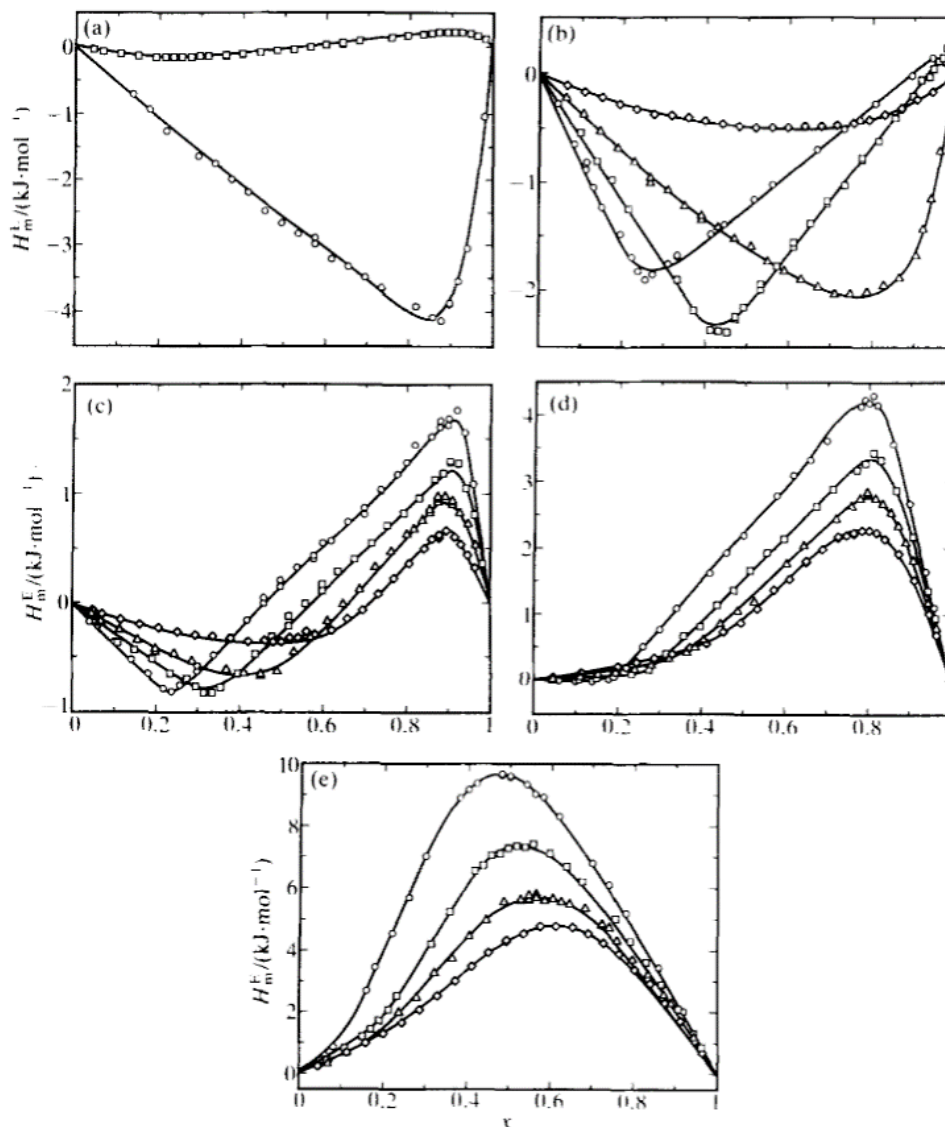


Figure 6: Plot of experimental data of excess enthalpy for CO_2 (x) - ethanol ($1-x$) mixture (Cordray *et al.*, 1988a) at (a). 308.15 K: \circ , 7.50 MPa; \square , 12.50 MPa; (b). 325.15 K: \circ , 5.00 MPa; \square , 7.50 MPa; \triangle , 10.00 MPa; \diamond , 12.50 MPa; (c). 373.15 K: \circ , 7.50 MPa; \square , 10.00 MPa; \triangle , 12.50 MPa; \diamond , 14.39 MPa; (d). 413.15 K: \circ , 7.50 MPa; \square , 10.00 MPa; \triangle , 12.50 MPa; \diamond , 14.39 MPa; (e). 473.15 K: \circ , 7.50 MPa; \square , 10.00 MPa; \triangle , 12.50 MPa; \diamond , 14.39 MPa; with curves calculated using proposed correlation.

1988). At 373.15K and 10 MPa, the excess enthalpy can be positive or negative, depending on the CO_2 composition. Other mixture systems have also been examined. Under high pressures, binary mixtures were injected into an isothermal calorimeter and excess molar enthalpies were measured for various solvent-antisolvent mixtures such as: CO_2 -N-methyl-2-pyrrolidone (Davila *et al.*, 2007), CO_2 -ethyl acetate (Zahran *et al.*, 2012) and CO_2 -acetone (Zahran *et al.*, 2010). An exothermic effect was detected for all these three binary fluid

systems and the values of excess enthalpy depended on temperature, pressure and mixture composition. Nevertheless, when the CO_2 molar composition is closed to 1, which is generally the case for SAS precipitation, this excess enthalpy is negligible. If the CO_2 composition drops to 0.9, for certain conditions, the excess enthalpy can no longer be neglected. In general, for a fixed temperature, a higher pressure in monophasic zone reduces the absolute value of excess enthalpy so the corresponding exothermal effect is less important, indicating that in these conditions, the thermal effect due to solvent-antisolvent mixing is weaker than in two-phase binary mixtures. Regarding the modeling, Escobedo-Alvarado and Sandler (2001) presented a prediction model to estimate excess enthalpies based on the Peng-Robinson equation of state coupled to the Wong-Sandler (WS) mixing rule. Rare numerical studies have taken into account the excess energy in the conservation energy equation. For example, Sierra-Pallares *et al.* (2016) reported numerically by CFD simulations the influence of the excess enthalpy in the case of the mixing of CO_2 and ethanol. As observed in Figure 7, the simulation result implied a temperature change in the droplet and in the mixing zone from 313K to 330K in a very short time (0.00296 s) due to the excess enthalpy of fluid mixing. These temperature increases may cause a local mixture from single phase to liquid-vapor two-phase state (Figure 8).

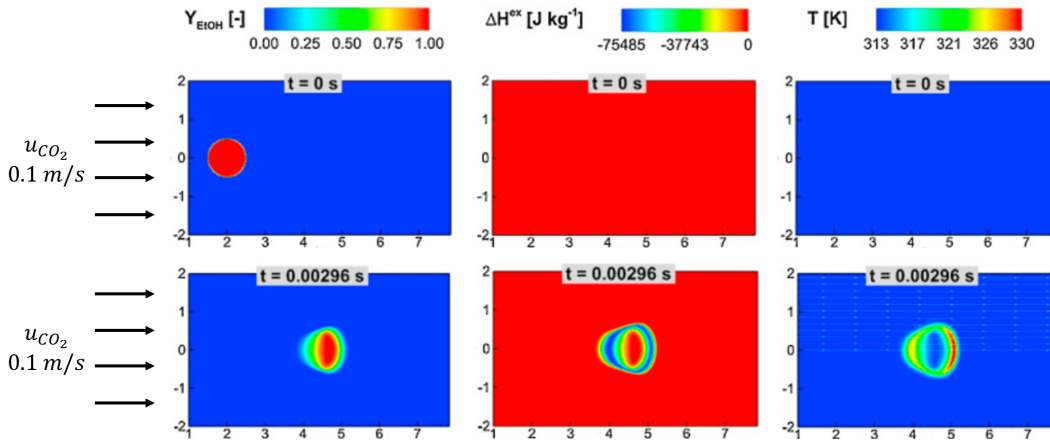


Figure 7: Numerical simulations of Sierra-Pallares *et al.* (2016) to examine the excess enthalpy effect on local temperature during the mixing of a CO_2 current and an ethanol drop.

As largely recommended in literature, to reach solvent-antisolvent miscible zone, a high pressure with a moderate temperature is the best choice for the SAS process. First, despite of local temperature change due to mixing effect, high pressure keeps the fluid system in completely miscible conditions without any phase change. Secondly, the excess enthalpy decreases at high pressure, leaving less energy change in the system, leading to a better

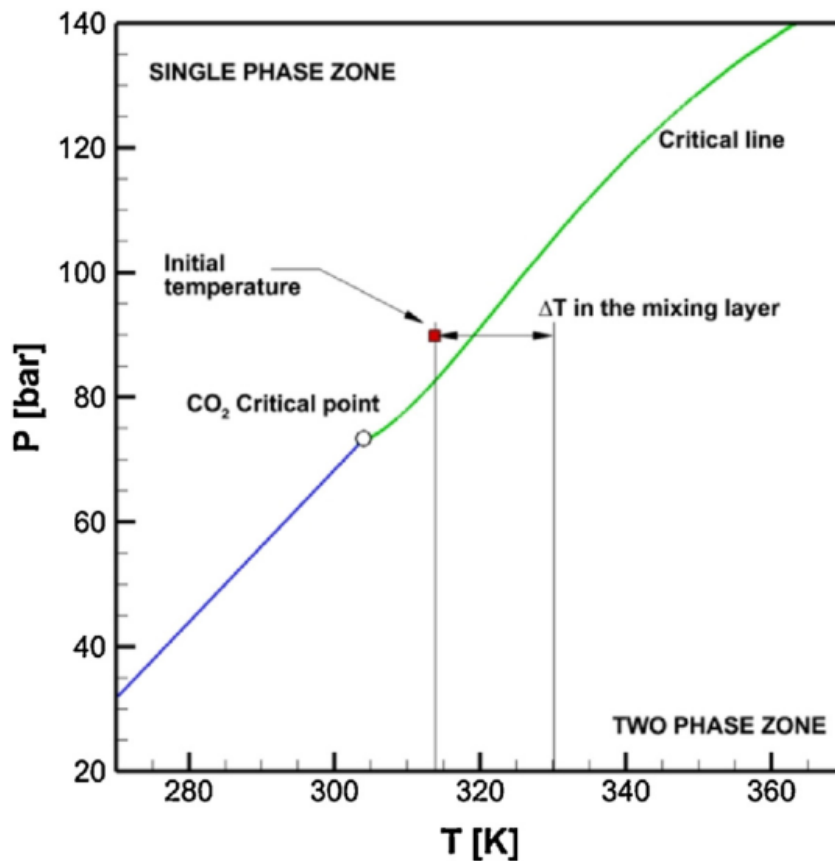


Figure 8: Simulated effects of the excess enthalpy on temperature change, inducing a monophasic mixture displacement to diphasic region, figure extracted from Sierra-Pallares *et al.* (2016).

control of the temperature. Even though one can also choose a CO_2 fraction closed to 1 to reduce excess enthalpy, proven in experiments, there may be locally solvent dominant zone related to unmixed solvent. It should be noticed that the simulation work of Sierra-Pallares *et al.* (2016) was examined only for laminar flow conditions. A fast mixing with high fluid velocity is therefore needed to prevent local temperature change by accelerating the heat transfer related to the excess energy.

We discuss in the next section the effects of the hydrodynamic phenomena on the SAS process.

1.3.2 Role of hydrodynamics in SAS

The mixing of the solution (solute + solvent) and the supercritical antisolvent plays a crucial role in SAS process. Indeed, the mixing affects directly the supersaturation, the driving force of the precipitation, and consequently the final particle size and size distribution (Shekunov *et al.*, 2001). Since the fluid mixing and the precipitation can be considered as two competitive processes, we aim to obtain a mixing time smaller than the nucleation time. In this case, the homogeneity of mixture attains before the nucleation so that the particles are precipitated at the same rate related to the same supersaturation everywhere in the reactor. However, this ideal mixing is not realistic so far but it is important to accelerate the fluid mixing for an intensification of SAS process. In this part, we are going to present different studies, which are mainly focused on the role of the hydrodynamics for the SAS process.

1.3.2.1 Solution jet break-up observation

Experimental studies have been carried out by optical analysis of the fluid mixing in SAS precipitators. Jet dynamics of pure solvent and solution (with solute) have qualitatively revealed fluid mixing behavior around the mixture critical point (Figure 9) (Reverchon *et al.*, 2010). Pictures figured out clear fluid separation between the injected solvent (dimethyl sulfoxide) and the antisolvent (CO_2) environment under subcritical conditions, around mixture critical point and supercritical conditions. Large heterogeneous droplets were formed after jet break-up under subcritical conditions for a low injection flow rate ($0.5 \text{ mL} \cdot \text{min}^{-1}$). The droplet size decreased as the injection velocity increased. For a flow rate of $3.5 \text{ mL} \cdot \text{min}^{-1}$, the atomization mode attained with uniform tiny droplets of solvent dispersed into the CO_2 . At constant flow rate, the phase boundary became more and more blurred when fluid was closed to supercritical conditions with smaller and more regular droplets released at the nozzle. It seems that the atomization mode can be more easily reached under a higher pressure for a fixed injection velocity. Eventually, for a high flow rate under supercritical conditions, the interfacial boundary vanished with only a plume-like jet of inner fluid. From these observations, we can clearly notice that when the fluid mixture is in its completely miscible zone above the mixture critical point, the two fluids involved are much better mixed, providing higher supersaturation degree so as smaller particles.

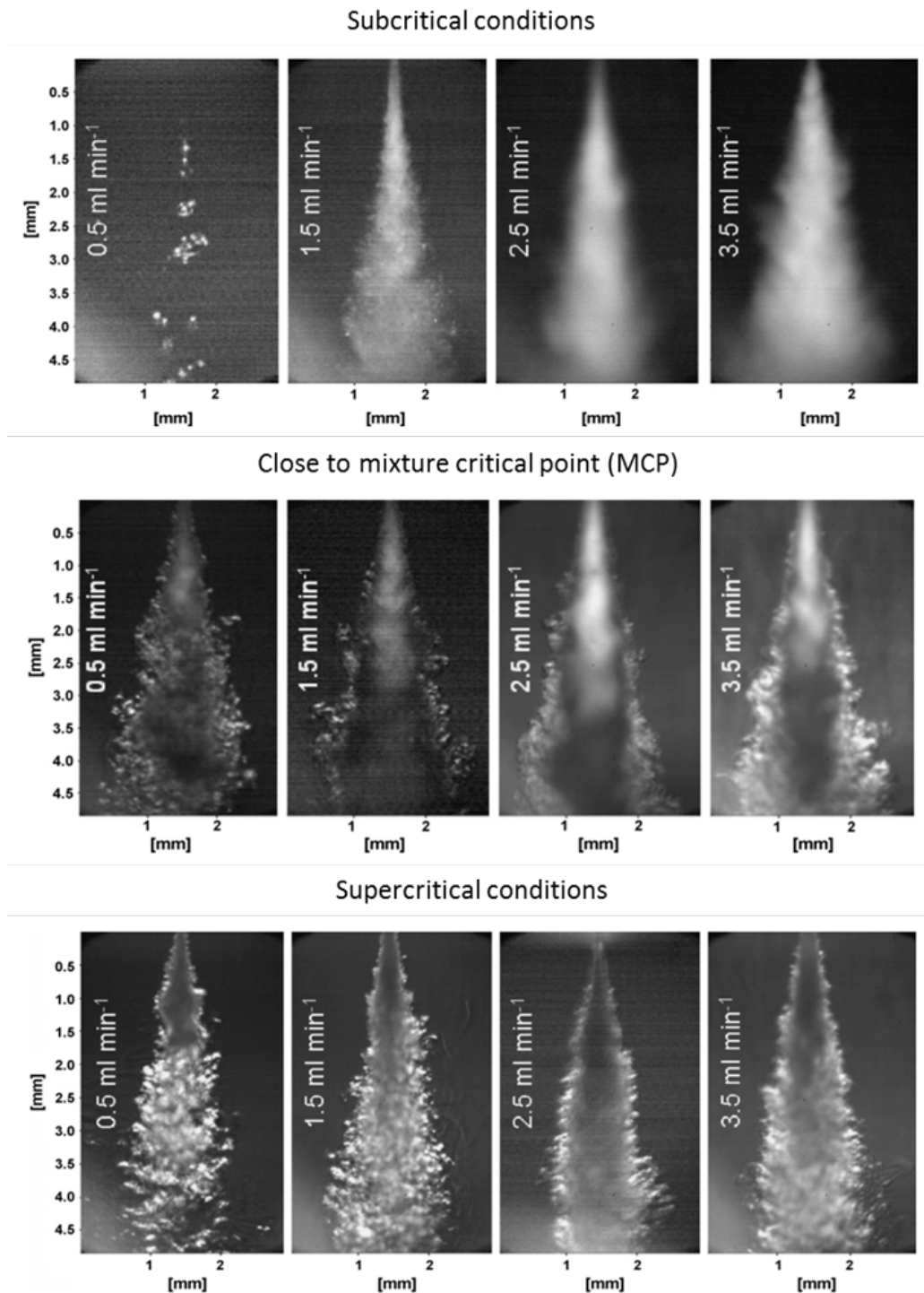


Figure 9: Light scattering images of dimethylsulfoxide (DMSO) injected into CO₂ at 40 °C through a nozzle to reveal effects of DMSO flowrate for different conditions (subcritical, close to MCP and fully supercritical states) (Reverchon *et al.*, 2010)

1.3.2.2 Jet break-up VS. dynamic surface tension

Even if the mixing conditions are in the miscible zone, slightly above the mixture critical

point, the interface between the liquid phase (solvent or solution with solute) and the supercritical antisolvent can be detected because the unmixed fluids contact each other at the mixing point and time is demanded to attain the thermodynamic equilibrium of a miscible monophasic mixture. This observation can be related to the dynamic critical point, meaning the critical point of a monophasic mixture during a real mixing with fluid velocities. Braeuer *et al.* (2011a) have found that the expansion of ethanol solvent injected into the supercritical CO₂ has no clear difference at the mixture critical point compared to the cases in subcritical conditions. At fixed temperature, the solvent expansion begins to be amplified for a higher pressure. This corresponds also to the mixing regime transition from a jet spray to a one phase plume-like mixing. Other experiments can be found for the jet observation by optical measurement techniques (Braeuer *et al.*, 2010). With the help of a 2D Raman scattering, Dowy *et al.* (2009) measured the CO₂ partial density distribution in the solution jet. They mentioned that the difference between the pure CO₂ density and its partial density in the solvent jet can be related to the interface between the liquid jet (solvent or solution) and the supercritical antisolvent CO₂. With fixed flow rates, a higher pressure reduces this density difference (Figure 10), implying the pressure influence on this jet mixing dynamics so that a better mixing is due to the pressure increase above the mixture critical point in this case.

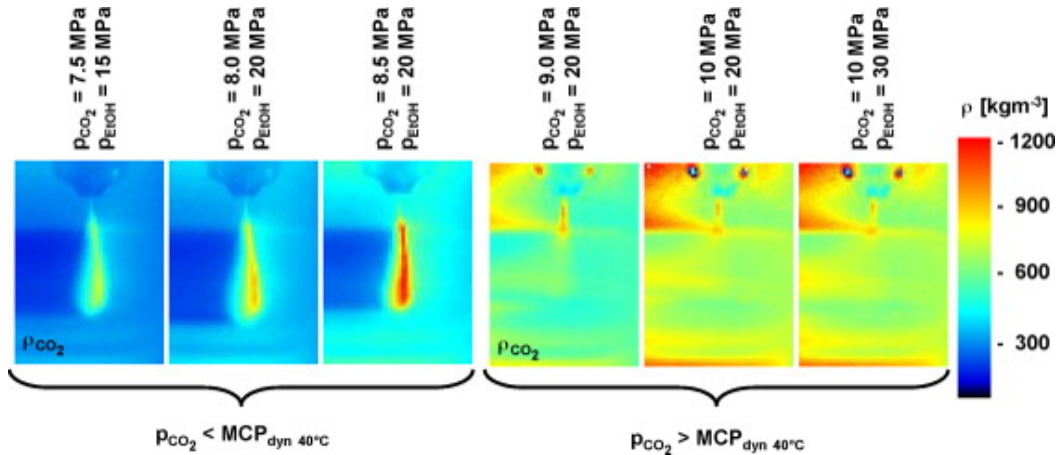


Figure 10: CO₂ partial density ρ_{CO_2} below and above the dynamic mixture critical point (MCP_{dyn}) at 40 °C (original figure from the article of Dowy *et al.* (2009)).

Similar studies have been carried out by Badens *et al.* (2005) to examine the fluid flow rate effects on the dynamic critical point. The authors determined fluid velocity thresholds for jet form transitions. They observed firstly the jet dispersion into dense CO₂ under partial miscible conditions. By increasing the jet flow rate and pressure, they measured the

jet length and noticed that the jet dispersion changed from an axisymmetrical jet to an asymmetrical one, then to an atomized jet and finally to a classical plume-like monophasic mixture. Similar results have been found by Erriguible *et al.* (2012) for a mixture of CO₂ and ethanol under subcritical conditions. In order to know the velocity threshold of a jet passing to monophasic mode, the critical velocity was determined as a function of the CO₂ density. Petit-Gas CO₂ (2009) estimated the velocity threshold for conditions above the mixture critical point (at thermodynamic equilibrium). They found that the values of the critical atomization velocity were smaller than the ones found in previous studies (Badens *et al.*, 2005) under partial miscible conditions. The critical velocity can be changed depending on many parameters, including the jet nozzle diameter, the temperature, the pressure, the solvent mass fraction and the flow configuration (co-current or counter-current). To resume, the particles formed by SAS precipitation tend to be more regular and homogeneous when the injection velocity is high enough above the critical velocity, *i.e.*, providing a better mixing due to a completely miscible mixture of solvent and antisolvent (CO₂), which leads to high and uniform supersaturation degrees.

The concept of two competitive characteristic times (jet break-up time and dynamic surface tension vanishing time) stated by several research groups (Lengsfeld *et al.*, 2000; Reverchon *et al.*, 2010) and modeled by Marra *et al.* (2012), explains the precipitate size dependence on jet break-up regimes. For diphasic flows or a mixture in phase transition, if solution jet break-up time is less than the dynamic surface tension vanishing time, dispersed solution droplets are formed and the phase separation prevents solute transport during mixing until the phase boundary disappears, so that the supersaturation degree is lower and particles are larger than that in monophasic conditions, in which case a plume-like jet of atomization mode is formed and no phase boundary can be observed (Campardelli *et al.*, 2017; De Marco *et al.*, 2015; Reverchon *et al.*, 2010). According to the model, these two characteristic times are both found to be proportional to the solute concentration and inversely proportional to the pressure. Since the surface tension vanishing time drops faster with pressure than the jet break-up time, when the former is lower than the later by increasing pressure, nanoparticles are precipitated instead of microparticles. However, for higher concentrations, it is more difficult to produce nanoparticles because the dynamic surface tension disappearing times are always over the jet break-up times for the reported pressure range because of a strong effect of the concentrated solute on the related solution viscosity. It should be questioned if it is suitable to apply this model for conditions far above

the mixture critical point, in which case single phase mixing was detected experimentally, but the surface tension vanishing time is not zero or even closed to zero based on the model results.

1.3.2.3 Direct experimental method for quantifying micromixing

As mentioned above, the mixing hydrodynamics at molecular diffusion microscales are essential for understanding and controlling the SAS process. A recent research, carried out by Bassing and Braeuer (2017), proposed an experimental technique to capture the micromixing of compressed CO₂ and ethanol directly by a one-dimensional *in situ* Raman spectroscopy approach (Figure 11). They separated the ethanol signal intensity into 6 peaks and one corresponds to the free hydroxyl groups (O-H) without influence of any hydrogen bond, meaning that the ethanol is dispersed into the CO₂ environment in the molecular diffusion scale without other ethanol molecule in the vicinity. As a consequence, the micromixing is assigned to the free ethanol intensity on the entire ethanol. From a global view, the macromixing is related to the CO₂ intensity over the sum of CO₂ and ethanol ($R_{macro} = \frac{I_{CO_2}}{I_{CO_2} + I_{EtOH}}$). Both macro and micromixing can be fitted and calculated with the CO₂ fraction through empirical correlations. The lag between macro and micromixing (the difference between the macro and micro CO₂ fraction) has been examined in the center line and the horizontal lines of the ethanol jet. The results indicate the lag evolution observed in different locations in the ethanol jet.

The difference between the macromixing and micromixing is reported in Figure 11a on the vertical center line. It is represented by the difference of the CO₂ molar fraction in the macromixing and micromixing ($X_{CO_2,macro} - X_{CO_2,micro}$). Its value increases first close to the injector outlet, meaning that the fluids start to mix at the macroscale but the mixing rate is slower at the microsacle at the beginning of the mixing. The difference reaches to the maximal value at 5 mm away from the nozzle. Then the macromixing rate slows down and the difference decreases until the homogeneity at all mixing scales. In Figure 11b, the lag is examined at these horizontal levels and the difference depends on both the vertical and horizontal locations. The lag has higher values at the ethanol jet boundaries, especially close to the nozzle, where the macromixing is much faster than the micromixing. Further studies are needed for understanding the effects of mixing conditions and an optimization work is required to reduce the lag, implying faster micromixing.

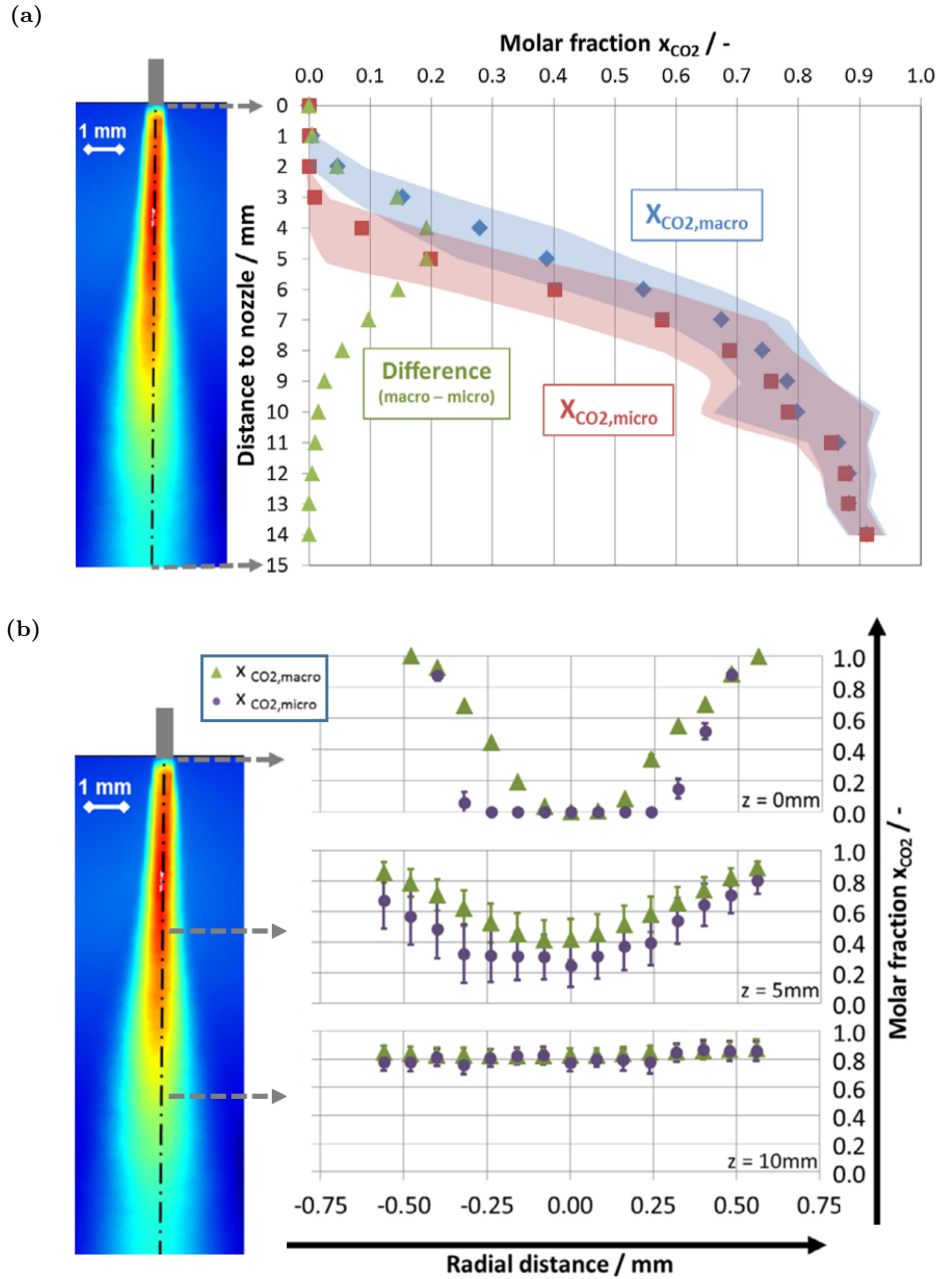


Figure 11: Detection of the lag between the micromixing and the macromixing from the experiments proposed by Bassing and Braeuer (2017) with modified images extracted from the original article: (a). the lag on the center line of the jet; (b). the lag on the horizontal lines at 3 different jet lengths.

1.3.2.4 Mixing hydrodynamics related to reactor configuration

Different SAS set-ups can be found in literature with various types of fluid introduction configurations. The typical ones are shown in Figure 67. They generally consist in the injection of the solution (solute + solvent) into a precipitator filled with antisolvent introduced by another pump. In most studies, the two fluids are mixed by co-current

flow (Figure 12a) (Petit-Gas *et al.*, 2009; Silva and Meireles, 2014) or counter current flow (Figure 12b) (Careno *et al.*, 2012) or they are premixed in a nozzle before released into precipitator (Figure 12c) (Baldyga *et al.*, 2010).

The performance of a concentric tube antisolvent reactor has been compared to an impinging jet precipitator (Boutin *et al.*, 2007; Calvignac and Boutin, 2009; Boutin *et al.*, 2009; Boutin, 2012) and no significant difference in particle size has been obtained for the tested process conditions. It seems that the precipitation was the dominant process in the reactor because the fluid mixing had almost no influence on the particle morphology, according to the authors. In this case, the mixing was fast enough compared to the nucleation and the kinetic of particle growth. However, they announced that other commonly used solutes should be analyzed to compare with classical introduction devices and equally to eliminate the solute intrinsic factors during precipitation. For instance, some selected solutes may have a slow kinetic to form particles due to the surface tension between the solute solid particle and the surrounding fluid. In this case, the improvement of mixing hydrodynamics has less effects if the mixing time is already lower than the nucleation time. Additionally, the particle agglomeration and flocculation can affect the sizes of the final particles.

In order to deeply investigate the influence of the reactor configuration and dimensions, a pure numerical study has examined the effects of different nozzle on the sizes of the simulated particles under regular SAS process conditions (Sierra-Pallares *et al.*, 2012) and the results were compared to a previous experimental study (Cocero *et al.*, 2002). They showed that the nozzle diameter has a strong effect on precipitates, from both experimental measurements and numerical simulations, resulting from tremendous change of the Reynolds number. A high value of Reynolds number, related to a smaller nozzle diameter, produces much smaller particles. However, for the same nozzle, the Reynolds number is no longer a decisive factor, emphasizing that instead of studying SAS through device types, process parameters and global conditions, mixing at all scales should be investigated, which is determinant in controlling particle size. Especially, mixing performance and hydrodynamic influences of SAS devices should be discussed at nucleation scales. As the micromixing is the essential part of this thesis, a focus on the fundamental mechanisms of mixing is proposed as introduction in the chapter 3, devoted to the mixing study in our process.

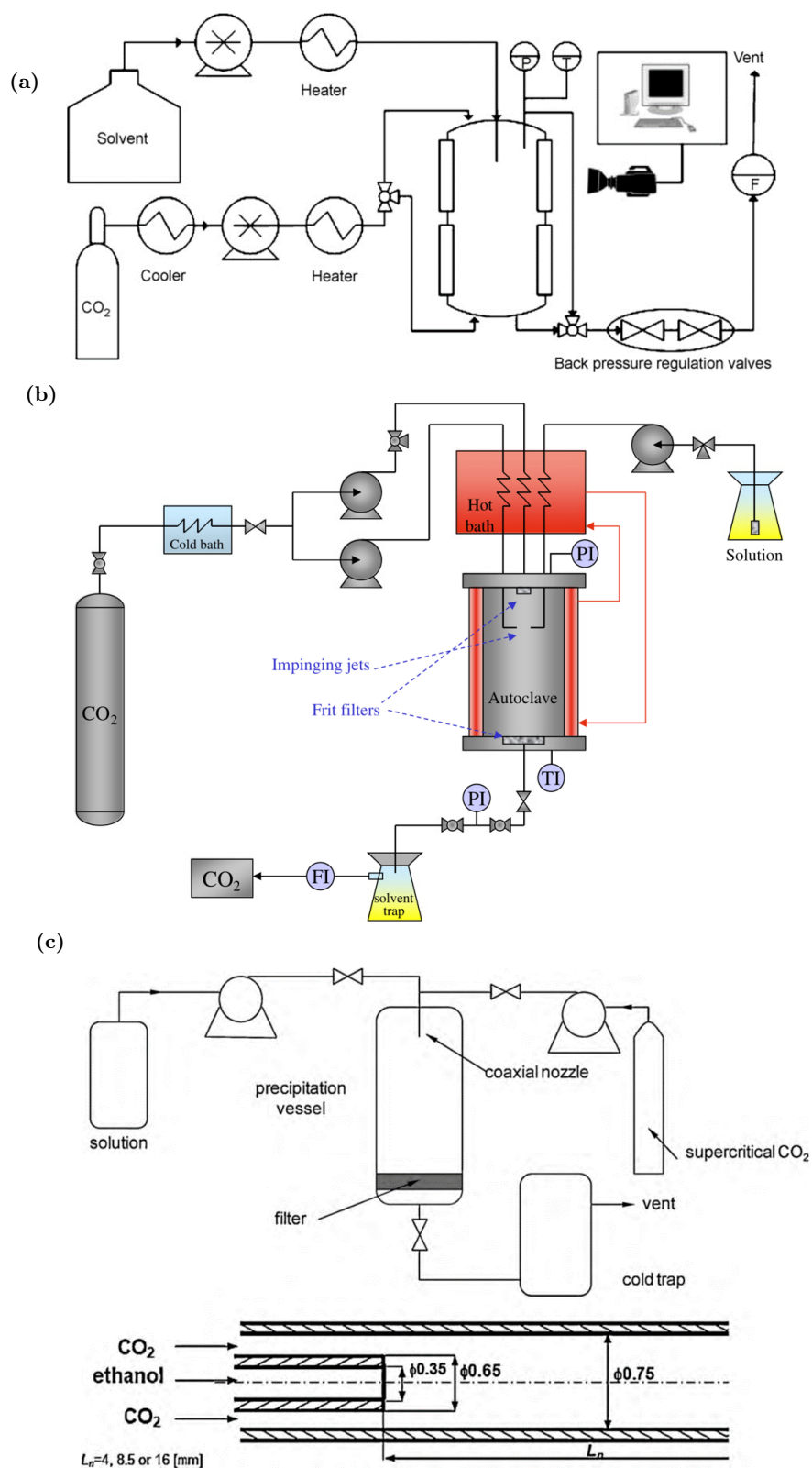


Figure 12: Classical experimental system of SAS (a). side by side co-current injection (Petit-Gas *et al.*, 2009); (b). impinging jet counter current configuration (Carena *et al.*, 2012); (c). reactor equipped with a coaxial nozzle (Baldyga *et al.*, 2010).

1.3.3 Phenomena of nucleation and particle growth

The mechanism of particle precipitation has been well studied for decades and its kinetic model is known and applied in many researches. However, for the SAS process, it is difficult to study experimentally the nucleation and particle growth because of an extremely fast nucleation rate. Even though high pressure facilities exist with optical access for experimental precipitation observation (Voisin *et al.*, 2017), as the important parameter, the surface tension between solid particle and supercritical fluid mixture is hardly experimentally measured. Commonly, in order to understand this phenomenon and the influence of the process parameters, numerical modeling is applied as an important tool to simulate particle synthesis, which are compared to the experimental results (Martin and Cocero, 2004; Sierra-Pallares *et al.*, 2011; Erriguible *et al.*, 2013; Erriguible *et al.*, 2015; Cardoso *et al.*, 2016). The simulation includes the general precipitation kinetics, coupled with the fluid thermo-hydrodynamics and the species transport. Generally, a population balance equation (PBE) (Marchisio and Fox, 2013) is chosen to take into account the nucleation and the particle growth phenomena. In order to solve the population balance equation, the moments' methods are classically used (SMOM, QMOM, etc...). The details of numerical modeling used in these approaches are presented in Chapter 2.

Even though the simulation results fit normally well with the experimental data, some difficulties are summarized in the literature for the numerical modeling of SAS process. The first is the turbulence model which is still a challenge till now. The statistic turbulence model ($k-\epsilon$) seems to be a suitable choice because of its acceptable accuracy for Reynolds number from 300 to 4000 (Liu *et al.*, 2014; Ouyang *et al.*, 2017; Li *et al.*, 2019). However, it is difficult to calculate the energy dissipation rate for turbulent conditions and some suppositions have to be made. Secondly, specific models of micromixing should be integrated to the CFD simulation to deal with the species transport at the molecular diffusion microscales for precipitation. It generally provides more accurate mass transfer normally by dividing each numerical cell into a few of different environments. This sub-grid type of micromixing models prevents non-realistic fast mixing related to the numerical discretization, which is much larger than the micromixing scales. The common micromixing models are presented in details in Chapter 3. Nevertheless, as far as we know, no published numerical simulation describes fluid mixing and species transport below the Kolmogorov scale with local turbulent energy dissipation rate. The last difficulty as mentioned previously is the surface tension

between the solid particles and the fluid phase, involved in the precipitation kinetics. It is challenging to obtain its precise value experimentally so it is often determined by fitting the simulation results to the experimental data.

Whatever the model used, all the simulations demonstrated the importance of the micromixing into the reactor. Furthermore, in the literature, the researchers also revealed the lack of knowledge on the surface tension between the supercritical fluid mixture and the solid particles. This implies that very precise and discrete experimental data are needed in order to fit the model. From this context, the high pressure microfluidic tools appear as the perfect apparatus due to their ability to make *in situ* observation and their excellent control over the operating conditions. As a consequence, the main improvement for the SAS precipitation is to seek for process intensification in high pressure microfluidic systems to accelerate fluid mixing and to better control the operating conditions. Thanks to the combination of the supercritical antisolvent and the microfluidic mixing, the mixing time t_m can be largely decreased and its value should be compared to the nucleation time t_n .

1.4 Intensification towards the μ SAS and our contribution

The very first article concerning the SAS precipitation in a microreactor (μ SAS) has been published in 2015 by Couto *et al.* from the supercritical fluid group in the ICMCB. This work demonstrates the possibility of processing SAS in a microsystem (Set-up scheme is shown in Figure 13) with a characteristic length of channel down to 200 μm . This facility was used to successfully synthesize semiconducting polymer nanoparticles of poly(3-hexylthiophene) (P3HT). The solvent selected was the tetrahydrofuran (THF) with the supercritical CO_2 as an antisolvent. The pressurized CO_2 was pumped into the microchannel and heated by a heating plate to attain the desired temperature (40 - 50 $^\circ\text{C}$ in their studies). Then it encountered the solution of P3HT and THF at the tip of a capillary injector. Because of the mixing of these two fluids, the supersaturation was created and particles began to precipitate and then to grow. The final particles obtained were almost homogeneous spheres with the average size of less than 50 nm .

As a first test, only two different conditions have been compared in the article with fixed low flow rates of solution and supercritical antisolvent. However, this first proof of concept opens avenues towards a deep research on it, because of the advantages as fast mixing and high supersaturation. The motivation of the thesis is to show that μ SAS offers very favorable

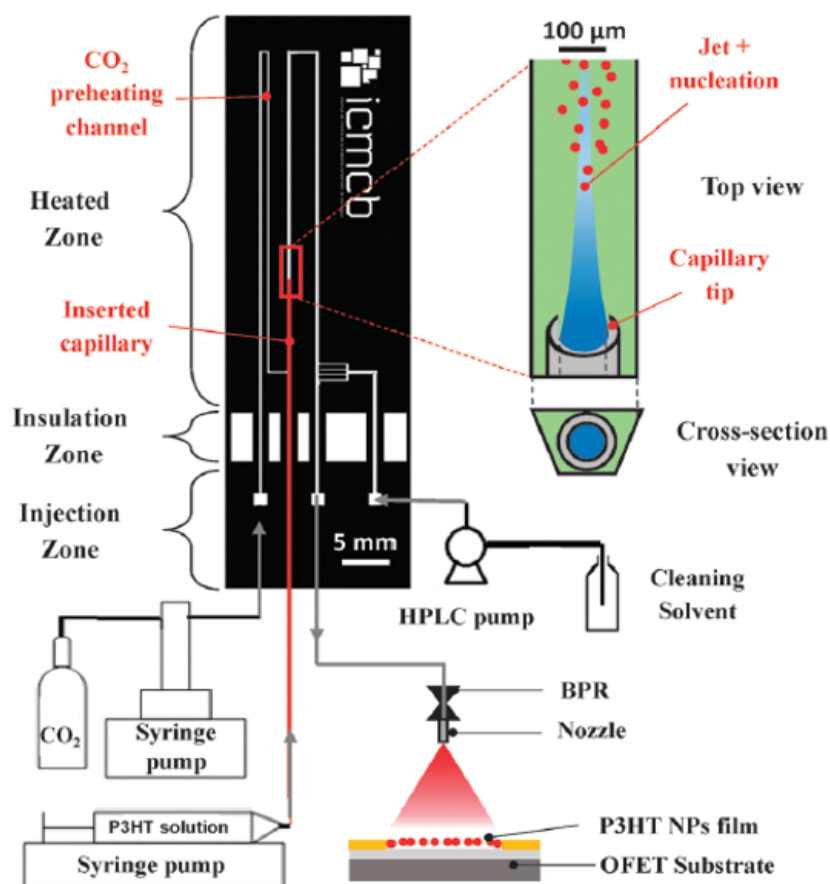


Figure 13: Microfluidic system of Couto *et al.* for the synthesis of polymer nanoparticles through μ SAS process, image extracted from the original article.

conditions for the supercritical antisolvent process. This will be done by conducting a complementary approach of both experiments and simulations through the use of advanced research techniques, such as the *in situ* characterization inside the microfluidic reactor - the Micro-Particle Image Velocimetry (μ PIV) and the High Performance Computing (HPC).

After the presentation in the next chapter of the investigation tools, including *in situ* experiments and numerical modeling, a deep understanding of the mixing mechanisms in our system will be proposed in the third chapter. The use of HPC will allow us for capturing mixing scales down to the Kolmogorov scales and will emphasize the great performance of our micromixer. Eventually, the influence of the mixing on the particle precipitation will be studied in the last chapter in which we propose a complete simulation of the μ SAS process, including thermo-hydrodynamics and nucleation/growth phenomena. The comparison with experimental results allows us to obtain, with confidence, the surface tension between the solid and the supercritical fluid mixture.

Chapter II: Tools and methodologies

In this chapter, we present the developed experimental system used to set insights in fluid mixing hydrodynamics through velocity field acquisition. In particular, we will first detail the microfabrication steps for fabricating pressure resistant microchip, and we will introduce the micro particle image velocimetry (μ PIV) facilities, the μ PIV principle and the software tools used to measure fluid velocity in the microchannel. Then, for the numerical modeling part, a general presentation is given to explain briefly how we calculated governing equations for each phenomenon involved in fluid mixing as well as in particle precipitation.

2.1 Experimental systems

For accessing local velocity fields experimentally, the system consists of two main parts: a home-made silicon-Pyrex microreactors fabricated in a clean room and a μ PIV system coupled with optical devices to detect fluid velocity field for laminar conditions. Meanwhile, a high speed camera is also used to observe *in situ* turbulent mixing in the microchannel. We detail hereafter the flow sheet for fabricating our microreactors and then the experimental set-up including μ PIV.

2.1.1 Microfabrication

The microreactors were made in silicon-Pyrex, which is a micro fabrication technology largely utilized for high pressure microfluidics (Couto *et al.*, 2015; Marre *et al.*, 2010), combining the mechanical properties of silicon and Pyrex with the good thermal conductivity of silicon and the visible transparency of Pyrex, thus providing an easy optical access. The microchannels are etched by chemical wet etching on a silicon wafer, which is anodically bonded to a top Pyrex cover to seal the channels and to give optical access thanks to its transparency. More details are presented in the following parts.

2.1.1.1 Materials

(i). Wafers and capillary

The silicon wafers used for microchannel etching are purchased from the company BT Electronics. The diameter of the wafers is 4 inches (10.16 cm) and their thickness is 1000

μm with an error of less than $25 \mu\text{m}$. The surface of silicon wafer is oxidized and the oxide layer (SiO_2) has a thickness of 500 nm . A picture of such wafer is shown in Figure 14a.

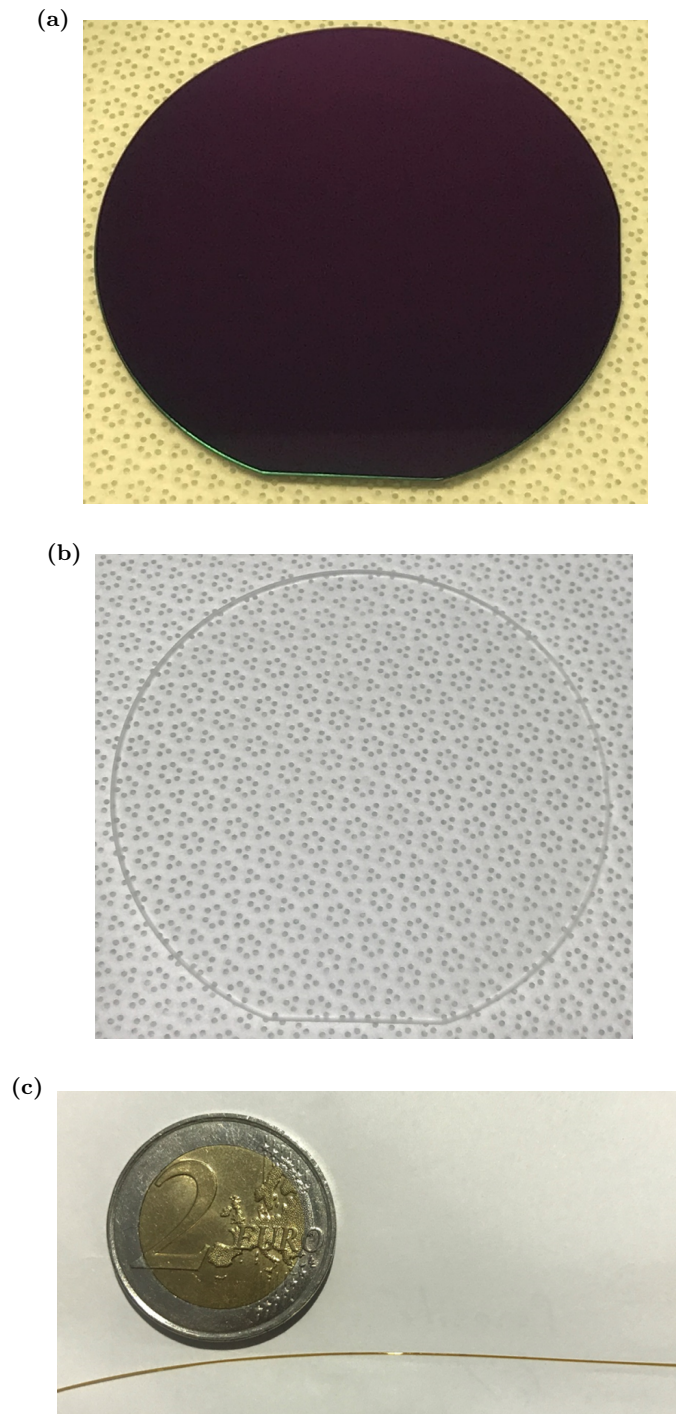


Figure 14: Wafers and capillary used for the microfabrication: (a). untreated silicon wafer to be engraved, with silica layer of each side; (b). transparent Pyrex wafer used as the topping of the microchip; (c). silica capillary to create coflow configuration in the microchannel.

Pyrex is a clear and opal ware material made of borosilicate glass and the wafer (Bo-

rofloat 33) for microreactor top cover is double side polished with the same diameter as the silicon wafer (10 cm). Its thickness is 2000 μm with an error of less than 10 μm (Figure 14b).

The silica capillary is purchased from Polymicro Technologies. It is inserted into the microreactor to form a coaxial flow geometry, possessing a mean inner diameter (D_{ID}) of $102.4 \pm 0.8 \mu\text{m}$ and a mean outer diameter (D_{OD}) of $167.35 \pm 0.35 \mu\text{m}$.

(ii). Chemicals

The photoresist used for UV exposure is named MicropositTM S1818TM G2 Positive Photoresist UN1866 Resin Solution, fabricated by the Dow company, containing propylene glycol methyl ether acetate. Its coupled developer used for the photolithography steps is MicropositTM MF-319, including tetramethylammonium hydroxide, from the same company. For wet etching procedure, a tetramethylammonium hydroxide solution of 25 wt.% in water and an ammonium fluoride - hydrofluoric acid solution are purchased from Sigma-Aldrich. Other common chemicals are 99+% isopropanol (or 2-propanol) from Alfa Aesar, sulfuric acid 95-97% from EMSURE, hydrogen peroxide solution from Scharlau, 96% ethanol and acetone provided by Xilab.

2.1.1.2 Facilities

The spin coating step is ensured by a POLOS200 spin coater from SPS-Europe incorporation, equipped with a vacuum pump. The lithography is processed in an exposure-masking system (UV-KUB 2) of UV light emitting diode (LED UV) from the Kloé company, with a resolution down to 2 μm and an insolation wavelength of 365 nm. A FisherbrandTM IsotempTM Advanced Stirring Hotplate from Fisher Scientific is used for silicon wafer wet etching. A sandblaster of Arena C60 is used to pierce the inlets and outlets of the devices on the wafer and then the oxidation of the etched silicon wafer is performed in an oven of Nabertherm P300 model with a heating capacity up to 1200 °C. Finally a home-made anodic bonding system is needed, equipped with an Eurotherm temperature controller and an electrical tension system from the BFi OPTiLAS company. The wafers are eventually processed with a die saw to reach the right microreactors dimensions thanks to a precision cutter (IsoMetTM 4000) of Buehler.

2.1.1.3 Microfabrication steps

This part describes the protocol of microreactor fabrication which contains six steps by different functions: spin coating, lithography, wet etching, sandblaster and oxidation, anodic bonding and cutting. A general scheme is shown in Figure 15 for the silicon wafer treatment.

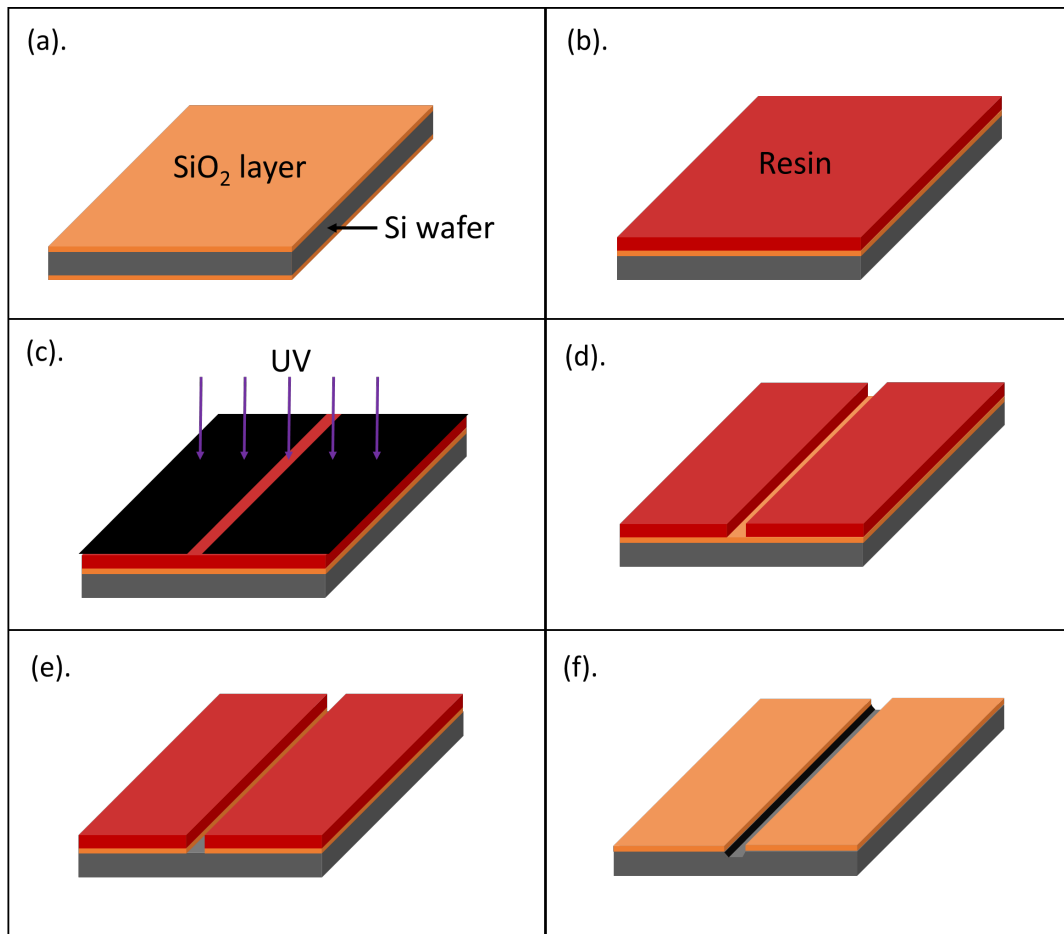


Figure 15: Description schema of the 3D trapezoidal microchannel formation: (a). raw silicon wafer; (b). resin layer after the spin coating; (c). UV treatment to change the resin properties; (d). resin removal onto the channel area by the developer for further etching; (e). silica layer removal onto the channel after the ammonium fluoride - hydrofluoric acid treatment; (f). trapezoidal channel formation at the end of TMAH wet-etching.

Step 1 : Spin coating

The silicon wafer surfaces should be cleaned with isopropanol and then ethanol and dried by compressed air. The photoresist resin is spread evenly on one side of the wafer by the spin coater (1200 rpm for 30 seconds). The wafer is then placed on a heating plate, previously heated at 115 °C for 4 minutes.

Step 2 : Lithography

A mask of the designed microreactor is positioned on the top of the resin layer and then the wafer is exposed to a UV irradiation in the UV device (UV-KUB 2) at a wavelength of 365 nm for 45 seconds. The transparent part on the mask corresponds to the channels. The wafer is finally dipped in the solution of MicropositTM MF-319 developer for 30 seconds and the exposed resin is faded from the wafer while rinsed by water. After cleaned by water, the wafer is deposited onto the heating plate for 6 minutes.

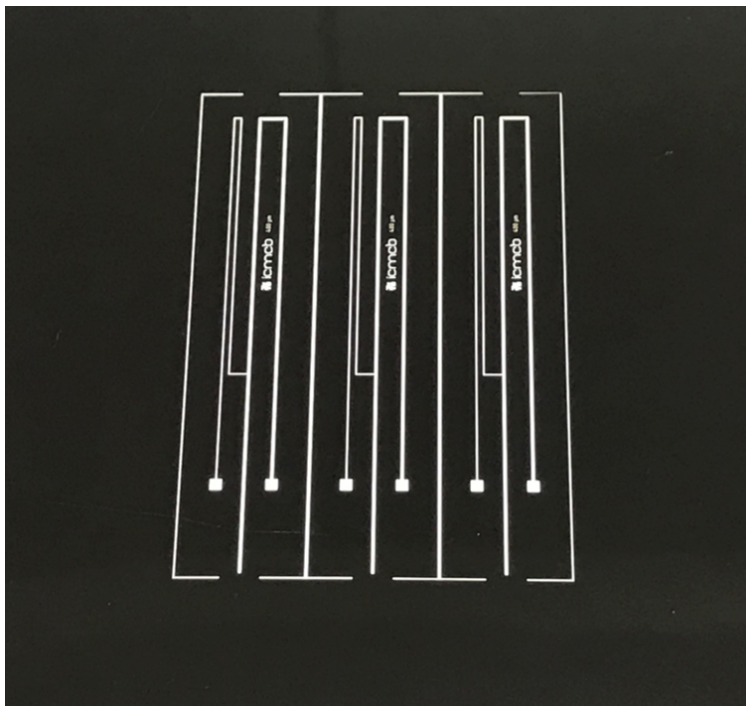


Figure 16: Mask used in this work for the microreactor design and used during the photolithography step.

Step 3 : Wet etching

In a Teflon crystallizer, the wafer undergoes an ammonium fluoride - hydrofluoric acid solution treatment to remove locally the exposed SiO_2 layer. After washed with abundance of water, then acetone and ethanol to remove the resin layer, the wafer is put in a heated bath of tetramethylammonium hydroxide (TMAH) solution, which is a typical etching solution for silicon. The reaction time depends on the desired microchannel depth, measured by a profilometer. A typical etching rate at 90 °C is about $30 \mu\text{m} \cdot \text{h}^{-1}$. The etched wafer at the end of this step is shown in Figure 17.

The cross-section of the engraved channels is trapezoidal because of the wet-etching process. Indeed, all the crystal planes of silicon do not undergo the same etching rate. The

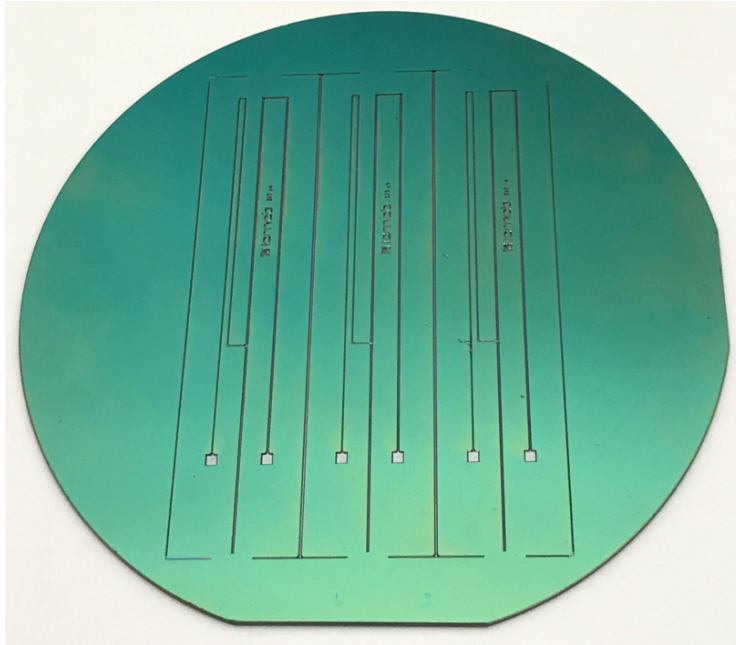


Figure 17: Silicon wafer with one side etched after the wet-etching step.

$\langle 100 \rangle$ plane etching rate is about 100 times faster than the $\langle 111 \rangle$ (Figure 18). Therefore, it is possible to estimate the local width of the channel at a depth " d ", knowing that the angle between the $\langle 100 \rangle$ and the $\langle 111 \rangle$ silicon crystal plane is 56.8° ($d_{\text{bottom}} = d_{\text{top}} - \sqrt{2}d$).

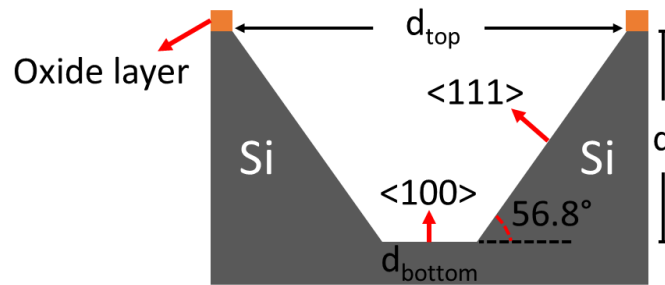


Figure 18: Cross-section of the trapezoidal microchannel.

Step 4 : sandblaster and oxidation

A sandblasting equipment is used to open the inlets/outlets holes inside the wafer. This is carried out at a pressure of 6 bar. The wafer is eventually oxidized in the oven at 1000°C for 2 hours under humid conditions. It means that during the oxidation, water is injected into the oven at a flow rate of 1 mL/h. At the end of this step, an obvious change of color on wafer surface confirms the growth of a silica layer of about 200 nm.

Step 5 : Anodic bonding

The final step consists in assembling the silicon wafer with a Pyrex wafer. To do so, both wafers are first immersed in a Piranha solution for 5 minutes, composed of 30 mL of hydrogen peroxide and 70 mL of sulfuric acid, to create hydroxylated surfaces. The wafers are well rinsed with water and then they are pressed together. The pre-bonded wafers are placed between two heating plates with temperature kept at 400 °C and an electrical tension is imposed onto wafers to be bonded through the heating plates. Once the electric current is stable, the tension is increased by 100 volts at a time from 250 till 1250 volt. 3 cycles are needed to insure a successful anodic bonding between wafers (Figure 19).

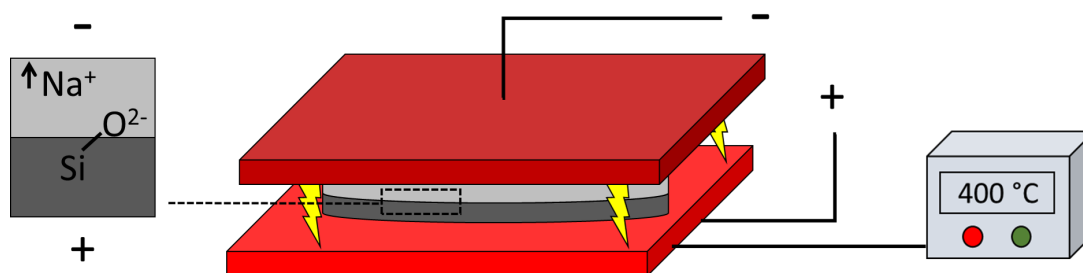


Figure 19: Illustration of the anodic bonding step.

Step 6 : Cutting

With the help of a precision cutter, the final microreactors are separated using a diamond saw and the inlet hole for capillary insertion should be exposed and the capillary is put into the main microchannel, with entrance sealed by Epoxy glue (Figure 20). The final microreactor is shown in Figure 21, ready to be further used for fluid mixing under high pressure and fixed temperature.

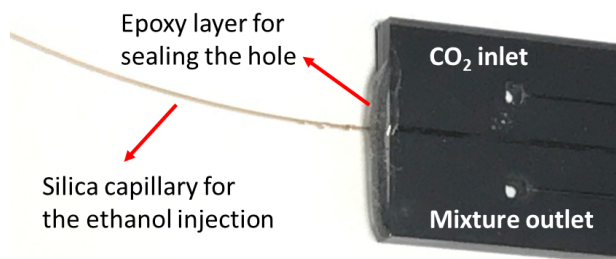


Figure 20: Epoxy sealing for the capillary insertion.

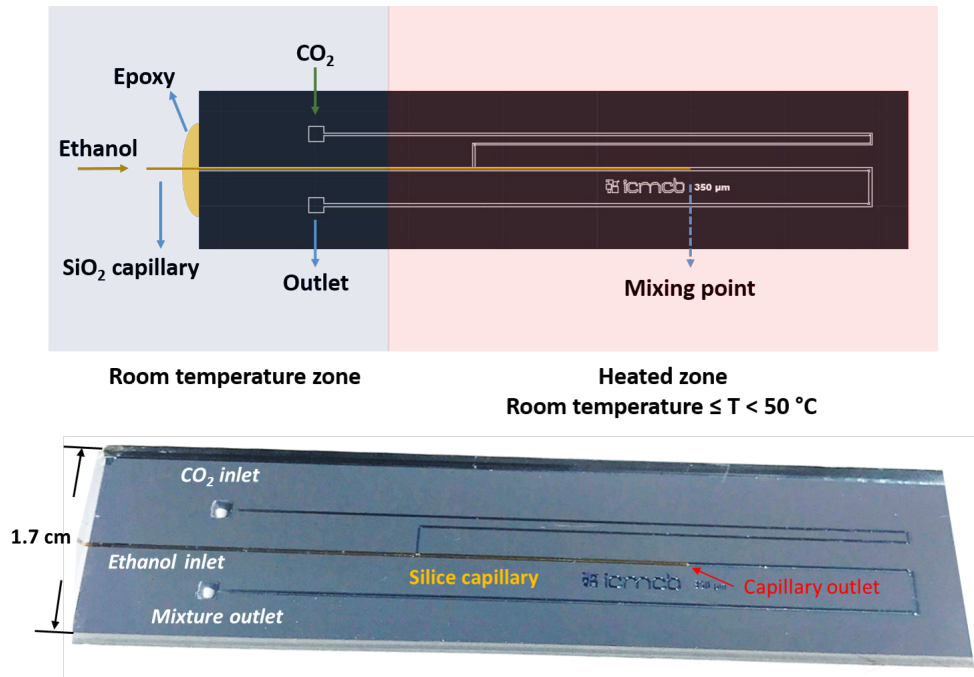


Figure 21: Illustration of the high pressure microchip made of silicon-Pyrex.

2.1.2 Micro Particle Image Velocimetry (μ PIV)

The μ PIV technique is used for measuring experimentally the velocity field of a fluid in a microchannel. Its principle is described first in this part, followed by the set-up used in our laboratory with details. In our case, we have developed the set-up for investigating a high pressure CO₂-ethanol mixture, as a model " μ SAS" mixture.

2.1.2.1 μ PIV principle

The general principle of this experimental characterization consists in tracking the displacement of fluorescent particles, which follow the streamlines of a fluid. The particles, in suspension in the fluid, are excited by a laser inducing the fluorescence of the particles, which can be captured by a camera. In a typical measurement procedure, by comparing the particles' positions between two pictures taken at a very short interval of time Δt , one can estimate the instantaneous velocity field and then the mean velocities of these particles, which are assumed to be the local velocity of the mixing fluids because the particle diameters are much smaller than the width of the microchannel, so they are supposed to follow the current streamlines in the fluid mixture.

2.1.2.2 Chemicals and materials

As mentioned above, we choose the CO₂-ethanol mixture as a model system for this study. The 100% CO₂ used in this work as antisolvent is supplied by the Messer company. The 96% ethanol solvent is provided by Xilab. The purchased fluorescent particles are polystyrene beads from Thermo Fisher Scientific and have a refractive index of 1.59, a density of 1.06 g/cm³ and an average diameter of 1 μm. They are doped with red fluorescent dyes and packaged in deionized water as an aqueous suspension at 1 wt.%, with an excitation maxima at 542 nm and an emission maxima at 612 nm (Figure 22).

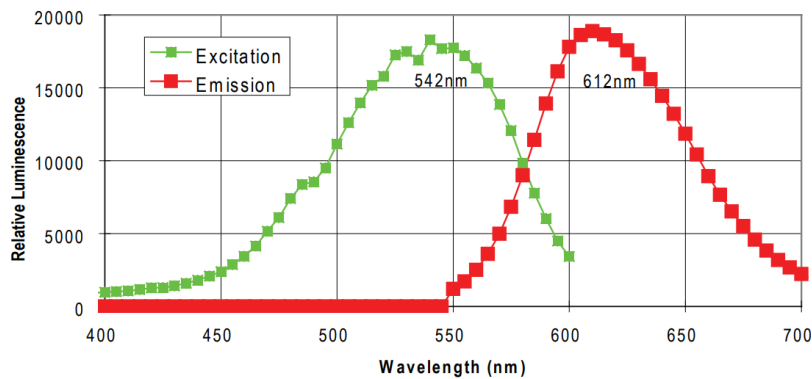


Figure 22: Excitation and emission curves of the Thermo Scientific red fluorescing particles (Duke, 2003).

2.1.2.3 Set-up

The microreactor is implemented in a general experimental set-up detailed in Figure 23. CO₂ and ethanol are injected with an ISCO 100 DM pump equipped with a cooling jacket, and a Harvard PhD 2000 high pressure syringe pump, respectively. The pumps are connected to the microreactor and the silica capillary thanks to a house-made compression part and Valco/Vici commercial fittings, respectively, as seen in Figure 23. The overall pressure is controlled using another ISCO pump working downstream in constant pressure mode. A heating plate is placed on the silicon surface of the microchip to control the temperature. In order to acquire locally the fluid velocities during the injection and mixing process, the hydrodynamic inside the microreactor was characterized by an *in-situ* μPIV system. The μPIV set-up includes a laser diode emitting at $\lambda = 532$ nm, which frequency is set to 4 Hz, with the pulse duration controlled at 15 μs with a time delay at 6 μs. The synchronization between the laser and the camera was set to ensure that the laser was turned on during the recording so that the particles were always excited and captured in each image. A ZEISS

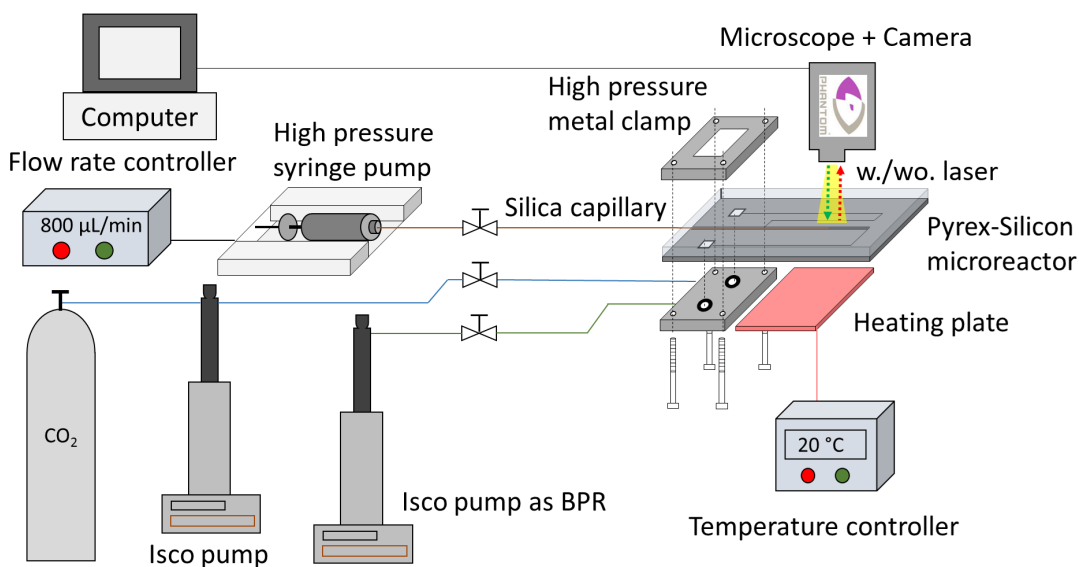


Figure 23: Microfluidic set-up developed for the μ PIV analysis with laser and for the high pressure turbulent mixing observation without laser.

Axiovert 200M microscope was used with a $20\times$ magnification objective to offer optical access to a CCD camera of the Vieworks company displaying a resolution of 3296×2472 pixels, with a frame rate of 10 fps.

2.1.2.4 μ PIV experiment procedures

The tracer particles are preliminarily dried and diluted about 100 times in ethanol (0.01% of volume). The set-up is first pressurized gradually up to 100 bar from downstream with an ISCO pump filled with pure ethanol as a back pressure regulator. The liquefied CO_2 is then injected by another ISCO pump in which the temperature is set originally at -5°C and the pressure at 100 bar to ensure that it is liquified. Once the pressure and temperature are stabilized, the particle suspension in ethanol is injected inside the capillary thanks to a high pressure syringe pump. The two fluids encounter at the outlet of the capillary, forming a coflow mixing. While the laser arrives through the focused mixing zone, the particles in the microchannel are excited and return red fluorescent light at a wavelength of about 612 nm through a dichroic filter and captured by the camera. In a recorded acquisition of 1000 images (500 pairs), the tracer particle displacements can be observed in a black background to determine the average particle velocity field with a fixed interframe time Δt of $100\ \mu\text{s}$. The images are recorded at the capillary outlet and integrated with a field depth of $10\ \mu\text{m}$.

The reproducibility has been tested and the measurements are reproduced 3 times under fixed conditions. During the experiment, no agglomeration of particles has been observed. However, some sedimentation is sometimes detected and some particles are trapped and attached to the wall. Nevertheless, according to the good reproducibility of the results, this effect could be neglected.

2.1.2.5 Software tools for processing velocity field

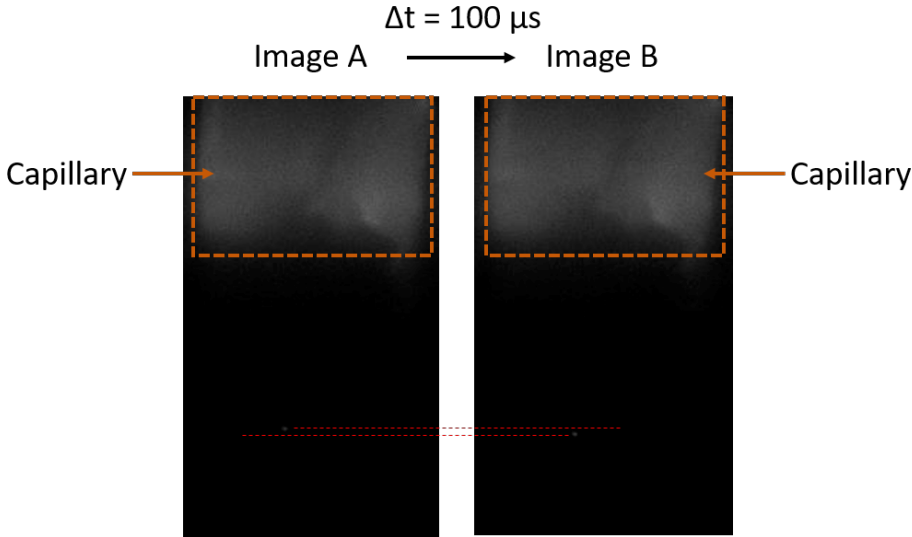


Figure 24: Displacement of fluorescent particles in a pair of recorded images in the μ PIV mode.

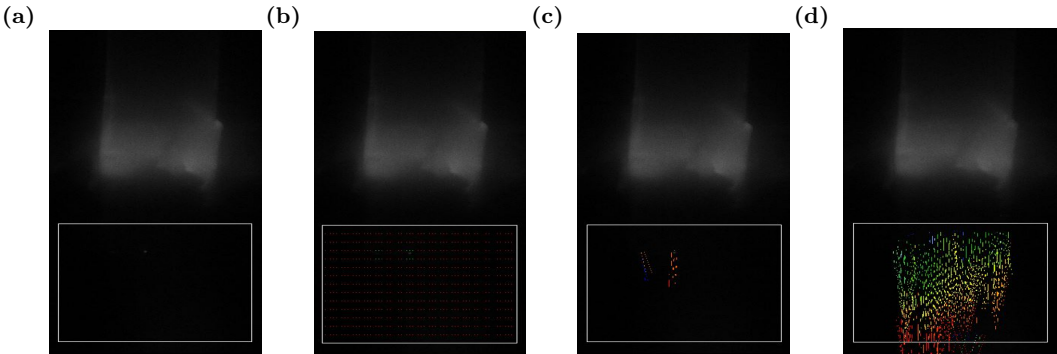


Figure 25: Steps of velocity field processing: (a). selection of the measurement zone; (b).luminosity filter set in the grid sizes; (c). processed instantaneous velocity field; (d). statistic mean time velocity field.

The μ PIV experimental data are processed using the software Hiris, developed by the R&D Vision company. As shown in Figure 24, a pair of images taken within a Δt of 100 μs , presents the displacement of fluorescent particles. The procedure of the post-processing

contains several steps detailed below. (i) The measurement zone should be first selected in the recorded images. The measured area is an adjustable rectangle of $0.5 \text{ mm} \times 0.3 \text{ mm}$ (Figure 25a). (ii) Based on the estimated fluid velocity derived from the known flow rate, the grid size is adjusted. Small grid sizes are used for low velocities with good precision. However, for higher velocities in the channel, larger grid sizes are needed to obtain velocity values. Theoretically, the μ PIV has some limitation for fluid velocity (maximal value about $0.4 \text{ m}\cdot\text{s}^{-1}$). Only laminar mixing can be studied with our system. For high velocities, it is not possible to detect the particles exit the measurement zone during the Δt . The conversion between pixel and length is then corrected according to the pixel length of the capillary outer diameter, which is known ($170 \text{ }\mu\text{m}$). In our cases, one pixel corresponds to $0.263 \text{ }\mu\text{m}$ and the grid size is chosen to be $64 \text{ pixels} \times 32 \text{ pixels}$, according to estimated fluid velocity. (iii) The luminosity filter should be adjusted to detect the fluorescent particles. When there are some particles in a grid, its color turns green and otherwise, the red color indicates that no particles are in the grid (Figure 25b). (iv) The instantaneous velocity field of fluids is calculated by the software for each pair of images (Figure 25c) and the average velocity field can be obtained by taking all the recorded images into consideration (Figure 25d).

2.1.3 Turbulent mixing observation

The turbulent mixing of ethanol and CO_2 has been observed in the same coflow high pressure microreactor in the 3D configuration at $20 \text{ }^\circ\text{C}$ and 100 bar to demonstrate experimentally that turbulent regimes can be reached in those conditions in the confined microfluidic device. Compared to the μ PIV system, the experimental set-up for pressurized turbulent mixing in the microchip is quite similar (Figure 23). The laser generation is no longer needed, neither the fluorescent particles. The μ PIV camera is replaced by a high speed camera (Phantom Miro Lab340, a product of Vision Research company) with its supporting software PCC 2.8 for video recording and post processing. The implemented high speed camera has a maximum resolution of 2560×1600 with a pixel pitch down to $10 \text{ }\mu\text{m}$ and a minimum exposure time of $1 \text{ }\mu\text{s}$. Extra LED light is required for extremely high picture record frequency.

The acquired images of turbulent mixing were post processed with the Matlab software to observe better the turbulent structures. The results are presented in the next chapter. If

2D observation allows for emphasizing the intense mixing due to turbulent flows, it becomes irrelevant for obtaining precise data on the mixing phenomenon. This is the reason why we propose to study the mixing of this system by numerical simulation. Indeed, high performance computing (HPC) code allows for describing, at the smallest scales, the mixing of the species. This approach can be considered as a real "numerical experimentation".

2.2 Numerical modeling

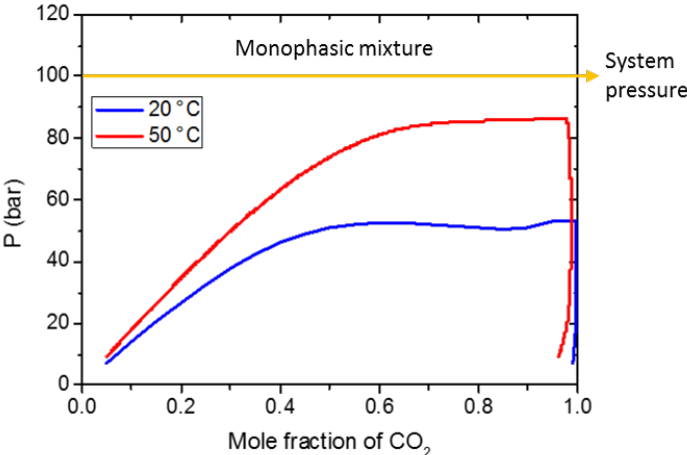


Figure 26: Phase diagram for determining the thermodynamic conditions for a monophasic mixture of CO₂ and ethanol.

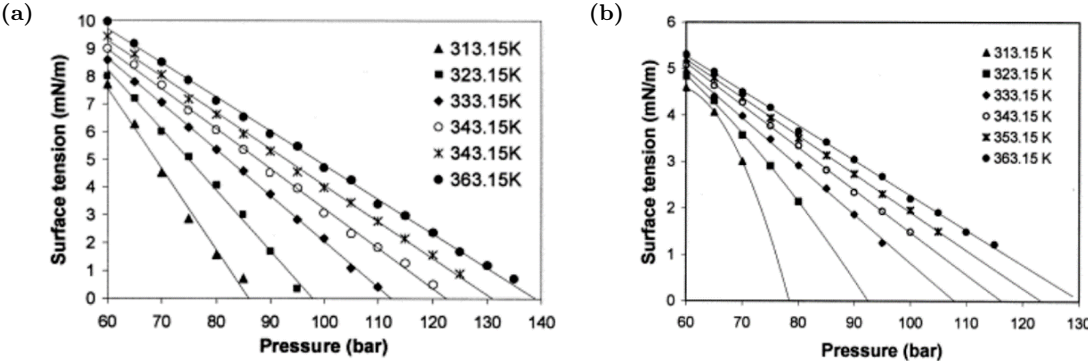


Figure 27: Variation of the surface tension between the CO₂ and ethanol as a function of temperature and pressure, figure extracted from its original paper (Sun and Shekunov, 2003), (a). ethanol droplets saturated in pure CO₂, (b). ethanol droplets equilibrated with CO₂-ethanol mixture.

The physical phenomena considered in the numerical modeling consist of solving the fluid velocity and the species concentration. Since the temperature is well controlled in the experimental part, no energy equation is involved in isothermal conditions. The fluid velocity

and the ethanol concentration field are obtained by the resolution of the continuity equation, Navier-Stokes (NS) equation and the species transport equation. For the simulations of the μ PIV experiments, the effects of the fluorescent particle presence on the fluid properties are neglected so the mixture contains only CO₂ and ethanol. In the studied conditions (40 °C, 100 bar), the pressure is above the critical pressure of the mixture CO₂-ethanol, according to their mixture phase diagram (Figure 26). The surface tension between the CO₂ and the ethanol which reaches 0 under conditions in the microchannel of mixing zone in Figure 27 (Sun and Shekunov, 2003), proves equally that the flow can be considered completely monophasic.

2.2.1 Governing equations of the fluid mixing

2.2.1.1 Mass and momentum conservation equations

The equation of continuity (Equation 1) and the NS equation (Equation 2) are solved for a completely miscible fluid. Furthermore, the fluid is far from the mixture's critical point so the isothermal compressibility is relatively low (between 10^{-8} and $10^{-9} Pa^{-1}$). The comparison of simulations between an incompressible and a compressible formulation has shown that the results were very close without significant difference (Amiroudine *et al.*, 2014; Sharma *et al.*, 2019). Because CPU time is much lower with the incompressible formulation, we consider the model for an incompressible single phase flow of a fluid mixture. The gravity is neglected in the confined microchip because of a small value of the Bond number. The continuity equation and the momentum conservation equation are (Erriguible *et al.*, 2013a; Erriguible *et al.*, 2013b):

$$\nabla \cdot \mathbf{u} = 0 \quad (1)$$

$$\rho \left(\frac{\partial \mathbf{u}}{\partial t} + \mathbf{u} \cdot \nabla \mathbf{u} \right) = -\nabla p + \nabla \cdot (\mu(\nabla \mathbf{u} + \nabla^T \mathbf{u})) \quad (2)$$

with \mathbf{u} the fluid velocity, p the pressure, μ the dynamic viscosity and ρ the fluid density. The left part of the NS equation concerns the fluid inertia in which the first term corresponds to the inertia variation with time and the second one corresponds to the advection. The first term on the right side is the pressure gradient and the second term allows for taking in consideration the viscous effects .

The mass fraction of each species in the fluid mixture is calculated by the conservation equation of the species (Equation 3), including the classical advection and the diffusion term. The species mass fractions can then be deduced for the n-1 species by the following set of equations:

$$\frac{\partial \rho x_j}{\partial t} + \nabla \cdot (\rho x_j \mathbf{u} - \rho D_j (\nabla x_j + d_j^{non-ideal})) = 0 \quad (for\ j = 1, 2, \dots, n-1) \quad (3)$$

with $d_j^{non-ideal}$ the non-ideal diffusion driving force of species j in the mixture. The generalized driving force of the non-ideality is given by (He *et al.*, 2015):

$$d_j^{non-ideal} = x_j \sum_{i=1}^n \left[\left(\frac{\partial \ln \hat{\varphi}_j}{\partial x_i} \right)_{T,P} \nabla x_i \right] \quad (4)$$

While it is set to be zero, the non-ideal model is not taken into account and Equation 3 expresses the classical mass transfer based on the Fick's law. Its influence in the numerical simulation is examined in the next chapter. The mass fraction of the last component, in our case the antisolvent CO₂, can then be directly deduced by Equation 5 once all the other fractions are known.

$$\sum_{j=1}^n x_j = 1 \quad (5)$$

2.2.1.2 Mixture thermophysical properties

In order to solve the equations mentioned in the model, it is necessary to calculate the thermophysical properties of the CO₂-ethanol mixture, such as density, viscosity and diffusion coefficient. Their values should be calculated in the simulated geometry based on the conditions and the composition.

There are several equations of state available to estimate fluid properties with certain mixing rules. We have decided to select the cubic Peng-Robinson equation of state (PREOS) (Equation 6), coupled with the Van der Waals mixing rule (Equation 7), because its simplicity and precision. It is classically adopted to estimate a binary mixture density at high pressure:

$$p = \frac{RT}{V_m - b_m} - \frac{a_m}{V_m(V_m + b_m) + b_m(V_m - b_m)} \quad (6)$$

$$a_m = \sum_i^n \sum_j^n x_i x_j a_{ij} \quad b_m = \sum_i^n \sum_j^n x_i x_j b_{ij} \quad (7)$$

$$\begin{aligned}
a_{ij} &= (1 - k_{ij})(a_{ii}a_{jj})^{0.5} & b_{ij} &= (1 - l_{ij})\frac{b_{ii} + b_{jj}}{2} \\
a &= \frac{0.45724\alpha R^2 T_c^2}{p_c} & b &= \frac{0.0778RT_c}{p_c} \\
\alpha &= \left(1 + (0.37464 + 1.5422\omega - 0.26992\omega^2)\left(1 - \sqrt{\frac{T}{T_c}}\right)\right)^2
\end{aligned}$$

In Equation 6 for a non-ideal fluid state, a_m and b_m represent respectively the attraction parameter and the covolume parameter for a mixture. The density of the fluid CO₂-ethanol is calculated in the model, depending on the composition, the temperature and the pressure. The parameters a and b of the PREOS are solved first for pure components and then for the mixture. The binary interaction parameters k_{ij} and l_{ij} vary in function of the temperature T (Maeta *et al.*, 2015):

$$k_{ij} = -0.4652 \cdot 10^{-3}T + 0.238 \quad (8)$$

$$l_{ij} = -0.8116 \cdot 10^{-3}T + 0.2491 \quad (9)$$

The viscosities of the pure fluids, CO₂ and ethanol, are obtained from the NIST database for the considered experimental conditions. Then, the mixture viscosity is evaluated by a logarithmic mixing rule, according to Equation 10 (Reid and Prausnitz):

$$\ln \mu_m = x_{EtOH} \ln \mu_{EtOH} + x_{CO_2} \ln \mu_{CO_2} \quad (10)$$

The diffusion coefficient of ethanol in CO₂ is estimated by applying the Hayduk-Minhas correlation (Equation 11) (Hayduk and Minhas, 1982; Fadli *et al.*, 2010). The molar volume of pure ethanol V_{EtOH} is calculated by the PREOS.

$$D_m = 1.33 \cdot 10^{-7} \cdot T^{1.47} \cdot V_{EtOH}^{-0.71} \cdot \mu_{CO_2}^{\frac{10.2}{V_{EtOH}^{-0.791}}} \quad (11)$$

Depending on this correlation, the diffusivity changes mainly as a function of temperature and it is supposed to be an isotropic parameter for the mixture of CO₂ and ethanol regardless of the composition.

2.2.2 Precipitation modeling

In this part, we introduce the involved equations applied in the particle precipitation phenomena.

2.2.2.1 Population balance equation

The formation of the solid particles is taken into account by the so-called population balance equation. As in our case, the precipitated particles obtained experimentally in the microreactor are very small, we assume that the effect of the breakage and the agglomeration can be neglected. According to the conservation law, the general equation of population balance is defined by:

$$\rho \frac{\partial n(L, X, t)}{\partial t} + \nabla \cdot (\rho \mathbf{u} n(L, X, t)) + \rho \frac{\partial n(L, X, t)G}{\partial L} = 0 \quad (12)$$

where $n(L, X, t)$ is the number density function with the particle size L as internal coordinate and the space coordinates $X(x, y, z)$ as external ones. The first term on the left side of Equation 15 corresponds to the change of number density with time. The second one is the variation due to the particle movement in the fluid. The third means the number density change related to particle growth, with G the growth rate. The coupling with the fluid dynamics allows for tracking the evolution of the particle size distribution in the reactor.

In order to solve numerically the population balance equation, we introduce the standard method of moments (SMOM). The j^{th} moment is defined by:

$$m_j = \int_0^\infty n(L, X, t) L^j dL \quad (13)$$

Based on its definition, the four first moments ($j = 0, 1, 2, 3$) have physical meanings and are solved in the simulation (m_0 the total particle number; m_1 the total particle length; m_2 the total particle surface area; m_3 the total particle volume). Once all moments are solved, the mean particle size \bar{d}_p can be obtained through the mean time fields of moments, in our case:

$$\bar{d}_p = \frac{\bar{m}_1}{\bar{m}_0} \quad (14)$$

The final population balance equation that we solve in the numerical model is:

$$\rho \frac{dm_j}{dt} + \nabla \cdot (\rho \mathbf{u} m_j) = \rho(0^j B + j G m_{j-1}) \quad (\text{for } j = 0, 1, 2, 3) \quad (15)$$

The first term on the left side means the variation of the j^{th} moment in time and the second term corresponds to the moment motion in space. The right side of Equation 15 is related to the nucleation and to the particle growth.

The coupling of the population balance equation with the fluid dynamics allows for tracking the evolution of the particle size and size distribution in the simulated microchannel. To obtain the moments m_j , we need to calculate the nucleation B and the particle growth rate G as well as their driving force, the supersaturation degree S , presented in the following parts.

2.2.2.2 Supersaturation

The supersaturation is first introduced as the driving force of the particle precipitation. The nucleation and the particle growth are induced by supersaturation effect. Based on the thermodynamic equilibrium of the precipitation, the driving force is actually the chemical potential difference $\Delta\mu_i$ of a solute molecule i in its supersaturated fluid phase and its saturated solution respectively:

$$\Delta\mu_i = k_b T \ln\left(\frac{C_i}{C_{i,sat}}\right) \quad (16)$$

with k_b the Boltzmann constant, T the temperature, C the solute concentration and C_{sat} its saturation concentration or solubility. It is possible to define more simply the solution conditions by using the supersaturation degree, the ratio of the solute concentration C to its solubility C_{sat} :

$$S = \frac{C}{C_{sat}} \quad (17)$$

Accordingly, the solubility data are fundamental for SAS simulation. The experimental data of solubility should be collected as results of temperature, pressure as well as mixture composition.

2.2.2.3 Nucleation kinetic

The nucleation can be described into four types according to the different mechanisms. The primary nucleation expresses the sudden appearance of nuclei taking place directly in the fluid mixture. New nuclei formed at the surface of solid particles and broken off into fluid phase refers to the secondary nucleation. The nucleation can also be classified into homogeneous and heterogeneous. The former indicates solid phase formed in the fluid environment without any influence of other solid particles and the later represents nuclei precipitated at the surface of other impure solid particles different from the solute or precipitator wall. Once nuclei are created, solute in saturated solution and antisolvent mixture is precipitated at the solid surface and particle sizes begin to rise until thermodynamic equilibrium ($S \leq 1$).

In this thesis, we consider that the primary homogeneous nucleation B is the main mechanism of the nuclei formation and it is expressed by (Mersmann, 2001):

$$B = 1.5D_{wC}(C_{sat}SN_a)^{\frac{7}{3}}\sqrt{\frac{\sigma}{k_bT}}V_{sm}exp\left(-\frac{16\pi V_{sm}^2}{3ln^2(S)}\left(\frac{\sigma}{k_bT}\right)^3\right) \quad (18)$$

with N_a the Avogadro constant, σ the solid-fluid interfacial tension, k_b the Boltzmann constant and V_{sm} the solute molecular volume, D_{wC} the solute diffusion coefficient calculated by the correlation proposed by Wilke and Chang (1955):

$$D_{wC} = \frac{7.4 \cdot 10^{-15}\sqrt{\phi M_m T}}{\mu_m V_s^{0.6}} \quad (19)$$

ϕ is the association factor of the solute in the fluid environment. M_m and μ_m are respectively the fluid mixture's molar mass and the viscosity. V_s is the molar volume of the solute. As the solid-fluid interfacial tension σ in Equation 18 is unknown, its value is fitted with experimental results. This kinetic expression is similar to the classical kinetic of chemical reactions represented by the Arrhenius law, with the exponential term depending on the energy barrier ΔG and the temperature. In literature, this critical activation energy can be found for primary homogeneous nucleation (Puel *et al.*, 2005; Mukhopadhyay and Dalvi, 2005).

The importance of this part lies in the kinetic of solute nucleation related to supersaturation. The nucleation time, or induction time, describes a characteristic time necessary to create a certain number of nuclei per unit volume and its value is inversely proportional to the nucleation rate which depends greatly on the supersaturation. It implies that this nucleation induction time is influenced principally by the supersaturation and its value can

vary in a huge range. This energy barrier is an intrinsic property of solute. Generally speaking, when supersaturation level is moderate, nucleation induction time is long due to a low nucleation rate. On the contrary, for immense supersaturation degree, nuclei are precipitated in a very short nucleation time.

2.2.2.4 Particle growth rate

The kinetics of particle growth during SAS can be found in a similar expression, as a function of supersaturation and process conditions (Erriguible *et al.*, 2015). The growth rate is derived from the variation of solute mass in time. From a point of view of particle volume change, this mass variation writes as:

$$\frac{dm}{dt} = \rho_p k_v \frac{dL^3}{dt} = \rho_p k_v 3L^2 \frac{dL}{dt} \quad (20)$$

From a view of the solute molecule transfer to the particle surface, the solute mass variation can also write as:

$$\frac{dm}{dt} = k_g A_p (C - C_{sat}) = k_g k_a L^2 C_{sat} (S - 1) \quad (21)$$

with A_p the particle surface ($A_p = k_a L^2$). By combining the two equation above, we can finally obtain the expression of the growth rate. The classical correlation with a mass transfer coefficient k_g is generally employed, indicating the particle length in function of time:

$$G = \frac{dL}{dt} = \frac{k_a}{3\rho_p k_v} k_g C_{sat} (S - 1) \quad (22)$$

with ρ_p the particle density, k_g the mass transfer coefficient. The k_a and k_v are respectively the surface and volume factors of the particle. For a sphere particle, their values are $k_a = \pi$ and $k_v = \frac{\pi}{6}$. The mass transfer coefficient k_g in Equation 22 can be related to the Sherwood number Sh and precipitated particle properties:

$$k_g = \frac{D_m Sh}{d_p} \quad (23)$$

with d_p the particle diameter. The Sherwood number and the size d_p should be estimated. For the former, one can apply the Froessling correlation (Armenante and Kirwan, 1989):

$$Sh = 2 + 0.6 Re^{\frac{1}{2}} Sc^{\frac{1}{3}} \quad (24)$$

with Re the Reynolds number of the particles and Sc the Schmidt number.

Other forms of growth rate can also be used, such as an equation of the Arrhenius law form (Boutin, 2009). At the molecular scales, solute molecules move onto particle surface, resulting in different growth rate and crystallinity. Normally nuclei and particles begin to grow while supersaturation is higher than 1. The particle growth rate can be approximated to a linear function of supersaturation. Compared to the nonlinear rate of nucleation, particle growth is predominant for moderate and low supersaturations. Otherwise, nucleation is dominant and the solute tends to form nuclei. From the view of mass transfer, the global particle growth rate on the surface of particles is equal to the rate of solute transported from fluid phase to precipitated solids, so one can also rewrite the kinetic equation of particle growth in respect of mass transfer phenomenon (Puel *et al.*, 2005).

2.2.3 Numerical procedure

2.2.3.1 Description of NOTUS CFD

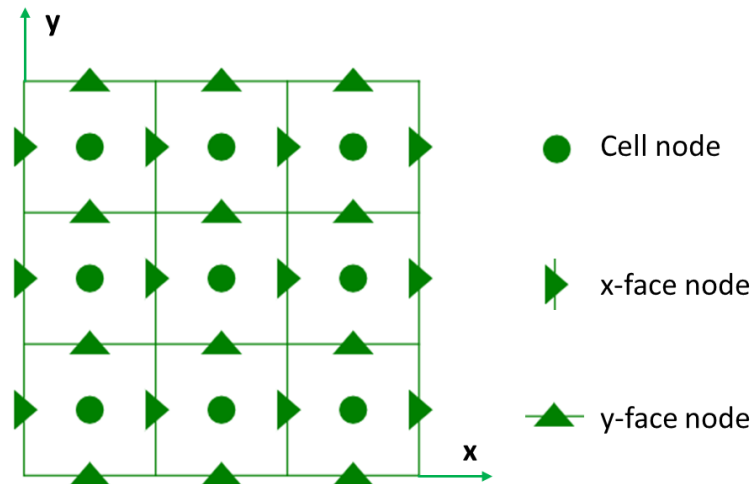


Figure 28: 2D scheme of the cell node and the face node in Notus.

The conservation equations of mass and momentum are numerically solved. The simulation tool for the computational fluid dynamics is the homemade Fortran CFD code "Notus", developed at the institute of mechanical engineering (I2M), department of energy, fluids and transfers (TREFLE). Notus is an open source software based on the finite volume method. The variable fields are solved on a fixed staggered grid, shown in Figure 28 for a 2D illustra-

tion in x and y directions. The scalar fields, as mass fraction, pressure and other variables, are represented as the cell nodes, obtained in the center of each cell (circles in Figure 28). Differently, the components of velocity vector are associated to the face nodes, corresponding to the triangles in Figure 28. Since Notus is massively parallel, it allows for simulating 3D configuration with a great precision.

2.2.3.2 Numerical methods

The formulation employed is totally explicit except the pressure correction step in the velocity-pressure coupling algorithm. The Navier-Stokes equation is solved in two steps by the time-splitting algorithm of Goda (1979). For the prediction step, a non-solenoidal predicted velocity $\mathbf{u}^{*,n+1}$ is calculated by an explicit time discretization scheme of first order:

$$\rho \left(\frac{\mathbf{u}^{*,n+1} - \mathbf{u}^n}{\Delta t} + \nabla \cdot (\mathbf{u}^n \otimes \mathbf{u}^{*,n}) \right) = -\nabla p^n + \nabla \cdot (\mu(\nabla \mathbf{u}^{*,n} + \nabla^T \mathbf{u}^{*,n})) \quad (25)$$

Concretely, the advection term is discretized by the second order scheme in space (total variation diminishing with superbee flux limiter function (TVD superbee)) (Roe, 1986) and an explicit second order central discretization is applied in space for the diffusion term. Then in the correction step, we compute the pressure increment $\varphi^{n+1} = p^{n+1} - p^n$ by a Poisson equation:

$$\nabla \cdot \left(\frac{\Delta t}{\alpha \rho} \nabla \varphi^{n+1} \right) = \nabla \cdot \mathbf{u}^{*,n+1} \quad (26)$$

It is solved by an explicit scheme proposed by Frantzis and Grigoriadis (2019). The linear system is solved by a massive parallel iterative solver (HYPRE BiCGSTAB II), preconditioned with a Jacobi method for the prediction step and the PFMG algorithm for the correction step (Falgout and Yang, 2002). The pressure and solenoidal velocity can be updated based on equations below:

$$p^{n+1} = p^n + \varphi^{n+1} \quad (27)$$

$$\mathbf{u}^{n+1} = \mathbf{u}^{*,n+1} - \frac{\Delta t}{\rho \alpha} \nabla \varphi^{n+1} \quad (28)$$

The species transport equations are solved explicitly using an Euler scheme of first order in time, with the velocity at t^{n+1} calculated anteriorly from the Navier-Stokes equation. For

a species j and its mass m_j , it writes:

$$\rho^n \left(\frac{x_j^{n+1} - x_j^n}{\Delta t} + \mathbf{u}^{n+1} \cdot \nabla x_j^n \right) = \nabla \cdot (\rho^n D_j^n \nabla x_j^n) \quad (29)$$

Similarly, as for the Navier-Stokes equation, the advection term is discretized by an explicit splitting Lax-Wendroff scheme with TVD SuperBee and the diffusion term by the explicit central scheme of second order.

2.2.3.3 Geometry and boundary conditions

Due to the trapezoidal asymmetrical geometry, a three-dimensional simulation is required. Since the μ PIV experiments and the turbulent observation are conducted in two microchips of the same design with slight difference of dimensions, the geometry in the simulations is made separately for laminar and turbulent conditions.

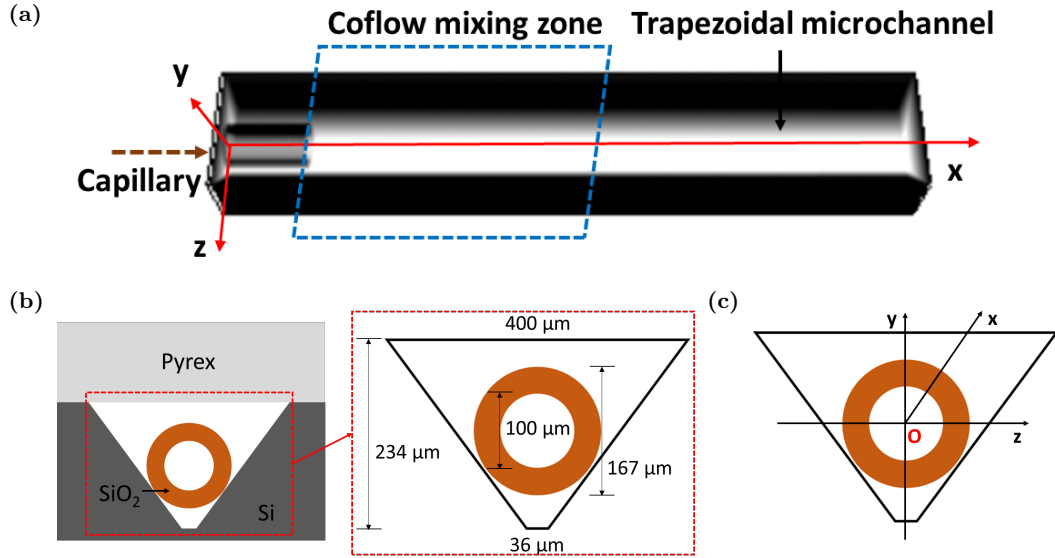


Figure 29: The geometry of the microchannel in the simulations for laminar conditions: (a). the numerical three-dimensional trapezoidal microchannel with an immersed injector; (b). the dimension of the cross-section at $x = 0$ of the microchip used for the μ PIV measurements under laminar conditions; (c). x , y and z axis.

For the simulations of laminar mixing, the whole shape of the simulated area is a cuboid of $0.6 \text{ cm} \times 0.023 \text{ cm} \times 0.04 \text{ cm}$. The circular injector has a length of 0.03 cm with an inner and an outer radius of $51 \mu\text{m}$ and $84 \mu\text{m}$. Solid walls are imposed by a first order accurate penalty method to shape the trapezoidal channel. The mean velocities for both CO_2 and ethanol are provided at $x = 0$ based on the fluid flow rates and the fluid velocity

is then developed by the simulation at the mixing point $x = 0.03$ cm. The ethanol mass fraction is defined to be 1 in the injector and 0 at the outside, leading to pure ethanol and pure CO_2 at $x = 0$ for the boundary conditions of species transport. The grid size is chosen to be $10 \mu\text{m}$, which is comparable to the resolution of μPIV measurement ($16.8 \mu\text{m} \times 8.4 \mu\text{m}$) so the total number of nodes is 552 000 ($600 \times 23 \times 40$). Given the high number of nodes required for describing the process with accuracy, the simulations are performed by a Message Passing Interface (MPI) parallel programming on 16 processors.

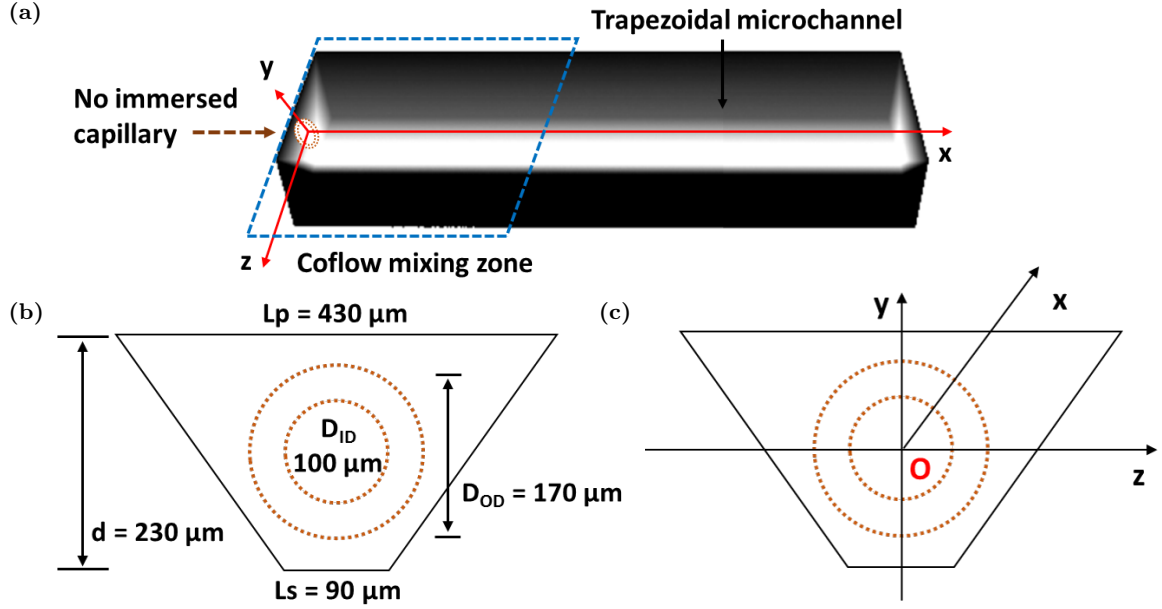


Figure 30: The geometry of the numerical microchannel for the turbulent mixing simulations (a). the three dimensional trapezoidal microchannel without immersed numerical injector; (b). the dimension of the cross-section at $x = 0$ of the microchip used for turbulent mixing observation and simulations (the dotted line indicates no capillary at the boundary); (c). the schema to illustrate x , y and z axis.

For the turbulent mixing simulations, the CPU time required is huge to obtain an established profile of the velocity in the coflow. Accordingly, as a first assumption, we decided to impose a flat profile with the CO_2 velocity mean value according to the fluid flow rate at $x = 0$ in the coflow zone. The ethanol velocity profile in the capillary is imposed as a Poiseuille profile, based on Equation 30 (the Reynolds number of the inner fluid ethanol is always less than 300).

$$u(j, k) = 2 \frac{Q_{EtOH}}{A_{in}} \left(1 - \left(\frac{j}{R_{ID}} \right)^2 \right) \left(1 - \left(\frac{k}{\sqrt{R_{ID}^2 - j^2}} \right)^2 \right) \quad (30)$$

At $x = 0$, the pure ethanol is considered to flow into the trapezoidal channel at the center

(Figure 56b. The initial mass fraction of ethanol is set to be 1 inside the area $\sqrt{j^2 + k^2} < D_{ID}$, and 0 for the outside $\sqrt{j^2 + k^2} > D_{OD}$, implying that it is occupied by pure CO_2 .

2.3 Summary

In this chapter, we have presented both experimental and numerical tools to study the fluid mixing behaviors for the SAS process in our microsystem. First, we introduce the home-made microreactor of silicon-Pyrex type with detailed fabrication procedures. The microreactor is associated to a microscope and a micro particle image velocimetry system to measure the fluid mixture's velocity field in the channel, where a 3D coflow configuration is designed for the mixing of solvent and antisolvent. However, this velocity field can be only obtained for laminar flow conditions due to the equipment limitation. Regarding the turbulent mixing, we propose to observe directly the fluid hydrodynamic by coupling the microscope with a high speed camera. This experimental observation served as a qualitative evidence to demonstrate that our microreactor is capable to reach turbulent regime under high pressure.

In the numerical modeling part, we described the governing equations for the fluid mixing phenomena and also for the particle precipitation. The continuity equation and the Navier-Stokes equation are used for calculating the fluid velocity field. The mass transfer is simulated by the species transport equation. The fluid mixture properties are estimated by the Peng-Robinson equation of state for its density (see Appendix I for more information), a logarithmic mixing rule and the Hayduk-Minhas correlation for the viscosity and the diffusion coefficient, respectively. By solving the population balance equation for the standard moments, we evaluate the particle size and size distribution. The numerical simulation is performed by using an open source CFD code "Notus", developed at the institute of mechanical engineering. The numerical methods, the simulated geometry in three dimensions, as well as the boundary conditions are discussed. We summarize in Figure 31 the set of equations solved for the fluid mixing and for the precipitation.

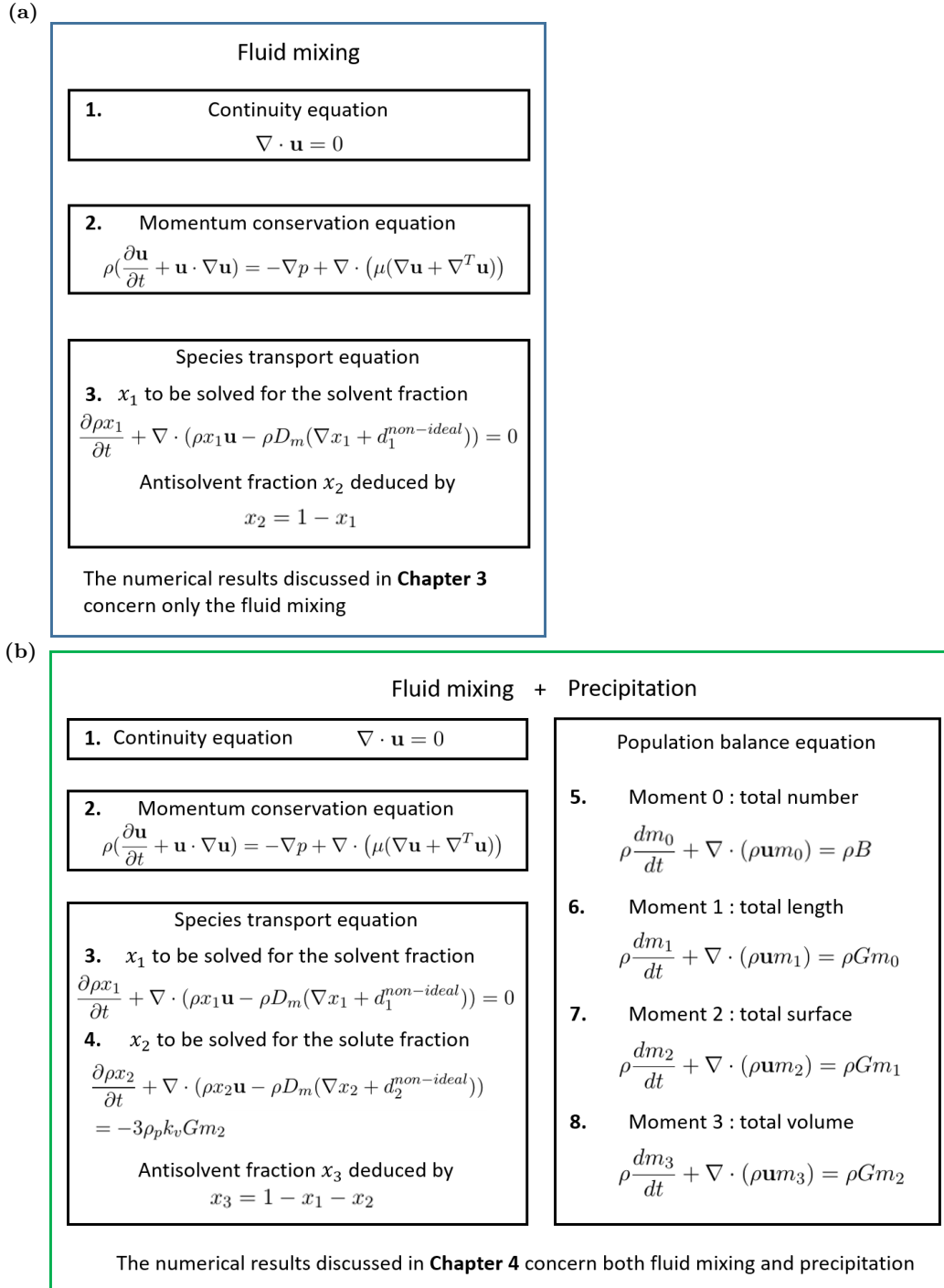


Figure 31: Summary of physical phenomenon equations used in the numerical modeling: (a). equations for the fluid mixing of solvent and antisolvent; (b). equations for both the fluid mixing and the particle precipitation.

Chapter III: Hydrodynamics in microreactor: quantification of mixing

Since nucleation and particle growth occur at molecular diffusion microscales also known as the Batchelor scale, solution and antisolvent turbulent mixing at this level is a key parameter in order to have a deep insight on supersaturation. With no inspection of micromixing, one can play parameter changes in a rough way to characterize SAS but without a profound comprehension, it is hard to give theoretical explanations.

In this chapter, we focus on the hydrodynamic behavior of the mixture of fluids in our high pressure microreactor. The study is conducted both by experiments and simulation. One of the originality of the approach consists by using HPC code to propose direct numerical simulation (DNS) to capture the main scales of the micromixing. In order to clarify the context, let us introduce in the first part the fundamentals of the mixing. The following parts are dedicated to the laminar and turbulent mixing in the microchannel.

3.1 Fundamental mechanism of mixing

3.1.1 Fluid mixing categories for turbulent conditions

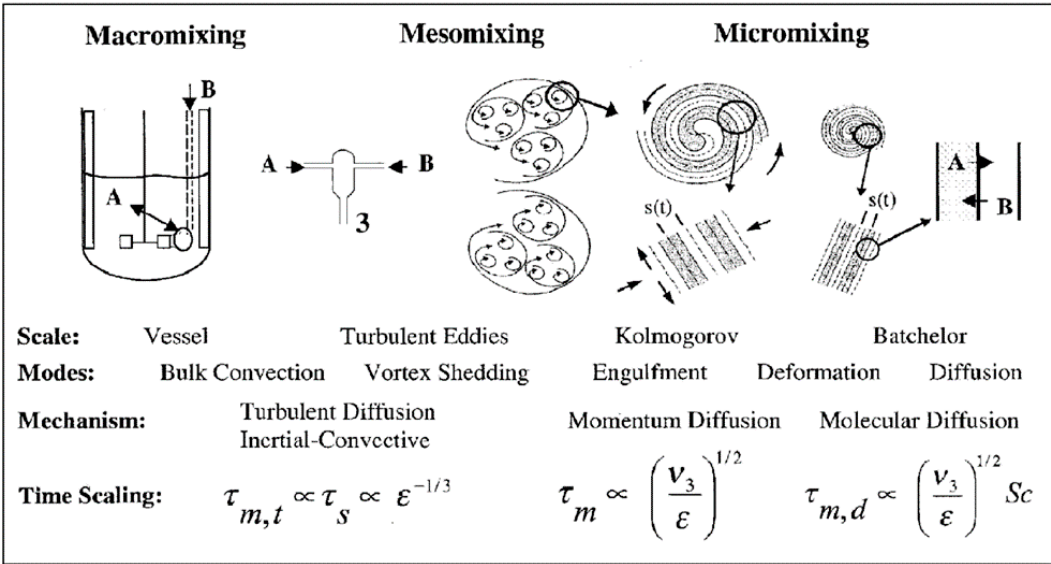


Figure 32: Illustration of macromixing, mesomixing and micromixing and their mixing mechanisms (Johnson and Prud'homme, 2003).

In order to illustrate the role of micromixing in SAS micronization, it is necessary to introduce characteristic scales and times of turbulent mixing. First, as shown in Figure 32, macromixing corresponds to bulk fluid mixing and turbulent mass transfer at large scale and its characteristic time can be described by a relationship between the mixing system dimension and the turbulent diffusivity (Shekunov *et al.*, 2001), with L_0 the characteristic dimension of the system and D_T the turbulent diffusivity.

$$\tau_D = \frac{L_0^2}{D_T} \quad (31)$$

Mesomixing takes place at the scale range between the length of large energy-containing eddies and the Kolmogorov length equal to the smallest eddy dimension (Kolmogorov 1941). In this mixing stage, large eddies are disintegrated to small ones, also known as the inertial-convective mixing. The characteristic time constant of mesomixing is defined by (Baldyga *et al.*, 1994):

$$\tau_s = \frac{C\Lambda_C^{2/3}}{\epsilon^{1/3}} \cong \frac{3L^{2/3}}{4\epsilon^{1/3}} \quad (32)$$

with Λ_C the integral scale for concentration fluctuations, ϵ the energy dissipation rate, C a parameter of about 1.2 and L the scale of large energy-containing eddies. The micromixing occurs at the range of scale around and smaller than the Kolmogorov length. At this stage, the smallest eddies are deformed because of vanished turbulent fluctuation and the mixing rate is related to the laminar stretching, which is proportional to $\sqrt{\epsilon/\nu}$, with ν the fluid kinetic viscosity and ϵ the energy dissipation rate. Its characteristic time is known as the Engulfment time constant proposed by Baldyga and Bourne (1989):

$$\tau_m = \frac{1}{E} = A\sqrt{\frac{\nu}{\epsilon}} \quad (33)$$

with E the Engulfment rate. The coefficient A , estimated to be 17.24, is derived from the hydrodynamic lifetime of vortex τ_v :

$$\tau_v = 12\sqrt{\frac{\nu}{\epsilon}} \quad (34)$$

The τ_v calculated with a coefficient 12 corresponds to the minimal value as a function of the wave number of vortices (Baldyga and Bourne, 1984), indicating the shortest time needed for the disappearance of the smallest vortex. As a matter of fact, this coefficient may vary depending on eddy sizes in mixture system. For instance, in the work of Guichardon and

Falk (2000), they estimated this factor to be 20 by fitting experimental data in a stirred vessel.

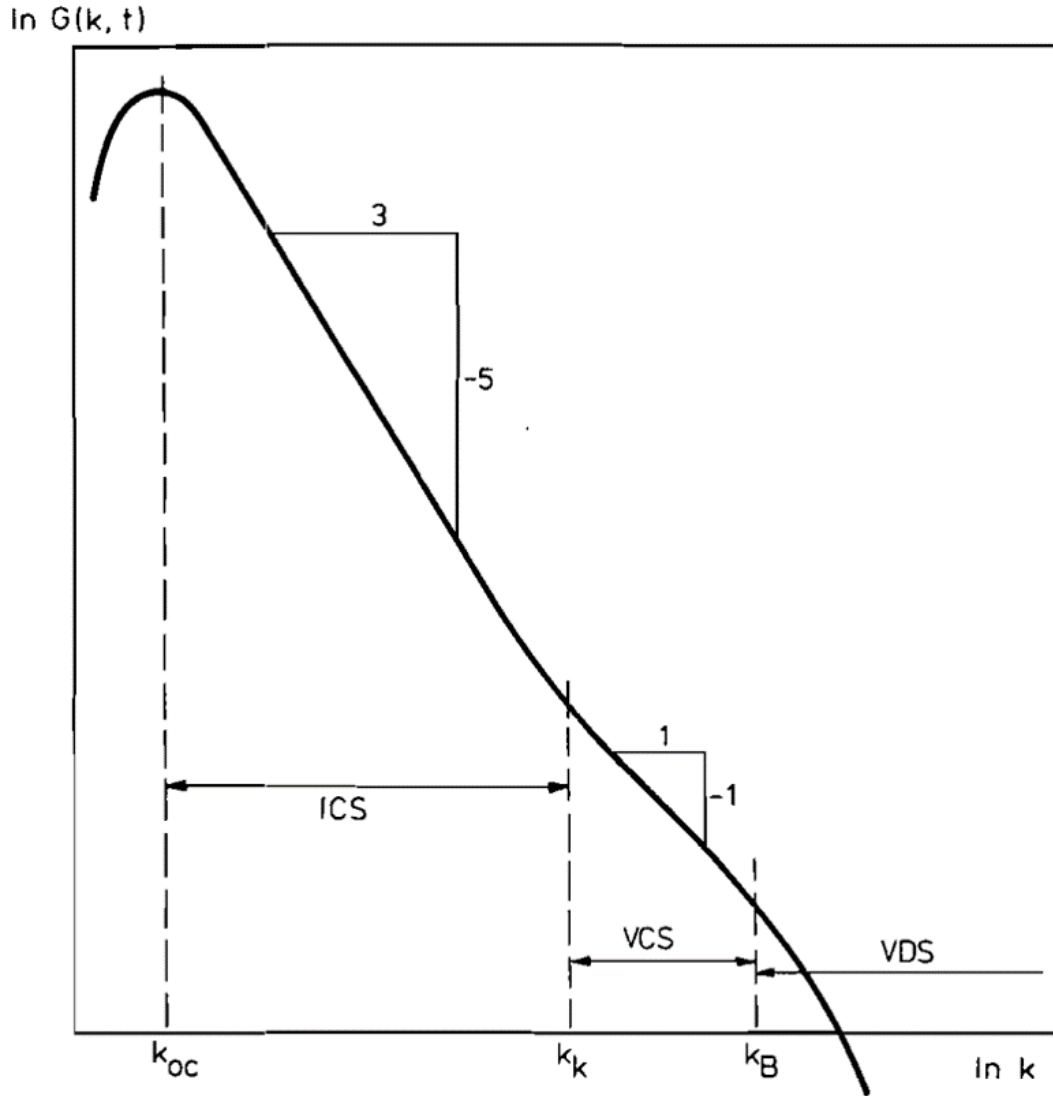


Figure 33: Concentration spectrum of a liquid mixture with Schmidt number $S_c \gg 1$ as a function of length scale k for inertial-convective subrange (ICS), viscous-convective subrange (VCS) and viscous-diffusive subrange (VDS). k_{oc} , k_K and k_B represent respectively the largest scale involved in a reactor, the Kolmogorov scale and the Batchelor scale (Figure extracted from Baldyga and Bourne (1984)).

As shown in Figure 33 which represents the spectrum of the scale concentration in function of the wave number, the turbulent mixing can be divided into three distinct stages, inertial-convective, viscous-convective and viscous-diffusive subrange (Baldyga and Bourne, 1984). The inertial-convective stage corresponds to the fluid mixing among and inside eddies from the largest scale down to the Kolmogorov scale k_K . Fluid kinetic energy is passed

through the deformation and the reduction of eddies without molecular diffusion so the concentration variance still remains significant and the mixing is incomplete at this stage. This result can be proven by the concentration spectrum of a liquid mixture (Figure 33). The integral of spectrum density G is not considerable in the range of scales superior to the Kolmogorov length k_K . While the considered length is reduced in the range between the Kolmogorov scale k_K and the Batchelor scale k_B , the viscous-convective mixing occurs mainly by laminar strain. In this subrange, the eddies are disappearing and the concentration variance drops dramatically so the mixing is highly efficient. The viscous-diffusive mixing is active for the subrange smaller than k_B and species transfer is achieved largely by diffusion. The micromixing is predominantly related to the mixing by molecular diffusion in the viscous-convective range around and below the Kolmogorov scale. From the figure of spectrum of concentration variance dissipation (Figure 34), the micromixing is quite effective with a variance dissipation rate twenty times higher than the mixing rate in inertial-convective mode.

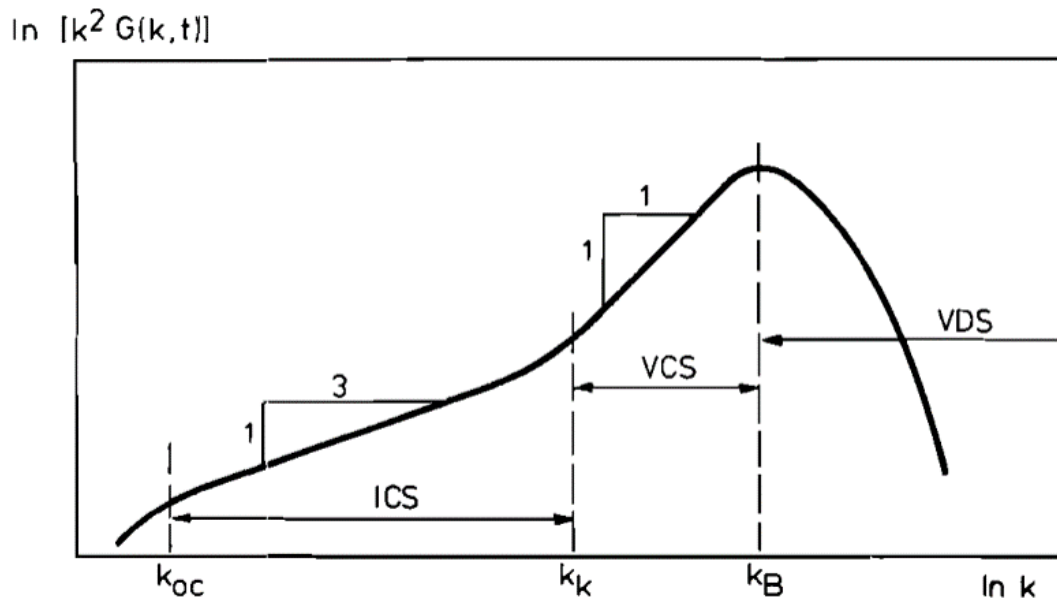


Figure 34: Spectrum of concentration variance dissipation with the same length range examined in Figure 33 (Figure extracted from Baldyga and Bourne (1984)).

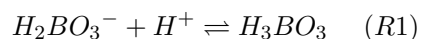
As nucleation and particle growth take place at the molecular length level, special attention should be paid to the micromixing which is a competitive phenomenon to the precipitation. In chemical engineering, characteristic times are often applied for studying competitive

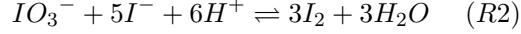
processes between reactions and mass transfer. If micromixing time is much smaller than the nucleation induction time and the growth time, indicating that the system tends to be homogenous, and the process is induced by a well distributed supersaturation, involving homogeneous nucleation and growth in the reactor. It leads to a production of small particles with narrow size distribution. Otherwise, when characteristic times of nucleation and growth are much smaller than micromixing time, particles are formed with a field of supersaturation far from a homogeneous system, leading to large particles in a wide size distribution. These competitive phenomena involved in the SAS process may explain controversial conclusions related to solute initial concentration in solvent. For a fixed micromixing time and unchanged thermodynamics in reactor, higher concentration means higher supersaturation and quicker nucleation and particle growth times. A good mixing performance in this case results in rapid precipitation in a well mixed mixture medium and the nucleation is the predominant mechanism. On the contrary, in a precipitator where mixing performance is mediocre, the increase of solute initial concentration enlarges the supersaturation gradient as well as the difference between precipitation time and micromixing time (an increase of supersaturation results in a higher nucleation rate). Large heterogeneous precipitates are formed. As can be seen, the micromixing is one of the most important factor for the general precipitation/crystallization and works should be carried out to capture micromixing effects.

3.1.2 Experimental method for micromixing analysis

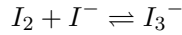
Even though observation is practical to analyze fluid mixing by injecting a flow of dye into another liquid, it is difficult to observe the micromixing in a turbulent flow by this sort of experiments. Some chemical reaction involved methods have been designed for capturing the micromixing in an indirect way and the mostly developed and applied is the competitive iodide iodate reaction, also known as Villermaux-Dushman method (Guichardon and Falk, 2000; Guichardon *et al.*, 2000). It has been developed into a protocol by Commenge and Falk (2011) for examining mixing performance in micromixers.

The theory of this method consists of two chemical reactions: a quasi-instantaneous neutralization reaction (*R1*) and a fast redox reaction (*R2*).





The reaction *R2*, much slower than the reaction *R1*, is fast enough with a reaction kinetic adjustable to be in the same time scale as the one of micromixing by changing the concentration of I^- and IO_3^- . The importance to realize this reaction set is to create stoichiometric defect of proton H^+ . For the ideal mixing case, which is unrealistic with a mixing time less than reaction time of *R1*, mixture becomes immediately homogeneous and all H^+ are consumed by *R1* so no I_2 can be detected. In a real mixing case, the time needed to transfer acid may larger than the characteristic reaction time of *R2* and I_2 is yielded due to local over-concentration of H^+ . A quasi-instantaneous equilibrium of iodine and iodide ions takes place in the mixing system and the equilibrium constant is estimated as a function of temperature. The concentration of triiodide ions can be quantified by UV/Vis spectrophotometry based on Beer-Lambert law and the acid H^+ involved in *R2* can equally be calculated.



A segregation index X_S was introduced to characterize mixing quality, with Y the ratio of acid consumed by *R2* to total acid moles and Y_{ST} the ratio of Y in the case of a total segregation whose value depends on the initial concentrations of IO_3^- and $H_2BO_3^-$.

$$Y = \frac{2(n_{I_2} + n_{I_3^-})}{n_{H_0^+}}$$

$$Y_{ST} = \frac{6n_{IO_3^-,0}}{6n_{IO_3^-,0} + n_{H_2BO_3^-,0}}$$

A higher value of X_S indicates a slower micromixing and similarly, a micromixedness α , proportional to the mixing fastness, was defined as the ratio of the perfectly mixed volume V_{PM} to the totally segregation volume V_{ST} , which is also related to the segregation index X_S :

$$\alpha = \frac{V_{PM}}{V_{ST}} = \frac{1 - X_S}{X_S}$$

Fournier *et al.* (1996) applied this method coupled to a modeling work to calculate the micromixing time and the results were in agreement with the relation given by Baldyga and Bourne (1990). Combined with their previous study (Falk and Commenge, 2010), Falk and Commenge (2011) presented a protocol to examine micromixing in micromixers and proposed an empirical correlation to calculate micromixing time as a function of iron

concentrations. However, this experimental approach is designed for aqueous fluid mixture at atmosphere conditions and micromixing has barely been analyzed experimentally in a supercritical fluid medium in which ions are not soluble.

In order to complete micromixing experiment for supercritical conditions, Carretier *et al.* (2005) developed another chemical method for testing the micromixing in supercritical CO₂ in a batch reactor. The principle is similar and the chemical reaction scheme is presented in Figure 35. Once again, the first reaction is an acid-base neutralization, considered to be instantaneous and the second one is a rapid esterification, slower than the reaction (1), with a first order reaction kinetic only regarding to the catalyst A which is in stoichiometric defect in the first reaction and consumed instantaneously by B. The product ethyl phenylacetate (R) of the second reaction is decisive for micromixing efficiency. A higher yield of this product at the end of mixing process corresponds to a worse micromixing performance in the reactor. The miscibility of reagents in supercritical CO₂ was ensured by optical observation under mixing conditions and although water is a product of the second reaction, they reported that a large amount of ethanol played as cosolvent for water. Despite the feasibility of this chemical method to evaluate micromixing in a batch reactor filled with supercritical CO₂, it has not been further developed for continuous SAS process in precipitators without mixing mechanical device.

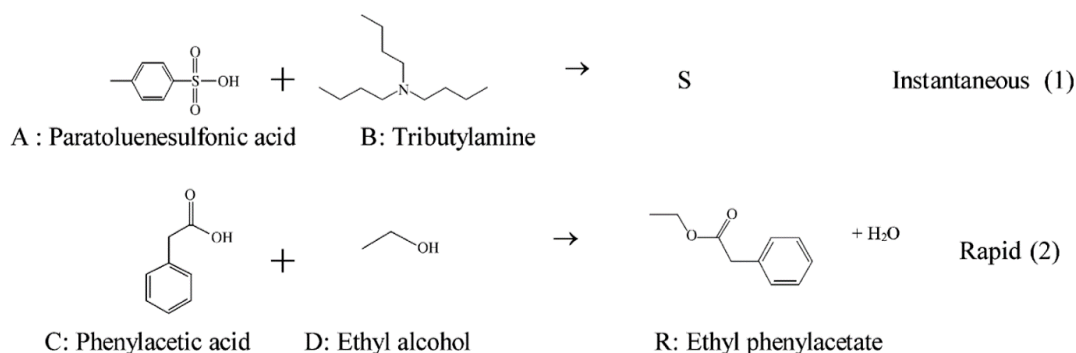


Figure 35: Reaction scheme for micromixing determination in supercritical CO₂ medium (Carretier *et al.*, 2005).

3.1.3 Micromixing modeling

Modeling devoted for micromixing has been studied for several decades and various models have been developed. Some most commonly used models are: the generalized mixing model (GMM) (Villermaux and Falk, 1994), the interaction by exchange with the mean (IEM) (Harada, 1962; Costa and Trevissoi, 1972; Villermaux and Devillon, 1972.) and the engulfment deformation diffusion (EDD) (Baldyga and Bourne, 1988).

3.1.3.1 Generalized mixing model (GMM)

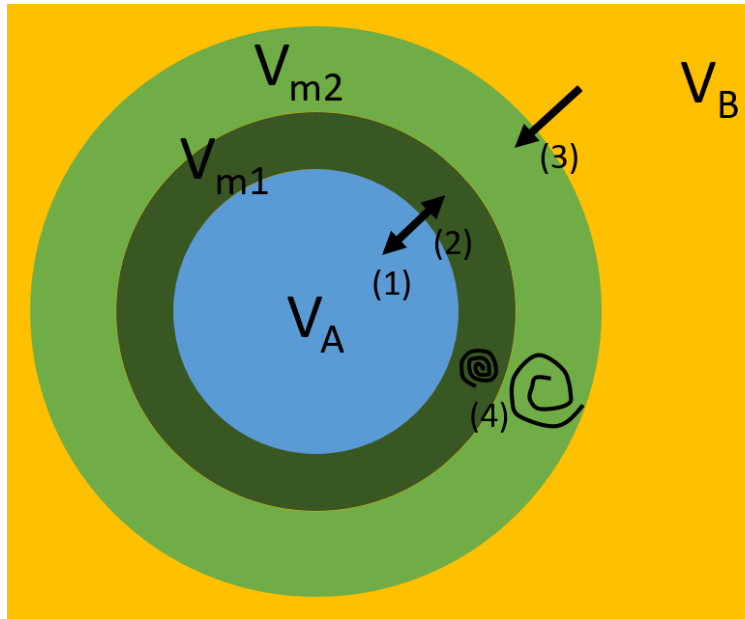


Figure 36: Representative schema of the generalized mixing model, inspired from Villermaux and Falk (1994).

This model interprets in a general manner the mechanism of one liquid A mixed and dispersed into another bulk fluid B.

(1). The first step is the erosion of pure fluid A and its volume V_A decreases as a function of time, where $f(t)$ is an erosion function with constrains $f(0) = 1$ and $f(\infty) = 0$:

$$V_A = V_0 f(t) \quad (35)$$

with V_0 the volume of pure A at $t = 0$.

(2). The dilution step describes the mass transfer of eroded fluid A into the mixing zone V_m

which is divided into two parts V_{m1} and V_{m2} and in this step, only the layer around fluid A V_{m1} is involved. The volume change of this part follows a dilution function $h(t)$, related to the initial volume of fresh incoming fluid A.

$$V_{m1} = V_0[h(t) - f(t)] \quad (36)$$

Apparently, $h(t)$ should satisfy three conditions $h(0) = 1$, $h(\infty) = 0$ and $h \geq f$.

(3). In the mixing cloud V_m , the incorporation of the fluid happens from the bulk B according to an incorporation function $g(t)$. Similarly, this step can be expressed as the total volume evolution of mixing zone and pure fluid A related to V_0 .

$$V_m = V_0[g(t) - f(t)] \quad (37)$$

$$V_{m2} = V_m - V_{m1} = V_0[g(t) - h(t)] \quad (38)$$

(4). Small eddies created by the previous steps interact among them in V_m . This modeled mixing mechanism can explain the micromixing in a tubular polymerization reactor and the micromixing time has been found to be related to the dilution time constant and the exchange time of the interaction step (step 4) (Villermaux and Falk, 1994).

3.1.3.2 Interaction by exchange with the mean (IEM)

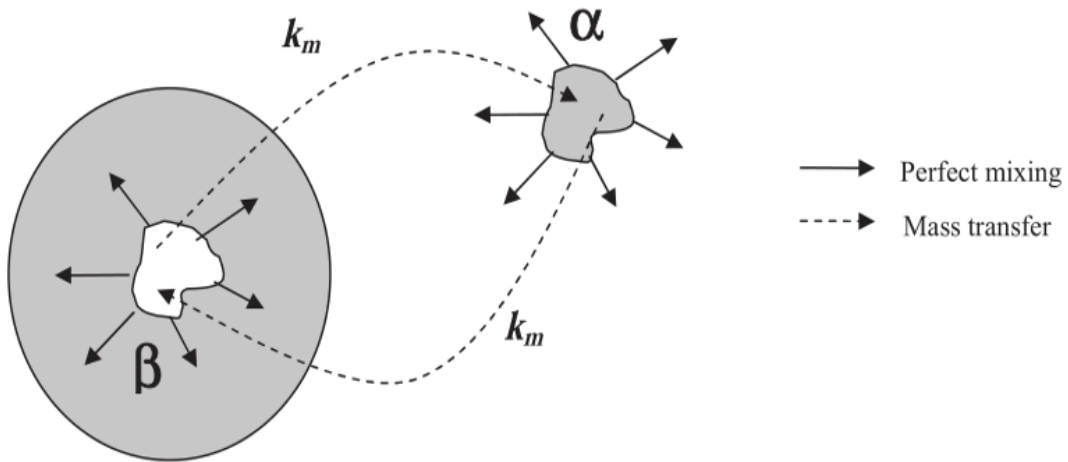


Figure 37: Model description of the interaction by exchange with the mean, figure extracted from Lemenand *et al.* (2017).

The principle of the IEM model is a mass exchange between two constant volumes. Each volume α or β represents homogeneous mixture (or pure fluid at $t = 0$), implying perfect mixing. The exchange rate between volumes is expressed by a coefficient k_m :

$$k_m = \frac{1}{C_1} \frac{\epsilon}{k} = \frac{1}{t_{mIEM}} \quad (39)$$

with t_{mIEM} the micromixing time of the model. The coefficient C_1 is of order 0.5 and k is the turbulent kinetic energy (m^2/s^2) with ϵ the energy dissipation rate (m^2/s^3). The concentration evolution is written based on the conservation of the mass:

$$\frac{dc_i}{dt} = k_m(\bar{c} - c_i) = \frac{\bar{c} - c_i}{t_{mIEM}} \quad (40)$$

$$\bar{c} = \frac{V_\alpha c_\alpha + V_\beta c_\beta}{V_\alpha + V_\beta}$$

where c_i is the scalar concentration of examined species in the fixed volume of environment α or β with the mean concentration \bar{c} .

Despite its simplicity, the IEM model presents imaginary mixing zones but not real physical ones so micromixing at small scales is not exactly defined for turbulent flow conditions (Lemenand *et al.*, 2017).

3.1.3.3 Engulfment deformation diffusion (EDD) model

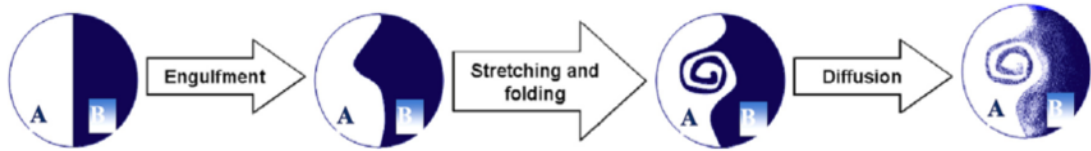


Figure 38: Sketch of the engulfment deformation diffusion model, figure extracted from Lemenand *et al.* (2017).

Like the IEM model, the EDD model has also two different environments A and B but only the environment B is considered to be perfectly mixed. Its volume increases with time during mixing instead to be constant in the IEM model. This model interprets the two fluid mixing by four steps: (1). one fluid is eroded into the other bulk through fluid breakage; (2). eddies are deformed into smaller ones by turbulent cascade in the inertial-convective subrange; (3). vortices are vanishing and laminar stretching takes place at the Kolmogorov

scale; (4). the engulfment step consists of volume incorporation through molecular diffusion at the Batchelor scale and the volume change in the homogeneous environment B $V(t)$ is defined by an exponential equation with a characteristic time of volume growth τ_w .

$$V(t) = V(0)2^{t/\tau_w} = V(0)\exp(Et) \quad (41)$$

The E in the equation above is the engulfment rate, mentioned earlier in the section 2.3.1 and its reciprocal is the engulfment time of EDD model t_{mEDD} . The mass balance is given by:

$$\frac{dc}{dt} = E(c_0 - c) = \frac{c_0 - c}{t_{mEDD}} \quad (42)$$

where c_0 is the concentration constant in environment A and c is the concentration in the growth volume B of concerned material.

The models described above have been compared and applied to qualify the micromixing (Lemenand *et al.*, 2017) but experiments are always required to validate the modeling results. The EDD model has been proven to be capable of providing precise results compared to other models (Baldyga and Bourne, 1990). The time constant of micromixing, as a criterion to characterize mixing quality accepted by most researchers in this domain, is the engulfment time constant of the EDD model (Equation 33).

After the introduction of the fundamental mixing mechanism and the mixing at microscales, we are going to present the methods to study the mixing quality in our microreactor.

3.2 Methods for mixing quality estimation in this thesis

In order to study the fluid mixing behavior in the microchannel under different conditions, some tools are required to characterize the mixing quality. For that purpose, we should first validate the numerical model with experimental data of fluid velocity field in different places of the microchannel. Based on the simulation results of the validated CFD model, the intensity of segregation has been applied to present the evolution of the mixture homogeneity in the channel. The evolution of the segregation intensity as a function of time allows for determining a characteristic mixing time, which fits well the theoretical equation of mixing time.

3.2.1 Model validation

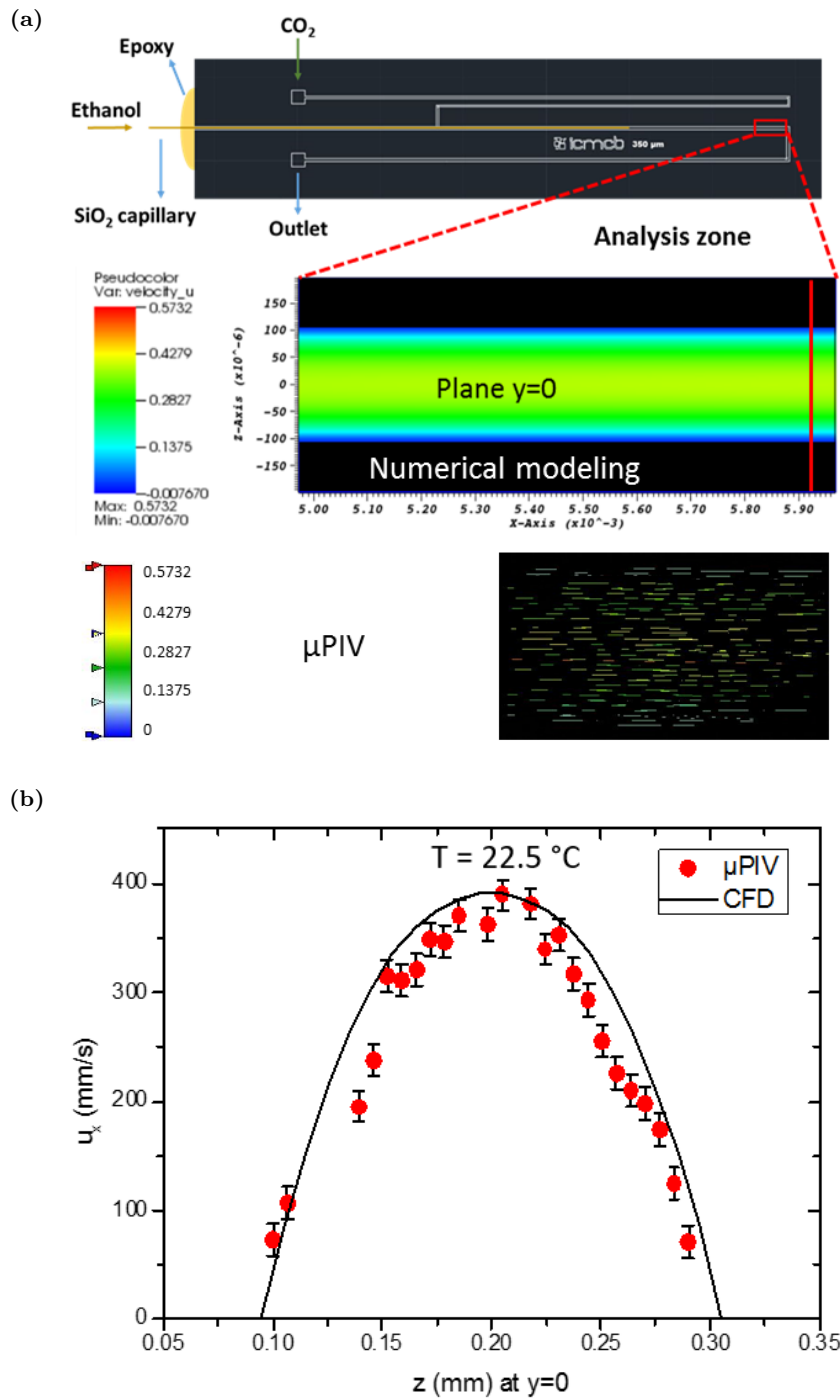


Figure 39: CFD validation for a fully developed flow (far from the injector): (a). velocity comparison in the plane $y = 0$ (with the unit of meter for x and z axes) between the numerical result and the μ PIV measurement for $T = 22.5\text{ }^{\circ}\text{C}$, CO_2 wt.% = 93.6 (test No. 11 in Table 2); (b). 1D comparison on the cut line (red line in (a)), with error bars according to experimental reproducibility.

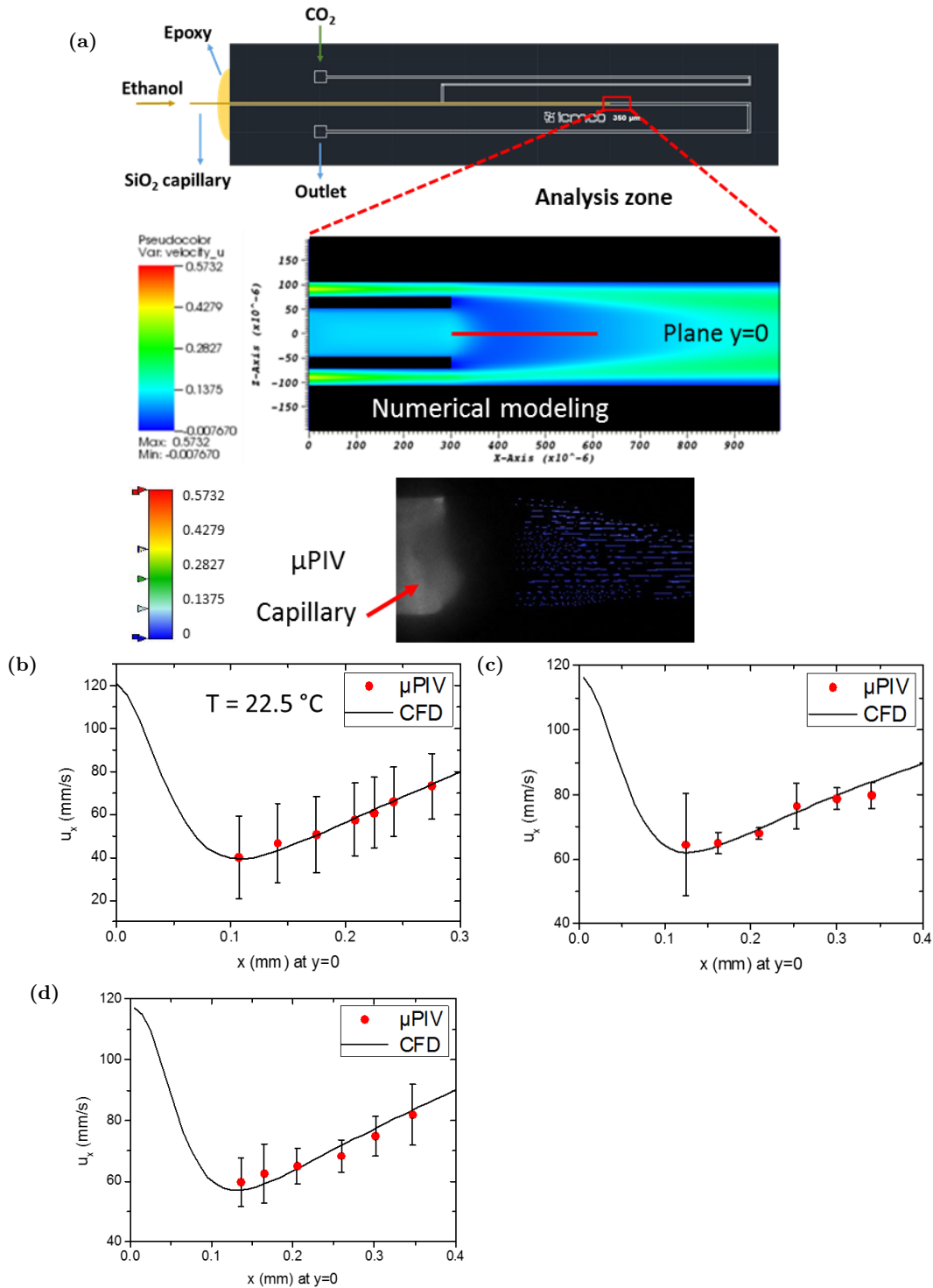


Figure 40: CFD validation in the vicinity of the injector: (a). velocity comparison between the numerical result and the μ PIV measurement in the plane $y = 0$ (with the unit of meter for x and z axes) at the capillary outlet for $T = 22.5$ °C, CO_2 wt.% = 93.6 (test No. 11); (b). 1D comparison at the mid-line (red line in (a)) with error bars according to experimental reproducibility for $T = 22.5$ °C, CO_2 wt.% = 93.6 (test No. 11) (c). $T = 38$ °C, CO_2 wt.% = 83.1 (test No. 4) (d). $T = 47.5$ °C, CO_2 wt.% = 83.1 (test No. 5) in Table 2.

In order to validate the numerical model, the experimental and simulated data obtained for the fluid velocities were compared. For the experimental part, it should be mentioned that our μ PIV system is not adapted for measuring velocities of a turbulent coflow mixing in the microchannel because the high fluid velocity under turbulent conditions exceeds the apparatus measurement limitation. Only laminar mixing has been performed experimentally by the μ PIV system. The measurement data were processed on the mid cross-section of the channel corresponding to the plane $y = 0$. First, the fluid velocities were measured in the microchannel far from the capillary tip, where the velocity profile is well developed and assumed to have a Poiseuille parabolic profile (Figure 39). Then, the mixing zone (Figure 40) near the capillary tip was also investigated. The particles taken into account for the μ PIV fluid velocity measurements can be actually at different height in the channel in a three-dimensional area with a fine thickness. However, as mentioned before, the thickness integrated with our equipment is $10\ \mu\text{m}$ and one can consider that all the recorded particle movements are in a two-dimensional plane. For the case far from the injector, a comparison is shown in Figure 39b and both μ PIV and numerical model provide similar results. The slight difference is probably due to the microfabrication procedure (wet etching step) as the microchannel can not be perfectly trapezoidal with smooth walls everywhere.

Secondly, the fluid velocity at the capillary tip has been examined for different temperatures and fluid flow rates. Based on the experimental results, the velocity of the inner fluid (ethanol) drops first at the injector outlet. Actually the ethanol velocity in the capillary cannot be correctly measured by μ PIV because the silica capillary reflects light and the particle movement inside it cannot be captured. However, the velocity of ethanol at the tip of the injector can be simply deduced from its flow rate. The fluid velocity increases then gradually in the x direction along with the outer fluid CO_2 . A one dimensional comparison is proposed in Figure 40 and numerical data are extracted from the mid-line of the 2D plane of $y = 0$ (red dashed line in Figure 40a).

In general, according to the two comparisons above, both experiments and simulations present very similar hydrodynamic behaviors. The numerical model has been validated with simulated velocities in agreement with measured velocity profiles obtained by μ PIV. Let us note that simulation have been performed without the non ideal diffusion term because of the validation of the μ PIV measurements. We then used the CFD code to investigate the influence of various parameters on the mixing quality in the microfluidic chip.

3.2.2 Turbulent mixing observed by the high speed camera

Regarding the fluid mixing in turbulent conditions, the μ PIV system is no longer adapted to measure the mixture velocity. As a consequence, we have carried out an experimental observation only to demonstrate qualitatively that our microreactor is capable of performing turbulent mixing under high pressure.

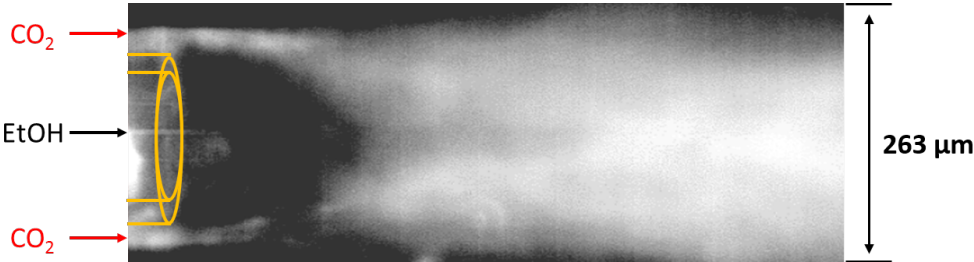


Figure 41: Instantaneous view of the CO₂-ethanol turbulent mixing, captured by the high speed camera, for conditions $Q_{CO_2} = 7000 \mu\text{L}/\text{min}$, $Q_{EtOH} = 800 \mu\text{L}/\text{min}$, $T = 20 \text{ }^\circ\text{C}$, $P = 100 \text{ bar}$.

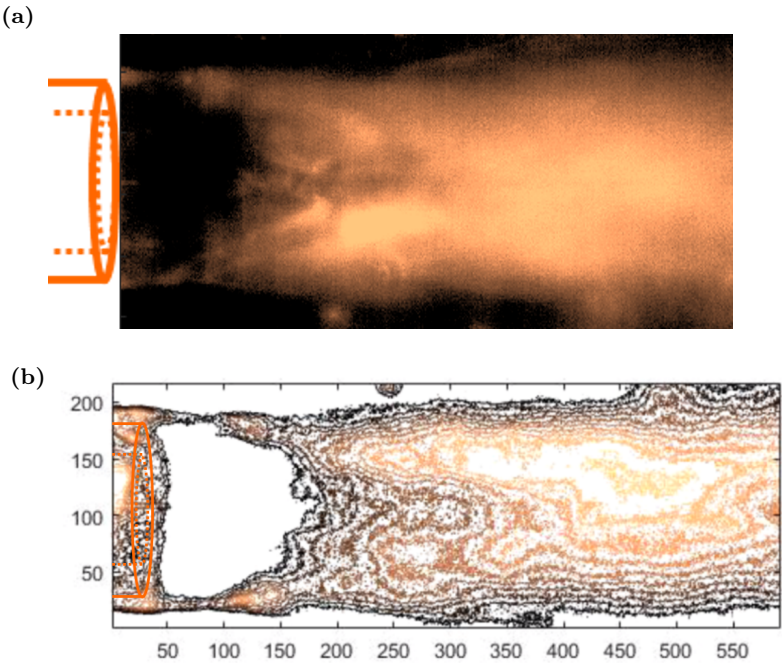


Figure 42: Processed images of CO₂-ethanol turbulent mixing in the microchannel: a. intensity field; b. contour field (with the unit of micrometer for the lengths).

The dense CO₂, the outer fluid, encounters the inner fluid ethanol at 20 °C and 100 bar. The fluid flowrates are 7000 and 800 $\mu\text{L}/\text{min}$ for the CO₂ and the ethanol, respectively, resulting in an analytical average velocities of 3.78 m/s for CO₂ and 1.70 m/s for ethanol. Eddies and vortices can be seen clearly thanks to the high speed camera with a recording

rate of 10000 frames per second. An instantaneous view of the turbulent mixing occurring at the capillary tip is shown on Figure 41.

With the software Matlab, we have standardized the color intensity field (between 0 and 1) shown in Figure 42a. This allows a better observation of turbulent structures, specially in Figure 42b, which represents the color intensity contours. This observation confirms the turbulence in the microchannel and it is essential for the numerical analysis of turbulent mixing discussed in the following parts.

3.2.3 Influence of non-ideal diffusion for turbulent mixing

Rigorously, the non-ideal mixing of the species should be taken into account in the numerical modeling when no experimental data can be served to validate the model. Some authors have shown that in the case of diffusion-predominant mixing close and above the critical point of the mixture, the effects of the non ideal mixing driving force is significant, especially at high temperature (He *et al.*, 2015; He and Ghoniem, 2017; He and Ghoniem, 2018; Sánchez *et al.*, 2019). In our case, we have applied the non-ideal diffusion in the CFD model. The species transport equation for the ethanol mass fraction x_{EtOH} writes below according to a generalized Maxwell–Stefan expression (He *et al.*, 2015):

$$\frac{\partial \rho x_{EtOH}}{\partial t} + \nabla \cdot (\rho x_{EtOH} \mathbf{u} - \rho D_m (\nabla x_{EtOH} + d_{EtOH}^{non-ideal})) = 0 \quad (43)$$

with D_m the diffusion coefficient calculated for CO₂-ethanol binary mixture by the Hayduk–Minhas correlation (Equation 11 in Chapter 2). The non-ideal diffusive driving force $d_{EtOH}^{non-ideal}$ becomes :

$$d_{EtOH}^{non-ideal} = x_{EtOH} \left(\frac{\partial \ln \hat{\varphi}_{EtOH}}{\partial x_{EtOH}} \nabla x_{EtOH} + \frac{\partial \ln \hat{\varphi}_{EtOH}}{\partial x_{CO_2}} \nabla x_{CO_2} \right)$$

The $\hat{\varphi}$ of the equation above is the fugacity coefficient. Its calculation is presented in Appendix I. For the simulation of turbulent mixing, only CO₂ and ethanol are considered so for this binary system, the final $d_{EtOH}^{non-ideal}$ can be expressed as:

$$d_{EtOH}^{non-ideal} = x_{EtOH} \left(\frac{\partial \ln \hat{\varphi}_{EtOH}}{\partial x_{EtOH}} - \frac{\partial \ln \hat{\varphi}_{EtOH}}{\partial x_{CO_2}} \right) \nabla x_{EtOH} = C \nabla x_{EtOH} \quad (44)$$

with C a term representing the difference of the non-ideal diffusion to the ideal case.

We have examined the value of C depending on the molar fraction of CO₂ x_{CO_2} . The

results are plotted in Figure 43 for $T = 40\text{ }^\circ\text{C}$, $P = 100\text{ bar}$.

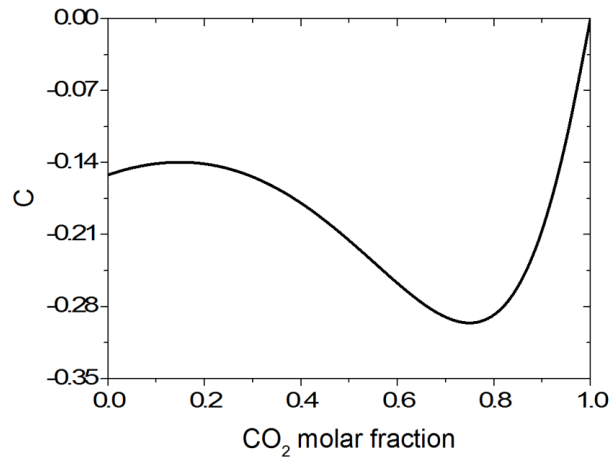


Figure 43: The difference (term C) between the ideal and non-ideal diffusion depending on the CO_2 molar fraction of the mixture CO_2 -ethanol, under the tested conditions $T = 40\text{ }^\circ\text{C}$, $P = 100\text{ bar}$.

Indeed, the value of the term C is not 0 for the mixture CO_2 -ethanol, and the non-ideal model affects truly the mass diffusion. However, when we check the mean time mass fraction of ethanol on the center line ($y = z = 0$) in Figure 44a, the curves are the same. Furthermore, based on the segregation intensity curves, an important criterion for the mixing efficiency which is introduced in the next part, the ideal and non-ideal models give exactly the same results (Figure 44b).

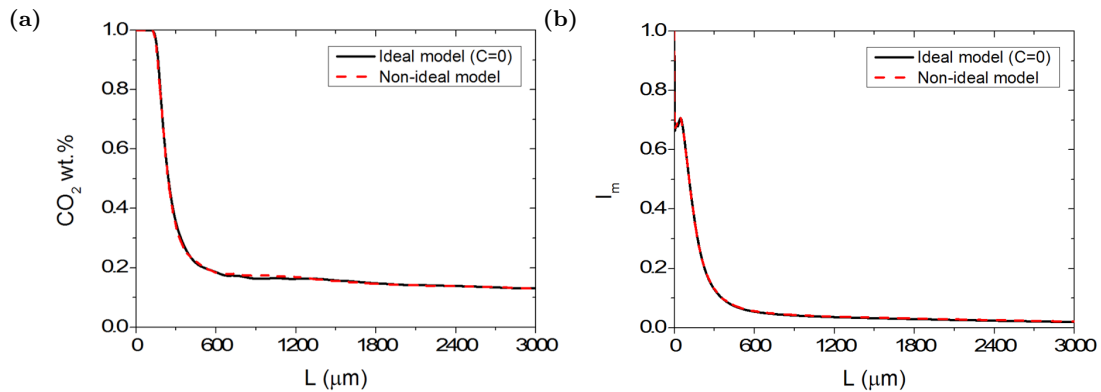


Figure 44: Comparison between the ideal diffusion model and the non-ideal one: (a). the time averaged mass fraction of ethanol on the center line of the microchannel; (b). the segregation intensity in the x direction.

It indicates that the effects of the non-ideal driving force are negligible. This is due to the fact that the diffusive contribution in the mixing is much less important than the convection. Indeed, the Peclet number in the simulations varies from 9000 to 25000 under

turbulent conditions and even for the laminar conditions this number is more than 500. For this reason, we are neglecting the non-ideal mixing in our simulations for the further analysis.

3.2.4 Mixing quality determination and mixing time estimation

The method applied to estimate the mixing quality in this thesis is based on the intensity of segregation. Depending on the form of the segregation intensity curve against a characteristic time axis, the mixing time is determined as the time constant of the first order system with or without time delay. Consequently, the analysis of the mixing will be performed thanks to the following criteria:

- The mixing quality estimated by the intensity of segregation I_m .
- The mixing time calculated in a global manner based on the intensity of segregation I_m and evaluated locally by calculating the energy dissipation rate ϵ in each cell of the simulations (only for turbulent mixing).

3.2.4.1 Intensity of segregation I_m

The mixing quality is related to the homogeneity of the fluid mixture, which may be expressed classically by a relation known as the intensity of segregation I_m defined by Danckwerts (1958). It has been selected to be the main criterion for this study. It is calculated through the x-direction of the flow and depending on the time average mixture composition:

$$I_m(i) = \frac{\sum (\overline{x_{jk}(i)} - \overline{x(i)})^2}{N \cdot \overline{x(i)} \cdot (1 - \overline{x(i)})} \quad (45)$$

$\overline{x_{jk}(i)}$ represents the time average of the ethanol mass fraction in the grid in the i^{th} cross-section with coordinates j and k for the y and z directions (Figure 45). This temporal statistical average is calculated by:

$$\overline{x_{jk}(i)} = \frac{\sum_1^n (x_{jk}^n(i) \Delta t^n)}{\sum_1^n \Delta t^n} \quad (46)$$

The statistical time average is calculated once the stationary regime of flow is reached in the simulated geometry. $x_{jk}^n(i)$ in the equation above is the instantaneous value of mass

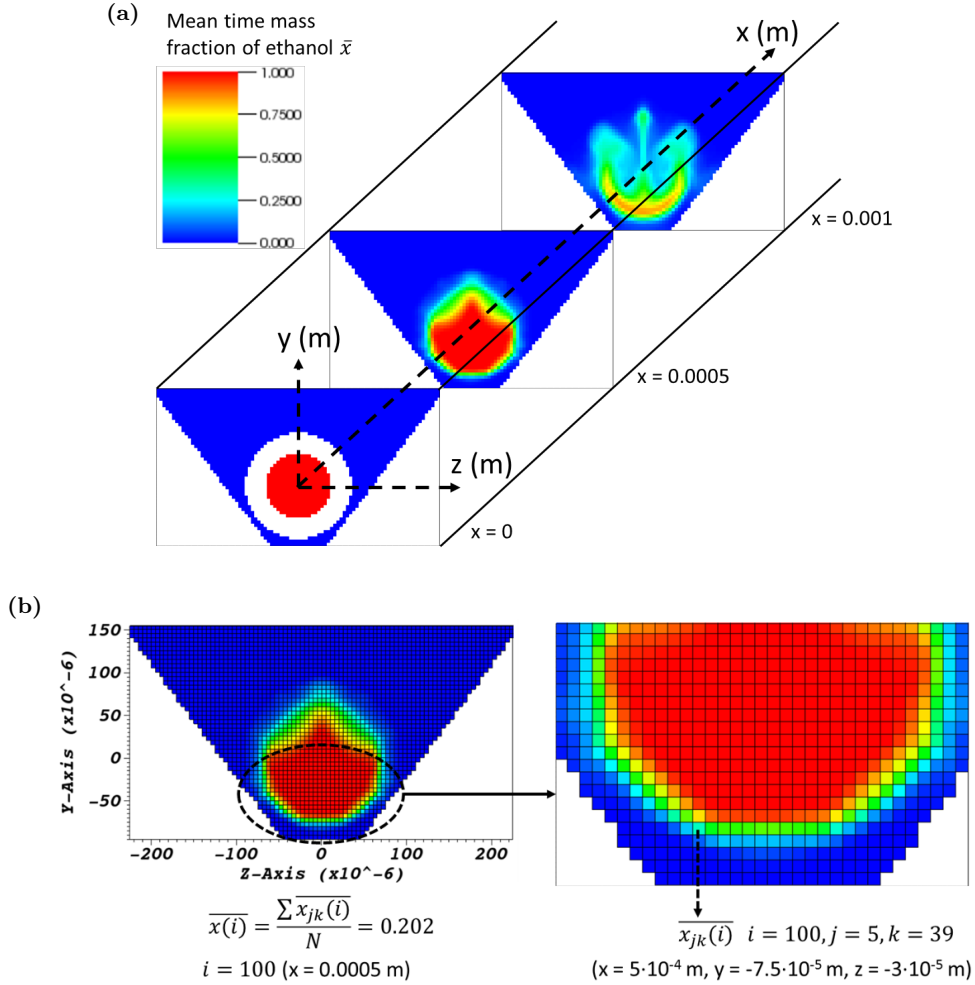


Figure 45: Simulation example for the calculation of mean time statistical value of ethanol mass fraction: (a). the illustration in the 3D microchannel; (b). the average mass fraction of ethanol $\bar{x}(i)$ calculated by its mean time values in all cells in the plane of i^{th} cross-section.

fraction at n^{th} iteration in the cell corresponding to the spatial coordinate (i, j, k) . Δt^n is the discretized time step at n^{th} iteration. $\bar{x}(i)$ in Equation 45 is the spatial average ethanol fraction of the i^{th} cross-section and N the total number of elements in the i^{th} cross-section. The relation between $\bar{x}_{jk}(i)$ and $\bar{x}(i)$ is then:

$$\bar{x}(i) = \frac{\sum \bar{x}_{jk}(i)}{N} \quad (47)$$

The intensity of segregation I_m has the similar meaning than the coefficient of variation, both implying the difference between the sample values and their mean, but I_m varies from 0 to 1, indicating respectively a homogeneous mixture ($I_m = 0$) and a total segregation ($I_m = 1$).

An example is illustrated in Figure 45a for a fluid mixing simulation of CO₂ and ethanol. For each cross-section on the x axis, we demonstrate the statistical mean time mass fraction of ethanol. The immersed boundary is filtered for the solid walls (the trapezoidal microchannel and the capillary at x = 0). Since in the simulation, the spatial geometry is discretized as $\Delta x = \Delta y = \Delta z = 5\mu m$, the 100th cross-section corresponds to a length at x direction $x = 0.0005 \mu m$. We calculate the mean mass fraction of ethanol in this cross-section $\overline{x(i)} = 0.202$ with all time averaged values of ethanol mass fraction $\overline{x_{jk}(i)}$ (Figure 45b). The segregation intensity $I_m(i)$ is calculated in the flow direction x. For the cross-section (i = 100, x = 0.0005 m), its value is determined to be 0.79.

3.2.4.2 Time axis t

The intensity of segregation indicates the homogeneity in each trapeze cross-section of the microchannel. This criterion evolves as a function of the channel length. In order to deduce a characteristic mixing time, we need to express the mixing quality in function of the time. A simple way consists in transforming the length axis by a time axis according to the following expression:

$$t = \frac{L}{u_x} \quad (48)$$

with L the distance from the capillary outlet in the channel and u_x the velocity of fluid in x direction. Whereas, it is sophisticated to select representative fluid velocity u_x for the time axis because in the cross-sections, its values can be quite different, depending on the y and z coordinates. Since the intensity of segregation is a one dimensional global parameter (one value for each cross-section) and not a local one, we choose to compute the overall mean fluid velocity component in the x direction $\overline{u_x}$ far from the injector for a fully developed and homogeneous flow, by taking account the mass flow rate conservation through the section:

$$\overline{u_x} = \frac{\rho_{CO_2}(T_0)Q_{CO_2} + \rho_{EtOH}(T'_0)Q_{EtOH}}{\overline{\rho}(T)A} \quad (49)$$

with $\rho_{CO_2}(T_0)$, $\rho_{EtOH}(T'_0)$ the densities of pure CO₂ and ethanol at the initial temperature in their pumps ($T_0 = -5$ °C and $T'_0 = 20$ °C), Q_{CO_2} , Q_{EtOH} the volumetric flow rates sent by the pumps, $\overline{\rho}$ the density of complete mixture calculated by the global composition at the temperature T in the channel as well as A the trapezoidal area of the microchannel.

Another possibility for u_x is the mean time velocity in each cross-section. The compar-

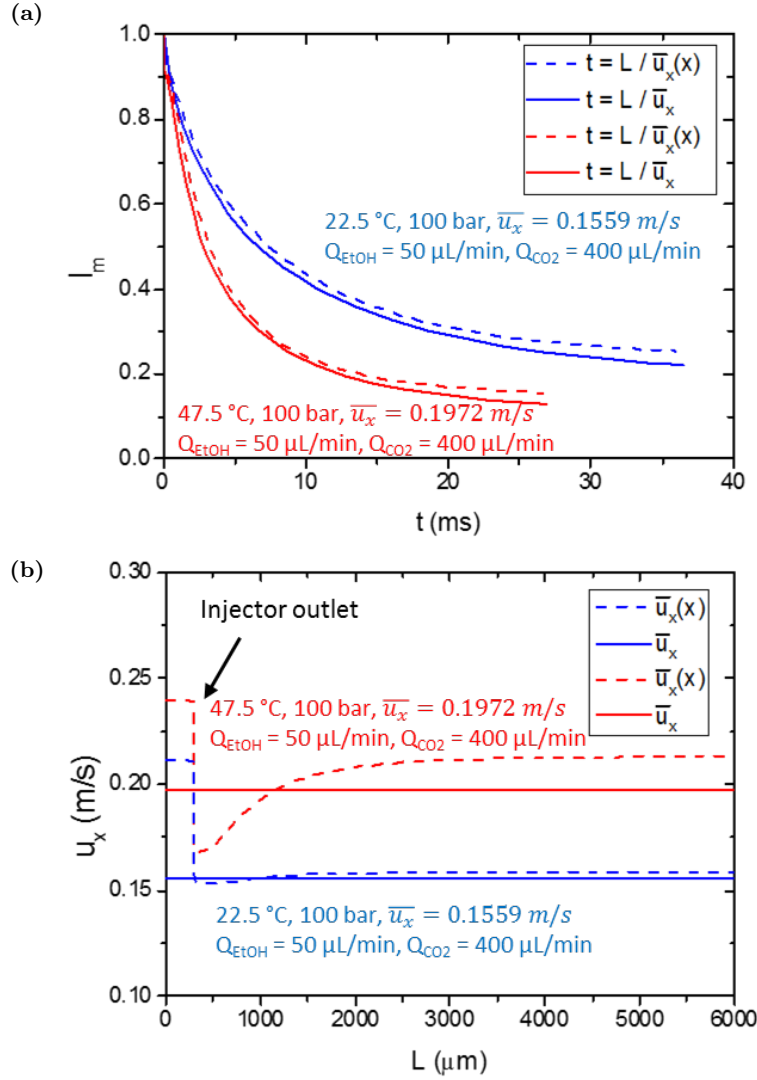


Figure 46: Comparison of time axis for laminar mixing conditions, calculated by the global mean fluid mixture velocity \bar{u}_x based on fluid mass flow rates and by the average velocity in each cross-section at x direction $\bar{u}_x(x)$: (a). effects of mean velocity choice on the intensity of segregation I_m ; (b). evolution of mean velocities along with the length of microchannel (test No.6 for the blue lines and No.10 for the red ones in Table 2).

Figure 46 shows that under laminar conditions, even if the global average velocity and the mean velocity in each cross-section can be different, the segregation intensity curves have almost no difference.

For turbulent mixing, however, it is no longer suitable to use the global mean velocity to calculate the time axis. The velocity profile becomes complicated locally and the overall average value of the mixture's velocity can be very different from the ones in the examined zone close to the injector outlet. According to the results of a simulation, the mean velocity

in each cross-section at x direction is always $1.65436 \pm 0.000007 m/s$ the test case No.5 in Table 3 in the simulated geometry but the global average velocity of the mixture is 1.19 m/s. The use of mean velocity in each cross-section has also been tested but it seems to be less appropriate because of the complicity of the turbulent structures. The vortices and recirculation accelerate the fluid mixing. However, they produce often low mean time absolute values of velocity in each cross-section, making a slower decrease of the intensity of segregation. It seems that this time axis is not representative. Consequently, for a better representativity, the time axis for the turbulent mixing is derived as $t = L/\overline{u_{xin}}$, with the microchannel length L or the distance from the capillary outlet and the mean velocity of the inner fluid ethanol in the capillary $\overline{u_{xin}}$:

$$\overline{u_{xin}} = \frac{Q_{EtOH}(T_0)\rho_{EtOH}(T_0)}{\rho_{EtOH}(T) \cdot A_{in}} \quad (50)$$

where A_{in} the inner circular area of the capillary, T_0 the room temperature at 20 °C and T the one in the microchip. We have considered that the use of the pure ethanol velocity is appropriate, implying the injected and mixed quantity of ethanol.

3.2.4.3 Characteristic mixing time t_m

The intensity of segregation expressed as a function of the time, allows us for determining the important criterion for the mixing characterization, the characteristic mixing time. For that, we considered that the segregation intensity can be simply modeled by a dynamic first order system model without ($\propto e^{-t/\tau}$) or with time delay ($\propto e^{-(t-t_d)/\tau}$) (Scholz and Scholz, 2015). In this case, the time constant of the mixing or the characteristic mixing time t_m can be deduced by the fitted curve of the first order system ($t_m = \tau$), as represented in Figure 47 (Figure 47a for the examples without time delay and Figure 47b for the case with time delay t_d only in turbulent conditions). The characteristic time determined by this method is a simple way to qualify chemical process, as characteristic reaction time (Guichardon and Falk, 2000; Metzger, 2017). Once the segregation intensity curve is derived, the mixing efficiency can be quantified by this mixing time.

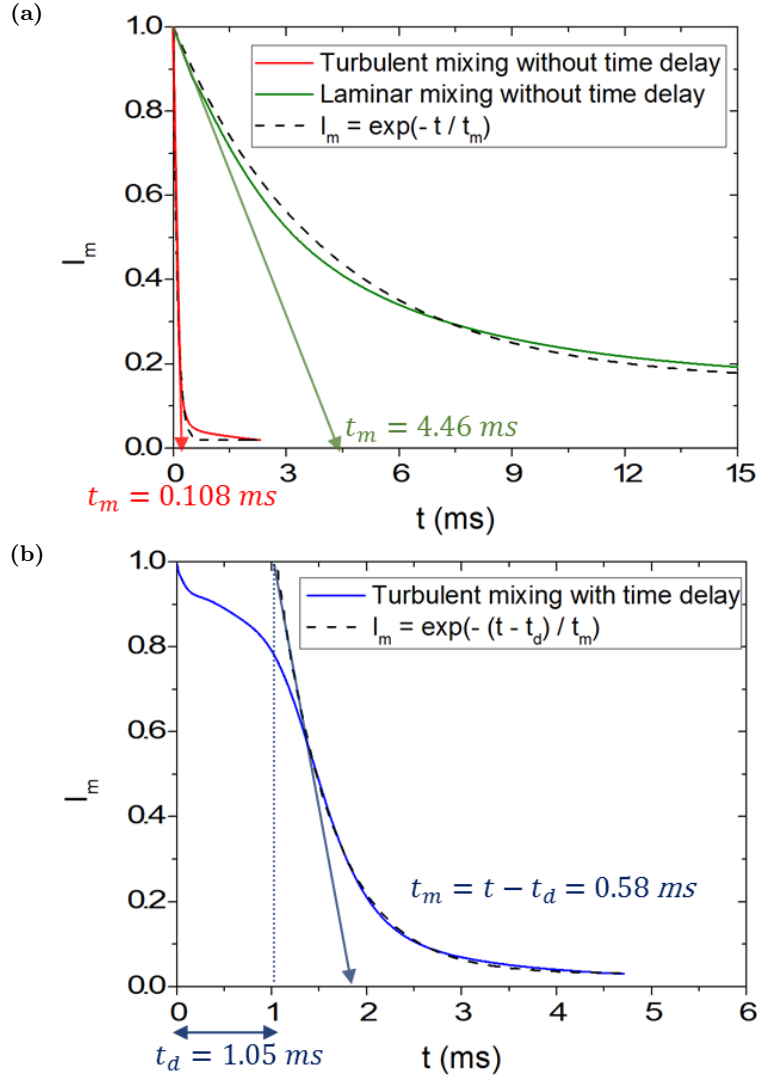


Figure 47: Method for determining the characteristic mixing time based on the curve of segregation intensity I_m as a function of time: (a). for the first order system without time delay t_d (laminar mixing case is the test No.10 in Table 2; turbulent mixing case is the test No.5 in Table 3); (b). for the first order system with time delay t_d only in turbulent conditions (test No.11 in Table 3).

3.2.5 Calculation of the energy dissipation rate ϵ

As well known and discussed in the literature, the energy dissipation rate ϵ is an essential parameter for the fluid mixing. Indeed, the theoretical mixing time is generally related to it. Increasing its value accelerates mixture homogeneity and reduces the mixing time. For a real case of fluid mixing, the method for estimating ϵ is different. In the case of the laminar flow, the energy dissipation is mainly due to the pressure drop. For a turbulent flow, the energy of the fluid passes from large eddies to small ones and dissipates into heat below the Kolmogorov scale due to the viscous forces. The estimation of the energy dissipation rate in

this case is generally challenging and most of the time calculated assuming hypothesis. As a consequence, it is much more complicated to estimate ϵ of a turbulent flow than a laminar one. The following parts introduce separately how we calculated ϵ under the two different regimes.

3.2.5.1 ϵ for laminar mixing

The energy dissipation rate for laminar mixing is classically expressed by the following equation:

$$\epsilon = \frac{Q\Delta p}{\rho V} = \frac{Q}{\rho A} \cdot \frac{\Delta p}{L} \quad (51)$$

with p the pressure, Q the flow rate, ρ the fluid density, V the container volume, A the cross-section surface and L the length of channel.

According to the Darcy-Weisbach equation (Equation 52) and the Darcy friction factor f_D in a circular tube (Equation 53), one can easily obtain (Equation 54):

$$\frac{\Delta p}{L} = f_D \cdot \frac{\rho}{2} \cdot \frac{\bar{u}^2}{D_h} \quad (52)$$

$$f_D = \frac{64}{Re} \quad (53)$$

$$\frac{\Delta p}{L} = \frac{128\mu Q}{\pi D_h^4} \quad (54)$$

with \bar{u} the mean velocity, D_h the hydraulic diameter, Re the Reynolds number, μ the fluid viscosity.

By combining Equation 51 and Equation 54, the energy dissipation rate ϵ is finally presented in Equation 55 for laminar flow in a circular tube and this equation has been used to calculate ϵ in many sorts of micromixers (Falk and Commenge, 2010):

$$\epsilon = \frac{32\nu(\bar{u})^2}{D_h^2} \quad (55)$$

The calculation of Equation 55 is only valid for round cross-section channel. Indeed, the coefficient 32 is different for different channel geometries. In our microreactor, the shape of the microchannel is trapezoidal so that the coefficient 32 has to be modified for this geometry. A similar correlation of Equation 53 is proposed for a trapezoidal shape channel,

given by Bahrami *et al.* (2005):

$$f_F Re_{\sqrt{A}} = \frac{8\pi^2(3\omega^2 + 1) + \beta(1 - 3\omega^2)}{9\sqrt{\omega}(\omega + \sqrt{\omega^2 - \beta\omega^2 + 1})} \quad (56)$$

in which f_F is the Fanning friction factor and the $Re_{\sqrt{A}}$ is the Reynolds number with the square root of cross-sectional channel area as the characteristic length instead of the hydraulic diameter.

The parameters ω and β are determined by the trapeze, shown in Figure 48.

$$\omega = \frac{a + b}{2h} \quad (57)$$

$$\beta = \frac{4ab}{(a + b)^2} \quad (58)$$

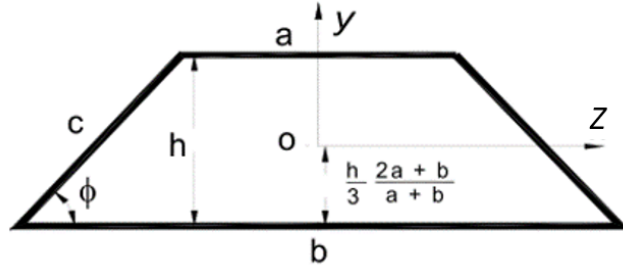


Figure 48: Schematic of trapeze cross-section geometry, extracted and modified from a published work (Bahrami *et al.*, 2005).

As known that the Darcy friction factor is 4 times of the Fanning friction factor, the former one can be calculated for a trapezoidal channel from Equation 59.

$$f_D = \frac{52.24}{Re} \quad (59)$$

By comparing Equation 53 and Equation 55 for the circular channel, the coefficient 26.12 is eventually derived for Equation 60.

The final equation for calculating the laminar energy dissipation rate in our channel is:

$$\epsilon = \frac{26.12 \cdot \nu \cdot \overline{u_x}^2}{D_h^2} \quad (60)$$

3.2.5.2 ϵ for turbulent mixing

Thanks to the use of the direct numerical simulation in our study, we are capable of calculating instantaneous and mean velocity fields. So the energy dissipation rate ϵ is directly calculated from the derivatives of the velocity component fluctuations and the local kinetic viscosity, according to:

$$\begin{aligned} \epsilon = & 2\nu \left[\left(\frac{\partial u'_x}{\partial x} \right)^2 + \left(\frac{\partial v'_y}{\partial y} \right)^2 + \left(\frac{\partial w'_z}{\partial z} \right)^2 + \frac{\partial u'_x}{\partial y} \frac{\partial v'_y}{\partial x} + \frac{\partial u'_x}{\partial z} \frac{\partial w'_z}{\partial x} + \frac{\partial v'_y}{\partial z} \frac{\partial w'_z}{\partial y} \right] \\ & + \nu \left[\left(\frac{\partial u'_x}{\partial y} \right)^2 + \left(\frac{\partial u'_x}{\partial w} \right)^2 + \left(\frac{\partial v'_y}{\partial x} \right)^2 + \left(\frac{\partial v'_y}{\partial w} \right)^2 + \left(\frac{\partial w'_z}{\partial x} \right)^2 + \left(\frac{\partial w'_z}{\partial y} \right)^2 \right] \end{aligned} \quad (61)$$

$$u'_x = u_x - \bar{u}_x \quad v'_y = v_y - \bar{v}_y \quad w'_z = w_z - \bar{w}_z$$

The fluctuations of the velocity components u'_x , v'_y , w'_z are the difference between the instantaneous and the mean time velocity components. The verification of the estimation of the turbulent energy dissipation rate ϵ in the code is reported in Appendix I.

The CFD code allows us to obtain both instantaneous and time averaged ϵ in each cell in the mixing zone. Consequently, the mixing quality can be examined locally and the theoretical micromixing times (the engulfment mixing time $t_{mE} = 17.24\sqrt{\nu/\epsilon}$) can be determined in the simulation field, in order to obtain a micromixing time cartography in the reactor.

3.3 Study of the laminar mixing in the microreactor

This section concerns the results of the mixing under laminar conditions (Zhang *et al.*, 2019a). The condition effects have been examined, namely the Reynolds number, the temperature and the CO₂ fraction. The characteristic time of laminar mixing has been determined based on the curve of the segregation intensity.

A series of the laminar mixing has been simulated with different operating conditions and parameters, reported in Table 2. We are going to first analyze the ethanol mass fraction in the microchannel for a representative simulation. Then, the influence of the main parameters will be presented.

Table 2: Mixing conditions for the different simulation cases, along with the average fluid mixture properties and the characteristic time constant of mixing (* initial velocity ratio of CO₂ to ethanol, based on the fluid flow rates).

No.	T (°C)	CO ₂ (wt.%)	Q_{EtOH} ($\mu\text{L}\cdot\text{min}^{-1}$)	Q_{CO_2}	\bar{u}_x ($\text{m}\cdot\text{s}^{-1}$)	$\frac{u_{CO_2}}{u_{EtOH}}$ *	$\bar{\rho}$ ($\text{kg}\cdot\text{m}^{-3}$)	$\bar{\mu}$ ($\mu\text{Pa}\cdot\text{s}$)	$D\cdot 10^8$ ($\text{m}^2\cdot\text{s}^{-1}$)	Re	ϵ ($W \cdot kg^{-1}$)	t_m (ms)
1	20.0	82.8	25	100	0.0386	1.22	935	118	1.58	62	0.12	28.92
2	28.0	82.8	50	100	0.0802	1.37	896	96	1.86	152	0.43	18.65
3	22.5	82.9	50	200	0.0827	1.39	923	111	1.65	136	0.55	18.64
4	38.0	83.1	50	200	0.0903	1.85	843	72	2.34	208	0.47	14.28
5	47.5	83.1	50	200	0.0959	2.66	786	51	3.12	295	0.39	11.21
6	22.5	90.6	50	400	0.1559	2.77	896	90	1.65	308	1.62	7.74
7	38.0	90.8	50	400	0.1767	3.70	789	58	2.34	478	1.52	6.45
8	24.0	93.5	50	600	0.2326	4.20	864	80	1.70	499	3.32	4.74
9	38.0	93.6	50	600	0.2816	5.50	713	53	2.34	749	3.93	3.18
10	47.5	90.9	50	400	0.1972	5.37	706	40	3.12	697	1.45	4.46
11	22.5	93.6	50	600	0.2318	4.16	875	83	1.65	486	3.38	4.77
12	47.5	93.7	50	600	0.3143	8.06	644	36	3.12	1109	3.69	3.18
13	47.5	93.7	22	266	0.1391	8.07	644	36	3.12	491	0.72	3.88
14	47.5	90.7	23	180	0.0889	5.29	704	40	3.12	312	0.30	6.77
15	38.0	94.8	25	371	0.1690	6.86	732	51	2.34	478	1.33	3.66
16	38.0	97.7	10	351	0.1693	16.23	671	47	2.34	478	1.34	3.86
17	38.0	84.6	100	447	0.1998	2.07	836	69	2.34	478	2.20	11.59

3.3.1 Fluid velocity and ethanol mass fraction field

Once the CFD model is validated, we studied numerically the CO₂-ethanol mixing in the microreactor. The three-dimensional geometry in the simulation is recalled in Figure 49, which is presented previously in Chapter 2 for the simulation studies of the laminar mixing of the mixture CO₂-ethanol.

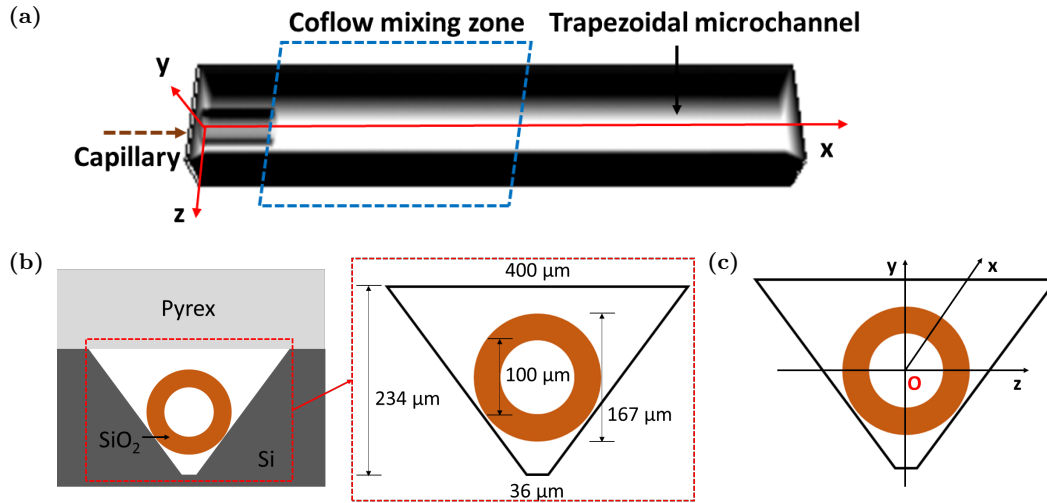


Figure 49: The geometry of the microchannel in the simulations for laminar conditions (previously presented figure in Chapter 2).

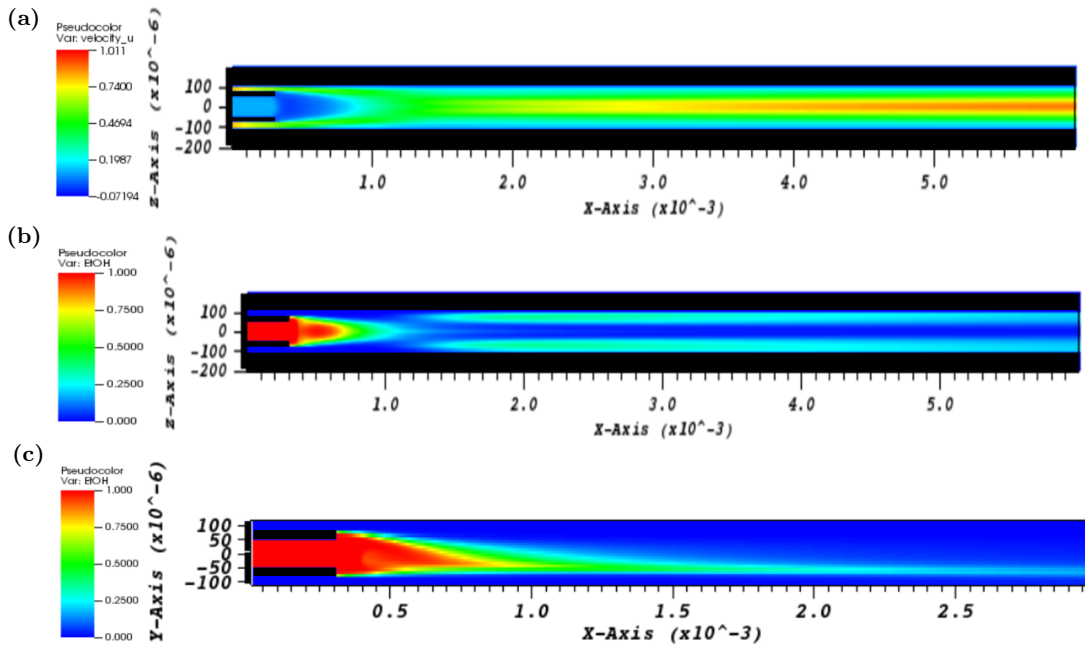


Figure 50: $y = 0, z = 0$ views of the 3D simulation of the CO₂-ethanol mixing in the microchip for $T = 47.5 \text{ }^\circ\text{C}$ and CO₂ wt.% = 93.7 (No.12 in Table 2): (a) Velocity component u_x field ($y = 0$ plane); (b) Ethanol mass fraction field ($y = 0$ plane); (c) Ethanol mass fraction field ($z = 0$ plane).

A simulation case is presented in Figure 50a. It corresponds to a 2D visualization for the velocity component u_x in the x direction of the 2D plane $y = 0$. Similarly, the ethanol mass fraction field is shown in the 2D plane $y = 0$ (Figure 50b) and $z = 0$ (Figure 50c) for a Reynolds number of 1109, the temperature of 47.5 °C and the total mass fraction of CO₂ of 93.7% (No.12 in Table 2). The black color symbolizes the silicon wall of the microchannel or the silica capillary tube. For the ethanol mass distribution, the red and blue colors represent the pure ethanol and the CO₂, respectively. As expected, the simulation exhibits a mean field flow as no turbulent fluctuation is present.

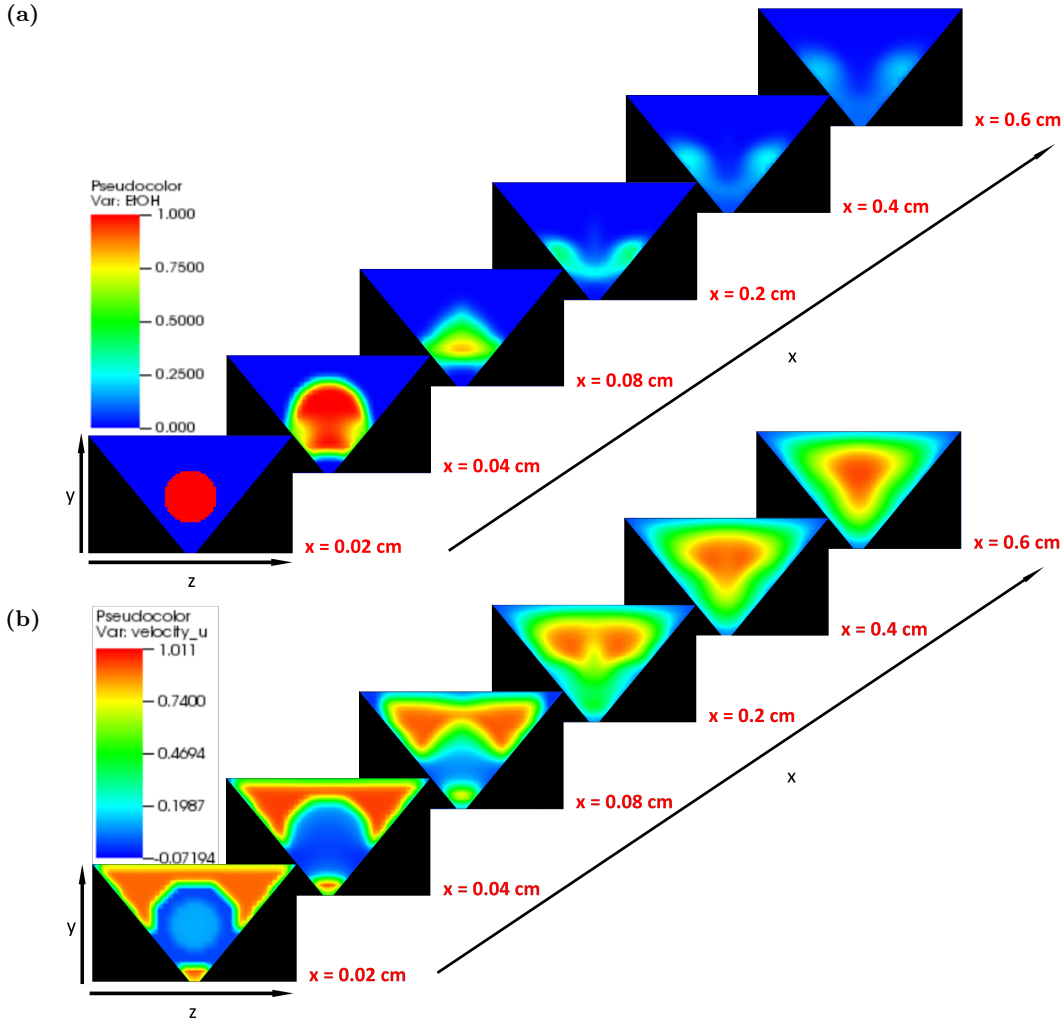


Figure 51: Ethanol mass fraction field and fluid velocity field variation in the asymmetrical 3D microchannel at steady state for $T = 47.5 \text{ }^\circ\text{C}$ and $\text{CO}_2 \text{ wt.\%} = 93.7$ (No.12 in Table 2): (a). Ethanol field evolution in the x direction; (b). Velocity component u_x evolution in the x direction.

Figure 50c shows the asymmetric ethanol mass fraction field in the plane $z = 0$. This result is related to the asymmetric trapezoidal shape of the channel and to the CO₂ velocity,

which is higher than the ethanol at the injector outlet. The flow of CO₂ first pushes the ethanol towards the bottom of the channel and the ethanol later goes up near the wall when the overall fluid velocity is higher in the center of the channel, as indicated in Figure 51.

3.3.2 Effects of the mixing conditions on the mixing quality

In this part, various simulation conditions have been performed to examine their effects on the mixing efficiency. For each condition, the segregation intensity of the characteristic mixing time is analyzed. All parameters are listed in Table 2, with the CO₂ mass fraction $CO_2\%$, the average values calculated for the fluid velocity component \bar{u}_x , the density $\bar{\rho}$, the viscosity $\bar{\mu}$ as well as the Reynolds number Re . These mixture properties are calculated in an overall manner. The CO₂ mass fraction or the ratio of CO₂ in the system is first estimated by:

$$CO_2(wt.\%) = \frac{u_{0CO_2} A_{out} \rho_{CO_2}(T)}{u_{0EtOH} A_{in} \rho_{EtOH}(T) + u_{0CO_2} A_{out} \rho_{CO_2}(T)} \times 100\% \quad (62)$$

with A_{in} , A_{out} the cross-sectional area of inner and outer fluid (ethanol and CO₂ respectively) before the mixing and u_0 the mean velocity of each fluid at the injector calculated by Equation 50. The average density $\bar{\rho}$ is then calculated by Peng-Robinson equation of state for the corresponding CO₂ ratio. The mean viscosity $\bar{\mu}$ is estimated similarly by the logarithmic correlation Equation 10. The fluid mean velocity \bar{u}_x introduced previously is calculated by Equation 49, by taking account of the mass conservation and the temperature change from the pump to the microreactor.

The characteristic mixing times of laminar mixing are equally listed in Table 2, which are deduced from the segregation intensity curve. Generally, the mixing times estimated are between 1 to 10 ms in our microreactor under laminar conditions, based on the simulation results.

3.3.2.1 Influence of the total Reynolds number

We first have investigated the effect of the global Reynolds number on the mixing efficiency. The average Reynolds number and the hydraulic diameter of microchannel are defined as:

$$Re = \frac{\bar{u}_x D_h \bar{\rho}}{\bar{\mu}} \quad (63)$$

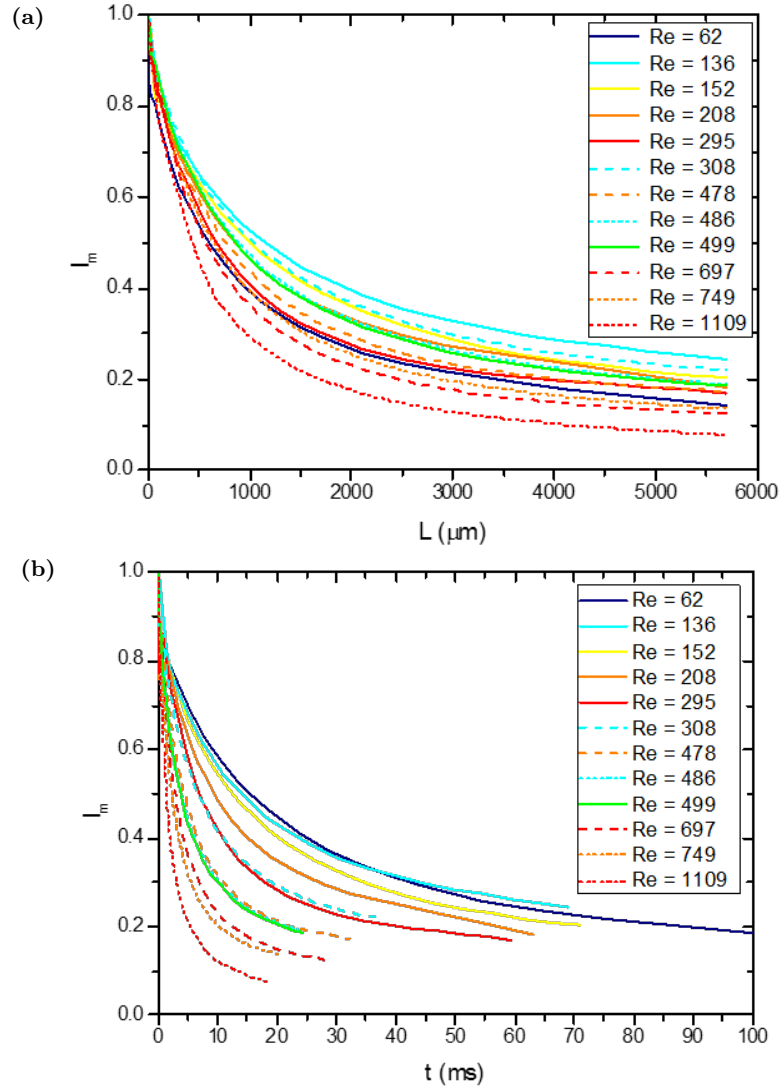


Figure 52: Effects of Reynolds number on the intensity of segregation I_m for laminar mixing cases in the microchannel: (a). I_m as a function of the distance from the injector tip; (b). I_m depending on the time.

where the hydraulic diameter of the microchannel is defined by $D_h = 4A/P$ (estimated to be $200 \mu\text{m}$ for the channel of the tested microreactor). Figure 52a and Figure 52b represent the evolution of the intensity of segregation calculated from the simulation for different average Reynolds numbers. Based on the simulation results, the I_m values never reached 0 within the channel whose the length is 6 mm, because a part of ethanol is pushed and trapped near the bottom wall by CO_2 with a high velocity due to the channel geometry, as shown in Figure 51. As discussed previously in the section of time axis, we replace the length axis by a time axis (Figure 52), in order to be able to determine the characteristics mixing time, and further to compare it to the theoretical mixing time and the ones of other

micromixers of the literature. Even if it is not clear to determine the effect related to the Re number based on Figure 52a because of different mean velocities, we can observe that an augmentation of the global Re number implies an improved mixing. As expected, an efficient mixing involves a higher global Reynolds number.

3.3.2.2 Influence of the temperature

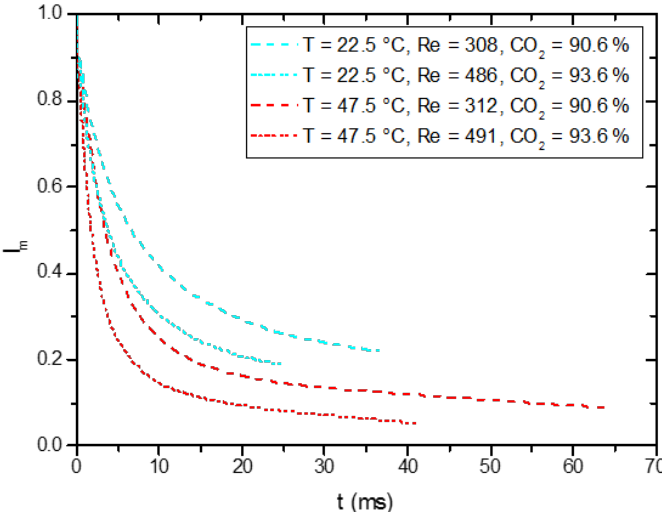


Figure 53: Temperature effects on I_m with equivalent CO_2 /ethanol ratio and Reynolds number.

The influence of the temperature has been also studied numerically and presented in Figure 53. Near the critical temperature of the CO_2 /ethanol mixture, the temperature change has a strong effect on the mixture properties, such as density and viscosity and also on the molecular diffusion coefficient of ethanol in CO_2 . For a fixed CO_2 flow rate, a higher temperature in the channel leads to a much lower CO_2 density therefore a higher velocity, according to the conservation of mass $\rho_0 \cdot Q_0 = \rho_T \cdot Q$, where ρ_0 is the fluid density in the cooling pump, Q_0 is the initial volumetric flow rate injected into the system by the pump, ρ_T is the fluid density in the microchannel at temperature T and Q is the real volumetric flow rate in the chip. Simulations have been performed to compare the evolution of the segregation intensity curve due to a temperature change, keeping an equivalent Reynolds number and a fixed CO_2 /ethanol ratio in the mixture. As a matter of fact, it is impossible to examine the effect of each parameter independently, because some parameters are related. For example, when the temperature varies, in order to keep the same Reynolds number and the same CO_2 fraction in the system, the injected flow rates must be changed so the velocity

ratio changes. Indeed, at laminar flow conditions, the mass transfer is related not only to the shear stress, but also to the diffusion in the perpendicular plane to the flow direction. As observed in Figure 53, a higher temperature results in a quicker decrease of the I_m value so the mixing quality is improved. This can be attributed to two main effects: first, the augmentation of the diffusion coefficient, and then, the change of the CO₂ velocity due to a density decrease, leading to higher velocity ratio and consequently a higher shear stress. For example, for the tests No.6 and No.14 in Table 2, the temperature increases from 22.5 °C to 47.5 °C, resulting in a rise of fluid velocity ratio (CO₂ initial velocity over ethanol initial velocity) from 2.77 to 5.29 m/s.

3.3.2.3 Influence of the CO₂ fraction

Eventually, we have investigated the effect of the CO₂ fraction which also indicates the CO₂/ethanol ratio on the mixing efficiency. Figure 54 illustrates that a higher ratio promotes the mixing quality. When this parameter increases, it results in a tremendous difference of the two fluids' velocities. The strong shear stress at the capillary outlet due to an important CO₂/ethanol ratio actually leads the CO₂ flow towards the ethanol in the middle of the channel and improves mixing. The mean velocity of CO₂ is 15 times higher than the ethanol velocity in the injector for the case of CO₂ mass fraction of 97.7%, even creating recirculation vortices that improve significantly the mixing (evidenced in Figure 55 in which the velocity vectors are superimposed with the ethanol mass fraction field in the plane $y = 0$). The same behavior has been captured in a numerical simulation for a two phase coflow in microfluidics (Zhang *et al.*, 2018). The article of the two phase mixing is added in Appendix II. However, for other cases of CO₂ lower than 97.7%, no recirculations were detected.

We conclude that even if it is complicated to extract the influence of a single parameter over the mixing efficiency, we could identify some general trends based on the considered simulated cases. First, a higher global Reynolds number results in a better mixing quality. As expected, the increase of Re number indicates normally a higher energy dissipation rate so the mixing time is reduced. An increase of the CO₂/ethanol ratio enhances mass transfer in the mixture by increasing the shear stress generated by an important difference between the inner and the outer velocities at the injector outlet. This shear stress results in some cases in the creation of vortices near the tip of the nozzle, which largely contribute in decreasing

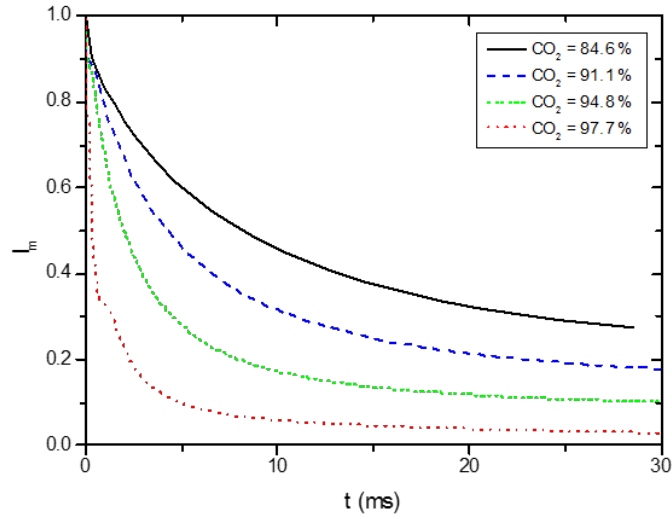


Figure 54: CO_2 /ethanol ratio effects on I_m with fixed temperature at 38°C and Reynolds number at 478.

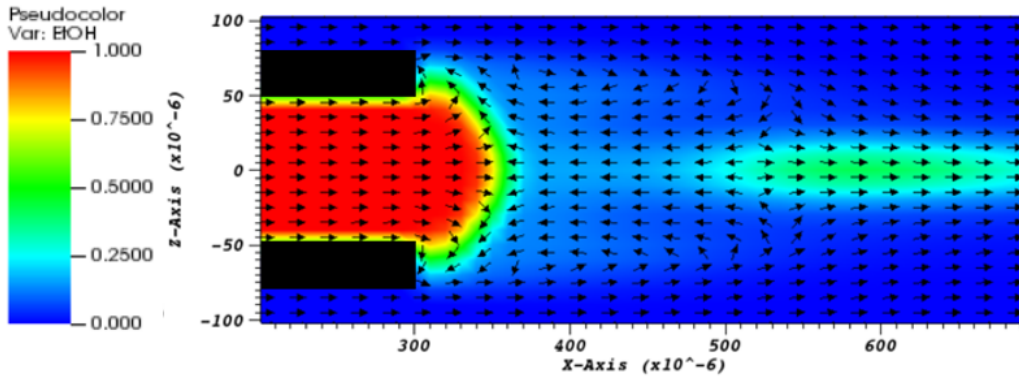


Figure 55: Recirculation detected in the mixing zone in the plane $y = 0$ for test case of which the CO_2 mass fraction is at 97.7%, with temperature at 38°C and mean Reynolds number at 478.

the mixing time. According to the simulation results, a temperature increase improves the mixing because of both increased diffusion and shear stress. In general, a higher Reynolds number, an increased temperature and a strong CO_2 /ethanol ratio are recommended to accelerate fluid mixing.

3.4 DNS study of turbulent mixing

As evidenced experimentally, our microreactor allows for reaching turbulent conditions (Zhang *et al.*, 2019b). The turbulent flows are studied by Direct Numerical Simulation (DNS). This is possible by the use of the HPC code Notus and the micro size of the simulated

domain. After the grid sensibility analysis, the optimal mesh is chosen to study the influence of the operating conditions on the mixing quality. The turbulent mixing has been simulated in the geometry previously represented in Figure 56.

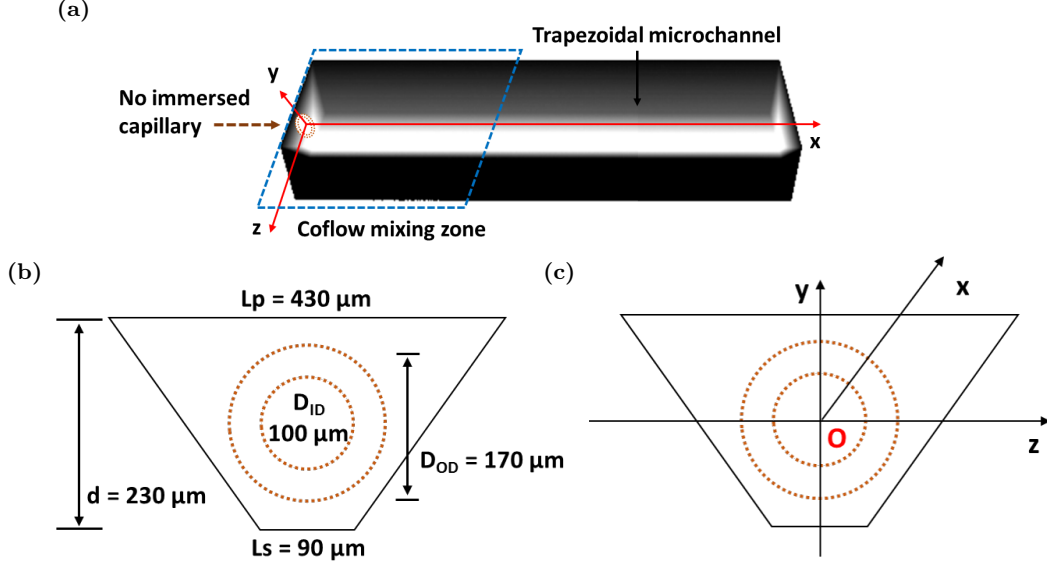


Figure 56: The geometry of the microchannel in the simulations for turbulent conditions (previously presented figure in Chapter 2).

3.4.1 Grid sensitivity analysis

In order to ensure that we catch all the relevant scales of the mixing, we performed a convergence study in space. As a first approximation, the rate of the turbulent kinetic energy can be estimated classically by $\epsilon = \overline{u_{x_{in}}^3}/D_{ID}$. Consequently, the Kolmogorov scale (Equation 64), in our range of the study, is of the order of the micrometer.

$$\lambda_K = \left(\frac{\nu^3}{\epsilon} \right)^{\frac{1}{4}} \quad (64)$$

Furthermore, the estimation of the Batchelor scale obtained by Equation 65, with a Schmidt number between 1 and 9, informs that this important scale varies from λ_K to $0.3\lambda_K$, *i.e.*, approximately in the same order of magnitude than the Kolmogorov scale.

$$\lambda_B = \left(\frac{\nu D^2}{\epsilon} \right)^{\frac{1}{4}} = \frac{\lambda_K}{Sc^{0.5}} \quad (65)$$

Therefore, the grid sensitivity analysis has been performed for 4 grid sizes, $\Delta x = \Delta y =$

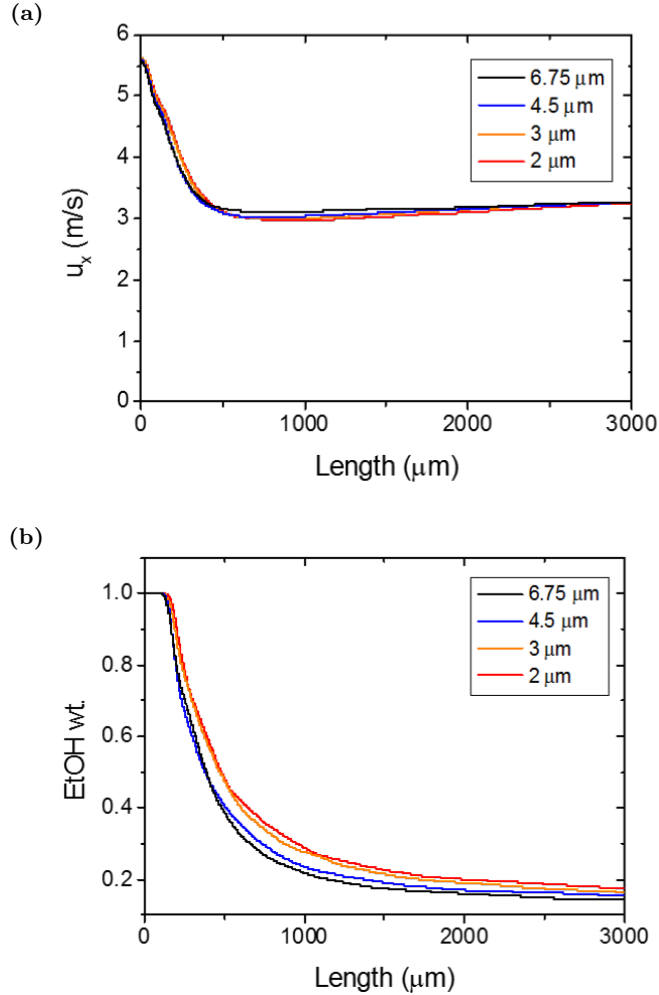


Figure 57: Grid size convergence study with time axis related to the inner fluid ethanol’s velocity for (a). velocity component u_x on the center line ($y=0, z=0$); (b). mass fraction of ethanol on the center line of the channel.

$\Delta z = 6.75\mu m$ (mesh ≈ 0.9 million cells), $\Delta x = \Delta y = \Delta z = 4.5\mu m$ (mesh ≈ 3 million cells), $\Delta x = \Delta y = \Delta z = 3\mu m$ (mesh ≈ 11 million cells) and $\Delta x = \Delta y = \Delta z = 2\mu m$ (mesh ≈ 37 million cells) and for a simulation with the higher mean Reynolds number ($Re > 5000$ of No.9 in Table 4). The Figure 57 represents the evolution of the time averaged velocity component u_x and the mean mass fraction of ethanol at the center midline of the channel. The Figure 58 represents the instantaneous ethanol mass fraction field in the plane $z = 0$ (the longitudinal section of the channel center representing the depth along with the fluid flow direction x) for the 4 selected grid sizes. Based on these results, the velocity profiles seems to converge for grid sizes around $5 \mu m$ but for the ethanol mass fraction, the convergent length is smaller, about $3 \mu m$. It indicates that the Kolmogorov scale is closed to $5 \mu m$ and a finer mesh is required to catch probably the Batchelor scale. This result

satisfies the relation between the 2 characteristic lengths (Equation 65). Indeed, the ratio of the two characteristic length $5 \mu\text{m} / 3 \mu\text{m}$ is close to \sqrt{Sc} (≈ 1.6) estimated for the relevant conditions.

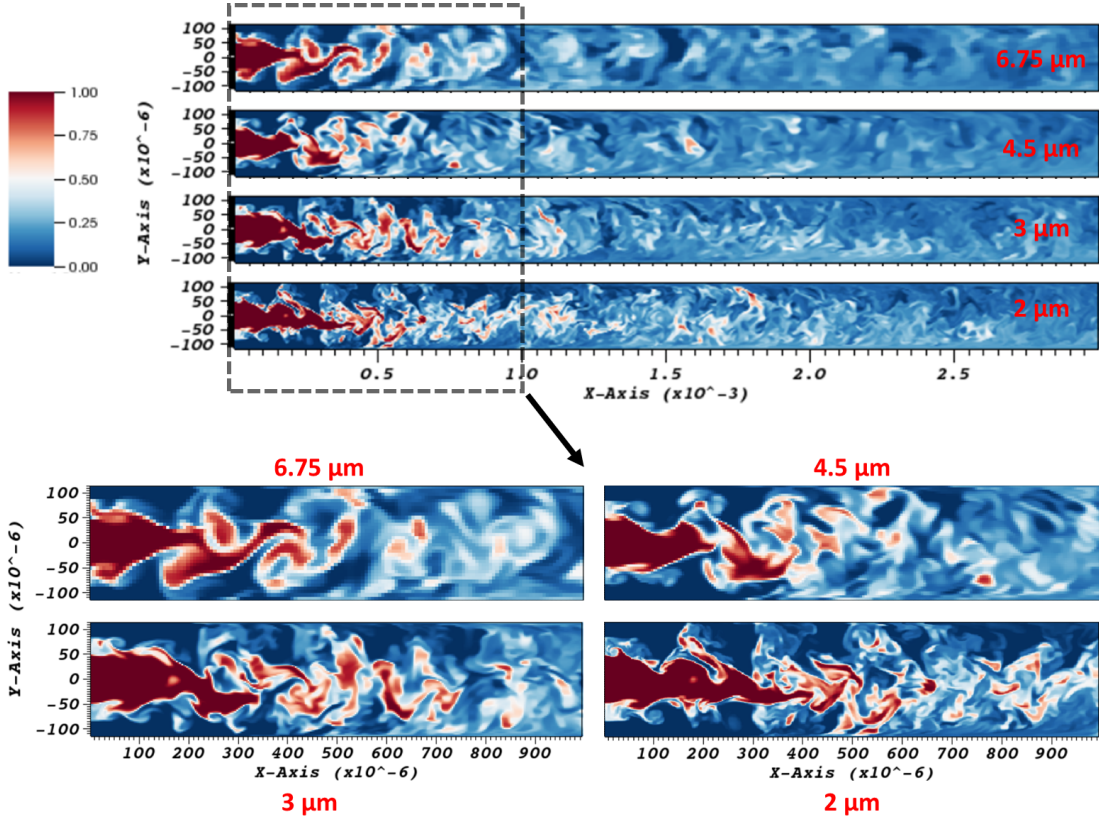


Figure 58: Instantaneous field of ethanol mass fraction in the plane $z=0$.

In this section, we have determined the appropriate grid size, $3 \mu\text{m}$, close to the Kolmogorov and Batchelor microscales to well describe the turbulent mixing. This value is a good compromise between precision of resolution and CPU time of the simulations.

3.4.2 Simulation cases and turbulent mixing time

3.4.2.1 Influence of operating conditions

Based on the mixing conditions for μSAS processes, we have performed a set of simulation cases listed in Table 3.

Table 3: Conditions and fluid global properties of simulation tests with pressure fixed at 100 bar (for both ethanol and CO₂ the initial velocities u_0 at the capillary outlet are calculated from the fluid flowrates, considering temperatures in the pumps and in the microchannel). The coefficient of diffusion is $1.55 \times 10^{-8} \text{ m}^2 \cdot \text{s}^{-1}$ at 20 °C and $2.45 \times 10^{-8} \text{ m}^2 \cdot \text{s}^{-1}$ at 40 °C

No.	T (°C)	$Q_{0_{EtOH}}$ ($\mu\text{L} \cdot \text{min}^{-1}$)	$Q_{0_{CO_2}}$	$u_{0_{EtOH}}$ ($\text{m} \cdot \text{s}^{-1}$)	$u_{0_{CO_2}}$	$\frac{u_{0_{CO_2}}}{u_{0_{EtOH}}}$	CO ₂ (wt.%)	\bar{u} ($\text{m} \cdot \text{s}^{-1}$)	$\bar{\rho}$ ($\text{kg} \cdot \text{m}^{-3}$)	$\bar{\mu}$ ($\mu\text{Pa} \cdot \text{s}$)	t_m (ms)
1		200	3000	0.43	2.38	5.50	95.3	1.25	701	47	0.360
2		300	3000	0.65	2.38	3.67	93.0	1.21	740	50	0.280
3		400	3000	0.87	2.38	2.75	90.9	1.19	769	53	0.370
4		500	3000	1.08	2.38	2.20	88.9	1.19	791	57	0.160
5	40	600	3000	1.30	2.38	1.83	87.0	1.19	808	60	0.108
6		700	3000	1.52	2.38	1.57	85.2	1.19	821	63	0.105
7		800	3000	1.73	2.38	1.38	83.4	1.20	832	67	0.102
8		1200	3000	2.60	2.38	0.92	77.0	1.27	856	81	0.186
9		1300	5000	2.81	3.97	1.41	83.7	2.00	830	66	0.064
10		200	5000	0.43	3.97	9.17	97.1	2.17	659	44	0.139
11		300	4500	0.64	2.43	3.81	95.3	1.49	881	84	0.580
12		400	4500	0.85	2.43	2.86	93.8	1.50	892	87	0.530
13		500	4500	1.06	2.43	2.29	92.3	1.50	901	91	0.480
14	20	600	4500	1.27	2.43	1.91	90.9	1.51	909	94	0.380
15		700	4500	1.49	2.43	1.63	89.6	1.53	915	98	0.187
16		800	4500	1.70	2.43	1.43	88.3	1.54	921	101	0.109
17		1300	4500	2.76	2.43	0.88	82.2	1.63	936	120	0.186
18		300	7250	0.64	3.91	6.14	97.0	2.40	865	80	0.230

Table 4: Results of simulation tests: global dimensionless numbers, average turbulent kinetic energy dissipation rate, micromixing times, ratio of mixing time to diffusion time and order of magnitude of the kinetic energy (CO₂ to ethanol).

No.	T (°C)	Re	Sc	$\bar{\epsilon}$ (W·kg ⁻¹)	t_{mE}	t_v (ms)	t_m	$\frac{\rho_{CO_2} u_{0CO_2}^2}{\rho_{EtOH} u_{0EtOH}^2}$	$\frac{t_m \cdot D}{D_h^2} \cdot 10^5$
1	40	4095	2.72	49.1	0.636	0.443	0.360	23.37	18.40
2		3926	2.76	81.3	0.497	0.346	0.280	10.39	14.31
3		3773	2.83	127.8	0.402	0.279	0.370	5.84	18.91
4		3633	2.92	196.5	0.329	0.229	0.160	3.74	8.18
5		3506	3.03	439.6	0.224	0.156	0.108	2.60	5.52
6		3389	3.15	509.0	0.212	0.148	0.105	1.91	5.34
7		3282	3.28	575.8	0.204	0.142	0.102	1.46	5.20
8		2932	3.86	601.6	0.216	0.150	0.186	0.65	9.52
9		5505	3.25	2429.8	0.099	0.069	0.064	1.54	3.26
10		7072	2.74	641.7	0.177	0.123	0.139	64.92	7.11
11	20	3444	6.14	66.1	0.653	0.455	0.580	16.21	18.69
12		3358	6.32	82.7	0.593	0.412	0.530	9.12	17.08
13		3277	6.51	68.6	0.660	0.459	0.480	5.83	15.47
14		3201	6.71	142.3	0.465	0.324	0.380	4.05	12.24
15		3130	6.91	301.5	0.325	0.226	0.187	2.98	6.01
16		3062	7.13	671.2	0.221	0.154	0.109	2.28	3.52
17		2778	8.30	696.7	0.234	0.163	0.186	0.86	6.00
18		5718	5.96	283.4	0.311	0.216	0.230	42.06	7.41
19		3720	3.03	234.0	0.307	0.214	0.250	4.38	15.45
20		3610	3.03	608.6	0.190	0.133	0.122	3.20	6.67
21	3417	3.03	438.5	0.224	0.156	0.132	2.41	6.78	
22	3720	3.03	368.8	0.245	0.170	0.219	4.14	13.09	
23	3950	3.03	610.5	0.190	0.132	0.180	6.50	12.17	
24	3828	3.03	609.3	0.190	0.132	0.160	4.80	9.81	
25	3620	3.03	353.9	0.250	0.174	0.226	4.11	14.21	
26	40	3391	3.03	422.0	0.229	0.159	0.117	2.15	5.68
27		3574	3.03	194.1	0.337	0.235	0.340	3.41	19.71
28		3480	3.03	506.0	0.209	0.145	0.116	2.57	5.98
29		3300	3.03	359.8	0.248	0.172	0.126	1.88	5.92
30		3506	3.03	270.2	0.286	0.199	0.195	0.64	9.97
31		3506	3.03	2533.3	0.093	0.065	0.031	0.05	1.58
32		3506	3.03	2174.7	0.101	0.070	0.035	0.03	1.79
33		2932	3.86	1266.4	0.149	0.104	0.123	0.16	6.29
34		5612	3.17	1774.2	0.114	0.079	0.098	0.44	5.01
35		20	1886	5.07	206.8	0.423	0.294	0.266	0.25
36	1575		7.07	4070.3	0.113	0.078	0.040	0.06	1.29

Two temperatures were selected, 20 and 40 °C. The volumetric flow rates chosen for the

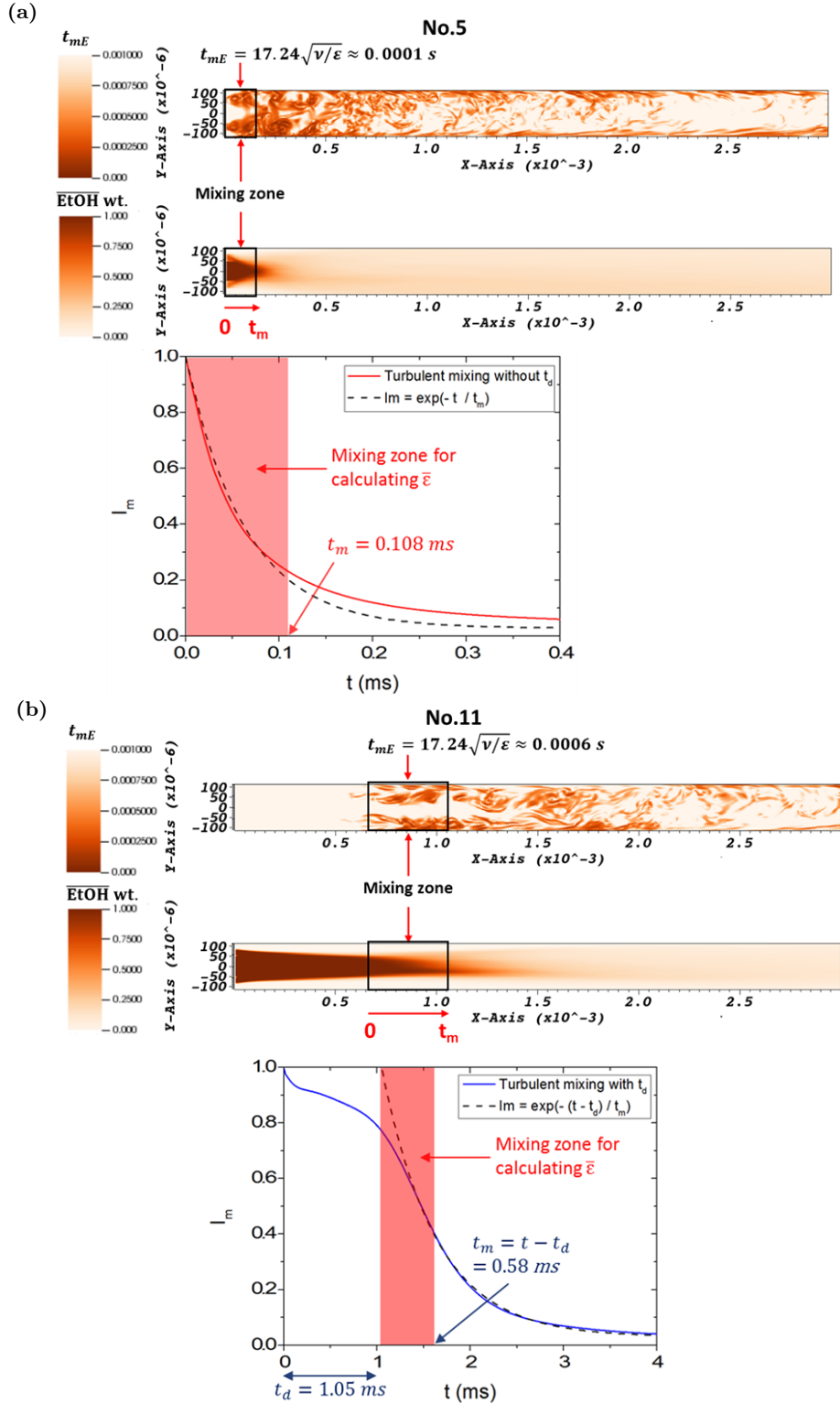


Figure 59: Instantaneous micromixing time fields calculated by Equation 33 ($t_{mE} = 17.24\sqrt{\nu/\epsilon}$) in the plane $z = 0$ (with the unit of meter for x and y axes) and mean time average ethanol mass fraction field: (a). test case No.5 in Table 3 at 40°C without time delay; (b). test case No.11 with time delay.

simulations vary and are realizable experimentally in the microreactor. The mixture properties, namely the CO₂ mass fraction, fluid mean velocity, density, viscosity and diffusivity, are calculated in a global manner for ultimate homogeneous mixtures. The segregation intensity curves are plotted with time axis related to the pure ethanol velocity in the capillary, as discussed previously in the section of time axis, and we are able to determine the characteristic mixing times t_m . The two ways are used for estimating the mixing and micromixing time. In Figure 59, we have represented the micromixing time ($t_{mE} = 17.24\sqrt{\nu/\epsilon}$) calculated locally in each cell and the evolution of the mean mass fraction of ethanol in the median x-y plane of the reactor. The mean mass fraction field allows for locating easily the intense mixing zone, in which we calculate the global energy dissipation rate $\bar{\epsilon}$. The local micromixing time values allow for comparing (and validating) the global value of the characteristic mixing time obtained simply by the evolution of the segregation intensity. Indeed, both values are in good agreement. The mixing times are posted in Table 4 with dimensionless numbers calculated by using the global average properties and the hydraulic diameter of the channel.

As a first remark and the most importantly, the mixing time is of the order of magnitude of 10^{-4} s. This means that the operating conditions allow for obtaining a very fast mixing with a mixing time smaller than those reported in the literature in micromixers (Falk and Commenge, 2010). Globally, the mixing times are comprised between 0.03 and 0.58 ms. The series of 40 °C tends to provide faster mixing due to an improved diffusion, proceeding that the segregation intensity curves fall more quickly compared to the simulations at 20 °C. In general, higher flowrates result in lower mixing times, because of a relatively higher energy dissipation rate. For a large change of the Reynolds number, the difference of mixing times is evident. Nevertheless, let us note that the global Reynolds number is also influenced by the mean mixture viscosity, which depends on the mixture composition. Therefore, for small variations of this value, the trend of mixing time is not so clear. As yet mentioned in the laminar mixing study, the effects of individual parameter are difficult to rationalize because most of parameters are correlated among them.

3.4.2.2 Influence of microchannel dimensions

As our numerical model provides precise evidences for fluid mixing in high pressure monophasic conditions, the influence on mixing time related to the microchannel dimensions can be determined to help the experimental design. To do so, several trapezoidal cross-

Table 5: Simulation conditions and tested data for microchannel and capillary dimension.

No.	Dimension change	T (°C)	$Q_{0_{EtOH}}$ ($\mu\text{L}\cdot\text{min}^{-1}$)	$Q_{0_{CO_2}}$	D_{ID}	D_{OD}	L_p (μm)	d	L_s	D_h	t_m (ms)
19		40	600	3000	100	170	430	170	173	199	0.250
20		40	600	3000	100	170	430	200	131	212	0.122
21		40	600	3000	100	170	430	260	41	219	0.132
22		40	600	3000	100	170	400	230	53	202	0.219
23		40	600	3000	100	170	400	170	143	190	0.180
24	Channel	40	600	3000	100	170	400	200	100	200	0.160
25		40	600	3000	100	170	400	260	0	197	0.226
26		40	600	3000	100	170	450	230	102	225	0.117
27		40	600	3000	100	170	450	170	198	206	0.340
28		40	600	3000	100	170	450	200	150	218	0.116
29		40	600	3000	100	170	450	260	60	229	0.126
30		40	600	3000	75	150	430	230	90	219	0.195
31		40	600	3000	40	150	430	230	90	219	0.031
32		40	600	3000	40	105	430	230	90	219	0.035
33	Capillary	40	1200	3000	75	150	430	230	90	219	0.123
34		40	1200	5000	75	150	430	230	90	219	0.098
35		20	800	3000	75	150	430	230	90	219	0.226
36		20	1600	3000	75	150	430	230	90	219	0.040

sections have been considered in the simulation. The trapeze area can neither be too small for the capillary insertion nor too large for moderate microfluidic scales. Another constraint of the microchannel designing is due to the wet etching of silicon during the microfabrication leading to a fixed angle between the larger base and the hypotenuse of the isosceles trapezoid (58.4°) no matter what the depth is. The tested geometries are posted in Table 5 with the test No.5 as reference for most cases (40 °C, 100 bar, ethanol flowrate at 600 $\mu\text{L}/\text{min}$ and CO_2 flowrate at 3000 $\mu\text{L}/\text{min}$). The characteristic length of the microchannel is its hydraulic diameter, defined as $D_h = 4A/P$, with A the area and P the wet perimeter of the trapezoidal cross-section.

For test No.19 to No.29, the cross-section changes by keeping the same capillary and the depth varies from the outer diameter (D_{OD}) 170 μm to 260 μm . In some extreme cases, the cross-section shape is tuned to a triangle as the depth d reaches to a high value (No.25). For test No.30 to No.36, the trapezoidal shape is the same of the simulations in Table 3 (Figure 56) and different diameters of capillary are examined.

Based on the mixing times in Table 5, the channel depth d of 200 μm results in a

slightly faster mixing. The difference is not much obvious except the cases of $d = D_{OD}$ at $170 \mu\text{m}$, in which the ethanol is not fully surrounded by CO_2 at the beginning of the mixing, leading to a longer mixing time. As observed, the microchannel dimension influences less than the capillary diameter. The decrease of the inner diameter D_{OD} from 100 to $40 \mu\text{m}$ induces a tremendous increase of the ethanol velocity for the same flowrate (from 1.30 to 8.12 m/s). The ethanol rushes into the mixing zone and generates strong energy dissipation rates (2533.3 W/kg for No.31 and 2174.7 W/kg for No.32), leading to smaller mixing times.

The change of channel shape and capillary type produces fluid velocity variations, which is a key factor discussed specifically in the next part for optimizing the mixing process in the studied device configuration.

3.4.3 General analysis of turbulent mixing conditions

Since most of parameters are strongly intercorrelated to each other, it is impossible to vary only one parameter while keeping the others constant. For instance, temperature change in the channel induces fluid density variations, especially for CO_2 . As a consequence, for the same flowrates $Q_{0_{\text{EtOH}}}$, $Q_{0_{\text{CO}_2}}$, the initial velocities $u_{0_{\text{EtOH}}}$ $u_{0_{\text{CO}_2}}$ are different at the injector outlet. It is the reason why we choose to analyze a general behavior of fluid mixing. We can show in Figure 60 that the ratio between the characteristic mixing time and the diffusion time $t_{diff}(T) = D_h^2/D(T)$ behaves similarly as a function of the kinetic energy ratio between CO_2 and ethanol (reported in Table 4 for pure fluids before mixing). The normalization of the characteristic time by the diffusion time allows for analyzing the only influence of the inertial effects in the microchannel.

Similarly to a previous study related to two phase flows in a microfluidic device (Zhang *et al.*, 2018), we can distinguish 5 zones of mixing behaviors. The velocity components v_y and w_z perpendicular to the fluid flow direction x can also explain different regions as a function of the ratio of this kinetic energy. These two velocity components affect strongly the form of the ethanol jet at the injector outlet and they play an important role for the species dispersion, which can be observed in Figure 61 which represents the velocity vector field in y and z directions. When the ethanol energy dominates (ratio less than 0.1 , No.31), it strikes into the CO_2 environment, engendering velocity drop and massive energy dissipation in the mixing zone. This phenomena is less intense for a ratio between 0.1 and 1 (No.8) because the CO_2 accompanies the inner fluid ethanol, flowing downstream with less interaction in

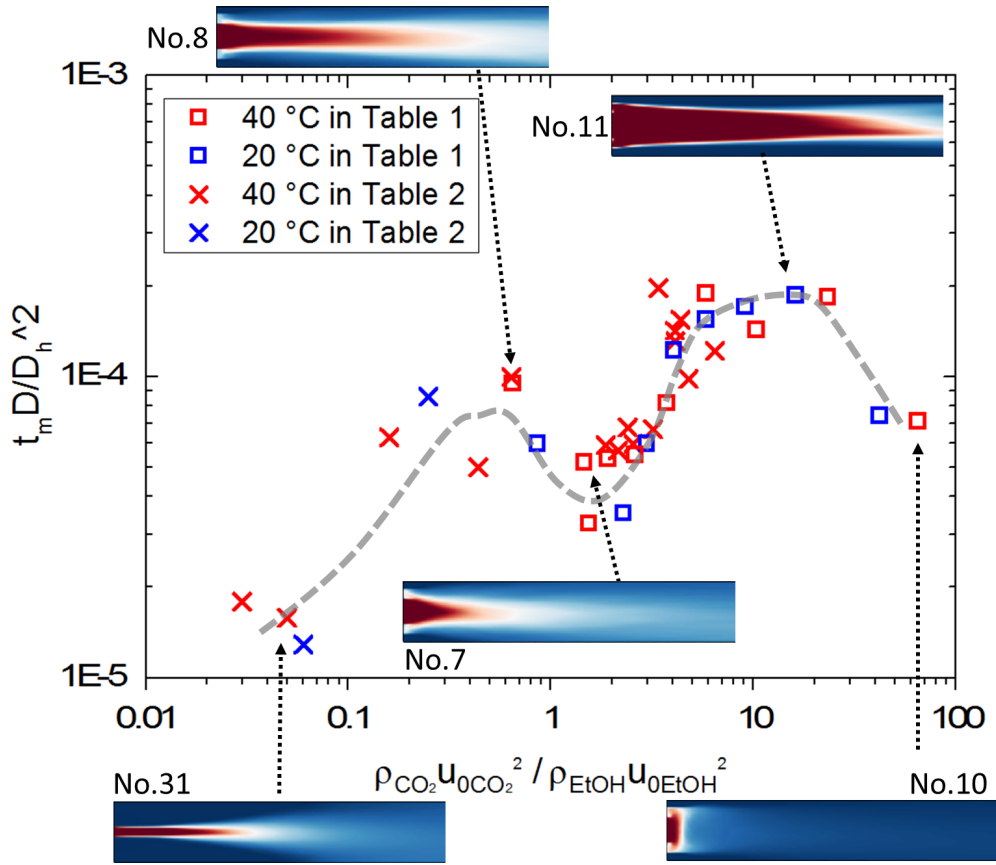


Figure 60: Evolution of the time ratio (mixing time to diffusion time) as a function of the kinetic energy ratio (CO_2 to ethanol), with 5 different regimes.

the y and z directions. As observed, compared to the former regime, the tests No.8 has less velocity dispersion at the injector outlet. The coflow mixing arrives into a local optimal region, while the energy ratio reaches about 1 to 3 (No.7). In these conditions, the CO_2 moves rapidly into the channel, surrounding and shearing the ethanol, which has a shorter jet length. The interaction between two fluids creates vortices in the channel so the mixing is enhanced. When the kinetic energy of CO_2 keeps increasing and the ratio steps into a range of 3 to 20 (No.11), the CO_2 , with a relative high inertial force in x direction, tends to produce longer jet, resulting in smaller magnitudes of velocity components in the y and z directions. Almost no fluctuations of velocity exist in the y and z directions without velocity dispersion at the injector outlet, resulting less interaction between inner and outer fluids, and so on, involving a slower mixing than the other cases. The last zone, corresponding to an energy ratio more than 40 (No.10), represents an intense kinetic energy of CO_2 . The CO_2 rushes into the microchannel and blocks the inner fluid of ethanol close to the tip,

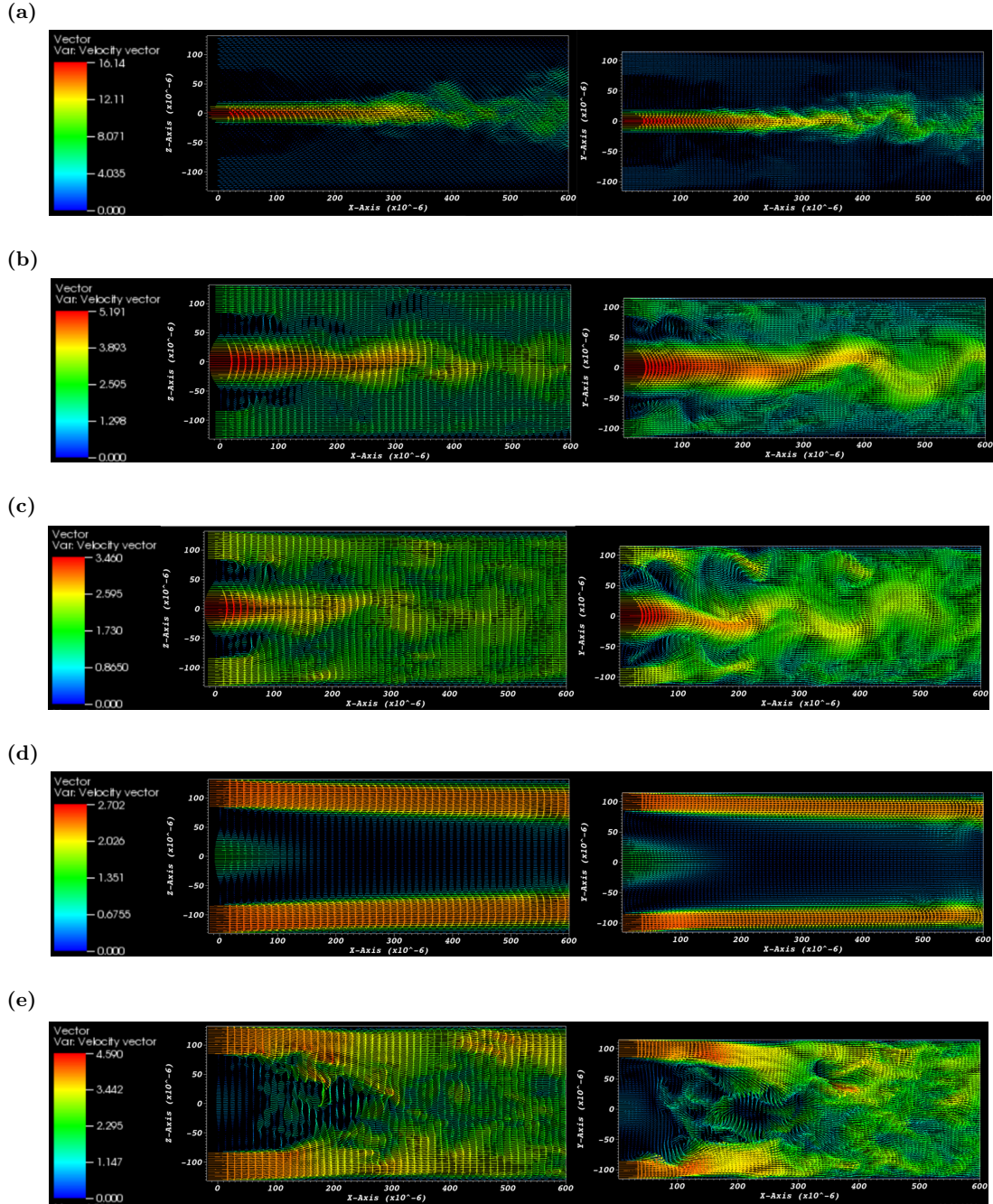


Figure 61: Instantaneous velocity vector fields in the planes of $y = 0$ and $z = 0$ for simulation tests in the mixing zone (a). No.31; (b). No.8; (c). No.7; (d). No.11; (e). No.10.

leading to a very short jet length. Consequently, these conditions provoke high dispersion (or vortices) and promote very short mixing time. This behavior has been already reported in a previous study in the case of two phase flow (Zhang *et al.*, 2018).

3.5 Mixing time analysis

This section is devoted to the analysis of the mixing time in function of the energy dissipation rate ϵ for both laminar and turbulent conditions. The results are in good agreement with those reported in the literature.

3.5.1 Mixing times for laminar conditions

The theoretical way to define the mixing time under laminar conditions was proposed by Baldyga and Bourne (1986). It is defined as the time required to obtain a homogeneous mixture in a slab, considering both diffusion and advection mixing, also known as the stretching efficiency model (Equation 66). This equation has been largely applied to determine micromixer efficiency (Baldyga and Bourne, 1984; Falk and Commenge, 2010; Ghanem *et al.*, 2014):

$$t_m = \frac{1}{\sqrt{2}} \sqrt{\frac{\nu}{\epsilon}} \ln \frac{1.52 \cdot L \cdot u}{D} \quad (66)$$

with ν the kinematic viscosity, ϵ the energy dissipation rate, L the characteristic length, u the fluid velocity and D the diffusion coefficient.

The characteristic mixing times in this study (red points framed by two dotted lines illustrating a 50% relative error) are in agreement with the theoretical behavior shown as the blue line in Figure 62 (Falk and Commenge, 2010). Therefore, it seems that the determination of the mixing time in this study is an appropriate method to evaluate the mixing performance under laminar flow conditions for microfluidic coflow.

3.5.2 Mixing times for turbulent conditions

In the laminar conditions, we consider a global value of the energy dissipation rate ϵ for the entire mixing zone. In order to compare the two flow regimes and also to compare the turbulent mixing time of our simulation to the theoretical relation, a mean ϵ is needed to represent an overall value in the examined microchannel. We decided to estimate it as the mean value of all cells in a considered mixing zone. We have defined the beginning of this zone as the tip of the injector for a system without time delay, or the coordinate corresponding to $t = 0$ for a system with time delay. The end of the mixing zone is defined as the coordinate indicating the characteristic mixing time $t = t_m$ in the fluid flow direction.

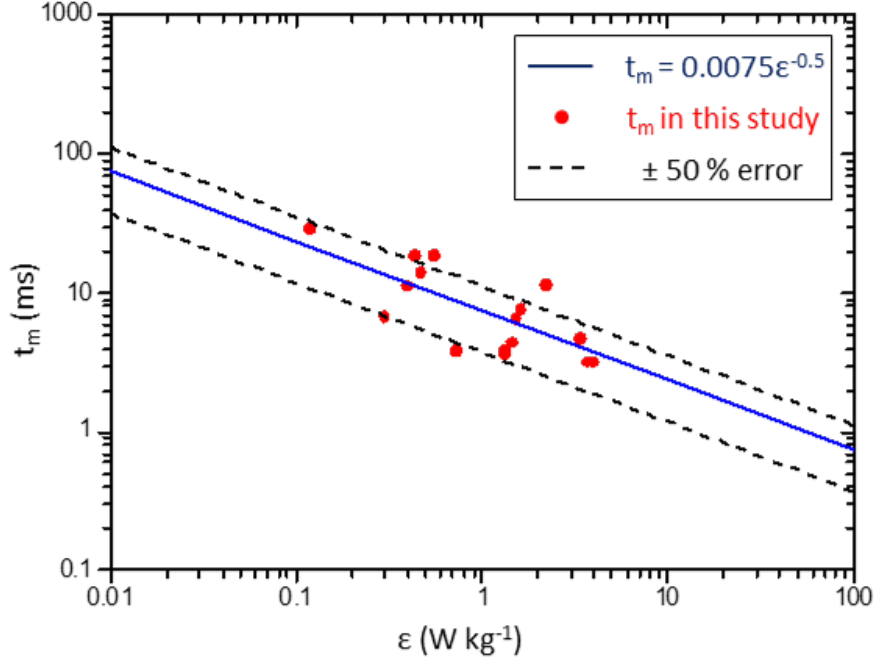


Figure 62: Comparison of characteristic time constant obtained in this study (red points) with the data published (blue line) in the literature (Falk and Commenge, 2010).

Examples are shown in Figure 63 for both cases.

The micromixing times $t_{mE} = 17.24\sqrt{\nu/\epsilon}$ and $t_v = 12\sqrt{\nu/\epsilon}$ are reported in Table 4, representing respectively the engulfment micromixing time and the theoretical hydrodynamic life time of vortices. As shown in Figure 64, the turbulent mixing times obtained in the current study are in the same order of magnitude than for the two models. According to the mixing time t_m determined in this study, the coefficient of the engulfment theory has been modified to 11.90 for our fluid system instead of 17.24. It appears that the estimation of the mixing time with the segregation intensity has been proven as a simple and efficient method to characterize the mixing performance and it is also validated for turbulent mixing. It has been additionally verified the capacity of capturing the micromixing in our numerical model under tested conditions (the global Reynolds number less than 7500 in Table 4). As for laminar cases, a correlation (Equation 67) has been determined to estimate mixing time as a function of the energy dissipation rate $\bar{\epsilon}$ (blue line in Figure 64), which conserves the same slope (-0.5) than the laminar mixing. The coefficient 0.0034 is smaller than the laminar one 0.0075 (Baldyga and Bourne, 1986), as expected, implying better mixing capacity

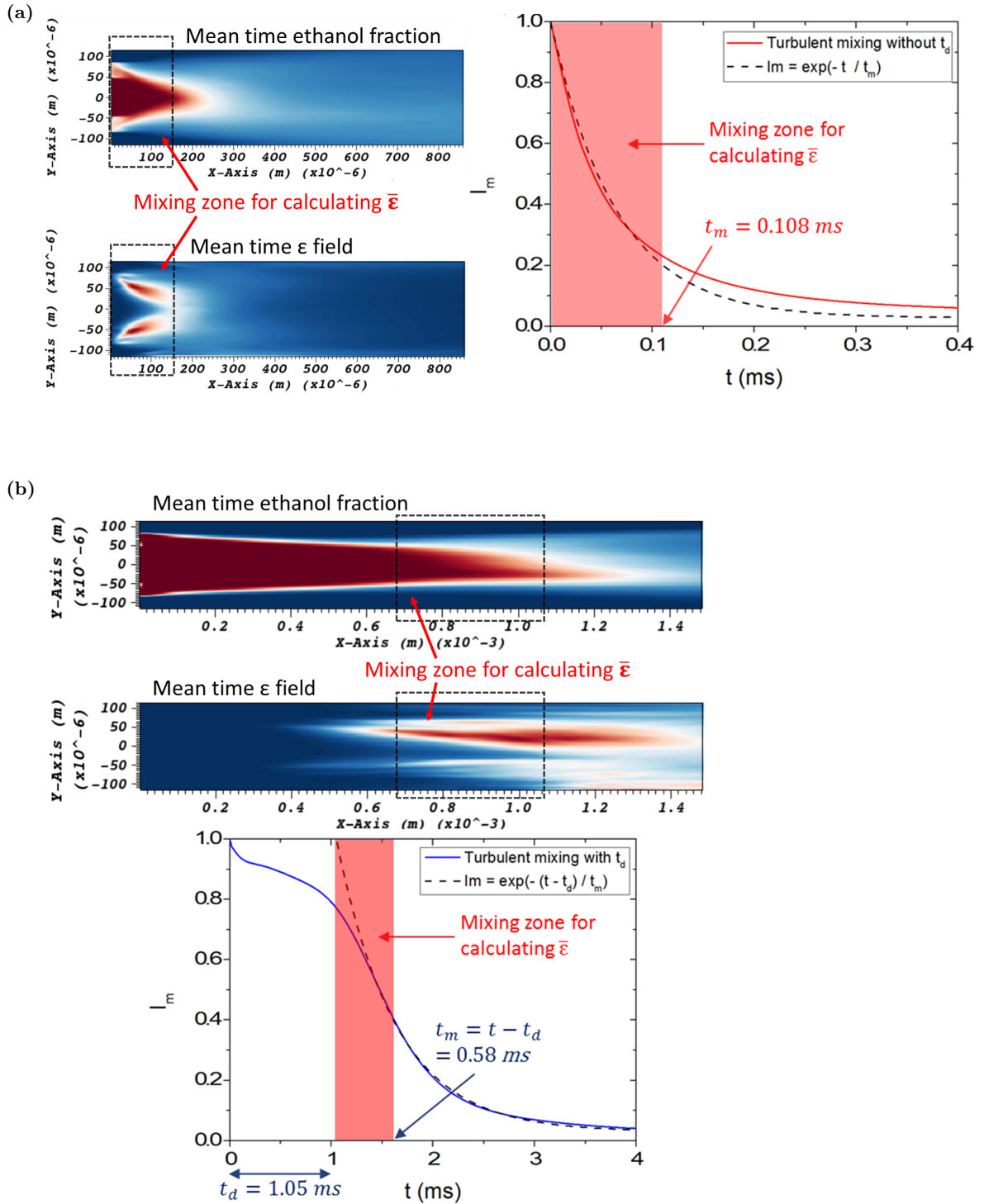


Figure 63: Determination of the turbulent mixing zone in which the average energy dissipation rate $\bar{\epsilon}$ is calculated, with the mean time ethanol mass fraction field to illustrate the corresponded physical area: (a). for cases without time delay t_d the mixing zone is from $t = 0$ to t_m (test No.5 in Table 3); (b). for cases with time delay t_d the zone is from t_d to t_m (test No.11 in Table 3).

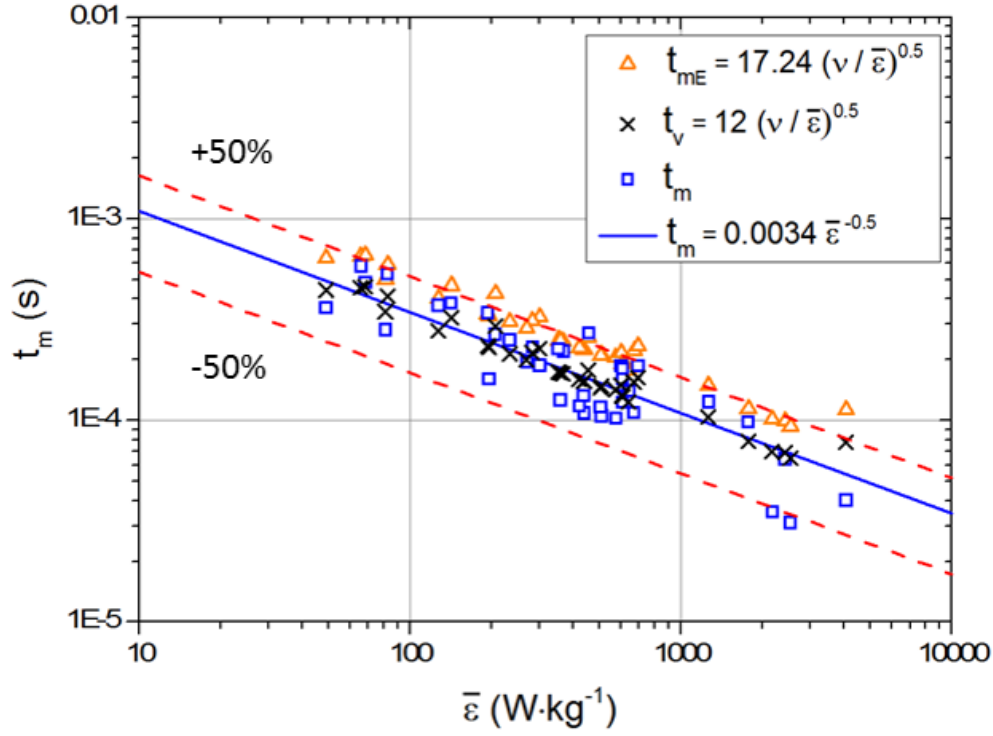


Figure 64: Mixing times acquired of turbulent mixing simulations with a correlation according to the average energy dissipation rate $\bar{\epsilon}$, compared to micromixing times and hydrodynamic life times of vortices under same conditions.

in turbulent conditions:

$$t_m = 0.0034 \cdot \bar{\epsilon}^{-0.5} \quad (67)$$

3.5.3 Comparison with other micromixers

The performance of other micromixers are collected in the literature (Falk and Commenge, 2010; Panić *et al.*, 2004; Kockmann *et al.*, 2006; Aoki and Mae, 2006; Keoschkerjan *et al.*, 2004; Schneider *et al.*, 2004; Men *et al.*, 2007) and their mixing times are mostly higher than 1 ms. It should be reminded that all experiments previously published have been performed with water at ambient pressure as a working fluid. A remarkable result has been found while the characteristic mixing time in our microreactor is compared to the mixing times in these micromixers. Under the conditions for SAS process in the microreactor (above the critical pressure of the mixture), a higher diffusivity and a lower viscosity are obtained for the system of CO₂ and ethanol. Our microreactor provides smaller mixing times in the order of magnitude of 0.1 ms, 10 times lower than other micromixers, probably

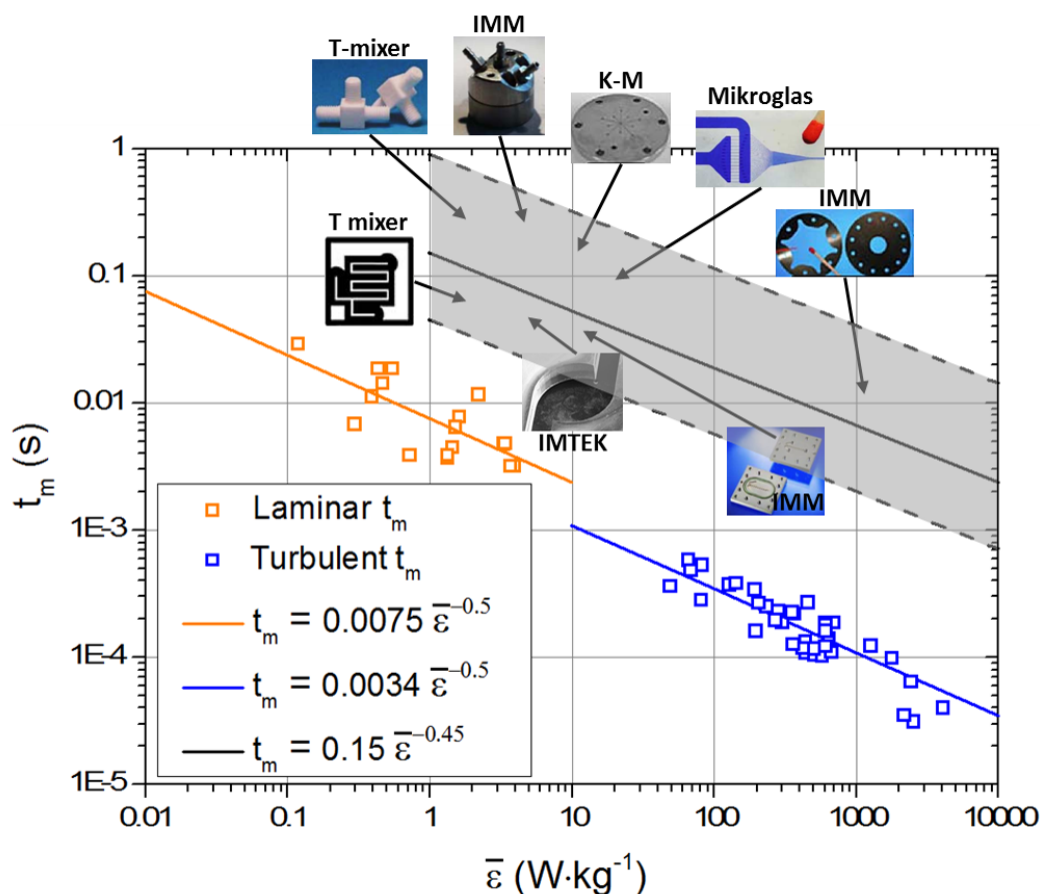


Figure 65: CO₂-ethanol mixing times at 100 bar in our microreactor for both laminar and turbulent conditions and rough comparison to other micromixers depending on the result of Falk and Commenge (2010).

due to the combination of turbulent conditions with supercritical fluids.

Another interesting remark is due to the mixing efficiency, proposed by Falk and Commenge (2010), when they examined several types of micromixers and they found that the real mixing times of these apparatus are much higher than the theoretical mixing time. The correlation modified is $t_m = 0.15\epsilon^{-0.45}$ with the coefficient from 0.0075 to 0.15 and the power from -0.5 to -0.45. This correlation corresponds to a mixing efficiency of only 3% compared to the mixing theory. Nevertheless, the mixing time determined for our microchip is close to the theoretical value. The mixing times obtained from our pressure resistant microchip are plotted in Figure 65, for the same $\bar{\epsilon}$ range, containing both laminar and turbulent conditions as well as laminar mixing model and turbulent correlation. As shown in Figure 65, our mixing times are close to the theoretical ones and the microreactor seems to be more

efficient than those reported in the literature.

3.6 Summary

In this chapter, we did a brief overview of the fundamental mechanism of mixing presented in the literature. We pointed out that the micromixing is essential for the fast particle precipitation/crystallization as the SAS process. The micromixing in a reactor can be analyzed experimentally by the competitive iodide iodate reaction (or Villermaux-Dushman reaction). However, few experimental studies are found for supercritical conditions (Carretier *et al.*, 2005). In terms of the micromixing modeling, even though the engulfment deformation diffusion (EDD) model is considered to offer adequate results, the assumptions of the model should always be verified by experimental data.

In this thesis, we propose an original approach to study the fluid mixing (solvent anti-solvent) of the SAS process. It is composed by both experiments and numerical simulations. In the experimental part, the *in situ* measurement of μ PIV offers the knowledge of the fluid velocity field for laminar conditions. Additionally, for the turbulent conditions, the fluid mixing has been recorded by a high speed camera in order to prove qualitatively the capacity of our microreactor to reach turbulent regime under high pressure. In the numerical simulation, we have first validated the CFD model with the μ PIV measurements for the laminar mixing. Thanks to the largely reduced dimension of the microreactor, we are able to capture the hydrodynamics of mixing at microscales down to the Batchelor scale. It is performed by a direct numerical simulation and converged profiles are obtained with a mesh of 11 million cells ($\Delta x = \Delta y = \Delta z = 3\mu m$).

Then, the fluid mixing of solvent and antisolvent has been numerically analyzed with an important criterion - the characteristic mixing time, deduced from the intensity of segregation I_m . The influence of the main parameters have been studied numerically. The characteristic mixing times estimated in our study are in good agreement with the theoretical relations. By comparing the performance of fluid mixing in our microreactor to the other micromixers in the literature, we emphasize the capacity of our microchip to reach mixing times of the order of magnitude until 0.01 ms, two orders of magnitude smaller than those reported in the literature. This result is attainable because of the use of supercritical fluids in microfluidic systems.

After demonstrating the high performance of fluid mixing in the microreactor, we are going to examine numerically the μ SAS precipitation in the next chapter, based on experimental results in the institute.

Chapter IV: Application on μ SAS precipitation

In this chapter, the numerical code is used to predict the particle size distribution in the case of the synthesis of fluorescent nanoparticles. The methodology consists, as explained in Chapter 2, in the coupling between the hydrodynamic equations and a population balance equation. Here, the main difficulty is to estimate the nucleation parameters, specially the surface tension between the solid and the supercritical mixture. That is why we are going to use the experimental data (particle size distribution) to fit the surface tension. This experimental numerical approach allows for determining this important parameter with a great confidence for two main reasons:

- The operating conditions in the microchannel are very well controlled. This fact reduces the discrepancies between the "ideal" operating conditions of the simulation and the experimental ones.
- The reactor dimension and the HPC code allows for obtaining very precise information for the hydrodynamics. Indeed, all the mixing length scales are caught (or almost). In this case, we get rid of the uncertainties related to the estimation of the supersaturation.

In this chapter, after a brief presentation of the experimental data obtained at ICMCB, we are going to focus more specifically on the simulation results.

4.1 μ SAS experiments in the microreactor

The experimental work of Thomas Jaouhari (Ph.D. student) at ICMCB is briefly introduced in this part, including the measurement of the selected solute solubility in the fluid mixture of solvent and antisolvent, the μ SAS set-up, and the characterization of the particle size distribution. The solute is the 1,1,2,2-tetraphenylethylene (TPE) from Sigma-Aldrich with a purity of 98%. The selected solvent is the tetrahydrofuran (THF) ($\geq 99.9\%$) of Sigma-Aldrich. The supercritical antisolvent is the CO_2 purchased from Messer.

4.1.1 Solubility study of the TPE

First, the solubility of TPE in the mixture of THF (solvent) and CO₂ (antisolvent) was measured in a high pressure resistant cell for T = 40 °C and P = 100 bar. The concentration measurements are performed by *in-situ* infrared spectrometry. The experimental points of TPE solubility $Solub_{TPE}$ have been fitted with the following simple relation based on the Wubbolts model (Neurohr *et al.*, 2016):

$$Solub_{TPE} = 0.0052C_{THF}^{0.1705-0.1384(1-C_{THF})+2.148(1-C_{THF})^2} + 5.1295 \cdot 10^{-5}(1 - C_{THF}) \quad (68)$$

with C_{THF} the molar fraction of the solvent THF in the CO₂-THF mixture. The fitted solubility curve is shown in Figure 66 with experimental points. As indicated in the figure, two remarkable points should be mentioned. The TPE has initially a low solubility in the pure solvent of THF, only about 0.5% in mass. Despite much smaller values for CO₂ fraction between 0.8 and 1, it seems that this mixture can not provide high supersaturations locally for a solution dominant composition when the solution meets the supercritical CO₂, because the solubility decreases slowly for the range of CO₂ fraction between 0 and 0.2.

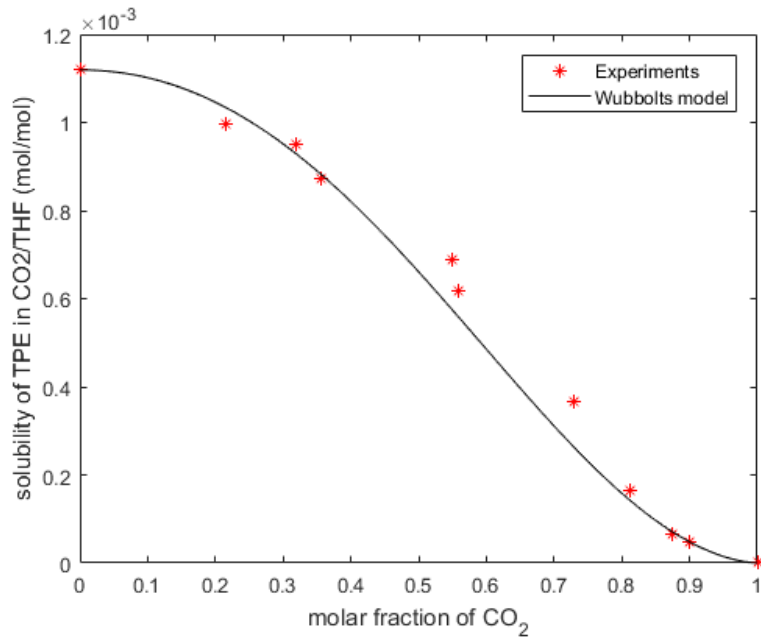


Figure 66: The solubility of TPE in the mixture of THF and CO₂ at 40 °C and 100 bar.

4.1.2 μ SAS set-up

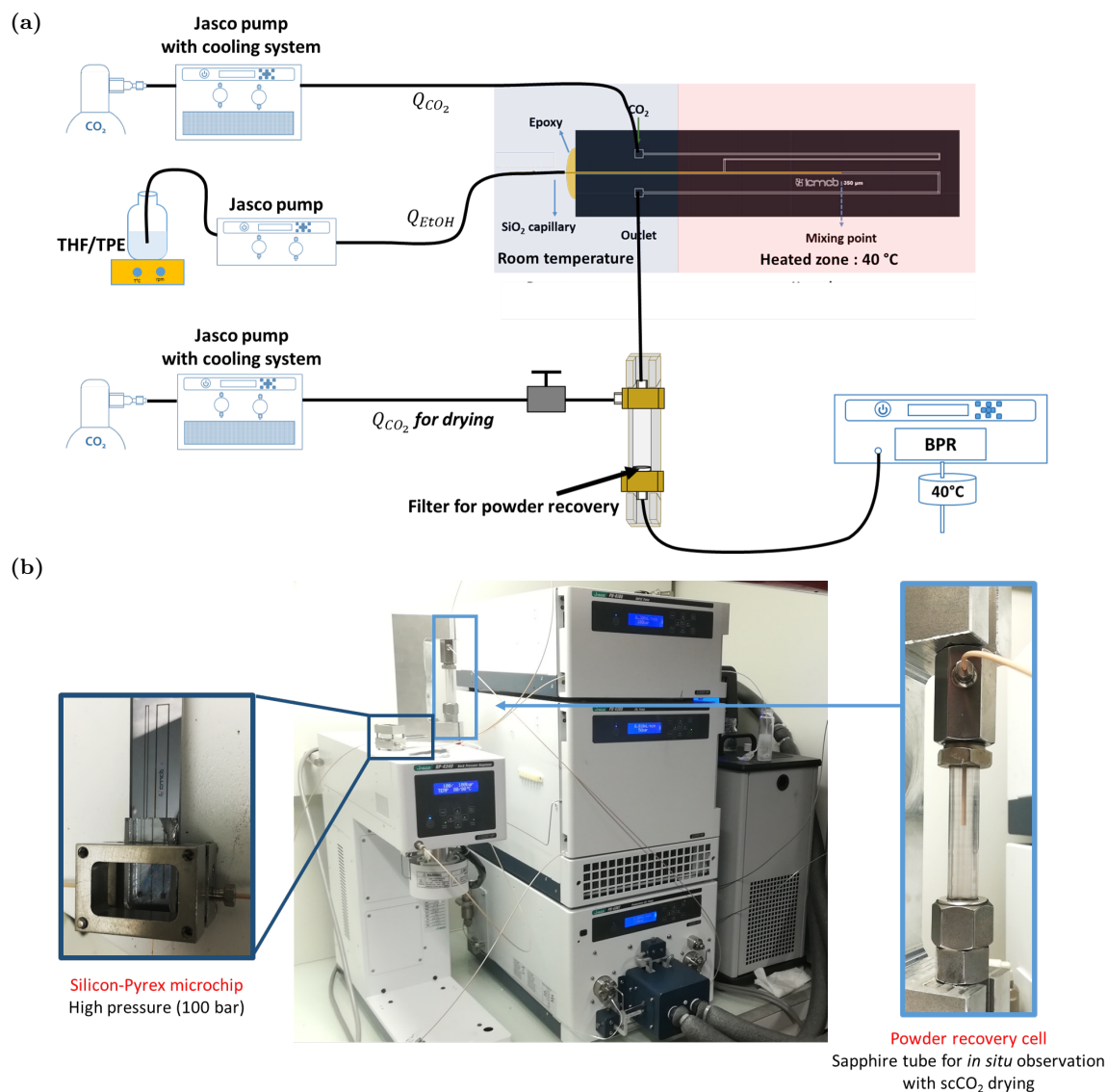


Figure 67: μ SAS experimental system applied for precipitating TPE nanoparticles (a). schema of the system; (b). some photos for better illustrating the essential parts of the μ SAS system.

The TPE solute was precipitated in the microchannel of the same geometry as previously studied for the turbulent mixing. The experimental system is presented in Figure 67. The TPE was initially dissolved in the THF solvent at room temperature (20 °C). At the beginning of the μ SAS process, the pressure increased to 100 bar and controlled by a back pressure regulator. The CO_2 was cooled down to -5 °C in a high pressure pump in which the pressure is slightly higher than 100 bar. The compressed liquid CO_2 was injected into the

preheating microchannel at controlled flow rate to attain the desired temperature (40 °C) by a heating plate attached onto the microreactor. Under these conditions in the mixing zone of the microchannel, the CO₂ became supercritical. When the pressure was stable in the system, the solution was pumped into the microchip at constant flow rate. The precipitation occurred while the two fluids were mixed at the tip of the capillary. The TPE particles were recovered both on a nano-filter with pores of 100 nm and on a TEM grid for the analysis. At the end of the process, the flow of the TPE-THF solution was stopped first and the flow of condensed CO₂ was kept to dry the particles at 100 bar for 30 minutes. This step is necessary to remove the THF solvent residue between the TPE particles.

The experimental conditions applied in the simulation are listed in Table 6 with the case No. 1 as the reference. The flow rates of two fluids $Q_{0_{THF}}$, $Q_{0_{CO_2}}$ were controlled by the pumps at initial temperatures, 20 °C for the TPE/THF solution and -5 °C for the compressed liquid CO₂. The initial velocities $u_{0_{THF}}$ and $u_{0_{CO_2}}$ were estimated by taking consideration of the temperature changes from the pumps to the heated microchannel ($u_{0_{THF}} = \frac{Q_{in}\rho_{THF}(T_0)}{A_{in}\rho_{THF}(T)}$, $u_{0_{CO_2}} = \frac{Q_{out}\rho_{CO_2}(T_0)}{A_{in}\rho_{CO_2}(T)}$). The precipitated TPE particle sizes were measured from images taken by the transmission electron microscopy (TEM) shown in Figure 68. The particles were spherical and quite uniform in size, possessing a mean diameter from 8 nm to 13 nm with narrow size distribution (± 3 nm). In order to obtain reliable information on particle size and its distribution, 100 particles were at least counted.

Table 6: μ SAS experimental conditions of the fluid hydrodynamics, with the temperature fixed at 40 °C and the pressure at 100 bar, as well as the particle properties (mean size \bar{d}_p and particle size distribution PSD)

No.	$C_{0_{TPE}}$ ($g \cdot L^{-1}$)	$Q_{0_{THF}}$ ($\mu L \cdot min^{-1}$)	$Q_{0_{CO_2}}$	$u_{0_{THF}}$ ($m \cdot s^{-1}$)	$u_{0_{CO_2}}$	CO ₂ (wt.%)	\bar{d}_p (nm)	PSD
1	2	440	8000	0.95	6.35		9.1	
2	2	110	2000	0.24	1.59	98	14.4	± 3
3	3	440	8000	0.95	6.35		9.7	

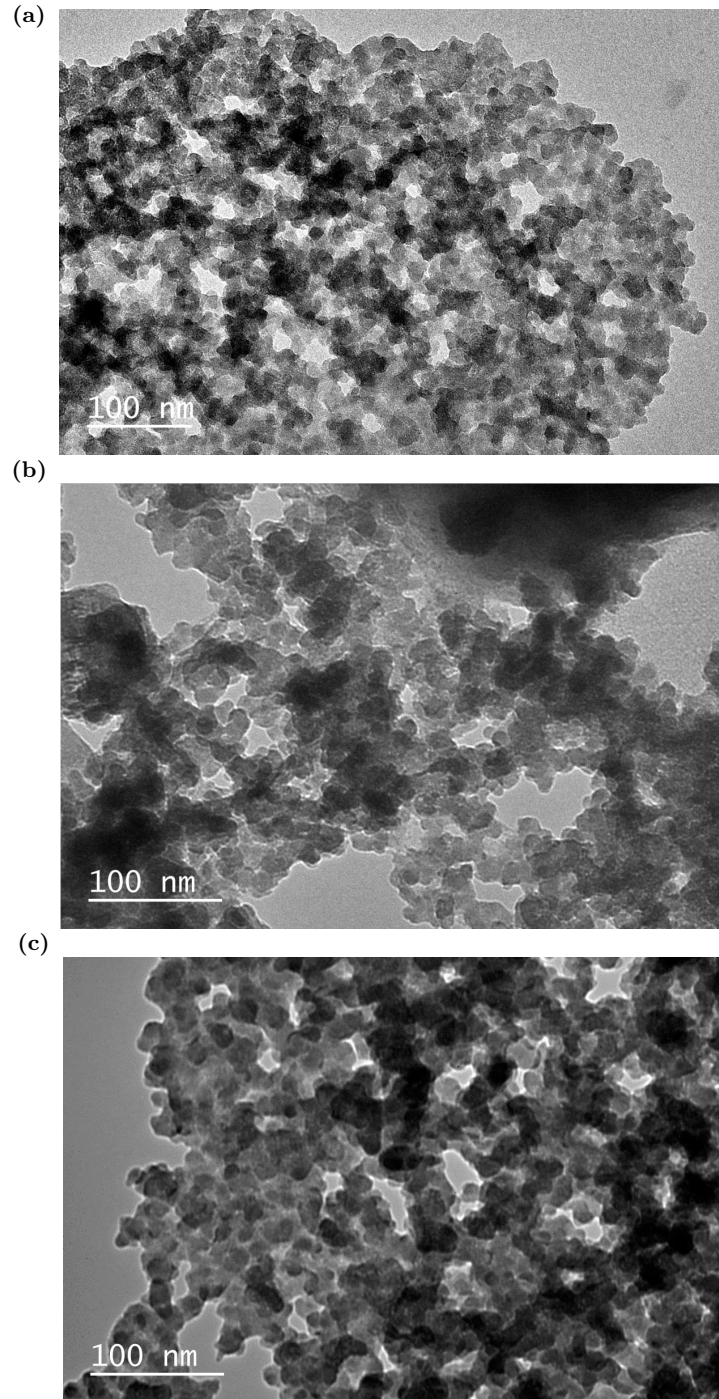


Figure 68: TEM images of the precipitated TPE particles by μ SAS process: (a). No. 1 (b). No. 2 (c). No. 3 in Table 6.

4.2 μ SAS simulation details

The precipitation simulations were carried out for the experimental cases in Table 6. The simulated microchannel has the same geometry as the one of the turbulent mixing part

(Figure 69). The mesh is uniform and the chosen grid size is $\Delta x = \Delta y = \Delta z = 3\mu m$.

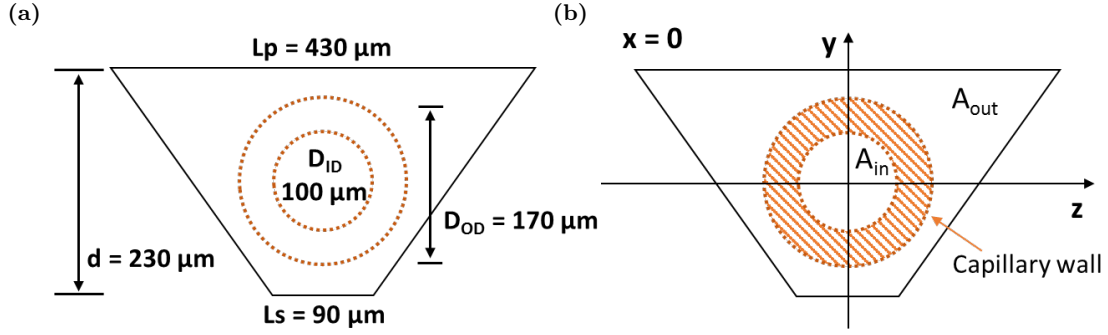


Figure 69: The numerical geometry to illustrate (a). the dimension of the trapezoidal cross-section and (b). the geometry at $x=0$ for the boundary conditions.

The boundary conditions of the hydrodynamics are similar to the cases of the turbulent mixing. The velocities of solution and CO_2 are fixed respectively to $u_{0_{THF}}$ in A_{in} and $u_{0_{CO_2}}$ in A_{out} in Figure 69b at the plane $x=0$, according to their flow rates. Since the initial concentration of TPE in THF is low, even for the case No.3 ($3 g \cdot L^{-1}$, 0.336 wt.%), the solution can be considered approximately to be the pure solvent of THF for the calculation.

The boundary conditions for the species transport should be considered this time for the solute TPE, the solvent THF and the moments. The 4 moments (m_0 to m_3) are set to be 0 at the inlet of the microchannel ($x=0$). In A_{in} , the mass fractions of TPE, THF are fixed respectively to 0.00224 and 0.99776 for the test cases No.1 and No.2, 0.00336 and 0.99664 for the test cases No.3.

As discussed in Chapter II, all parameters of the numerical simulation can be estimated except the interfacial tension σ between the solid and the fluid phase. Because of the lack of knowledge of this crucial parameter, we estimated its value by fitting the simulation results to the experimental data.

4.3 Determination of the interfacial tension σ

The particle size distribution is calculated by applying a log-normal distribution according to the time average values of the moments (Neurohr *et al.*, 2016):

$$N(L) = \frac{1}{L \sqrt{\ln\left(\frac{m_0 m_2}{m_1^2}\right)} \sqrt{2\pi}} \exp\left(\frac{-\ln^2\left(\frac{L m_0 \sqrt{m_2 m_0}}{m_1^2}\right)}{2 \ln\left(\frac{m_0 m_2}{m_1^2}\right)}\right) \quad (69)$$

with L the length of particle characteristic length (the axis d_p in Figure 70), \overline{m}_i the average value of the moment i in the cross-section of the right side of the channel ($x = 4$ mm).

The interfacial tension σ was estimated to be 2.25 mN/m for the test case of reference No.1. This value resulted in the best agreement with the particle size and distribution obtained from the μ SAS experiment. The comparison between the numerical particle size distributions and the experimental one is represented in Figure 70.

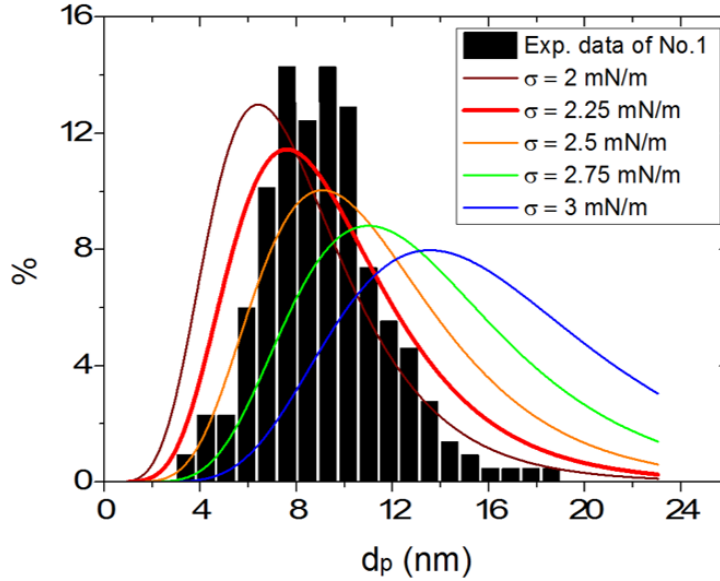


Figure 70: The precipitated TPE particle sizes and size distribution obtained experimentally in bar chart for the reference test case No.1 in Table 6 and the simulated particle distributions in curves as a function of the interfacial tension σ .

As a first remark, we can observe a very strong influence of the surface tension σ on the distribution. Indeed, a variation between 2 and 3 mN/m can lead to very different distribution (size and width of the distribution).

Few information can be found for the interfacial tension of a solid in a supercritical fluid. Debenedetti (1990) reported his studies of the homogeneous nucleation of the phenanthrene in supercritical CO_2 , according to the classical nucleation theory. He observed a relationship between the nucleation rate and the pressure for different surface tension σ (0.05, 0.02, 0.01 N/m). Figure 71 emphasizes that for a fixed pressure, a smaller σ corresponds to a higher nucleation rate.

The instantaneous nucleation rate field B of the test No.1 is shown in Figure 72 as well as the field of its logarithmic value $\ln B$, at the plane $y=0$ close to the tip of the injector.

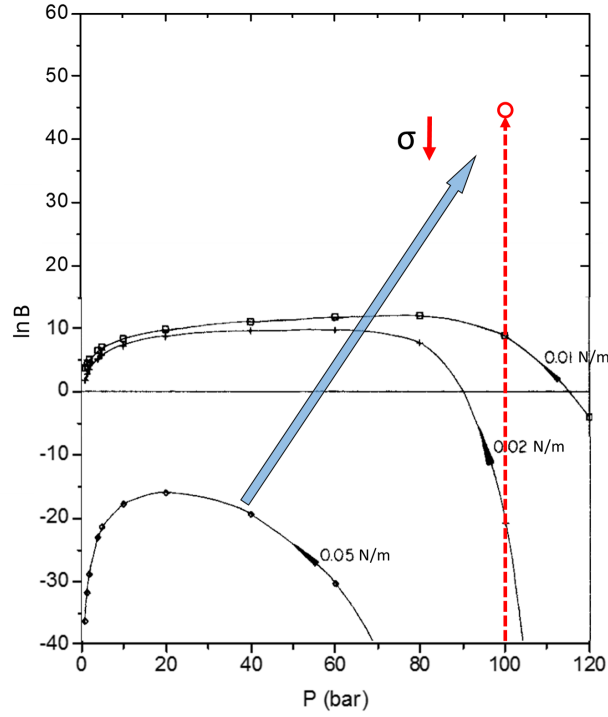


Figure 71: The primary homogeneous nucleation rate ($\ln B$) as a function of pressure P , with the determined surface tension σ from the simulation of this study (red circle), compared to the work published by Debenedetti (1990), figure modified from its original paper.

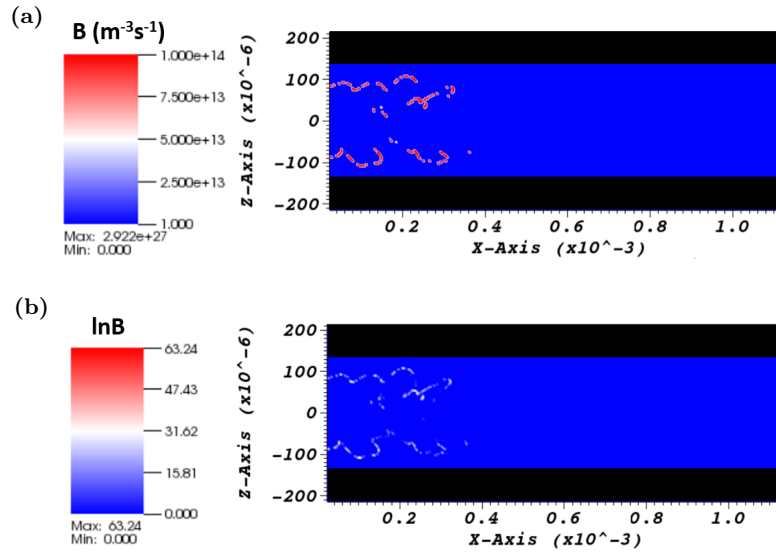


Figure 72: The instantaneous fields of (a). nucleation rate B and (b). its logarithmic value in the microchannel (plane $y = 0$, with the unit of meter for x and z axes).

As can be observed, the average value of $\ln B$ is around 44 for the pressure at 100 bar, corresponding to the red point illustrated in Figure 71. The value is 2 times higher than the curve of the surface tension at 0.01 N/m. The determined surface tension 2.25 mN/m

seems to be consistent with the results of Debenedetti (1990).

4.4 Interpretations of μ SAS simulation

Several fields of important variables are illustrated and analyzed as the general analysis. We are going to focus only on the numerical results of the reference test No.1. The effects of operating parameters are presented after the general analysis.

4.4.1 General observations of the test No.1

a. Mass fraction fields of THF and TPE

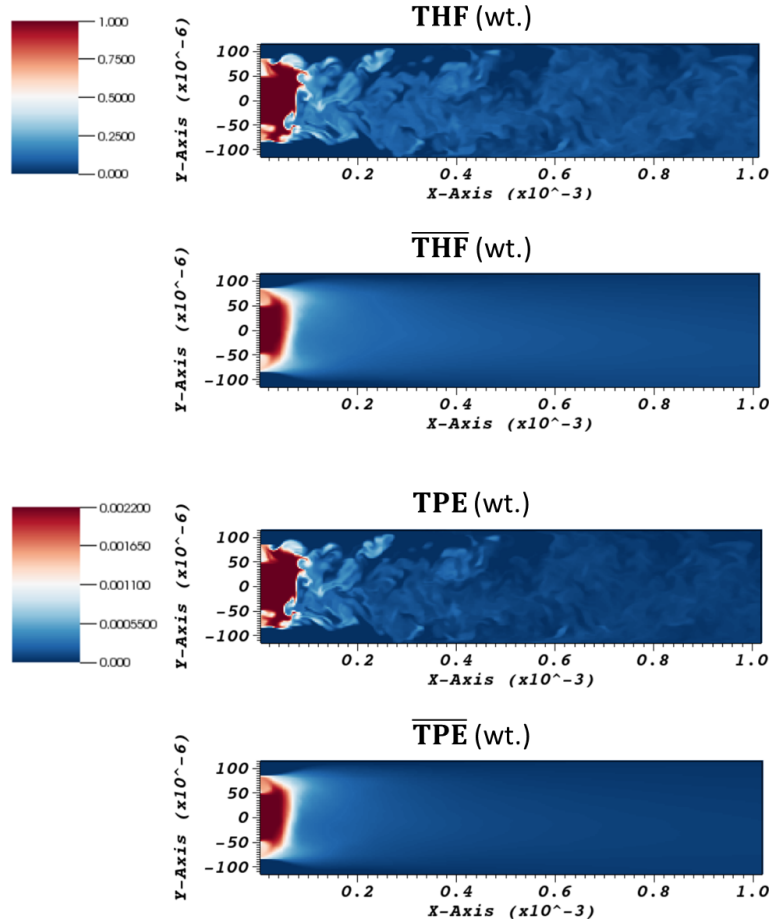


Figure 73: The instantaneous and mean time fields of the solvent THF and the solute TPE mass fractions in the microchannel of the plane $z = 0$ (with the unit of meter for x and y axes) for the reference case No.1.

In order to illustrate the general mixing quality of the μ SAS process, we have examined first in Figure 73 the instantaneous and time averaged fields of mass fractions of THF and TPE in the plane of $z = 0$ (which represents the depth of the channel). The species transport is very fast for both solute and solvent in the conditions of the reference test case No.1 and a homogeneous mixture is obtained within 1 mm from the capillary outlet, according to the time averaged fields. We observe that the solute TPE dissolved in the fluid mixture is consumed by the particle precipitation. Although the diffusivities of the TPE and THF in CO_2 are different, the similarity is obtained between the solute TPE and the solvent THF mass fractions, resulting from much stronger effects of convection compared to the diffusion for the operating conditions.

b. Mixing time analysis

After the first observation on the mixing quality by the mass fraction distributions, we analyze quantitatively the fluid mixing by providing the instantaneous and mean time fields of the engulfment micromixing time ($t_{mE} = 17.24\sqrt{\nu/\epsilon}$) in the plane $z = 0$ (Figure 74). In order to better illustrate the difference, the upper bound is set to be 0.0002 s.

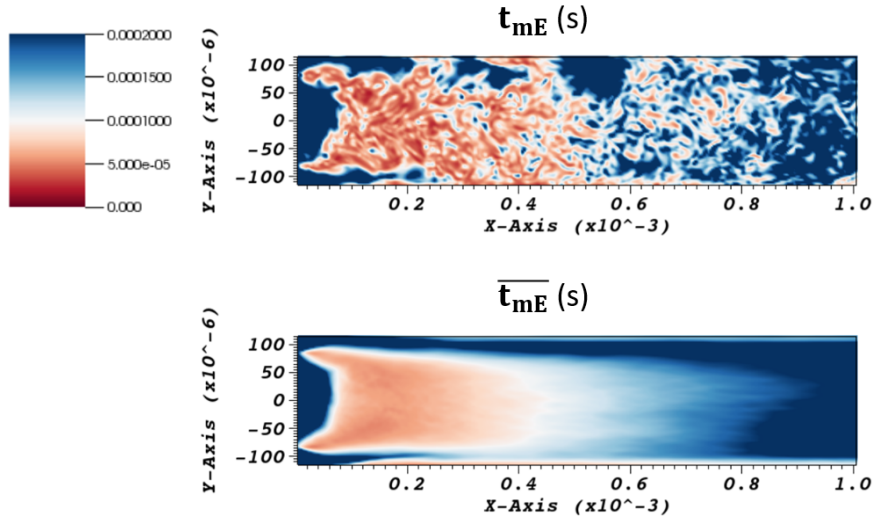


Figure 74: Engulfment micromixing time in the microchannel of the plane $z = 0$ (with the unit of meter for x and y axes) for the reference test No.1.

The engulfment micromixing time t_{mE} is in the order of magnitude of 10^{-5} s (0.01 ms) for the examined conditions, illustrating that the mixing rate is extremely high, especially at the beginning of the mixing close to the capillary outlet. This result is related to the high velocity fluctuations of fluid mixture in this zone, creating high turbulent energy dissipation

rate up to $10^5 W \cdot kg^{-1}$ locally in certain cells (Figure 75). According to the mean field of the engulfment micromixing time $\overline{t_{mE}}$, its value drops to 0 at a distance of 1 mm from the injector tip. It means that the mixing is completed due to no more energy dissipation and the mixture fluid becomes homogeneous, corresponding well to the mass fraction field of the solvent THF in Figure 73.

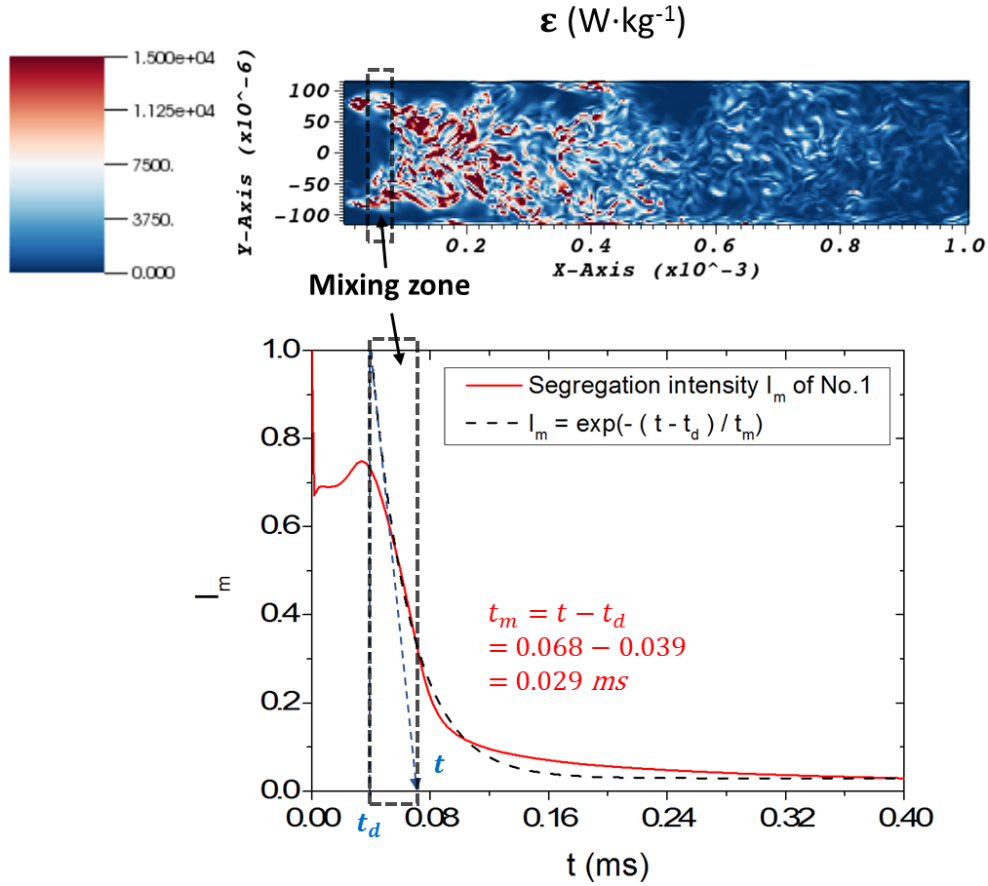


Figure 75: Instantaneous field of the energy dissipation rate ϵ of the plane $z = 0$ (with the unit of meter for x and y axes) and the characteristic mixing time t_m determined by the segregation intensity I_m for the reference test No.1.

In order to quantify the mixing efficiency with a single representative value, we have determined the characteristic mixing time of the test case No.1, based on the intensity of segregation I_m (Figure 75).

By applying the first order system with time delay t_d , the characteristic mixing time is obtained $t_m = 0.029$ ms and its value also in the order of magnitude of 10^{-5} s, is in good agreement with the engulfment micromixing theory. From this μ SAS simulation, we

have also verified the good agreement between the mixing time determination from the segregation intensity I_m and the mixing relation developed by Baldyga and Bourne (1989). According to both the characteristic mixing time t_m and the engulfment micromixing time t_{mE} , we have proven an excellent mixing efficiency in our microreactor under the μ SAS conditions.

c. Estimations of the supersaturation, the nucleation and the growth rates

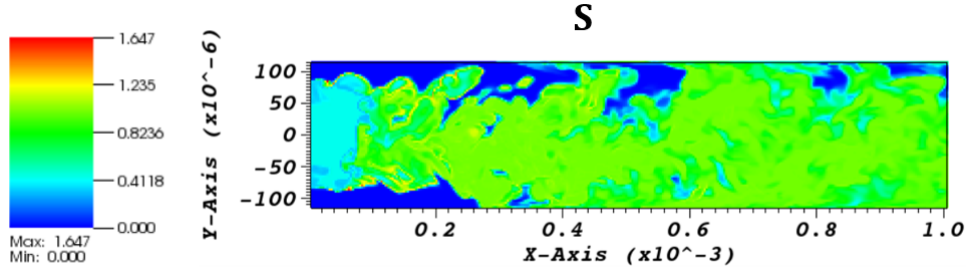


Figure 76: Instantaneous fields of supersaturation S in the plane $z=0$ of the test case No.1.

The influence of this fast mixing of the test No.1 can be reflected on the instantaneous fields of the supersaturation S , nucleation B and growth rate G . As the driving force of the precipitation, the supersaturation $S = C/C_{sat}$ has been calculated in the microchannel. The instantaneous field of supersaturation is shown in Figure 76. Thanks to the efficient mixing in this case, no effective gradient is observed in the microchannel. However, the value of supersaturation is generally low with a maximum of 1.647. The first explanation is the low TPE concentration even in the initial solution. The TPE can not be dissolved in a large quantity in the THF, implying that the THF is not a good solvent for the TPE but compared to other common organic solvent, the solubility of TPE in THF is the largest. So, the low concentration of TPE can not offer a high value of supersaturation. It is true that the antisolvent of supercritical CO_2 decreases the TPE solubility in the fluid mixture, in particular for a high CO_2 fraction. Whereas, in the mixing zone close to the tip of the injector, the mass fractions of CO_2 are locally far from the global value of 98%. Indeed, even for a local mixture in certain discretized cells in which the CO_2 fraction is close to 1, the solubility C_{sat} is significantly low, but the TPE concentration in this local mixture is equally low because of a solution (TPE + THF) fraction close to 0.

Another reason of the general low supersaturation is related to the nucleation rate B and the particle growth rate G . In order to clearly present the relation between the nucleation and the supersaturation in Figure 77, the instantaneous field of the supersaturation is reset

with a superior limit at 1.3 and an inferior boundary at 1 because the precipitation occurs only while the supersaturation degree is higher than 1.

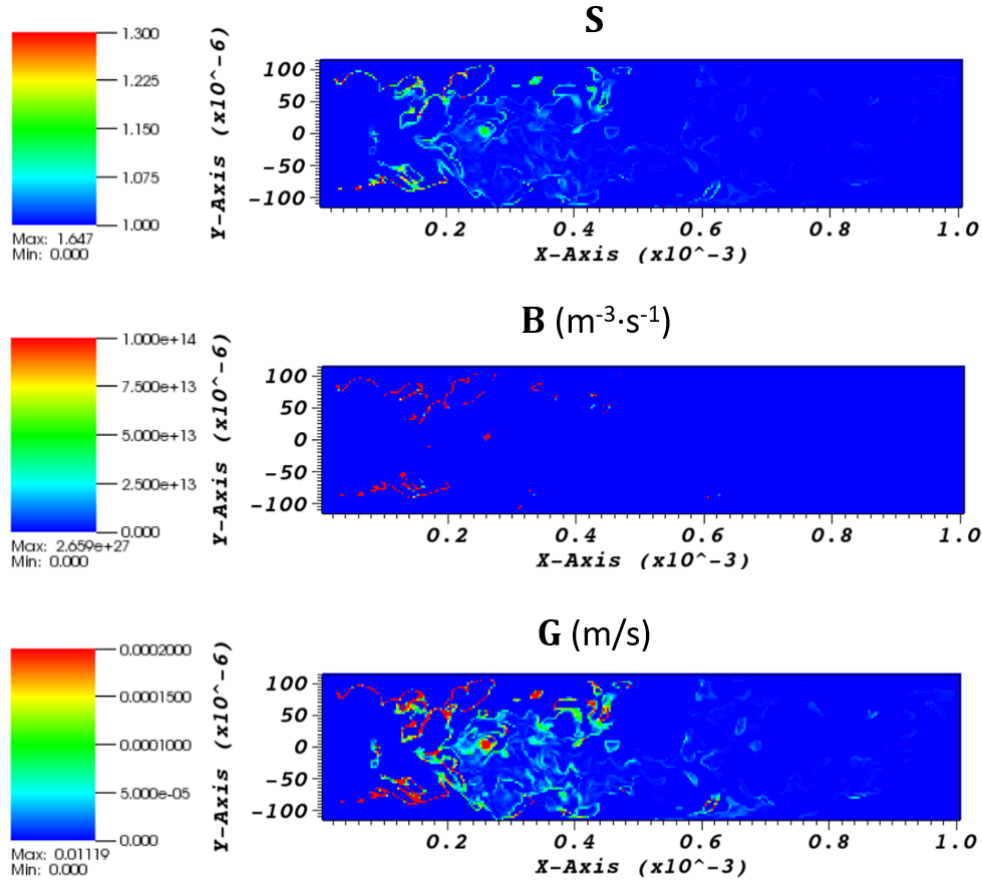


Figure 77: Instantaneous fields of supersaturation S in the plane $z=0$ of the test case No.1.

The evolution of the supersaturation can be considered as a combination of its generation by fluid mixing and its consumption by the nucleation and the particle growth (for $S > 1$). The extremely high rate of nucleation decreases fast the supersaturation degree once it exceeds 1. The similarity of these two fields can be observed in Figure 77, also for the relationship between the supersaturation and growth rate. However, the nucleation is favorable because of the fast fluid mixing. The supersaturation S drops quickly after the nucleation, leaving a lower driving force S for particle growth. The high nucleation rate results from the small value of the surface tension ($\sigma = 2.25 \text{ mN/m}$) and a significant diffusion coefficient for TPE particle D_{WC} (up to $1.4 \cdot 10^{-8} \text{ m}^2 \cdot \text{s}^{-1}$) under the supercritical mixture conditions due to a gas-like viscosity μ_m of the fluid mixture (about $43 \mu\text{P} \cdot \text{s}$). Based on the definition of the primary homogeneous nucleation rate (Equation 18) presented in Chapter 2, these two parameters affect decisively the nucleation and contribute to fast

rates in the simulation case No.1.

e. Analysis of the moments

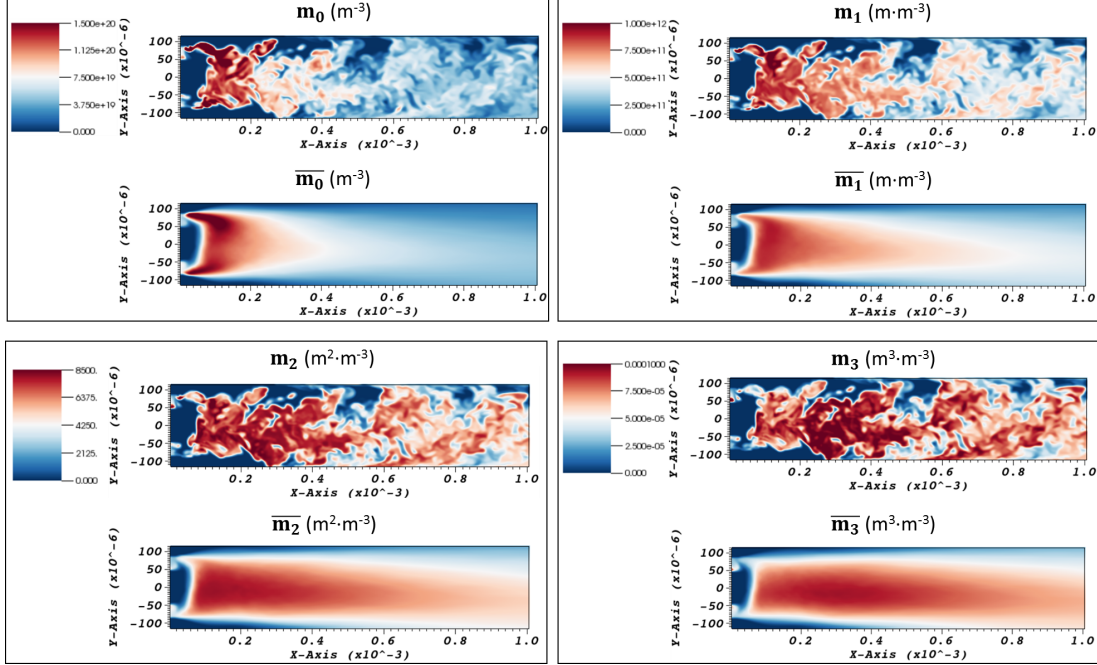


Figure 78: The fields (instantaneous and average) of the moments m_0 , m_1 , m_2 and m_3 of the test No.1.

As a reminder, the moments m_0 , m_1 , m_2 and m_3 are, per volume of the reactor, the total number of particles, the sum of the particle length, the sum of the particle surface and the total particle volume, respectively ($m_j = \int_0^\infty n(L, X, t)L^j dL$). These moments are represented in Figure 78 with their instantaneous and time averaged fields.

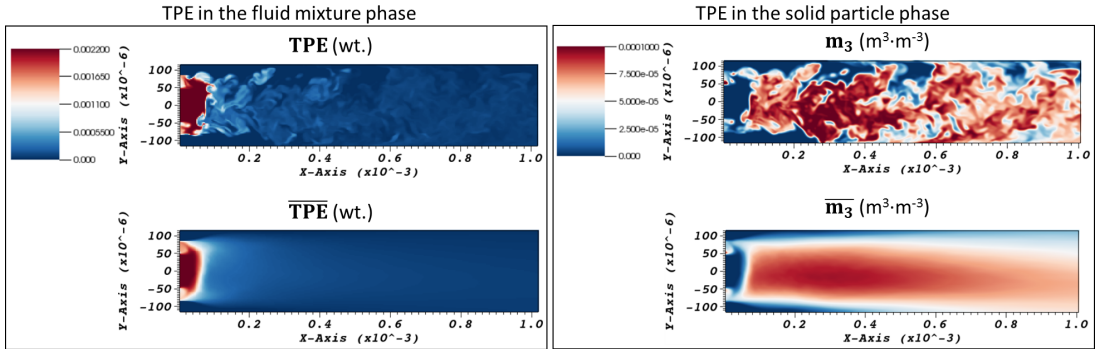


Figure 79: TPE mass fractions in the fluid phase (left) against its solid phase represented by the moment m_3 of the total volume.

As expected, the mean fields of the moments show equally that the fast fluid mixing contributes to reach the homogeneity at 1 mm from the injector outlet. Figure 79 illus-

trates qualitatively the solute TPE in the fluid phase and in the solid phase (which can be considered as the moment m_3 for the total particle volume). This consistency proves the robustness of the numerical modeling.

d. Evaluations of the particle size

The most important product yielded through the simulation is the particle size d_p . With the average values of the moments, we are able to estimate its mean value \bar{d}_p . We choose the first two moments to express the mean particle size \bar{d}_p in our study: $\bar{d}_p = \bar{m}_1 / \bar{m}_0$. The fields of both the instantaneous and the mean particle sizes can be seen in Figure 80.

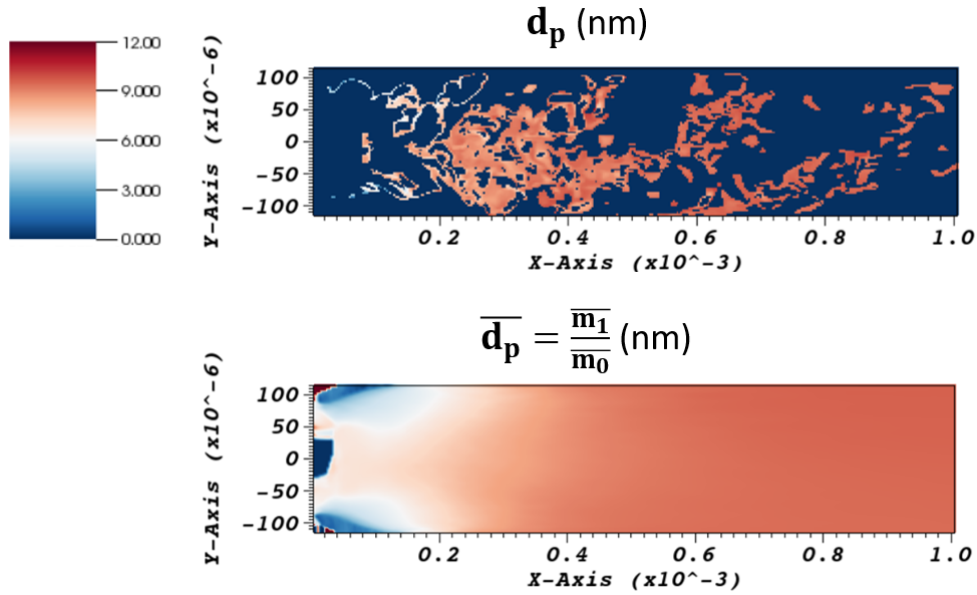


Figure 80: The instantaneous particle size d_p field and the its mean time value \bar{d}_p calculated by the average moments m_0 and m_1 : $\bar{d}_p = \bar{m}_1 / \bar{m}_0$ in the plane $z=0$ of the test case No.1.

According to the instantaneous particle size d_p , one can observe the particle growth at different locations in the microchannel and the sizes vary from 6 to 15 nm, corresponding well to the experimental measurements of the test case No.1. The mean values of the particle sizes \bar{d}_p become stable and stop changing at 1 mm from the capillary tip, which is a coherent result regarding the other time averaged fields.

After the analysis of the reference case No.1, we are going to present the other test cases with different operating conditions.

4.4.2 Effects of operating parameters

The test case No.2 for lower flow rates has been simulated with the same surface tension $\sigma=2.25$ mN/m obtained from the reference simulation No.1. The test No.3 has a higher TPE concentration in the initial THF solution and the surface tension σ is also at 2.25 mN/m. The last case No.4 corresponds to the same conditions as the case No.3 but with a different interfacial tension $\sigma=2.75$ mN/m, obtained by fitting the particle mean size and size distribution between the simulation and the experimental data. The main information is reported in Table 7.

Table 7: The TPE particle mean sizes of the experiments ($\bar{d}_{p_{exp}}$) and the simulations ($\bar{d}_{p_{num}}$), the surface tension used in the simulations σ , the mixing times t_m at fixed temperature (40 °C) and pressure (100 bar) under tested μ SAS conditions (the initial concentration of TPE in THF $C_{0_{TPE}}$, the fluid flow rates $Q_{0_{THF}}$, $Q_{0_{CO_2}}$ and the fluid mean velocities at the injector outlet $u_{0_{THF}}$, $u_{0_{CO_2}}$).

No.	$C_{0_{TPE}}$ ($g \cdot L^{-1}$)	$Q_{0_{THF}}$ ($\mu L \cdot \text{min}^{-1}$)	$Q_{0_{CO_2}}$	$u_{0_{THF}}$	$u_{0_{CO_2}}$	$\bar{d}_{p_{exp}}$	$\bar{d}_{p_{num}}$	σ	t_m
				($\text{m} \cdot \text{s}^{-1}$)		(nm)		(mN/m)	(ms)
1	2	440	8000	0.95	6.35	9.1	9.5	2.25	0.029
2	2	110	2000	0.24	1.59	14.4	16.6	2.25	0.59
3	3	440	8000	0.95	6.35	9.7	8.6	2.25	0.029
4	3	440	8000	0.95	6.35	9.7	10.6	2.75	0.029

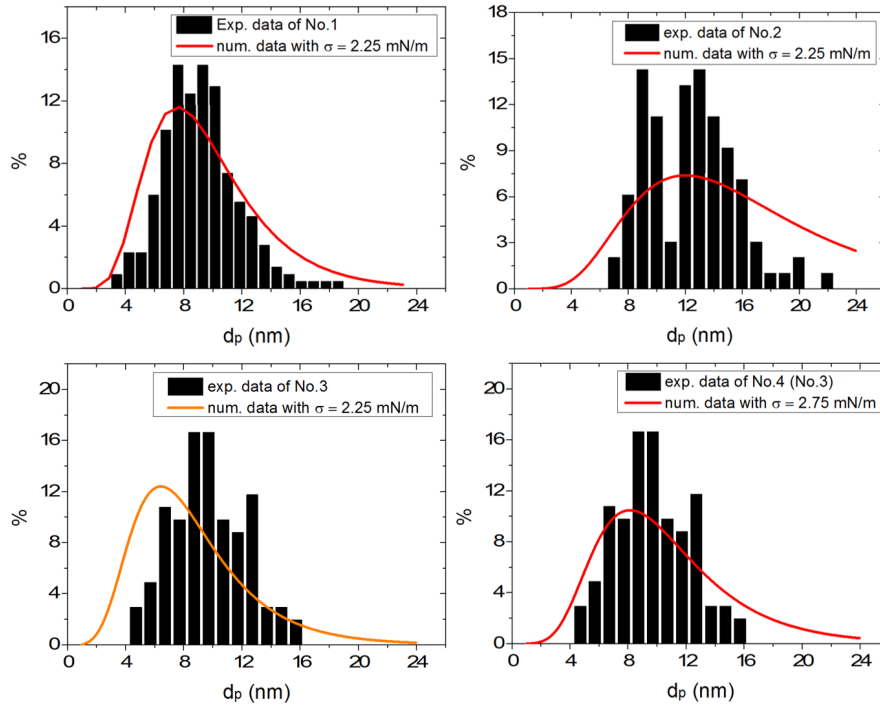


Figure 81: Particle size distribution comparison between the experimental results and the simulations for 4 tested cases.

The results of comparison between experimental distributions and simulation ones are shown in Figure 81. The simulations yield generally acceptable results on the particle sizes and the size distributions for the test cases No.1, No.2 and No.4 but not for the case No.3.

a. Influence of fluid velocities

While the flow rates of No.2 reduced to $110 \mu L \cdot min^{-1}$ and $2000 \mu L \cdot min^{-1}$ respectively for the TPE/THF solution and the antisolvent CO_2 , compared to the reference test case No.1, the mean size of TPE increased from 9.1 nm to 14.4 nm, according to the experimental results, with the same total CO_2 mass fraction at 98%. In fact, an relative inefficient mixing in case No.2 can be represented by the mean time mass fractions of the solvent THF and the solute TPE (Figure 82). A long length of solvent jet can be observed. In spite of a mixture homogeneity at $x = 1$ mm, the fluid is quite heterogeneous in the vicinity of the injector tip.

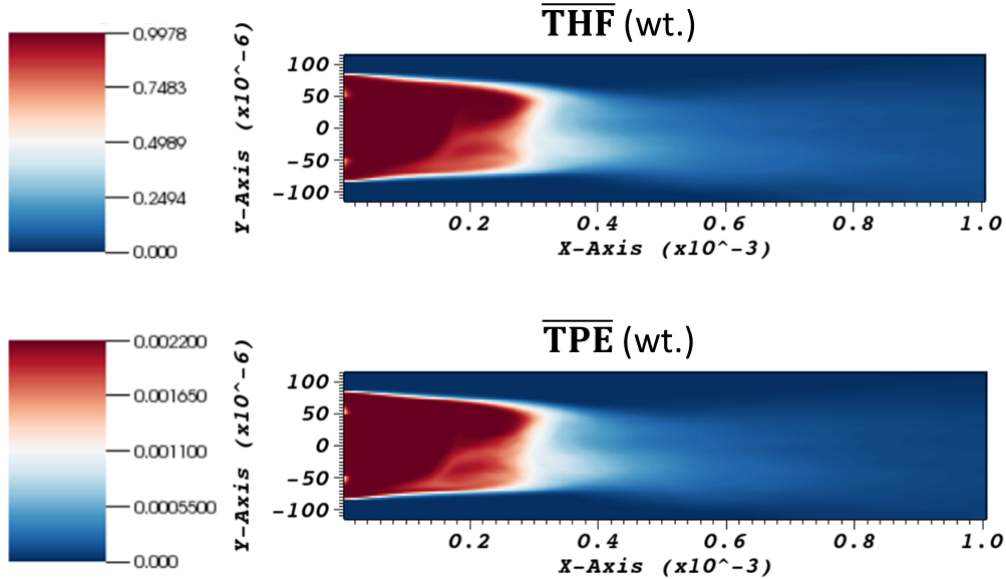


Figure 82: The mean time fields of the THF and TPE mass fractions in the test case No.2 of lower flow rates.

More specifically, in order to analyze the velocity effect on the mixing time t_m , we deduce it from the evolution of the segregation intensity (Figure 83). The decrease of fluid flow rates in test No.2 leads to a slower mixing compared to the reference test No.1, with a mixing time of 0.59 ms, one order of magnitude higher than the mixing time of the reference case (0.029 ms). This less efficient mixing influences the supersaturation degree, which is slightly smaller in No.2 than in No.1, especially at the outlet of the injector. The slower mixing in

No.2 generates also a quite heterogeneous field of the supersaturation around the long jet of the TPE/THF solution. This less uniform supersaturation field promotes the particle growth instead of the nucleation. In other words, the supersaturation is mainly consumed by the nucleation in the test No.1 close to the injector outlet once the fluids encounter to each other. Whereas, in the test No.2, the length of the region where the supersaturation is more than 1 is two times (1 mm) of the reference test No.1 (0.5 mm), leaving to a longer distance and more time for the growth of the nuclei formed upstream than the case in No.1. The slower mixing in the case No.2 can explain the increase of the mean TPE particle size.

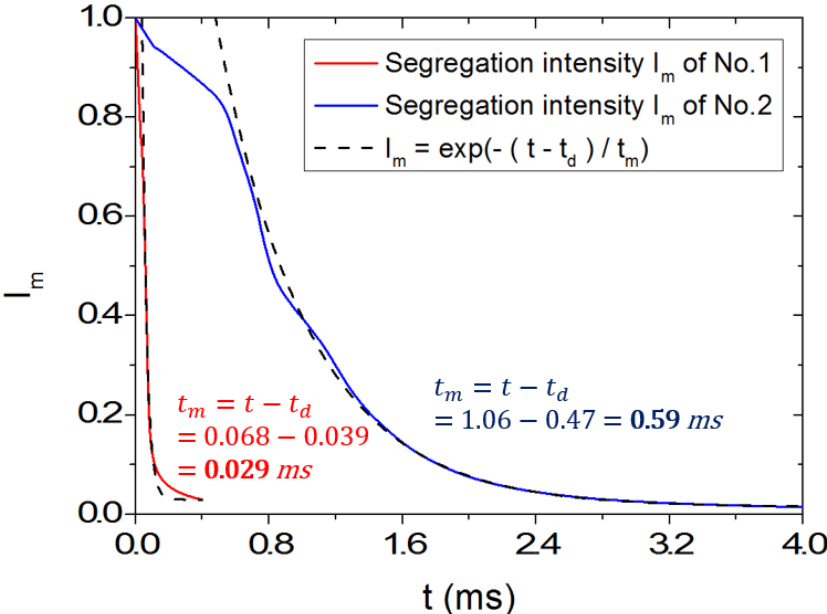


Figure 83: Intensity of segregation curves of test No.1 and No.2 as a function of time with the determination of mixing time.

The comparison between No.1 and No.2 confirms the importance of the hydrodynamic behavior of mixing in the microreactor that we emphasize before. Higher flow rates (fluid velocities) trend towards faster mixing, so as smaller particle sizes and a narrower size distribution.

b. Influence of the TPE initial concentration on particle size d_p

The hydrodynamic behaviors of tests No.3 and No.4 have no difference compared to the reference case No.1 because of the identical fluid flow rates in these cases. The same mixing time is obtained ($t_m = 0.029$ ms) for all the three simulations. Only one parameter - the TPE concentration is changed between the test No.1 and No.3, whereas, two parameters

changed in the test No.4, the TPE concentration and the surface tension σ . While the surface tension was kept constant at 2.25 mN/m in the test No.3, according to the simulation, the increase of the TPE initial concentration leads to a slightly higher supersaturation in the microchannel. As a consequence, more nuclei precipitate at higher nucleation rate, resulting in smaller particles with a mean diameter $\overline{d}_{p_{num}}$ of 8.6 nm than the ones in the reference case ($\overline{d}_{p_{num}}$ of 9.5 nm). However, the experimental measurement provides a slightly increased mean size $\overline{d}_{p_{exp}}$ of 9.7 nm.

In order to understand this opposite result, in the test No.4, we propose to fit the surface tension according to the experimental results. A slightly higher value of the surface tension is obtained at 2.75 mN/m. Although it is hardly to measure the interfacial tension between the fluid mixture and the solid particle under μ SAS conditions, the variation of the initial TPE concentration in the TPE/THF solution (from 2 to 3 g/L) may probably influence the surface tension. Cahn (1977) and Sullivan (1980) mentioned in their publications that the contact angle of solid-liquid interface can be changed with the composition. With a lack of measurement method, this assumption would not be verified so far and more comparisons between experiments and simulations are needed to correlate the effects of TPE concentration in the initial solution on the interfacial tension σ of solid and fluid.

Above all, our numerical model provides reliable results compared to the experimental data, as the surface tension σ remains the only adjustable parameter. In the next part, according to the simulation results, we are going to compare the characteristic times of mixing and precipitation.

4.4.3 Characteristic times of the precipitation

In order to compare the characteristic time of the precipitation and the fluid mixing, the time of precipitation t_p has been estimated. In Figure 84, we have represented the evolution on the center line of the mean particle size \overline{d}_p in function of the time. The time axis t is defined as: $t = L/\overline{u}_{x_{in}}$, the same one used for the turbulent mixing analysis in Chapter III, with L the length of microchannel, $\overline{u}_{x_{in}}$ the average velocity of the inner fluid TPE/THF solution, depending on its flow rate and the inner surface of the capillary.

The characteristic time of precipitation t_p is defined in this study as the time when the mean particle size \overline{d}_p reaches a stable value (Figure 84). Another important characteristic

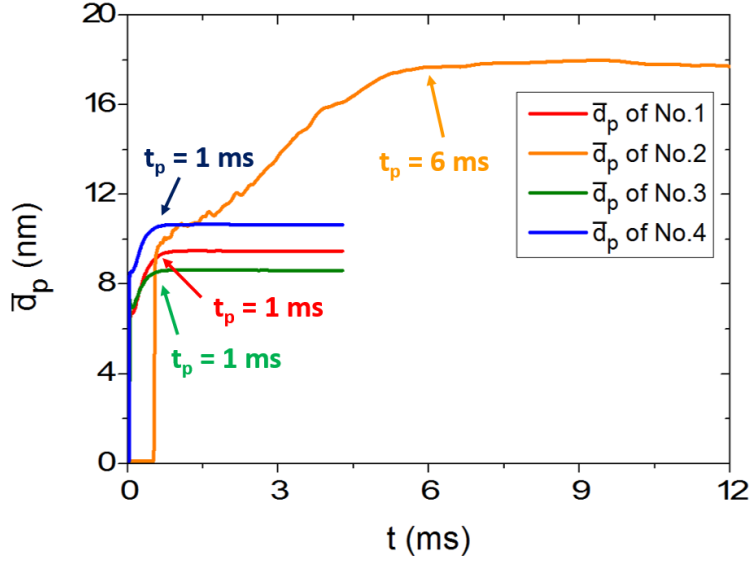


Figure 84: Determination of precipitation time t_p according to the mean particle size \bar{d}_p .

time for the particle precipitation process is the nucleation time, which is generally not clear to be defined. Several methods have been used to determine the nucleation time. The different characteristic times are reported in Table 8 in order to compare their orders of magnitude.

Table 8: Characteristic times (precipitation time t_p , nucleation time t_n estimated in three methods, particle growth time t_{g2} of the second method) with the average nucleation rate \bar{B} , the mean particle growth rate \bar{G} and the Da numbers (Da_p for fluid mixing and precipitation, Da_n for fluid mixing and nucleation).

No.	t_p (ms)	t_{n1} (ms)	r^* (nm)	$\bar{G} \cdot 10^5$ ($m \cdot s^{-1}$)	t_{n2} (ms)	t_{g2} (ms)	$\bar{B} \cdot 10^{-21}$ ($m^{-3} s^{-1}$)	t_{n3} (ms)	t_m (ms)	Da_p	Da_n
1	1	0.031	1.59	5.28	0.88	0.12	2.15	0.017	0.029	0.029	1.7
2	6	0.521	2.15	3.43	5.64	0.36	1.72	0.021	0.59	0.098	28.1
3	1	0.037	1.13	3.66	0.83	0.17	6.67	0.006	0.029	0.029	4.8
4	1	0.031	1.27	4.01	0.80	0.20	1.85	0.020	0.029	0.029	1.5

Determination of the nucleation time: below, we present the three methods of determination of the nucleation time.

Method 1:

The simplest way is to detect the moment in Figure 85 when the average particle size starts to grow. This moment can be considered as the nucleation time t_{n1} .

Nevertheless, this method do not provide the real t_n . Precisely speaking, it is rather

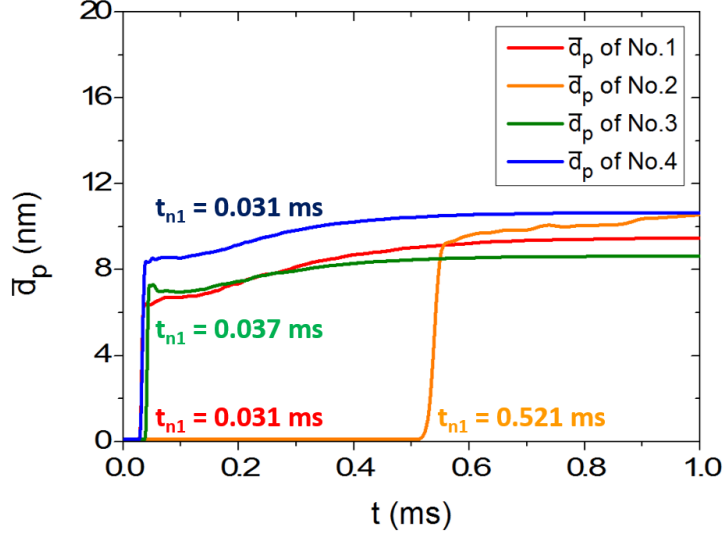


Figure 85: Determination of the nucleation time t_{n1} by the mean particle size \bar{d}_p on the center line of the microchannel.

the time for the dynamic solution jet breakup than the nucleation time. For instance, at the injector outlet, no fluid mixing is detected inside the solvent jet. This is the real reason that the particle size remains zero and it does not associate to the nucleation time. As a consequence, the nucleation time evaluated is probably overestimated by this method.

Method 2:

If we consider that the precipitation time is composed by the nucleation time and the particle growth time, we can calculate both characteristic times from the the final mean particle size \bar{d}_p , the mean growth rate \bar{G} and the critical size of nucleus r^* . The mean growth rate \bar{G} is averaged in the plane $y = 0$ and its small value does not change much among all the test cases (from $3.43 \cdot 10^{-5}$ to $5.28 \cdot 10^{-5}$ m/s). The critical radius of nucleus r^* can be calculated according to the classical nucleation theory:

$$r^* = \frac{2V_m\sigma}{k_b T \ln S} \quad (70)$$

with V_m the molecular volume in the nucleus, k_b the Boltzmann constant, σ the surface tension and S the supersaturation degree. We chose r^* here the smallest size of nuclei which corresponds to the highest value of the supersaturation degree.

The total precipitation time t_p is then considered to be the sum of the nucleation time

t_{n2} and the particle growth time t_{g2} . They can be estimated by:

$$t_{g2} = \frac{\overline{d_p} - 2r^*}{\overline{G}} \quad (71)$$

$$t_{n2} = t_p - t_{g2} \quad (72)$$

The critical radius of nuclei obtained is comprised between 1.13 and 2.15 nm for all tests. Based on the results of this method, the nucleation time t_{n2} is generally much higher than the growth time t_{g2} , almost close to the total precipitation time t_p . The reason is that the nucleation is favorable compared to the particle growth, with an extremely high nucleation rate B . Indeed the nucleation rate B decreases the supersaturation degree (only slightly higher than 1 because of the low concentration TPE in the initial solution). However, the t_{n2} does not correspond well to the mean particle size field (Figure 84), in which it is clear that the particles start to grow before the detected nucleation time t_{n2} . Additionally, the values of t_{n2} are even higher than t_{n1} which is already overestimated as mentioned above.

Method 3:

In the last method, the nucleation time is directly related to the average value of the nucleation rate \overline{B} . It is the global mean value of space and time in the simulated microchannel and is also given in Table 8 for all tested cases. We have taken the volume of the discretized cell ($V_{cell} = 3 \times 3 \times 3 \mu m^3$) as the considered volume and the characteristic nucleation time t_{n3} can be estimated this time:

$$t_{n3} = \frac{1}{\overline{B}V_{cell}} \quad (73)$$

This method provides reasonable nucleation time in term of the order of magnitude. By comparing the test No.3 to No.4, we can see that the nucleation kinetic is very sensitive to the solid-fluid surface tension σ . An slight increase of σ from 2.25 mN/m in No.3 to 2.75 mN/m in No.4 results in a t_{n3} variation of more than three times, from 0.006 ms to 0.020 ms. This small increase of σ raises the barrier energy to form nuclei, so that the nucleation rate \overline{B} in No.4 is lower with a longer characteristic time t_{n3} . The t_{n3} seems to be the most appropriate among the three methods, and we take it to compare the characteristic times of the fluid mixing and the nucleation.

To do that, we introduce here the dimensionless Damköhler number Da , often used to

relate the reaction rate to the species transport rate:

$$Da = \frac{\text{mixing time}}{\text{reaction time}} \quad (74)$$

We have calculated the Da number for both TPE precipitation (Da_p) and nucleation (Da_n), with t_m , t_p and t_{n3} in Table 8. We confirm and emphasize that our microreactor can provide a high efficient fluid mixing under μ SAS conditions with a very low Da number of precipitation Da_p , even for a relatively slow mixing (test No.2), indicating that the fluid mixing is much faster than the entire precipitation process. The mixture becomes homogeneous much before the end of particle growth. Regarding the nucleation time t_{n3} , the Da number is in the order of magnitude $o(1)$ for the tests of high flow rates (No.1, No.3 and No.4). The slower mixing due to the lower flow rates in No.2 has a high value of Da number, implying that when the nucleation occurs, the fluid mixture is far from the homogeneity. The lowest Da number is found for the test No.4, meaning that the fluid mixing is faster than the nucleation. Whereas, the particles yielded in this case have a mean size slightly bigger than the one of the reference case. This frustrating result can be related to the changed interfacial tension σ , which reduces the nucleation rate in the test No.4 and increases consequently the nucleation time. This makes the particle growth favorable with a relatively high supersaturation due to the higher TPE concentration (3 g/L in the tests No.3 and No.4, compared to 2 g/L in tests No.1 and No.2). It should be emphasized that it is more logical to consider the nucleation time for the estimation of the Da number to discuss the mixing effects. In general, an extremely fast mixing can be reached in our microreactor for the μ SAS process with a mixing time of the order of the magnitude of 10^{-5} s (0.01 ms). The same order of time is found for the nucleation but much smaller than the global precipitation time. Consequently, these conditions are very favorable to precipitate, through μ SAS conditions, the nanoparticles of TPE with a narrow particle size distribution.

4.5 Summary

In this chapter, we introduce first the experimental system to produce TPE nanoparticles by the μ SAS process in our microreactor. Some details of simulation are presented, as the numerical geometry, the boundary conditions and how we calculate the particle size and the size distribution. By comparing the simulation results to the experimental data, we have determined the solid-fluid interfacial tension σ , which is hardly to acquire by experimental

measurement. It seems that its value changes while the mixture composition varies. After the determination of the surface tension σ , the numerical model provides appropriate particle size d_p and size distribution, in good accordance with the experimental results. In order to have a deep insight in the mixing zone of the precipitation, some important fields have been analyzed numerically, namely: the mass fractions, the mixing time, the supersaturation and the mean particle size. We discussed the effects of fluid hydrodynamics and the initial TPE concentration on particle size. At last, we have evaluated the characteristic times of precipitation, nucleation and they have been compared to the mixing time determined under corresponding conditions in the microreactor. It has been demonstrated that the fluid mixing is an essential part in μ SAS precipitation and our microreactor can offer an extremely fast mixing with a mixing time down to 0.01 ms, at the same time order of the nucleation. It has been proven by both experiment and numerical modeling the high performance of the microreactor on fluid mixing and particle precipitation by μ SAS process.

General conclusion and perspectives

The SAS process is a key operation in powder technology, but one of the major issues is the poor understanding of the involved coupled phenomena, which directly control the nanoparticle characteristics. We proposed in this thesis to study the fundamental mechanisms for an intensified μ SAS process thanks to complementary numerical/experimental approaches.

The main objective of this thesis was therefore to examine and to quantify the mixing behaviors under SAS process conditions inside a microfluidic reactor. Especially, to do the proof that the μ SAS offers very favorable conditions for the supercritical antisolvent process, attentions have been paid on capturing micromixing for turbulent conditions at lengths between the Kolmogorov scale and the Batchelor scale. Our main works and contributions are listed below.

- The microfabrication of a home-made microreactor has been carried out to perform a coflow fluid mixing. Both laminar and turbulent conditions have been tested in this microreactor under high pressure up to 150 bar.
- Thanks to the semi-transparency of the microreactor, we can perform *in situ* measurements. Micro Particle Image Velocimetry (μ PIV) characterization technique provided an opportunity to access the fluid velocity fields in microchannels, while high pressure turbulent mixing filmed by a high speed camera gave qualitatively evidence on the microreactor capacity for efficient mixing.
- In the largely reduced microchannel, it has been possible to model the fluid mixing and the involved phenomena through a direct numerical simulation (DNS) down to micromixing scales of few micrometers. This numerical model has been validated by comparing the velocity field calculated in the simulations to the μ PIV experimental measurements in laminar conditions.
- The DNS for turbulent conditions has been also proven robust through a convergence study. The Kolmogorov scale and the Batchelor microscale have been estimated numerically. The energy dissipation rate due to turbulence has been calculated directly by the velocity fluctuations, allowing the estimation of the micromixing time from the theoretical relation.

- With the segregation intensity extracted from the simulation, a mixing time has been proposed to characterize the mixing efficiency. The influence of mixing conditions has been analyzed according to the obtained mixing times, which are close to their theoretical values.
- Finally, the CFD model has been combined with a common used precipitation model to simulate nucleation and particle growth. The obtained particle size and size distribution from simulations have been then compared to experimental results, conducted by Thomas Jahouari, a Ph.D. student in the group.

The originality of this thesis work was to offer insights in micromixing under SAS conditions by both experiments and numerical methods. Thanks to verified simulation results on thermal-hydrodynamics of mixing, we are capable of providing correct process parameter effects and predicting precise properties of precipitates in our microreactor.

However, some issues still remain unverified and need to be discussed in the future work:

- Additional experimental results are required to verify the relation between the composition of TPE and the surface tension σ . As we mentioned in Chapter 4, a slight increase of the surface tension may be associated to the initial concentration of TPE in the solvent THF (from 2 to 3 g/L). Because of the difficulty to measure directly the value of the surface tension in the μ SAS experiments, their relation should be analyzed by both experimental method and numerical simulation.
- Other systems solute/solvent with much greater solubility have to be tested to confirm the hydrodynamic effects of the μ SAS process. Due to the low solubility of TPE in THF, the thermodynamic has strong effects on the precipitated particles. The particle sizes are not sensible enough to the hydrodynamic conditions. Other solutes and solvents should be taken into consideration and in those systems, the solubility should be much higher than the TPE solution in the THF. It will provide potentially a large variation of the supersaturation degree depending on the fluid mixing conditions.
- A scale-up study will be performed by HPC simulation. The aim of this simulation will be to propose the same description of the mixing (down to Kolmogorov scale) but for larger volume. We can eventually compare our model of the direct numerical simulation to other turbulent models and conventional micromixing models. Through

these comparisons, we will be able to prove the capture of the micromixing in our numerical model even for regular sized reactors.

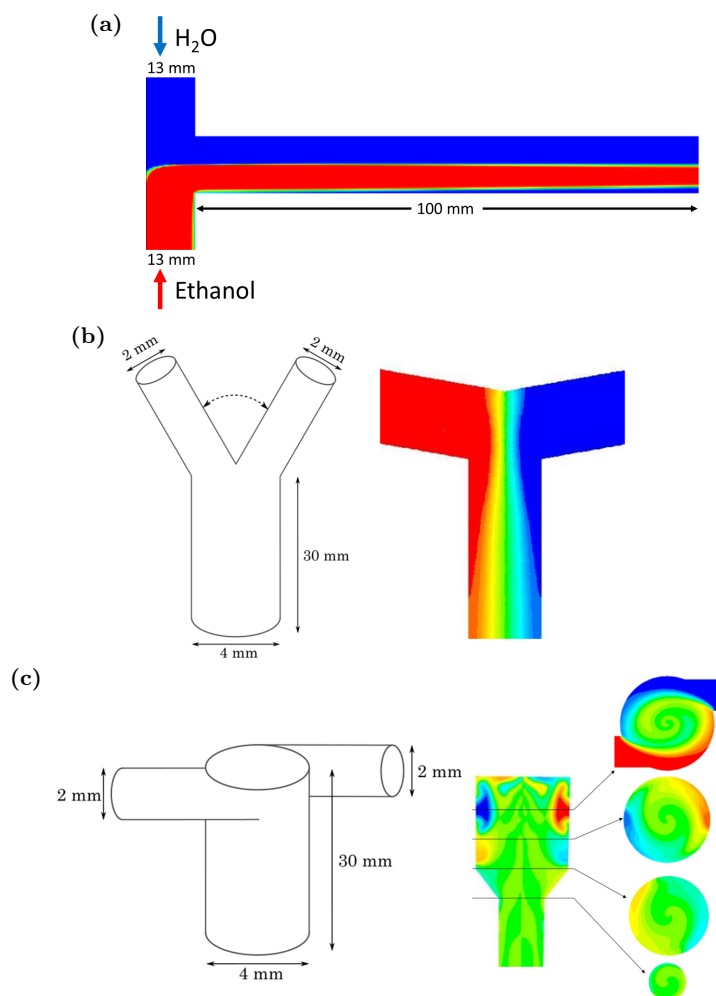


Figure 86: Simulations of other types of mixing: (a). the mixing of ethanol and water by an impinging flow; (b). the mixing of two fluids with the same properties as the water in a Y-mixer (Kirchner, 2015); (c). the mixing of two fluids with the same properties as water in a Hartridge-Roughton mixer (Kirchner, 2015).

- The simulation could be used to design the reactor based on the mixing quality. Since the TPE precipitations by the μ SAS process were completed within 1 mm (the distance from the capillary injector outlet) in our microreactor, the actual design can be improved by reducing the main channel length. The saved materials can be used to fabricate more microreactor with smaller sizes to yield a considerable production. Additionally, the mixing configuration can be modified and thus, the mixing performance of other types of micromixers can be examined numerically via our model. A 2D simulation has been already performed by using Notus code for a laminar mixing of

ethanol and water by an impinging flow at 25 °C and 1 bar (Figure 86a). Simulation studies for other geometries (Y mixer and Hartridge-Roughton mixer) are illustrated in Figure 86b, 86c (Kirchner, 2015).

References

- Amiroudine, S., Caltagirone, J.P., Erriguible, A., 2014. A Lagrangian-Eulerian compressible model for the trans-critical path of near-critical fluids. *Int. J. Multiph. Flow* 59, 15-23.
- Badens, E., Boutin, O., Charbit, G., 2005. Laminar jet dispersion and jet atomization in pressurized carbon dioxide. *J. Supercrit. Fluids* 36, 81-90.
- Baldyga, J., Bourne, J.R., 1984. A fluid mechanical approach to turbulent mixing and chemical reaction part II micromixing in the light of turbulence theory. *Chem. Eng. Commun.* 28, 243-258.
- Baldyga, J. and Bourne, J. R., 1988, Calculation of micromixing in inhomogeneous stirred tank reactors. *Chem. Eng. Res. Des.* 66, 33-38.
- Baldyga, J., Bourne, J.R., 1989. Simplification of micromixing calculations I. derivation and application of new model. *Chem. Eng. J.* 42, 83-92.
- Baldyga, J., Bourne, J.R., 1990, Comparison of the engulfment and the interaction-by-exchange-with-the-mean micromixing models. *Chem. Eng. J.* 45, 25-31.
- Baldyga, J., Bourne, J.R., Zimmermann, B., 1994. Investigation of mixing in jet reactors using fast, competitive-consecutive reactions. *Chem. Eng. Sci.* 49, 1937.
- Baldyga, J., Kubicki, D., Shekunov, B.Y., Smith, K.B., 2010. Mixing effects on particle formation in supercritical fluids. *Chem. Eng. Res. Des.* 88, 1131-1141.
- Bassing, D., Braeuer, A., 2017. The lag between micro- and macro-mixing in compressed fluid flows. *Chem. Eng. Sci.* 163, 105-113.
- Beckman, E.J., 2004. Supercritical and near-critical CO₂ in green chemical synthesis and processing. *J. Supercrit. Fluids* 28, 121-191.
- Boutin, O., Maruejols, C., Charbit, G., 2007. A new system for particle formation using the principle of the SAS process: The Concentric Tube antisolvent Reactor. *J. Supercrit. Fluids* 40, 443.
- Boutin, O., Petit-Gas, T., Badens, E., 2009. Powder Micronization Using a CO₂ Supercritical Antisolvent Type Process: Comparison of Different Introduction Devices. *Ind. Eng. Chem. Res.* 48, 5671-5678.
- Boutin, O., 2012. Influence of introduction devices on crystallisation kinetic parameters in a supercritical antisolvent process. *J. Cryst. Growth* 342, 13-20.
- Braeuer, A., Dowy, S., Schatz, R., Rossmann, M., Schluecker, E., Leipertz, A., 2010. Supercritical Antisolvent Particle Precipitation: In Situ Optical Investigations. *Chem. Eng. Technol.*, 33, No. 1, 35-38.
- Braeuer, A., Adami, R., Dowy, S., Rossmann, M., Leipertz, A., 2011a. Observation of liquid solution volume expansion during particle precipitation in the supercritical CO₂ antisolvent process. *J. Supercrit. Fluids* 56, 121-124.
- Braeuer, A., Dowy, S., Torino, E., Rossmann, M., Luther, S.K., Schluecker, E., Leipertz, A., Reverchon, E., 2011b. Analysis of the supercritical antisolvent mechanisms governing particles precipitation and morphology by in situ laser scattering techniques. *Chem. Eng.*

J. 173, 258–266.

Cahn, J.W., 1977. Critical point wetting. *J. Chem. Phys.* 66, 3667-3672.

Calvignac, B., Boutin, O., 2009. The impinging jets technology: a contacting device using a SAS process type. *Powder Technol.* 191, 200–205.

Campardelli, R., Reverchon, E., De Marco, I., 2017. Dependence of SAS particle morphologies on the ternary phase equilibria. *J. Supercrit. Fluids* 130, 273–281.

« Carbon dioxide ». Immediately Dangerous to Life and Health Concentrations (IDLH). National Institute for Occupational Safety and Health (NIOSH).

Careno, S., Boutin, O., Badens, E., 2012. Drug recrystallization using supercritical anti-solvent (SAS) process with impinging jets: Effect of process parameters. *J. Cryst. Growth* 342, 34–41.

Carretier, E., Wyart, Y., Guichardon, P., Badens, E., Boutin, O., Vallejos, J.C., Charbit, G., 2006. New insight into micromixing in supercritical CO₂ using a chemical method. *J. Supercrit. Fluids* 38, 332–338.

Chang, S., Lee, M., Lin, H., 2008. Role of phase behavior in micronization of lysozyme via a supercritical anti-solvent process. *Chem. Eng. J.* 139, 416–425.

Christensen, J.J., Cordray, D.R., Oscarson, J.L., Izatt, R.M., 1988. The excess enthalpies of four carbon dioxide + an alcohol mixtures from 308.15 to 573.15 K at 7.50 to 12.50 MPa. *J. Chem. Thermodyn.* 20, 867– 875.

Cocero, M.J., Ferrero, S., Miguel, F., 2002. Crystallization of b-carotene by continuous gas process. Effect of mixer on crystals formation. In: 4th International symposium on high pressure process technology and chemical engineering. Venice, Italy.

Commenge, J.M., Falk, L, 2011. Villermaux-Dushman protocol for experimental characterization of micromixers. *Chem. Eng. Process.* 50(10), 979-990.

Cooper, A.I., 2000. Polymer synthesis and processing using supercritical carbon dioxide. *J. Mater. Chem.* 10, 207–234.

Cordray, D.R., Christensen, J.J., Izatt, R.M., 1987. A Calorimetric Method for the Determination of Binary Phase Compositions at High Temperatures and Pressures. *Sep. Sci. Technol.* 22, 1169-1181.

Cordray, D.R., Izatt, R.M., Christensen, J.J., Oscarson, J.L., 1988a. The excess enthalpies of (carbon dioxide + ethanol) at 308.15, 325.15, 373.15, 413.15, and 473.15 K from 5.00 to 14.91 MPa. *J. Chem. Thermodynamics* 20, 655-663.

Cordray, D.R., Christensen, J.J., Izatt, R.M., Oscarson, J.L., 1988b. The excess enthalpies of (carbon dioxide + toluene) at 390.15, 413.15, 470.15, and 508.15 K from 7.60 to 17.50 MPa. *J. Chem. Thermodynamics* 20, 877–888.

Cordray, D.R., Izatt, R.M., Christensen, J.J., 1988c. The excess enthalpies of (carbon dioxide + cyclohexane) at 390.15, 413.15, 438.15, 498.15 and 508.15 K from 7.50 to 14.39 MPa. *J. Chem. Thermodynamics* 20, 225–234.

Costa, P. and Trevisoi, C., 1972, Reactions with non-linear kinetics in partially segregated fluids. *Chem. Eng. Sci.* 27, 2041-2054.

- Couto, R., Chambon, S., Aymonier, C., Mignard, E., Pavageau, B., Erriguible, A., Marre, S., 2015. Microfluidic supercritical antisolvent continuous processing and direct spray coating of poly(3-hexylthiophene) nanoparticles for OFET devices. *Chem. Commun.* 51(6), 1008–1011.
- Danckwerts, P.V., 1958. The effect of incomplete mixing on homogeneous reactions. *Chem. Eng. Sci.* 8(1-2), 93-102.
- Davila, M.J., Cabañas, A., Pando, C., 2007. Excess molar enthalpies for binary mixtures related to supercritical antisolvent precipitation: Carbon dioxide+N-methyl-2-pyrrolidone. *J. Supercrit. Fluids* 42, 172–179.
- Day, C.-Y., Chang, C.J., Chen, C.-Y., 1996. Phase equilibrium of ethanol + CO₂ and acetone + CO₂ at elevated pressures. *J. Chem. Eng. Data* 41, 839-843.
- De Marco, I., Reverchon, E., 2011. Influence of pressure, temperature and concentration on the mechanisms of particle precipitation in supercritical antisolvent micronization. *J. Supercrit. Fluids* 58, 295–302.
- De Marco, I., Rossmann, M., Prosapio, V., Reverchon, E., Braeuer, A., 2015. Control of particle size, at micrometric and nanometric range, using supercritical antisolvent precipitation from solvent mixtures: Application to PVP. *Chem. Eng. J.* 273, 344–352.
- Debenedetti, P.G., 1990. Homogeneous nucleation in supercritical fluids. *AIChE J.* Vol. 36, No. 9, 1289-1298.
- "Dimethyl Sulfoxide (DMSO) – Technical". Atofina Chemicals, inc. Retrieved 26 May 2007.
- Dowy, S., Braeuer, A., Schatz, R., Schluucker, E., Leipertz, A., 2009. CO₂ partial density distribution during high-pressure mixing with ethanol in the supercritical antisolvent process. *J. Supercrit. Fluids*, 48, 195-202.
- Duke, S.D., 2003. Particle Retention Testing of 0.05 to 0.5 Micrometer Membrane Filters. Technical Note: TN-020.03. Thermo Fisher Scientific.
- Elliott, J.R., Lira, C.T., 2012. *Introductory Chemical Engineering: Thermodynamics*, 2nd ed., Prentice Hall.
- Erriguible, A., Vincent, S., Subra-Paternault, P., 2012. Numerical investigations of liquid jet breakup in pressurized carbon dioxide: Conditions of two-phase flow in Supercritical Antisolvent Process. *J. Supercrit. Fluids* 63, 16-24.
- Erriguible, A., Laugier, S., Late, M., Subra-Paternault, P., 2013a. Effect of pressure and non-isothermal injection on re-crystallization by CO₂ antisolvent: solubility measurements, simulation of mixing, and experiments. *J. Supercrit. Fluids* 76, 115–125.
- Erriguible, A., Fadli, T., Subra-Paternault, P., 2013b. A complete 3D simulation of a crystallization process induced by supercritical CO₂ to predict particle size. *J. Comput. Chem. Eng.* 52, 1–9.
- Erriguible, A., Neurohr, C., Revelli, A.L., Laugier, S., Fevotte, G., Subra-Paternault, P., 2015. Cocrystallization induced by compressed CO₂ as antisolvent: Simulation of a batch process for the estimation of nucleation and growth parameters. *J. Supercrit. Fluids* 98, 194–203.

- Escobedo-Alvarado, G.N., Sandler, S.I., 2001. Prediction of Excess Enthalpies Using a Gex/EOs Model. *Ind. Eng. Chem. Res.* 40, 1261-1270.
- Falgout, R.D., Yang, U.M., 2002. hypre: A library of high performance preconditioners. In: *Proceedings of the international conference on computational science*. Springer, 632-41.
- Falk, L., Commenge, J.M., 2010. Performance comparison of micromixers. *Chem. Eng. Sci.*, 65(1), 405-411.
- Giufreda, W.M., Favareto, R., Cabral, V.F., Meireles, M.A.A., Cardozo-Filho, L., Corazza, M.L., 2010. High-Pressure Vapor-Liquid Equilibrium Data for Ternary Systems CO₂ + Organic Solvent + Curcumin. *Open Chem. Eng. J.* 4, 3-10.
- Goda, K., 1979. A multistep technique with implicit difference schemes for calculating two- or three-dimensional cavity flows. *J. Comput. Phys.* 30 (1), 76-95.
- Guichardon, P., Falk, L., 2000. Characterisation of micromixing efficiency by the iodide-iodate reaction system. Part I. Experimental procedure. *Chem. Eng. Sci.* 55, 4233-4243.
- Guichardon, P., Falk, L., Villermaux, J., 2000. Characterisation of micromixing efficiency by the iodide-iodate reaction system. Part II. Kinetic study. *Chem. Eng. Sci.* 55, 4245-4253.
- Harada, M., 1962, Micromixing in a continuous flow reactor (coalescence and redispersion models). *The Memoirs of the Faculty of Engineering. Kyoto University* 24, 431.
- He, P., Raghavan, A., Ghoniem, A.F., 2015. Impact of non-ideality on mixing of hydrocarbons and water at supercritical or near-critical conditions. *J. Supercrit. Fluids* 102, 50-65.
- He, P., Ghoniem, A.F., 2017. A sharp interface method for coupling multiphase flow, heat transfer and multicomponent mass transfer with interphase diffusion. *J. Comput. Phys.* 332, 316-332.
- He, P., Ghoniem, A.F., 2018. Phase separation during mixing of partially miscible fluids under near-critical and supercritical conditions, and the phenomenon of uphill diffusion. *J. Supercrit. Fluids* 135, 105-119.
- Johnson, B.K., Prud'homme, R.K., 2003. Chemical Processing and Micromixing in Confined Impinging Jets. *AIChE J.* 49, No. 9.
- Jung, J., Perrut, M., 2001. Particle design using supercritical fluids: Literature and patent survey. *J. Supercrit. Fluids* 20, 179-219.
- Kalani, M., Yunus, R., 2011. Application of supercritical antisolvent method in drug encapsulation: a review. *Int. J. Nanomedicine* 6, 1429-1442.
- Kirchner, S., 2015. Approche multi-échelle de l'agrégation dans le procédé de précipitation de boehmite. PhD thesis, Université de Toulouse.
- Kolmogorov, A.N., 1941. The local structure of hit turbulence in incompressible viscous fluid for very large Reynolds numbers. *Dokl Akad Nauk SSSR* 30, 299-304.
- Lemenand, L., Della Valle, D., Habchi, C., Peerhossaini, H., 2017. Micro-mixing measurement by chemical probe in homogeneous and isotropic turbulence. *Chem. Eng. J.* 314, 453-465.

- Lengsfeld, C.S., Delplanque, J.P., Barocas, V.H., Randolph, T.W., 2000. Mechanism Governing Microparticle Morphology during Precipitation by a Compressed Antisolvent: Atomization vs Nucleation and Growth. *J. Phys. Chem. B* 104, 2725-2735.
- Li, W., Xia, F., Qin, H., Zhang, M., Li, W., Zhang, J., 2019. Numerical and experimental investigations of micromixing performance and efficiency in a pore-array intensified tube-in-tube microchannel reactor. *Chem. Eng. J.* 370, 1350–1365.
- Liu, Z.W., Guo, L., Huang, T.H., Wen, L.X., Chen, J.F., 2014. Experimental and CFD studies on the intensified micromixing performance of micro-impinging stream reactors built from commercial T-junctions. *Chem. Eng. Sci.* 119, 124–133.
- Loppinet-Serani, A., Aymonier, C., Cansell, F., 2010. Supercritical water for environmental technologies. *J. Chem. Technol. Biotechnol.* 85, 583-589.
- Machlin, E.S., 2007. *An Introduction to Aspects of Thermodynamics and Kinetics Relevant to Materials Science (Third Edition)*.
- Majer, V., Svoboda, V., 1985. *Enthalpies of Vaporization of Organic Compounds: A Critical Review and Data Compilation*. Blackwell Scientific Publications, Oxford, 300.
- Marra, F., De Marco, I., Reverchon, E., 2012. Numerical analysis of the characteristic times controlling supercritical antisolvent micronization. *Chem. Eng. Sci.* 71, 39–45.
- Marre, S., Adamo, A., Basak, S., Aymonier, C., Jensen, K.F., 2010. Design and packaging of microreactors for high pressure and high temperature applications. *Ind. Eng. Chem. Res.* 49(22), 11310–11320.
- Martin, A., Cocero, M.J., 2008. Micronization processes with supercritical fluids: Fundamentals and mechanisms. *Adv. Drug Deliv. Rev.* 60, 339–350.
- Mersmann, A., 2001. *Crystallization technology handbook*. New York: Marcel Dekker Inc.
- Metzger, L., 2017. *Process Simulation of Technical Precipitation Processes The Influence of Mixing*. PhD thesis, Karlsruhe Institute of Technology.
- Miguel, F., Martin, A., Mattea, F., Cocero, M.J., 2008. Precipitation of lutein and coprecipitation of lutein and poly-lactic acid with the supercritical anti-solvent process. *Chem. Eng. Process.* 47, 1594–1602.
- Montes, A., Pereyra, C., Martinez de la Ossa, E.J., 2015. Screening design of experiment applied to the supercritical antisolvent precipitation of quercetin. *J. Supercrit. Fluids* 104, 10–18.
- Mukhopadhyay, M., Dalvi, S.V., 2005. Analysis of supersaturation and nucleation in a moving solution droplet with flowing supercritical carbon dioxide. *J. Chem. Technol. Biotechnol.* 80, 445–454.
- Neurohr, C., Erriguible, A., Laugier, S., Subra-Paternault, P., 2016. Challenge of the supercritical antisolvent technique SAS to prepare cocrystal-pure powders of naproxen-nicotinamide. *Chem. Eng. J.* 303, 238–251.
- NIST (National Institute of Standards and Technology).
<<http://www.webbook.nist.gov/chemistry/>>.
- Ouyang, Y., Xiang, Y., Zou, H.K., Chu, G.W., Chen, J.F., 2017. Flow characteristics and

- micromixing modeling in a microporous tube-in-tube microchannel reactor by CFD. *Chem. Eng. J.* 321, 533–545.
- Peng, D.Y., Robinson, D.B., 1976. A new two-constant equation of state. *Ind. Eng. Chem. Fundam.* 15, 59–63.
- Petit-Gas, T., Boutin, O., Raspo, I., Badens, E., 2009. Role of hydrodynamics in supercritical antisolvent processes. *J. Supercrit. Fluids* 51, 248–255.
- Prosapio, V., Reverchon, E., De Marco, I., 2015. Control of Powders Morphology in the Supercritical Antisolvent Technique Using Solvent Mixtures. *Chem. Eng. Trans.* 43, 763–768.
- Puel, F., Veessler, S., Mangin, D., 2005. *Cristallisation – Aspects théoriques*. Techniques de l'Ingénieur.
- Reid, R.C., Prausnitz, J.M., Sherwood TK (1977). *The properties of gases and liquids*. McGraw-Hill, New York. doi: 10.1002/aic.690240634
- Reverchon, E., De Marco, I., 2006. Supercritical fluid extraction and fractionation of natural matter. *J. Supercrit. Fluids* 38, 146–166.
- Reverchon, E., Torino, E., Dowy, S., Braeuer, A., Leipertz, A., 2010. Interactions of phase equilibria, jet fluid dynamics and mass transfer during supercritical antisolvent micronization. *Chem. Eng. J.* 156, 446–458.
- Roe, P.L., 1986. Characteristic-based schemes for the Euler equations. *Annu. Rev. Fluid Mech.* 18, 337–365.
- Rossmann, M., Braeuer, A., Schluecker, E., 2014. Supercritical antisolvent micronization of PVP and ibuprofen sodium towards tailored solid dispersions. *J. Supercrit. Fluids* 89, 16–27.
- Sahena, F., Zaidul, I.S.M., Jinap, S., Karim, A.A., Abbas, K.A., Norulaini, N.A.N., Omar, A.K.M., 2009. Application of supercritical CO₂ in lipid extraction - A review. *J. Food Eng.* 95(2), 240-253.
- Sánchez, F.A., He, P., Ghoniem, A.F., Pereda, S., 2019. Modeling hydrocarbon droplet dissolution in near-critical or supercritical water using GCA-EOS and non-ideal diffusional driving force in binary mixtures. *J. Supercrit. Fluids* 146, 1-14.
- Sharma, D., Erriguible, A., Gandikota, G., Beysens, D., Amiroudine, S., 2019. Vibration-induced thermal instabilities in supercritical fluids in the absence of gravity. *Phys. Rev. Fluids* 4, 033401.
- Silva, E.K., Meireles, M.A.A., 2014. Encapsulation of Food Compounds Using Supercritical Technologies: Applications of Supercritical Carbon Dioxide as an Antisolvent. *Food and Public Health* 4(5), 247-258.
- Shekunov, B.Yu., Baldyga, J., York, P., 2001. Particle formation by mixing with supercritical antisolvent at high Reynolds numbers. *Chem. Eng. Sci.* 56, 2421.
- Sierra-Pallares, J., Marchisio, D.L., Parra-Santos, M.T., Garcia-Serna, J., Castro, F., Cocero, M.J., 2012. A Computational Fluid Dynamics Study of Supercritical Antisolvent Precipitation: Mixing Effects on Particle Size. *AIChE J.* 58, 385–398.

- Sierra-Pallares, J., Raghavan, A., Ghoniem, A.F., 2016. Computational study of organic solvent–CO₂ mixing in convective supercritical environment under laminar conditions Impact of enthalpy of mixing. *J. Supercrit. Fluids* 109, 109–123.
- Sullivan, D., 1981. Surface tension and contact angle of a liquid–solid interface. *J. Chem. Phys.* 74, 2604-2615.
- Sun, Y., Shekunov, B.S., 2003. Surface tension of ethanol in supercritical CO₂. *J. Supercrit. Fluids* 27 (1), 73-83.
- Thorat, A.A., Dalvi, S.V., 2012. Liquid antisolvent precipitation and stabilization of nanoparticles of poorly water soluble drugs in aqueous suspensions: Recent developments and future perspective. *Chem. Eng. J.* 181-182, 1-34.
- Villiermaux, J. and Devillon, J. C., 1972. Représentation de la coalescence et de la redispersion des domaines de ségrégation dans un fluide par un modèle d’interaction phénoménologique, in *Proceed, 2nd Inc. Symp. Chem. React. Eng. Amsterdam B*, 1-13.
- Villiermaux, J., Falk, L., 1994. A generalized mixing model for initial contacting of reactive fluids. *Chem. Eng. Sci.* 49, 5127-5140.
- Voisin, T., Erriguible, A., Philippot, G., Ballenghien, D., Mateos, D., Cansell, F., Iversen, B.B., Aymonier, C., 2017. Investigation of the precipitation of Na_2SO_4 in supercritical water. *Chem. Eng. Sci.* 174, 268-276.
- Wilke, C.R., Chang, P., 1955. Correlation of diffusion coefficients in dilute solutions. *AIChE J.* 1(2), 264–270.
- Zahran, F., Pando, C., Renuncio, J.A.R., Cabañas, A., 2010. Excess Molar Enthalpies of CO₂ + Acetone at Pressures from (9.00 to 18.00) MPa and Temperatures from (313.15 to 333.15) K. *J. Chem. Eng. Data* 55, 3649–3654.
- Zahran, F., Pando, C., Renuncio, J.A.R., Cabañas, A., 2012. Excess molar enthalpies for mixtures of supercritical CO₂ and ethyl acetate and their role in supercritical fluid applications. *J. Chem. Thermodynamics* 51, 59–64.
- Zhang, F., Erriguible, A., Gavaille, T., Timko, M.T., Marre, S., 2018. Inertia-driven jetting regimes in microfluidic coflows, *Phys. Rev. Fluids* 3, 092201(R).
- Zhang, F., Erriguible, A., Marre, S., 2019a. Investigating laminar mixing in high pressure microfluidic systems, *Chem. Eng. Sci.* 205, 25–35.
- Zhang, F., Marre, S., Erriguible, A., 2019b. Mixing intensification under turbulent conditions in a high pressure microreactor. *Chem. Eng. J.* <https://doi.org/10.1016/j.cej.2019.122859>

Appendix I: Complementary details

(1). Solution of the Peng-Robinson equation of state

For a binary mixture, the Peng-Robinson equation of state is transformed in cubic equation:

$$Z^3 + c_2Z^2 + c_1Z + c_0 = 0$$

with c_0 , c_1 , c_2 coefficients of the cubic equation and Z is the compressibility factor, defined as:

$$Z = \frac{pV_m}{RT}$$

The V_m is the molar volume of the mixture.

The coefficients c_0 , c_1 , c_2 of the cubic equations can be calculated by:

$$\begin{aligned}c_2 &= B - 1 \\c_1 &= -3B^2 - 2B + A \\c_0 &= B^3 + B^2 - AB\end{aligned}$$

The parameters A and B can be determined by:

$$\begin{aligned}A &= \frac{a_m p}{R^2 T^2} \\B &= \frac{b_m p}{RT}\end{aligned}$$

with a_m the attraction parameter and b_m the covolume parameter of the binary system in the Peng-Robinson equation, presented previously in Chapter 2 (Equation 7).

For a mixture above its critical point, only one solution exists for the cubic equation because the two fluids are completely miscible in one phase. As a consequence, by solving the cubic equation, one can obtain the solution Z then the molar volume and the density of the mixture.

(2). Fugacity coefficient estimation

The fugacity coefficient of a species i $\hat{\varphi}_i$ can be calculated from the Peng-Robinson equation of state with the one-fluid mixing rules (Elliott and Lira, 2012; He *et al.*, 2015):

$$\ln(\hat{\varphi}_i) = -\ln \left[Z \left(1 - \frac{b_m}{V_m} \right) \right] + \frac{b_i}{b_m} (Z - 1) - \frac{a_m}{\sqrt{8}b_m RT} \left(\frac{1}{a_m} \frac{\partial a_m}{\partial x_i} - \frac{b_i}{b_m} \right) \ln \left[\frac{V_m + (1 + \sqrt{2}) b_m}{V_m + (1 - \sqrt{2}) b_m} \right]$$

with a_m , b_m the attraction parameter and the covolume parameter of the binary system in the Peng-Robinson equation, respectively, b_i the parameter of the species i , x_i the molar fraction of the species i , Z the compressibility factor and V_m the molar volume of the mixture.

For a mixture, we should calculate the partial derivatives of the fugacity coefficients in the non-ideal diffusion model (He *et al.*, 2015):

$$\begin{aligned} \left(\frac{\partial \ln \hat{\varphi}_i}{\partial x_j} \right)_{T,P} &= -\frac{(\partial V_m / \partial x_j) - b_j}{V_m - b_m} - \frac{b_i b_j}{b_m^2} (Z - 1) + \frac{b_i Z}{b_m V_m} \frac{\partial V_m}{\partial x_i} \\ &\quad - \frac{a_m [b_j V_m - b_m (\partial V_m / \partial x_j)] [(1/a_m) (\partial a_m / \partial x_i) - (b_i / b_m)]}{RT b_m V^*} \\ &\quad - \frac{1}{2\sqrt{2}RT b_m} \left(\frac{\partial^2 a_m}{\partial x_i \partial x_j} - \frac{b_j}{b_m} \frac{\partial a_m}{\partial x_i} - \frac{b_i}{b_m} \frac{\partial a_m}{\partial x_j} + \frac{2a_m b_i b_j}{b_m^2} \right) \ln \left[\frac{V_m + (1 + \sqrt{2}) b_m}{V_m + (1 - \sqrt{2}) b_m} \right] \end{aligned}$$

where

$$V^* = V_m^2 + 2b_m V_m - b_m^2$$

The partial derivatives of the fugacity coefficients can now be calculated for the binary mixture of CO₂-ethanol to verify the non-ideal diffusion effects in the CFD model.

(3). Verification of the numerical estimation of the turbulent energy dissipation rate ϵ

We propose to compare the numerical estimation of ϵ with an analytical solution calculated for a known velocity field given by:

$$u_x = \sin(x) \sin(y)$$

$$v_y = \sin(y) \sin(z)$$

$$w_z = \sin(z) \sin(x)$$

with u_x , v_y , w_z the velocity components in the x, y and z directions, respectively. Their partial derivatives are given by:

$$\frac{\partial u_x}{\partial x} = \cos(x) \sin(y) \quad \frac{\partial u_x}{\partial y} = \sin(x) \cos(y) \quad \frac{\partial u_x}{\partial z} = 0$$

$$\frac{\partial v_y}{\partial x} = 0 \quad \frac{\partial v_y}{\partial y} = \cos(y) \sin(z) \quad \frac{\partial v_y}{\partial z} = \sin(y) \cos(z)$$

$$\frac{\partial w_z}{\partial x} = \sin(z) \cos(x) \quad \frac{\partial w_z}{\partial y} = 0 \quad \frac{\partial w_z}{\partial z} = \cos(z) \sin(x)$$

The analytical value of the energy dissipation rate ϵ_a is finally obtained:

$$\begin{aligned} \epsilon_a = \nu \cdot & (2 \cos^2(x) \sin^2(y) + \sin^2(z) \cos^2(x) + \sin^2(x) \cos^2(y) \\ & + 2 \cos^2(y) \sin^2(z) + \sin^2(y) \cos^2(z) + 2 \cos^2(z) \sin^2(x)) \end{aligned}$$

with ν the CO₂ kinematic viscosity at the tested conditions.

Table 9: The difference between the analytical and the numerical values $|\epsilon_n - \epsilon_a|$ at the origin point (0, 0, 0) for different meshes.

Number of cells	$ \epsilon_n - \epsilon_a $
512 (8^3)	0.034067
4096 (16^3)	0.008721
32768 (32^3)	0.002193
262144 (64^3)	0.000549
2097152 (128^3)	0.000137

In Figure 87, we compare the evolution of the error between the numerical and analytical estimations. As expected, we found a slope of convergence of -2 which corresponds to the order of the discretization scheme of the velocity.

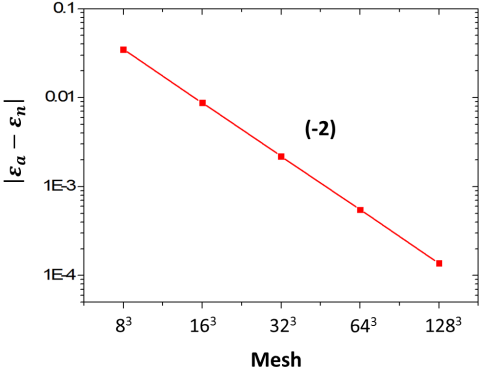


Figure 87: The difference between the analytical and the numerical values of the energy dissipation rate ϵ as a function of the mesh size.

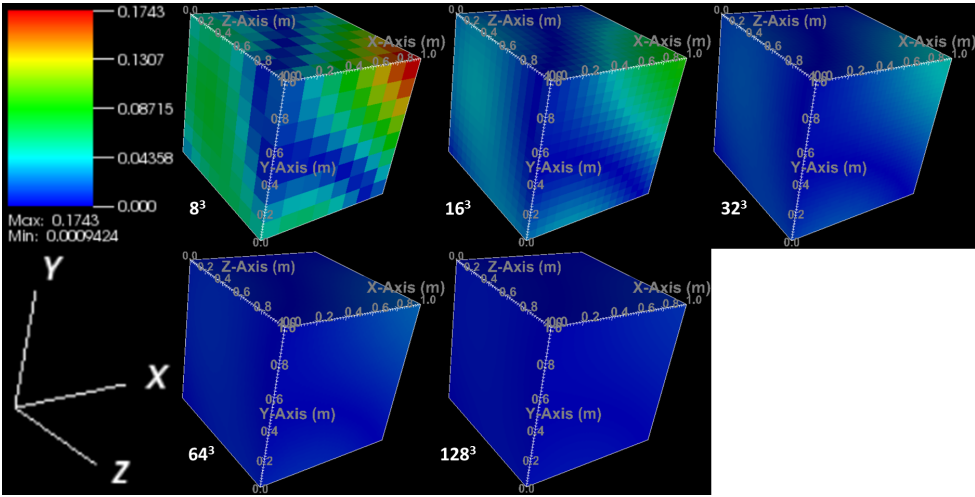


Figure 88: The difference between the analytical and the numerical values of the energy dissipation rate $|\epsilon_n - \epsilon_a|$ in the simulation domain.

Appendix II: Inertia-driven jetting regimes in microfluidic coflows

Inertia-driven jetting regimes in microfluidic coflowsFan Zhang,¹ Arnaud Erriguible,^{1,2,*} Théo Gavaille,^{1,3} Michaël T. Timko,⁴ and Samuel Marre^{1,†}¹*CNRS, Université Bordeaux, Bordeaux INP, ICMCB, UMR 5026, F-33600 Pessac, France*²*CNRS, Université Bordeaux, I2M, UMR 5295, F-33600 Pessac, France*³*IFPEN, 1 & 4, Avenue de Bois-Préau, 92852 Rueil-Malmaison, France*⁴*Department of Chemical Engineering, Worcester Polytechnic Institute, 100 Institute Road, Worcester, Massachusetts 01609, USA*

(Received 4 May 2018; published 17 September 2018)

Microfluidics have been used extensively for the study of flows of immiscible fluids, with a specific focus on the effects of interfacial forces on flow behavior. In comparison, inertia-driven flow of confined coflowing fluids has received scant attention at the microscale, despite the fact that the effects of microscale confinement are expected to influence inertia-driven flow behavior as observed in free jets. Herein, we report three distinct modes for breakup of coflowing, confined, microscale jets: the conventional Rayleigh mode and two additional inertia-driven modes occurring at higher Reynolds number flows, namely, a sinuous wave breakup and an atomizationlike mode. Each of the three modes is differentiated by a characteristic droplet size, size distribution, and dependence of the jet length as a function of the external fluid velocity (v_{ext}). A unified phase diagram is proposed to categorize the jet breakup mechanisms and their transitions using, as a scale-up factor, the ratio of the jet inertial forces to the sum of the viscous and interfacial forces for both the inner and outer fluids. These results provide fundamental insights into the flow behavior of microscale-confined coflowing jets.

DOI: [10.1103/PhysRevFluids.3.092201](https://doi.org/10.1103/PhysRevFluids.3.092201)

Droplets and jets are of primary importance for applications such as generation of emulsions with sub-micron scale droplets, sprays, and other multiphase flows, all of which are involved in a wide variety of chemical and industrial processes. Multiphase flows have been especially useful to the microfluidics community since dripping and jetting can be used to generate nearly monodisperse droplets that act as nanoliter reactors in series to ensure precise control of residence time and residence time distributions, with enhancing mixing [1]. Such approaches have been extensively used for microfluidics applications including foam generation [2–4], droplets-based microfluidics [5], jet stabilization [6,7], organic and inorganic micro- and nanostructures synthesis [8], and chemical reactions [9,10].

Jets are metastable hydrodynamic structures, which eventually break into droplets. Jet breakup is a well-known behavior, which occurs via various mechanisms, depending on the properties (velocity, density, viscosity, surface tension, etc.) of the fluid forming the jets and of the outer fluid [11]. Coflow geometries have been considered extensively to study the dripping-to-jetting transition in confined geometries, both for liquid-liquid and liquid-gas coflows [12–15]. This transition depends on the propagation of an absolute instability originating from a growing disturbance downstream, itself arising from the Rayleigh-Plateau instability [16].

Several works report detailed comprehensive modeling of the dripping-to-jetting transition observed in liquid-liquid and liquid-gas microsystems [13,17–19] for low Reynolds number flows

*erriguible@enscbp.fr

†<http://www.icmcb-bordeaux.cnrs.fr>; Samuel.Marre@icmcb.cnrs.fr

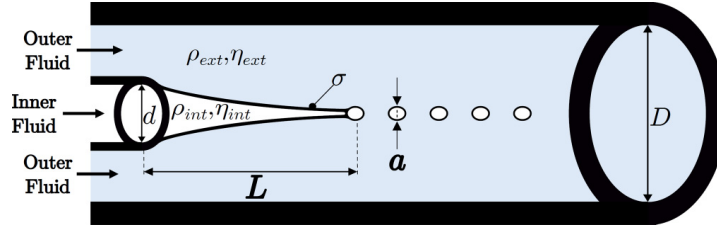


FIG. 1. Coflowing setup developed for this study. D and d are the inner diameters of the outer and inner tubing, respectively. L is the jet length, while a is the droplets diameter.

[$Re \equiv (v\rho d)/\eta$], typically $Re < 10$, where ρ is the fluid density, v is the fluid velocity, d is the flow characteristic length, and η is the dynamic viscosity. In such cases, the dripping and Rayleigh jetting regimes and the transitional boundaries between them can be organized using a map of the inner fluid Weber number [$We_{in} \equiv (v_{int}^2 \rho_{int} d)/\sigma$], where σ is the interfacial tension between the two immiscible fluids, versus outer fluid capillary number [$Ca_{ext} \equiv (v_{ext} \eta_{ext})/\sigma$], as previously described [13,14].

Aside from the Rayleigh regime observed for confined flows, jets exhibit other breakup modes that have been investigated for jetting into quiescent outer fluids [20]. Four distinct jetting regimes have been identified and reported so far [21] including the Rayleigh mode, the first and second wind-induced breakup modes, and the atomization regime [22,23]. These regimes and the transitions between them depend on several factors such as inertia, interfacial tension, and viscosity ratio of the fluids [24].

Even though inertia-driven jet breakup regimes occurring at larger Reynolds numbers ($Re > 100$) have been identified and detailed in several experimental works of unconfined jets, the case of microscale confined jetting has received scant attention. This is primarily due to the technical difficulties encountered when studying the high flow rates required to reach high Re regimes and the resulting high pressure drops, which complicate experimental investigation.

Studies using high-pressure microsystems can access high Re regimes consisting of gas-liquid, liquid-liquid, and even supercritical fluid (SCF)–liquid components. Recent publications have demonstrated the use of microfluidic systems at high pressures [25–27]. SCFs are of particular interest as working fluids, as they combine liquidlike densities and gaslike viscosities [28]. Moreover, SCF properties can be adjusted with minor changes of pressure and/or temperature, permitting study of inertial-viscous regimes that might otherwise be difficult to access experimentally. Accordingly, the use of high-pressure microsystems and SCFs permits the study of new conditions of flow fragmentation that have not been investigated previously. Of particular interest are inertia-driven regimes, where inertial forces ($F_{iner} = \rho v^2 d^2$) can overcome viscous ($F_v = \eta v d$) and interfacial ($F_{ITF} = \sigma d$) forces that typically dominate at the microscale. Previous work has exploited the experimental flexibility afforded by SCFs, and the dripping-to-jetting transition has been reported previously for a microconfined liquid/SCFs cocurrent flow [29,30]. In this Rapid Communication, we identify three jetting modes observed for coflows of either dense CO_2 (liquid or supercritical) or liquid pentane and water in a capillary microreactor. Each mode was identified by distinctive droplet sizes, size distributions, and the evolution of the jet length and shape. Here we report observations of such modes under microscale confined conditions.

The experimental high-pressure setup is composed of two silica capillaries inserted within one another (outer capillary: $D = 247 \pm 6 \mu\text{m}$ and inner capillary $d_{ext} = 167 \pm 6 \mu\text{m}$ and $d = 100 \pm 3 \mu\text{m}$), as shown in Fig. 1. Accordingly, the external hydraulic diameter D_h of the outer fluid is defined as $D_h = (D^2 - d_{ext}^2)/d_{ext}$. Two high-pressure syringe pumps (Teledyne ISCO 100DM) were used to feed CO_2 or pentane and water at constant flow rates, while a third pump was used in constant pressure mode as a back pressure regulator to maintain constant the outlet pressure at $p = 10 \text{ MPa}$ for the CO_2 -water system, i.e., above the critical pressure of CO_2 [$p_{c(CO_2)} = 7.38 \text{ MPa}$] or at $p = 0.1 \text{ MPa}$ for the pentane–water system. The capillary assembly was placed in

TABLE I. Physical properties and corresponding values for the dimensionless numbers (We, Ca, and Re) of CO₂ or pentane and water flows at $p = 10$ MPa (or $p = 0.1$ MPa) for $T = 20^\circ\text{C}$ (liquid CO₂ and liquid pentane) and $T = 48^\circ\text{C}$ (sc-CO₂), respectively. For the calculation, we have used: $d = 100 \mu\text{m}$, $D = 250 \mu\text{m}$; $25 < Q_{\text{CO}_2}(\mu\text{l min}^{-1}) < 1000$; $50 < Q_{\text{H}_2\text{O}}(\mu\text{l min}^{-1}) < 10\,000$; and $25 < Q_{\text{pentane}}(\mu\text{l min}^{-1}) < 1000$.

T	20 °C		48 °C		20 °C
P	10 MPa		10 MPa		0.1 MPa
Fluid	Liquid CO ₂	H ₂ O	sc-CO ₂	H ₂ O	Pentane
σ^{a} (mN m ⁻¹)	37.1	/	28.8	/	51.2
η (μPa s)	81.5	998.8	30.6	567.3	227.5
ρ (kg m ⁻³)	856.3	1002.7	421.6	993.2	625.8
We ^b	8×10^{-3}	0.01	0.02	0.01	3×10^{-3}
	—	—	—	—	—
Ca ^b	1.2	71.9	3.48	91.6	5.5
	1.3×10^{-4}	1.6×10^{-3}	1.3×10^{-4}	1.3×10^{-3}	2.3×10^{-4}
Re ^b	1.5×10^{-3}	0.15	1.6×10^{-3}	0.11	9.4×10^{-3}
	62.9	5	159	8.8	14.6
	—	—	—	—	—
	782.8	463	2217	837	583.7

^aVersus water.

^bDepending on flow rates.

a temperature-controlled bath [$20 < T(^{\circ}\text{C}) < 50$] and the coflow was monitored using a high-speed CCD camera (Phantom Miro 340; Vision Research, Inc.) mounted on a binocular microscope. Image resolution was $\sim 1.5 \mu\text{m}/\text{pixel}$, which allowed resolution of features larger than about $5 \mu\text{m}$. Jet lengths, droplets sizes, and size distributions were extracted from still images using the IMAGEJ software.

Actual fluid velocities inside the microchannel (v_{int} , v_{ext}) were estimated from the pump flow rates and accounting for the temperature dependence of density: $v_i = \frac{Q_{i(\text{pump})}}{S_i} \times \frac{\rho_{i(\text{pump})}}{\rho_{i(\text{bath})}}$, where S_i is the internal cross section area out of which the fluid i is passing, $Q_{i(\text{pump})}$ is the pump volumetric flow rate, while $\rho_{i(\text{pump})}$ and $\rho_{i(\text{bath})}$ are the fluid density in the pump (at $p = p_{\text{exp}}$ and room temperature) and in the capillary ($p = p_{\text{exp}}$ and $T = T_{\text{exp}}$), respectively. The physical properties of CO₂ and H₂O at experimental conditions were obtained from the REFPROP software [31] or from the literature [32]. Table I summarizes relevant physical properties and dimensionless numbers used in this work.

The conventional strategy to classify the jet breakup regimes is to monitor the evolution of the length of the coherent portion of the jet, the mean droplet size, and the droplet size distribution as functions of the external fluid velocity (v_{ext}). In a typical case, four flow regimes can be distinguished (Fig. 2).

Dripping. At low flow velocities, the classical dripping regime is observed, displaying an absence of jets with generation of large, monodisperse droplets at the tip of the inner capillary [Fig. 2(a)].

Rayleigh jetting. With increasing external flow velocity, classical dripping transitions to jetting occur. Jet length grows almost linearly with the external fluid velocity, as shown in Fig. 3(a). Downstream, the jet eventually breaks into monodisperse droplets due to the Rayleigh-Plateau instability [Figs. 2(b) and 2(c) and Supplemental Material movie [33]]. Breakup results from the growth of long-wavelength perturbations when the inertial forces ($F_{\text{iner}} = \rho v^2 d^2$) become equal to or greater than the interfacial forces ($F_{\text{ITF}} = \sigma d$), i.e., $\text{We} \sim 1$. These two first regimes, mostly

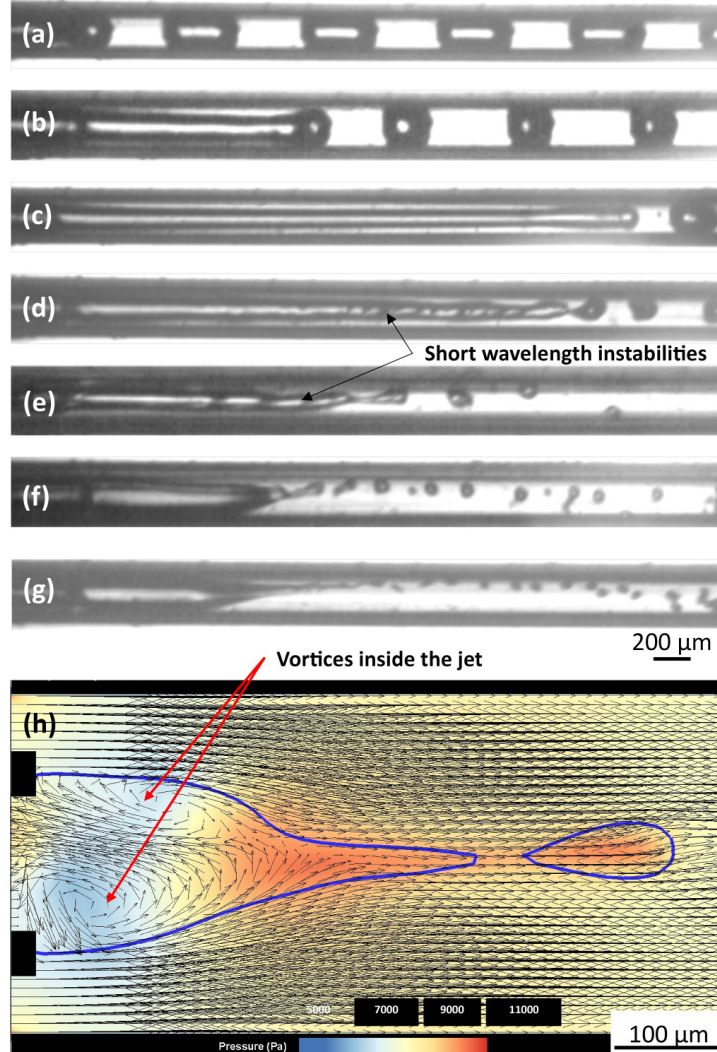


FIG. 2. (a) Optical images of the evolution of the jetting as a function of the outer fluid velocity: (a) dripping; (b),(c) Rayleigh jetting; (d),(e) sinuous wave breakup mode; (f),(g) atomizationlike mode. The pictures were obtained for $p = 10$ MPa, $T = 20$ °C; inner fluid: liquid CO_2 ; outer fluid: water, $v_{\text{int}}(\text{CO}_2) = 0.25$ m s $^{-1}$. (h) Median plane visualization of the 3D numerical modeling of the atomizationlike jetting mechanism displaying the velocity vectors inside the core of the jet ($p = 10$ MPa, $T = 20$ °C, $v_{\text{int}}(\text{CO}_2) = 0.25$ m s $^{-1}$; $v_{\text{ext}}(\text{H}_2\text{O}) = 4$ m s $^{-1}$). The arrows represent the velocity vectors, whose magnitudes are proportional to their length, while the color represents the relative pressure (P_r) spatial variations (the total pressure can be calculated as $P = P_r + 10$ MPa).

driven by interfacial forces, have been observed and studied several previous times at the microscale for liquid-liquid [13,14], liquid-gas [19], and supercritical fluid-liquid [29] coflows.

Inertia-driven jetting–sinuous wave breakup. With increasing velocity, the jet undergoes destabilization due to the effects of external inertial forces, in contrast with the behavior observed in the Rayleigh jetting mode. The viscous forces ($F_v = \eta v d$), which tend to stabilize the jet, are largely overcome by the inertial forces for $\text{Re} > 500$, resulting in the formation of sinuous waves, as previously observed for unconfined flows [22,24]. In the sinuous wave breakup regime, breakup stems primarily from the unstable growth of short-wavelength perturbations, probably arising from Kelvin-Helmholtz instabilities. The Kelvin-Helmholtz instabilities form due to the localized high-velocity ratio ($\frac{v_{\text{ext}}}{v_{\text{int}}}$) present on the surface of the jet (Figs. 2(d) and 2(e) and

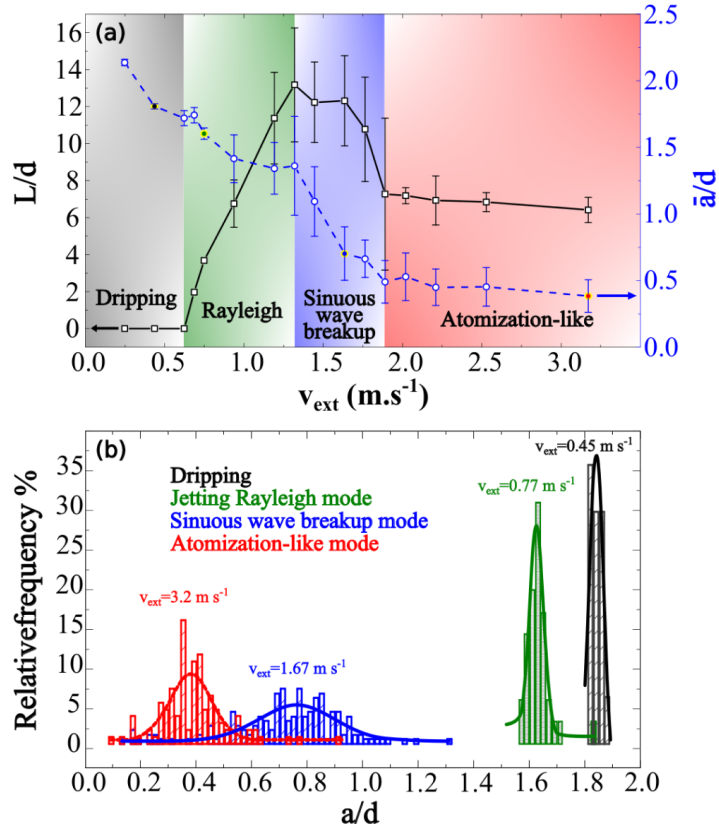


FIG. 3. Example of the regime characteristics used to categorize the breakup mechanisms. (a) Evolution of the jet length and the droplets mean size $\frac{\bar{a}}{d}$ as a function of v_{ext} and (b) the droplets size distributions for different values of v_{ext} , corresponding to the yellow circled point in (a). The data were obtained for $p = 10$ MPa, $T = 20$ °C; inner fluid: liquid CO₂; outer fluid: water, $v_{int(CO_2)} = 0.25$ m s⁻¹.

Supplemental Material movie [34]). Two important characteristics can be highlighted: (i) the jet length continuously decreases with increasing outer fluid velocity and (ii) the polydispersity of the droplet size increases, relative to the distributions observed in the Rayleigh jetting mode, since the jet breaks into fluid ligaments through a pullout mechanism, with the fragments later forming droplets due to Rayleigh mechanism or minimization of surface energy. Filament breaking, which can be described as secondary atomization [35], produces a droplet distribution with much greater polydispersity than is observed in the dripping or Rayleigh jetting regimes [Fig. 3(b)].

Inertia-driven jetting–atomizationlike. At high values of external fluid inertial force ($F_{iner,ext}$), the jet length stabilizes with increasing fluid velocity (Figs. 2(f) and 2(g) and Supplemental Material movies [36]). Smaller ligaments form, which transform nearly instantaneously into droplets. In this regime, droplet size can reach values as small as $0.4d$ (Fig. 3). One of the main distinguishing features of this regime is characterized by an enlargement of the jet diameter, relative to the nozzle diameter. To confirm this unexpected behavior, we have performed numerical simulations using a three-dimensional (3D) incompressible one-fluid model [37], already validated for liquid jet breakup in pressurized CO₂ [30]. This model is selected since the flow behavior is clearly nonaxisymmetrical for inertial modes (sinuous wave breakup and atomizationlike modes). Compressed CO₂ and water used in this work are considered as immiscible fluids in the investigated conditions, so the computational study must account for two-phase flow. Accordingly, the Brackbill model [38] was employed to compute the interfacial forces, while the Volume Of Fluid (VOF) approach was used with a piecewise linear interface construction for the interface tracking [39]. As observed in numerical simulations (Fig. 2(h) and Supplemental Material movies [40]), the high velocity ratio

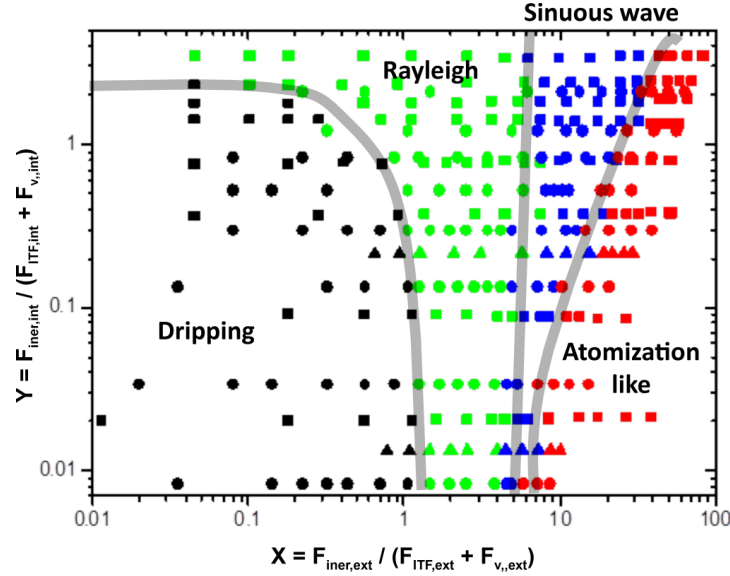


FIG. 4. Log-log plot of the ratio ($X:Y$) of the inertial forces over the sum of the viscous and interfacial forces for the sc-CO₂–water ($p = 10$ MPa, $T = 48$ °C : ■), pentane–water ($p = 0.1$ MPa, $T = 20$ °C : ▲), and liquid CO₂–water ($p = 10$ MPa, $T = 20$ °C : ●) systems. The dripping regime is indicated in black, the Rayleigh type jets in green, the sinuous wave breakup mode is in blue, and the atomizationlike mode points are in red.

($\frac{v_{\text{ext}}}{v_{\text{int}}} > 10$) generates hydrodynamic recirculating vortices within the jet, which confine the inner fluid at the tip and lead to noticeable jet enlargement.

Next, we sought to generalize our observations by studying the effects of the experimental parameters (inner and outer fluid velocities, p , T) on the interfacial and viscous forces which govern jet behavior. Three fluid–fluid systems (i.e., sc-CO₂ water, liquid CO₂ water, and pentane water) were studied so that the widest possible range of experimental parameters could be included in this work and to arrive at the most general possible conclusions. We varied the experimental parameters to investigate the effects of inertia compared to interfacial and viscous forces. These conditions result in high Reynolds number flows for both the inner and outer fluid (up to $\text{Re} = 2200$; Table I), which have not been previously investigated due to the practical restrictions associated with working with high flow rates and the resultant high-pressure drops. Investigating these effects provides data to unify the four distinct coflow regimes in a single picture. Utada *et al.* [6] proposed categorizing the transition between the dripping and the jetting regime in micro-coflows using the $[\text{We}_{\text{int}}, \text{Ca}_{\text{ext}}]$ diagram, which takes into account the inner flow inertial and interfacial forces, and the outer flow viscous and interfacial forces. These previous studies considered only inner and outer flows with very low inertial forces ($\sim 10^{-3}$ μN), possibly preventing observations of the sinuous wave and atomization breakup regimes shown here. In contrast, we explored conditions where the inertial forces are in a much wider range: 10^{-2} – 10^1 μN .

We categorize the jetting regimes and their domains of existence by using the ratio of the inertial forces over the sum of the other forces (viscous and interfacial) for both the inner and outer fluid. This approach makes possible the representation of the jet phase diagram, $Y = f(X)$ consisting of a log-log plot of nondimensional scaling parameters: $X = \frac{F_{\text{iner,ext}}}{(F_{\text{ITF,ext}} + F_{\text{v,ext}})}$ and $Y = \frac{F_{\text{iner,int}}}{(F_{\text{ITF,int}} + F_{\text{v,int}})}$. This nondimensionalization emphasizes the effects of inertial forces over viscous and interfacial ones.

In Fig. 4, we have represented all available experimental data and categorized their flow behavior into one of the four regimes. Figure 4 provides data for the sc-CO₂/water (48 °C, 10 MPa), the liquid CO₂/water (20 °C, 10 MPa), and the liquid pentane–water (20 °C, 0.1 MPa) systems.

As a first observation, Fig. 4 shows that the transition from dripping to jetting occurs when $X > 1$ and/or $Y > 1$ (Fig. 4), as expected. Indeed, the inertial forces at these conditions are greater than the interfacial and viscous forces, leading to jetting.

A remarkable result arises at the transition from Rayleigh jetting to sinuous wave breakup regime. Indeed, the experimental data indicate that, independent of the inner fluid force ratio, the “inertial regime” (i.e., sinuous wave and/or atomizationlike breakup) is never attained, provided that $X < 5$ (Fig. 4). For $X < 5$, the outer fluid viscous and interfacial forces are sufficient (although smaller than the inertial forces) to stabilize the jet and prevent unstable growth of short-wavelength, Kelvin-Helmholtz perturbations that would otherwise lead to the sinuous wave breakup regime. With increasing X , the jet enters the atomization regime. Atomization occurs when the inner fluid viscous and interfacial forces overcome the inertial forces (low Y values; Fig. 4). In contrast, when the inertial forces of the inner fluid are sufficient (higher Y values), they tend to extend the length of the jet, stabilizing the sinuous wave breakup mode (Fig. 4).

The observations and diagram presented here are not unique to [dense CO₂ (liquid or supercritical)–water] micro coflows. Indeed, the pentane–water system (Fig. 4, triangles) obeys the same jetting behavior as the sc-CO₂–water system (Fig. 4, squares) and the liquid CO₂–water (Fig. 4, circles), when nondimensional scaling parameters X and Y are used for data interpretation. Therefore, while supercritical fluids are convenient for this type of study, the conclusions are not restricted to cases in which one of the fluids is at supercritical conditions.

In conclusion, we have studied the jetting behavior of micro-confined co-flows using a high pressure microchannel device. Several fluid-fluid systems were studied, including sc-CO₂–water, liquid CO₂–water, and pentane–water. In addition to the well-known dripping and Rayleigh jetting modes, two new inertia-driven modes were observed, namely, the so-called sinuous wave breakup and the atomizationlike regime. We find that all the available data can be captured by a log-log plot using dimensionless scaling parameters. This study extends previous work on microscale-confined coflowing liquids to permit observation of qualitatively new behavior and unifies previous studies by mapping jet behavior onto a single diagram.

This work provides the basis for many new microfluidics experiments, including those involving production of submicron droplets, as reported by other approaches [41]. Future fundamental studies should investigate areas of the phase diagram which remain to be explored, especially those for $Y < 10^{-2}$ and $Y > 10^1$. Data are required at these conditions to provide a full understanding of the transition between viscous/interfacial-driven flows and inertia-driven flows.

Acknowledgments. This study was supported by the French National Research Agency (projects: ANR-17-CE07-0029 - SUPERFON and ANR-12-SEED-0001 - CGS μ Lab), the University of Bordeaux (Ph.D. funding of F.Z.), the IFPEN (Ph.D. funding of T.G.), the CNES. and the Région Nouvelle Aquitaine. This work has received funding from the European Research Council (ERC) under the European Union’s Horizon 2020 research and innovation program (Grant Agreement No. 725100, project Big Mac). M.T.T. thanks the U.S. National Science Foundation for support (CBET 1554283). S.M. and A.E. thank Fabien Palencia for technical support.

-
- [1] R. Seemann, M. Brinkmann, T. Pfohl, and S. Herminghaus, Droplet based microfluidics, *Rep. Prog. Phys.* **75**, 016601 (2012).
 - [2] R. K. Shah, H. C. Shum, A. C. Rowat, D. Lee, J. J. Agresti, A. S. Utada, L. Y. Chu, J. W. Kim, A. Fernandez-Nieves, C. J. Martinez, and D. A. Weitz, Designer emulsions using microfluidics, *Mater. Today* **11**, 18 (2008).
 - [3] V. Chokkalingam, S. Herminghaus, and R. Seemann, Self-synchronizing pairwise production of monodisperse droplets by microfluidic step emulsification, *Appl. Phys. Lett.* **93**, 254101 (2008).
 - [4] M. Hashimoto, P. Garstecki, and G. M. Whitesides, Synthesis of composite emulsions and complex foams with the use of microfluidic flow-focusing devices, *Small* **3**, 1792 (2007).
 - [5] S.-Y. The, R. Lin, L.-H. Hung, and A. P. Lee, Droplet microfluidics, *Lab Chip* **8**, 198 (2008).

- [6] A. S. Utada, L. Y. Chu, A. Fernandez-Nieves, D. R. Link, C. Holtze, and D. A. Weitz, Dripping, jetting, drops, and wetting: The magic of microfluidics, *MRS Bull.* **32**, 702 (2007).
- [7] T. M. Keenan, C. H. Hsu, and A. Folch, Microfluidic “jets” for generating steady-state gradients of soluble molecules on open surfaces, *Appl. Phys. Lett.* **89**, 114103 (2006).
- [8] S. Marre and K. F. Jensen, Synthesis of micro and nanostructures in microfluidic systems, *Chem. Soc. Rev.* **39**, 1183 (2010).
- [9] H. Song, D. L. Chen, and R. F. Ismagilov, Reactions in droplets in microfluidic channels, *Angew. Chem., Int. Ed.* **45**, 7336 (2006).
- [10] K. S. Elvira, X. Casadevall, I. Solvas, R. C. R. Wootton, and A. J. deMello, The past, present and potential for microfluidic reactor technology in chemical synthesis, *Nat. Chem.* **5**, 905 (2013).
- [11] L. Rayleigh, On the instability of jets, *Proc. London Math. Soc.* **s1**, 4 (1878).
- [12] P. Guillot, A. Colin, A. S. Utada, and A. Ajdari, Stability of a Jet in Confined Pressure-Driven Biphasic Flows at Low Reynolds Numbers, *Phys. Rev. Lett.* **99**, 104502 (2007).
- [13] A. A. Utada, A. Fernandez-Nieves, H. A. Stone, and D. A. Weitz, Dripping to Jetting Transitions in Coflowing Liquid Streams, *Phys. Rev. Lett.* **99**, 094502 (2007).
- [14] S. Y. Mak, Y. Chao, and H. C. Shum, The dripping-to-jetting transition in a co-axial flow of aqueous two-phase systems with low interfacial tension, *RSC Adv.* **7**, 3287 (2017).
- [15] C.-X. Zhao and A. P. J. Middelberg, Two-phase microfluidic flows, *Chem. Eng. Sci.* **66**, 1394 (2011).
- [16] A. S. Utada, A. Fernandez-Nieves, J. M. Gordillo, and D. A. Weitz, Absolute Instability of a Liquid Jet in a Coflowing Stream, *Phys. Rev. Lett.* **100**, 014502 (2008).
- [17] M. A. Herrada, A. M. Gañán-Calvo, A. Ojeda-Monge, B. Bluth, and P. Riesco-Chueca, Liquid flow focused by a gas: Jetting, dripping, and recirculation, *Phys. Rev. E* **78**, 036323 (2008).
- [18] M.-L. Cordero, F. Gallaire, and C. N. Baroud, Quantitative analysis of the dripping and jetting regimes in co-flowing capillary jets, *Phys. Fluids* **23**, 094111 (2011).
- [19] S. Haase, Characterisation of gas-liquid two-phase flow in minichannels with co-flowing fluid injection inside the channel, part I: Unified mapping of flow regimes, *Int. J. Multiphase Flows* **87**, 197 (2016).
- [20] M. Birouk and N. Lekic, Liquid jet breakup in a quiescent atmosphere: A review, *Atomization and Sprays* **19**, 501 (2009).
- [21] R. D. Reitz and F. V. Bracco, Mechanisms of breakup of round liquid jets, *Encyclopedia of Fluid Mechanics* (Gulf Publishing Co., Houston, 1986), Vol. 3, pp. 233–249.
- [22] S. P. Lin and R. D. Reitz, Drop and spray formation from a liquid jet, *Annu. Rev. Fluid Mech.* **30**, 85 (1998).
- [23] A. Erriguible, S. Vincent, and P. Subra-Paternault, Numerical investigations of liquid jet breakup in pressurized carbon dioxide: Conditions of two-phase flow in supercritical antisolvent process, *J. Supercrit. Fluids* **63**, 16 (2012).
- [24] A. H. Lefebvre and V. G. McDonell, in *Atomization and Sprays*, Combustion: An international series, edited by N. Chigier (Hemisphere Publishing Corp., New York, 1989).
- [25] S. Marre, Y. Roig, and C. Aymonier, Supercritical microfluidics: Opportunities in flow-through chemistry and materials science, *J. Supercrit. Fluids* **66**, 251 (2012).
- [26] S. Ogden, R. Boden, M. Do-Quang, Z. Wu, G. Amberg, and K. Hjort, Fluid behavior of supercritical carbon dioxide with water in a double-Y-channel microfluidic chip, *Microfluid. Nanofluid.* **17**, 1105 (2014).
- [27] N. Qin, J. Z. Wen, and C. L. Ren, Highly pressurized partially miscible liquid-liquid flow in a micro-T-junction. I. Experimental observations, *Phys. Rev. E* **95**, 043110 (2017).
- [28] A. Loppinet-Serani, C. Aymonier, and F. Cansell, Current and foreseeable applications of supercritical water for energy and the environment, *ChemSusChem* **1**, 486 (2008).
- [29] S. Marre, C. Aymonier, P. Subra, and E. Mignard, Dripping to jetting transitions observed from supercritical fluid in liquid microflows, *Appl. Phys. Lett.* **95**, 134105 (2009).
- [30] R. Guillaument, A. Erriguible, C. Aymonier, S. Marre, and P. Subra-Paternault, Numerical simulation of dripping and jetting in supercritical fluids/liquid micro coflows, *J. Supercrit. Fluids* **81**, 15 (2013).
- [31] See <https://www.nist.gov/srd/refprop>.

- [32] A. Hebach, A. Oberhof, N. Dahmen, A. Kogel, H. Ederer, and E. Dinjus, Interfacial tension at elevated pressures—Measurements and correlations in the water + carbon dioxide system, *J. Chem. Eng. Data* **47**, 1540 (2002).
- [33] See Supplemental Material at <http://link.aps.org/supplemental/10.1103/PhysRevFluids.3.092201> for the Rayleigh breakup regime movie.
- [34] See Supplemental Material at <http://link.aps.org/supplemental/10.1103/PhysRevFluids.3.092201> for the sinuous wave breakup regime movie.
- [35] A. Zandian, W. A. Sirignano, and F. Hussain, Planar liquid jet: Early deformation and atomization cascades, *Phys. Fluids* **29**, 062109 (2017).
- [36] See Supplemental Material at <http://link.aps.org/supplemental/10.1103/PhysRevFluids.3.092201> for the atomization-like breakup regime at 1000 and 50,000 frames per second, respectively.
- [37] I. Kataoka, Local instant formulation of two-phase flow, *Int. J. Multiphase Flow* **12**, 745 (1986).
- [38] J. U. Brackbill, A continuum method for modeling surface tension, *J. Comput. Phys.* **100**, 335 (1992).
- [39] D. L. Youngs, Time-dependent multi-material flow with large fluid distortion. In K. W. and M. J. Baines, *Numerical Methods for Fluid Dynamics* (Academic, New York, 1982).
- [40] See Supplemental Material at <http://link.aps.org/supplemental/10.1103/PhysRevFluids.3.092201> for (i) the velocity vectors and pressure field in the meridian plane of the reactor obtained by 3D simulation of the atomizationlike breakup regime and (ii) the evolution of the phase function in the reactor for the same 3D simulation.
- [41] W. C. Jeong, J. M. Lim, J. H. Kim, Y. J. Lee, S. H. Kim, G. Lee, J. D. Kim, G. R. Yi, and S. M. Yang, Controlled generation of submicron emulsion droplets via highly stable tip-streaming mode in microfluidic devices, *Lab Chip* **12**, 1446 (2012).